Oriented Magnetic Field Measurements during IODP Expedition 330 to the Louisville Seamount Chain

Von der Fakultät für Elektrotechnik, Informationstechnik, Physik
der Technischen Universität Carolo-Wilhelmina zu Braunschweig zur
Erlangung des Grades eines Doktors der Naturwissenschaften
(Dr.rer.nat.)
genehmigte Dissertation

von Sebastian Ehmann
aus Ansbach, Mittelfranken

Eingereicht am: 09.02.2016

Mündliche Prüfung (Disputation) am: 20.07.2016

1. Referent: Prof. Dr. Andreas Hördt

2. Referent: Prof. Dr. Karl-Heinz Glaßmeier

Druckjahr: 2016

Table of Contents

Vorveröffentlichungen der Dissertation

Teilergebnisse aus dieser Arbeit wurden mit Genehmigung der Fakultät für Elektrotechnik, Informationstechnik, Physik, vertreten durch den Betreuer der Arbeit, in folgenden Beiträgen vorab veröffentlicht:

Publikationen

Ehmann, S., Hördt, A., Leven, M., Virgil, C. *Paleomagnetic inclination and declination from three-component borehole magnetometer data-New insights from logging in the Louisville seamounts* J. Geophys. Res. Solid Earth, 120, doi:10.1002/2014JB011531.

Vorträge

Ehmann, S., Hördt, A., Virgil, C., Leven, M. *Bestimmung der Magnetisierungsrichtung aus dreikomponentigen Magnetfeldmessungen in tiefen Bohrungen.* 74. Jahrestagung der Deutschen Geophysikalischen Gesellschaft, 2014

Ehmann, S., Anderson, L., Hördt, A., Leven, M., Virgil, C. *Rock magnetization from three component magnetic logging data measured on the Louisville Hotspot trail during IODP Expedition 330.* IODP/ICDP Kolloquium Freiberg, 2013

Ehmann, S., Anderson, L., Hördt, A., Leven, M., Virgil, C. *Berechnung von Magnetisierungen aus dreikomponentigen Magnetfeldmessungen in den Louisville Seamounts während IODP Expedition 330.* 73. Jahrestagung der Deutschen Geophysikalischen Gesellschaft, 2013

Ehmann, S., Anderson, L., Hördt, A., Leven, M., Virgil, C., Expedition 330 Scientists. *Dreikomponentige Magnetfeldmessungen in den Louisville Seamounts während IODP Expedition 330.* 72. Jahrestagung der Deutschen Geophysikalischen Gesellschaft, 2012

Ehmann, S., Anderson, L., Hördt, A., Leven, M., Virgil, C., Expedition 330 Scientists. *Dreikomponentige Magnetfeldmessungen in den Louisville Seamounts während IODP Expedition 330.* 24. Schmucker-Weidelt-Kolloquium für Elektromagnetische Tiefenforschung, 2011

Poster

Ehmann, S., Hördt, A., Leven, M., Neuhaus, M., Virgil, C. *Bestimmung der Magnetostratigraphie aus Bohrlochmessungen.* IODP/ICDP Kolloquium Erlangen 2014

Ehmann, S., Anderson, L., Hördt, A., Leven, M., Virgil, C., Expedition 330 Scientists. *Three-component magnetic downhole measurements on the Rigil and Burton Guyots, Louisville Seamount Trail, IODP Expedition 330.* IODP/ICDP Kolloquium Kiel, 2012

Ehmann, S., Anderson, L., Hördt, A., Leven, M., Virgil, C., Expedition 330 Scientists. *Three-component magnetic downhole measurements on the Rigil and Burton Guyots, Louisville Seamount Trail, IODP Expedition 330.* Fall Meeting of the American Geoscience Union, 2011

Ehmann, S., Virgil, C., Hördt, A., Leven, M. *Magnetic Measurements in Boreholes – Influence of Tool Strings.* IODP/ICDP Kolloquium Münster, 2011

Abstract

The major objective of this thesis is to reorient and analyze three component magnetic field data recorded in two boreholes during Integrated Ocean Drilling Program (IODP) Expedition 330 to the Louisville Seamount Chain. One aim of the expedition was to determine whether the hotspot that created the seamount chain during the past 80 million years is moving relative to the Hawaiian-Emperor hotspot or if it remained stationary within the mantle.

The magnetic field measurements were conducted with the Göttinger Bohrlochmagnetometer, which comprises fibre optic gyros that measure the rotations of the tool within the borehole. In this thesis, I use different algorithms to reorient the measured magnetic field from the tools reference frame into the geographical reference frame. This purpose requires sensors of high accuracy and careful data processing, as, for example, an error in orientation of 1° in a typical magnetic field of 40000 nT leads to errors of 700 nT in the individual components of the magnetic field. I present several algorithms that use various combinations of the available sensors to achieve the best reorientation possible. Among others, I introduce two new sensor fusion algorithms for gyro and inclinometer data based on a Kalman filter.

Oriented magnetic field data can be used to determine both the inclination and declination of the magnetization of the rocks surrounding the borehole by the application of appropriate models. Measurements on drill core samples can typically only be used to determine the inclination of magnetization, as cores are usually azimuthally unoriented.

In the subsequent analysis of the oriented magnetic field data, I use different models for the drilled igneous layers to calculate the magnetization of the subsurface. As horizontal layers turn out to be insufficient to explain the data, I extend the interpretation to inclined layers. I introduce a new approximation for the magnetic field of inclined layers that can be used to separate the calculation of magnetization in an inversion using horizontal layers and a following consideration of potential layer geometries. My approximation additionally reveals possible ambiguities and errors of the measurements.

Using images of the borehole wall that give additional information about the possible geometry of a drilled layer inside Burton Guyot (Site U1376), I determine a mean inclination of magnetization of 58.9° and a mean declination of magnetization of 0.4°. These results agree with current theories of a stationary Louisville hotspot. In addition, the result for the declination suggests that Burton Guyot has not been rotated since its formation.

Zusammenfassung

Das Thema dieser Doktorarbeit ist die Reorientierung und Auswertung von vektoriellen Magnetfelddaten, die in zwei Bohrungen während der IODP Expedition 330 zu den Louisville Seamounts aufgezeichnet wurden. Ein Ziel der Expedition war festzustellen, ob der Hotspot, der für die Entstehung dieser Inselkette im Laufe der vergangenen 80 Millionen Jahre verantwortlich ist, sich relativ zu dem Hawaiian-Emperor Hotspot im Erdmantel bewegte oder ob er stationär blieb.

Für die Magnetfeldmessungen wurde das Göttinger Bohrlochmagnetometer verwendet, dessen faseroptische Kreisel in der Lage sind, die Drehungen der Sonde im Bohrloch zu bestimmen, wodurch das gemessene Magnetfeld aus dem Bezugssystem der Sonde in das geographische Koordinatensystem reorientiert werden kann. Hierfür ist eine hochgenaue Sensorik und sorgfältige Datenprozessierung nötig, da beispielsweise ein Orientierungsfehler von 1° bei einem typischen Hintergrundfeld von 40000 nT zu Fehlern von 700 nT in den Einzelkomponenten des Magnetfelds führt. Ich stelle verschiedene Algorithmen vor, die auf unterschiedliche Art und Weise die vorhandenen Sensoren kombinieren um die Daten bestmöglich zu orientieren, unter anderem zwei neue Sensorfusionsalgorithmen für Faserkreisel- und Inklinometerdaten die auf einem Kalman Filter basieren.

Der Vorteil von orientierten Magnetfeldmessungen ist, dass man über entsprechende Modelle neben der Inklination der Magnetisierung auch die Deklination der Magnetisierung des die Bohrung umgebenden Gesteins bestimmen kann. Anhand von Messungen an Bohrkernen lässt sich im Regelfall nur die Inklination der Magnetisierung bestimmen, da die Kerne meist unorientiert entnommen werden.

Für die weitere Auswertung der Magnetfelddaten verwende ich verschiedene Schichtmodelle. Da horizontale Schichtmodelle nicht ausreichen um die vorhandenen Daten zu erklären, weite ich die Interpretation auf geneigte Schichten aus. Hierzu stelle ich eine neue Näherung vor, die es ermöglicht, die Inversion der Magnetisierung in zwei Schritte aufzuteilen. Im ersten Schritt wird ein Horizontalschichtmodell berechnet, woraufhin getrennt davon im zweiten Schritt mögliche Schichtgeometrien berücksichtigt werden. Die Näherung kann auch dafür benutzt werden, um Aussagen über mögliche Uneindeutigkeiten und Fehler von Messungen zu treffen.

Unter Zuhilfenahme von Informationen über mögliche Schichtgeometrieen aus Bildern der Bohrlochwand ermittle ich aus den Daten einer Schicht des Seamounts Burton Guyot (Site U1376) eine mittlere Inklination der Magnetisierung von 58.9° und eine mittlere Deklination der Magnetisierung von 0.4°. Diese Ergebnisse stimmen mit gängigen Theorien überein, die von einem stationären Louisville-Hotspot ausgehen. Zusätzlich deuten die Ergebnisse für die Deklination darauf hin, dass Burton Guyot seit seiner Entstehung nicht gedreht wurde.

1 Introduction

1.1. Motivation and Objectives

Ever since the ground breaking publication of Wegener (1915), who postulated continental drift based on geological evidence, and the following works of other authors on the topography (e.g. Hess, 1962) and magnetic structure of the ocean floor (Vine and Matthews, 1963; Pitman and Heirtzler, 1966), the theory of plate tectonics explains the history of formation, movement and distribution of the continents and tectonic plates. Wegener's theory can explain a wide and diverse range of topics such as fossil findings (Wegener, 1915) and migration patterns of turtles (Carr and Coleman, 1974).

McElhinny and McFadden (2000) consider the publications of Irving (1956) and Runcorn (1956) as key points for the paleomagnetic aspect of plate tectonics, as both authors showed that measurements of the direction of magnetization of rock samples allow for a reconstruction of the paths of continents. Since then, more than 9259 paleomagnetic poles have been published (Pisarevsky, 2005) and, together with other data, allow for a reconstruction of the history of the continents for more than the last 500 Ma (Gubbins and Herrero-Bervera, 2007). However, many questions remain to be answered, in particular about the oceanic plates: obtaining oriented rock samples for detailed paleomagnetic studies is challenging, and therefore their history of movement is not known in similar detail as of the continents (Sager, 2006). Most of the published data stems from measurements on only partially oriented core samples or inversion of ship-based magnetic field measurements (Beaman et al., 2007) and thus do not give a complete view of the magnetization.

Detailed information about plate movements in the past also serves as validation for large scale simulations of mantle flow (Steinberger and Calderwood, 2006). An observation of the processes within the mantle is only possible using seismic tomography (e.g. Boschi et al., 2009), which, due to the lower number of earthquakes and seismic observatories, is limited in resolution below the oceanic plates (French and Romanowicz, 2015). Additionally, seismic tomography can only give a present-day snapshot of the state of the mantle; here, the past movements of the plates determined from paleomagnetic measurements can be used to assess the validity of flow models.

Island chains of volcanic origin play an important role in the discussion about the dynamics of the upper mantle and the origin of intraplate volcanism: following the hypothesis that some of them are formed by narrow conduits of magma uprising from Earth's mantle, so-called mantle plumes (Morgan, 1971), the past movement of these island chains gives insight into the convection patterns of the mantle.

However, the problem of the paleomagnetic data coverage for oceanic plates remains, as many of the volcanoes that have formed the island chains are now extinct and the

islands have submerged and are no longer easily accessible. Therefore, sampling these so-called seamounts is mostly limited to dredging and drilling. Dredged rock samples can only be used to estimate the strength of the paleomagnetic field and most drill core samples are azimuthally unoriented and only allow for a measurement of the inclination of magnetization (Gubbins and Herrero-Bervera, 2007).

Some solutions that allow for a determination of the declination are described by Morris et al. (2009), who for their part match structures both visible in oriented images of the borehole wall and visible on drill cores to reorient drill core samples from Integrated Ocean Drilling Program (IODP) Expedition 304/305. Fontana et al. (2010) give a comprehensive overview of core reorientation techniques using borehole images and state that image matching is impeded by the different diameters of borehole and core, which causes a difference in the vertical amplitude of structures. Hurst et al. (1994) (as cited by Morris et al., 2009) were the first to use a submersible (the Alvin) to gain oriented cores of the uppermost meter of the oceanic crust. Allerton and Tivey (2001) use a remotely operated drill system that can be lowered on a wireline to collect oriented samples of the uppermost meter of the crust. The orientation of the drill is determined using a magnetic compass, and technical measures assure that the core receives a continuous marking indicating its orientation. However, the compass is considerably affected by the metallic parts of the drill rig. A compensation is possible in parts, but the compass data becomes invalid when the slope of the seafloor is above 10° (Smith et al., 2001), which, in combination with the shallow depth of penetration, limits the use of the drill system.

The approach chosen in this thesis for the determination of the declination of magnetization is the measurement of the geographically oriented magnetic field vector within a borehole and the subsequent calculation of the vector of magnetization.

The capabilities of oriented magnetic field measurements have long been recognised, and were initially focussed on the detection of off-borehole bodies (Levanto, 1959; Silva and Hohmann, 1981). Here, for example, they can be used to unambiguously determine the location of pipes or other metallic objects (Ehmann, 2010).

Bosum and Scott (1988) were the first to deploy an oriented downhole magnetometer in order to determine the direction of magnetization of oceanic crust during Ocean Drilling Program (ODP) Leg 102 (see also Shipboard Scientific Party, 1986; Bosum et al., 1988, for more detail). Further measurements were supposed to be made during ODP Leg 106/109, but the magnetometer got damaged and could only measure the vertical magnetic field (Shipboard Scientific Party, 1988; Bosum and Kopietz, 1990). A second japanese magnetometer used during Leg 106/109 was only able to measure the total magnetic field (Shipboard Scientific Party, 1988; Hamano and Kinoshita, 1990).

During ODP Leg 118, an oriented magnetometer built by the USGS (Scott and Olson, 1985) was used to conduct measurements of the magnetic field (Shipboard Scientific Party, 1989; Pariso et al., 1991). A german oriented magnetometer was supposed to be run during ODP Leg 148, but the mechanical gyro was not delivered in time, so only the vertical and horizontal components could be measured (Shipboard Scientific Party, 1993).

The Göttingen Borehole Magnetometer (GBM, Leven, 1997), which was used for the measurements during IODP Expedition 330, was introduced to ODP during Leg 197 (Gaillot et al., 2004). It was also deployed during IODP Expedition 304/305 (Expedition 304/305 Scientists, 2006) and IODP Expedition 351. The GBM is, to my knowledge, the only scientific borehole magnetometer that uses fiber optic gyros for orientation, which is a considerable advantage over mechanical gyros, whose function is negatively affected by the shocks and vibrations occurring within a borehole.

IODP Expedition 330 to the Louisville Seamount chain took place in the south-west Pacific Ocean from 13 December 2010 to 11 February 2011. A major goal of the Expedition is the determination of possible past movement of the Louisville Hotspot by means of paleomagnetic measurements. The GBM was deployed during the Expedition in order to aid with the determination of the direction of magnetization, in particular the declination. There are several challenges associated with oriented measurements of the magnetic field and the calculation of the magnetization vector:

- Reorientation of the magnetic field data
- Choosing the appropriate model for the data
- Estimating the errors

A key part of vector magnetic measurements is the reorientation of the magnetic field data from the internal reference frame of the tool to the geographic reference frame. Here, algorithms used by one tool can not necessarily be used by a different tool without modification, as the type, amount and data rate of sensors typically differ. There are several publications describing the reorientation methods used for GBM data (Klein, 2009; Ehmann, 2010; Virgil et al., 2010, 2011; Virgil, 2012; Virgil et al., 2015; Ehmann et al., 2015), but every new data set presents its own challenges. A key aspect of this thesis is therefore the enhancement of existing algorithms and the development of new algorithms, with a special focus on sensor-fusion methods for gyro and inclinometer data.

After reorientation of the magnetic field data, the information about the magnetization has to be extracted. Existing publications on the interpretation of downhole magnetic field measurements (both oriented and unoriented data) typically use horizontal layers intersected by a circular borehole as a representation of the subsurface (Bosum et al., 1988; Pozzi et al., 1988; Fieberg, 1994; Nogi et al., 1995; Williams, 2006). Other authors suggest inclined circular layers (Gallet and Courtillot, 1989) or rectangular layers (Hamano and Kinoshita, 1990). As the lateral extent of the drilled structures is not always known, typically an infinite outer radius is chosen. Virgil (2012) uses elliptical disks to interpret data from the Outokumpu formation and provides detailed information about the influence of the geometry and outer radius of the layers on the magnetic field. I am focussing on models using horizontal and inclined layers of infinite extent. In particular, I am introducing an approximation for the magnetic field of inclined layers that allows to separate data modeling in an inversion for horizontal layers and a subsequent consideration of possible dips and azimuths.

The geometry chosen for the models of the subsurface has a large effect on the results. Based on a model of circular inclined layers given by Gallet and Courtillot (1989), Tivey et al. (2005) discuss the influence of the layer dip on the inclination calculated for ODP Leg 129 data and find that, for example, a layer dip of 50° can cause an error in the inclination of magnetization of 70°, but they do not consider the effect of the layer azimuth. Gallet and Courtillot (1989) discuss the effect of dip and azimuth of a layer, but mostly focus on details of the magnetic field and not on errors in the determination of the magnetization. Other authors (Steveling et al., 2003, for example) acknowledge the importance of the geometry of the layers for the interpretation of the data, but do not give an estimate of the error caused by a potentially wrong geometry. Here, my approximation for inclined layers can be used to efficiently assess the influence of uncertainties in the geometric parameters of a layer on the direction of magnetization. Without further knowledge about the magnetization and geometry of an inclined layer, a linear dependence of the error in the declination on the error in the azimuth of the layer should be assumed.

1.2. Thesis Structure

In Section 2.1, I give an introduction to the theory and history of Earth's magnetic field, followed by a summary of paleomagnetism (Section 2.2) and magnetic potential field theory (Section 2.3). The main purpose of these sections is to recall the most important aspects into the memory of the reader and to include all information and background necessary for an understanding of this thesis. The following Section 2.4 gives a historic overview of the methods used for magnetic field measurements in boreholes as well as details of the Göttingen Borehole Magnetometer, the tool that is used for the measurements described in this thesis. Chapter 3 then gives more detail about Expedition 330, its scientific background and the questions that it was supposed to answer.

The following chapters form the core of this thesis: they guide through the data processing steps necessary to transform raw data into interpretable values (Chapter 4), different methods of reorienting the magnetic field data (Chapter 5) as well as different methods of data interpretation (Chapter 6). After describing reorientation methods using one fiber optic gyro and inclinometers (Section 5.3), explaining the standard method for data reorientation developed during recent years (Section 5.4) and a new method for treating uncorrected offsets of the fiber optic gyros (Section 5.5), I am introducing two new reorientation methods based on a sensor fusion of gyro and inclinometer data by means of a Kalman filter (Section 5.6). The following reorientation of the Louisville magnetic field data is then conducted using the most appropriate algorithm for each data set.

As an interpretation using horizontal layers causes a discrepancy between the calculated magnetizations and the magnetization measured on drill core samples (Section 6.5), it becomes necessary to incorporate information about the geometry of the subsurface and to use inclined layers for the interpretation of the data (Section 6.7). Most importantly, I am introducing a new approximation for the magnetic field of inclined layers that is closely related to the horizontal layer interpretation, and which is faster than a complete,

accurate calculation of the magnetic field. This approximation also enables us to quickly assess possible ambiguities during the inversion (Section 6.7.3 and following).

Finally, in an exemplary analysis of an igneous layer that is both identifiable in images of the borehole wall and in the magnetic field, I derive a value for the declination of magnetization that agrees with existing theories about the movement of the Louisville hotspot (Section 6.7.8).

In a concluding remark I demonstrate that there is at least a theoretical possibility to obtain some information about the declination of magnetization from unoriented measurements of the magnetic field, provided that high quality geometrical information and magnetization data from drill cores are available (Section 6.8).

2 Scientific Background

2.1. Earth's Magnetic Field

The use of the magnetic field of the Earth for navigation predates the understanding of its origin by several centuries. Chinese travellers have used magnetized needles floating on water for orientation as early as the beginning of the 10th century (Lowrie, 1997). Around 1600, William Gilbert was the first to describe that the magnetic field of the Earth resembles that of a magnetic rock approximately aligned with the axis of rotation of Earth (Telford et al., 1990). In 1838, Carl Friedrich Gauss, who was also the first to determine absolute values of the magnetic field intensity, used the spherical harmonic analysis he invented to show that the source of Earth's magnetic field is primarily within the Earth itself (Gubbins and Herrero-Bervera, 2007).

For a long time, the origin of the magnetic field was thought to be magnetized rocks within the Earth, but that theory could neither explain the time varying behaviour of the magnetic field nor that the expected temperature of Earth's core and mantle is in large parts above the Curie temperature of all ferromagnetic materials (see Section 2.2.1). Only in 1939, Walter Elsasser published his first ideas on a dynamo mechanism within the electrically conductive fluid outer core of the Earth that is now the accepted theory for the origin of Earth's magnetic field. (Gubbins and Herrero-Bervera, 2007)

The magnetic field at a particular point on Earth is commonly described using either its geographic components, i.e. north, east and vertical downward (B_N, B_E and B_V), or its total value and two angles: inclination I and declination D. The inclination is the angle of the magnetic field respective to the horizontal plane; the declination is the angle between the projection of the magnetic field on the horizontal plane and geographic north. The total intensity of the magnetic field is given by:

$$B = \left|\vec{B}\right| = \sqrt{B_N^2 + B_E^2 + B_V^2} \tag{2.1}$$

Figure 2.1b shows the global coordinate system of the Earth, given by longitude and latitude in comparison to the local definition of the coordinate system used for the magnetic field (Fig. 2.1a). Also shown is the horizontal component of the magnetic field B_H, defined by:

$$B_H = \sqrt{B_N^2 + B_E^2}. \tag{2.2}$$

The magnetic field is measured in units of Tesla (1 T = 1 $\mathrm{Vs/m^2}$), but due to the relatively low strength of Earth's magnetic field, it is usually given in nT or μT.

Earth's magnetic field is mainly dipolar in nature and only about 25% are attributed to non-dipolar components. At the time of writing of this thesis, the axis of the dipole does

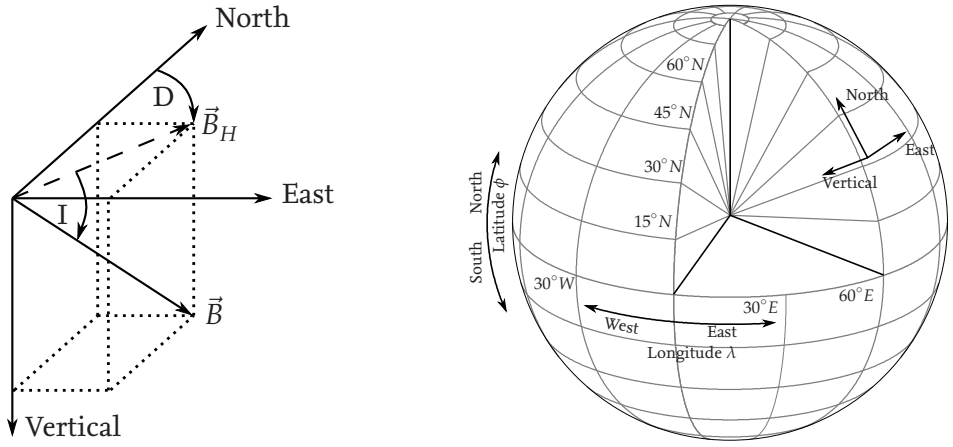

(a) (b)

Figure 2.1.: a) The local reference frame for the magnetic field. I: Inclination, D: Declination, B_H: Horizontal Magnetic Field, $\vec{B}$: Magnetic Field Vector. (adapted from Merrill, 1996) b) The global coordinate system with longitude λ and latitude ϕ in comparison to the local reference frame, North, East and Vertical. (adapted from de Lange, 2013)

not coincide with the axis of rotation of the Earth but is inclined by about 10° and offset from the center of the Earth by 575 km (calculated using formulas given in Fraser-Smith, 1987 and values given in Finlay et al., 2010).

Measurements of the direction of the magnetization of rock samples and models of magnetic field anomalies of the seafloor show that the direction of the magnetic field of the Earth has reversed several times within history. The mechanism of those so-called pole reversals is chaotic in nature and not yet completely understood. The current state of the magnetic field with a magnetic south pole near the geographic north pole is referred to as the normal state of the magnetic field, in contrast to the reversed state. (Gubbins and Herrero-Bervera, 2007)

Depending on the duration of a particular state, the history of the magnetic field is divided into polarity chrons, with durations from 50 kA to 5 Ma, subchrons, with durations from 20 kA to 50 kA, and short lived (i.e. about 10 kA) magnetic excursions, during which the magnetic pole starts to wander in the direction of the equator, but does not reverse completely. The formal definition of a magnetic excursion requires that the magnetic pole is at an angular distance of more than 45° from the geographic pole. As long as the magnetic pole is closer than that, the variation of the magnetic field is counted as part of the regular, long-term variation of the magnetic field, the so-called secular variation. (Gubbins and Herrero-Bervera, 2007)

An important point for the differentiation between magnetic excursions and a full reversal is the time that it takes for the magnetic field of Earth's solid inner core to reverse, which is believed to be in the order of 9.2 kyr. This magnetic "inertia" has to be overcome for a complete reversal of the magnetic field (Gubbins, 1999; Gubbins et al., 2015). Currently,

the magnetic field on average reverses approximately each 250 kA, but, for example, the so-called Cretacious Normal Polarity Superchron that started about 121 MA ago had lasted for 38 MA (Lowrie, 1997). It is currently not possible to reliably predict the time of the next reversal of the magnetic field.

The magnetic field is also subject to variations of shorter timescales which are of external origin and are mainly caused by interactions of the solar wind with the magnetosphere, the magnetospheric ring current and ionospheric current systems. The periods of those variations vary between several years, e.g. variations related to the solar cycle with a period of 11 years and typical amplitudes of 10 nT to 20 nT, daily variations with typical amplitudes of 20 nT to 100 nT, and so-called pulsations with periods between 0.2 s and 600 s. The strongest variations can occur during solar storms with amplitudes of several hundred nT and periods of several hours to weeks (Gubbins and Herrero-Bervera, 2007).

Approximately 180 geomagnetic observatories continuously monitor the temporal and spatial variability of the magnetic field. In conjunction with satellite measurements, these observatory data are used to generate models of Earths magnetic field that can be used to estimate strength and direction of the magnetic field anywhere on Earth. The most commonly used models are the World Magnetic Model (WMM) and the International Geomagnetic Reference Field (IGRF). These models are limited in so far that they only include the magnetic field originating in the fluid outer core and their accuracy depends on the density of measurements within a certain region. Crustal magnetization and other sources of magnetic fields can cause differences of several hundreds of nT between the modeled field and the actual value of the magnetic field at a particular location (Gubbins and Herrero-Bervera, 2007).

Figure 2.2 shows the total value of the magnetic field (see Eq. 2.1) calculated for January 1st, 2011, at an altitude of 0 m above the reference ellipsoid, using the International Geomagnetic Reference Field (IGRF, Finlay et al., 2010). Typical strengths of the magnetic field are in the order of 30000 nT in equatorial and 50000 nT in polar regions. Figure 2.3 shows the distribution of the inclination of the magnetic field and Fig. 2.4 the distribution of the declination. The maps use a Mercator projection, which is frequently used for navigation purposes but which diverges at the poles, and are therefore truncated at latitudes of $\pm 75°$. When the magnetic field is used for navigation, especially the spatial and temporal variability of the declination has to be taken into account, as this can otherwise cause significant errors in the determination of the direction of travel. Consequently, the magnetic declination for the area in question is commonly shown on navigational maps, and those maps are updated frequently to account for temporal variation of the declination.

If the magnetic field of Earth was purely dipolar, with a dipole in parallel to the axis of rotation, the isolines in the figure for the inclination would be in parallel to the meridians; the declination would be constantly zero everywhere on Earth.

The prominent region of low total magnetic field strength that overlaps parts of South America and the Atlantic is referred to as South Atlantic Anomaly (SAA). Within this region, with minimum values of down to 22500 nT, the magnetic field is weakened to such an

extent that charged particles of solar origin can disturb satellites and, during solar storms, endanger astronauts (Heirtzler et al., 2002). The magnetic field in this region has been decreasing since more than 50 years and there are no signs that the decrease is slowing down (Finlay et al., 2010). The SAA is believed to be associated to a large low shear wave velocity province underneath southern Africa. Recent research suggests that it potentially is the origin and trigger of many of the past geomagnetic reversals (Tarduno et al., 2015).

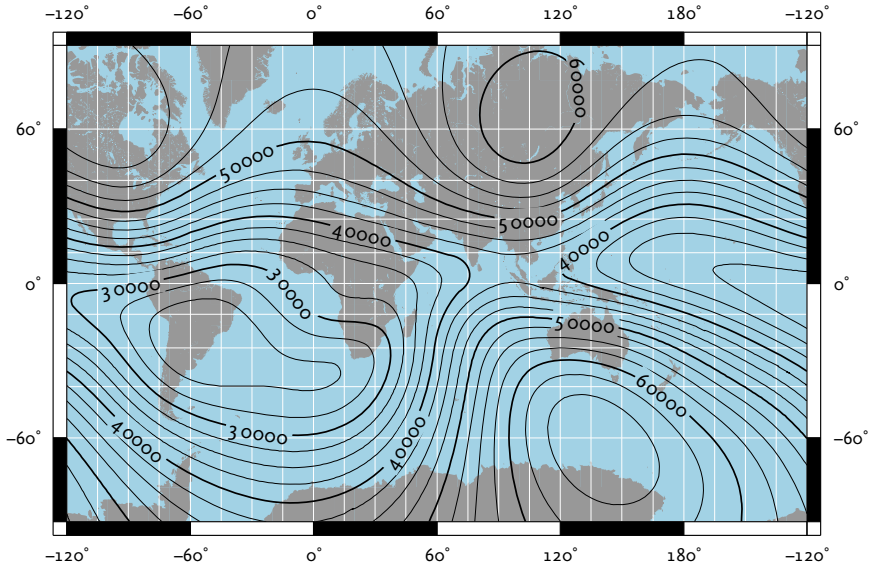

Figure 2.2.: Total value of the magnetic field according to the International Geomagnetic Reference Field (IGRF). Values are given in nT. Map generated using IGRF-11 data (Finlay et al., 2010).

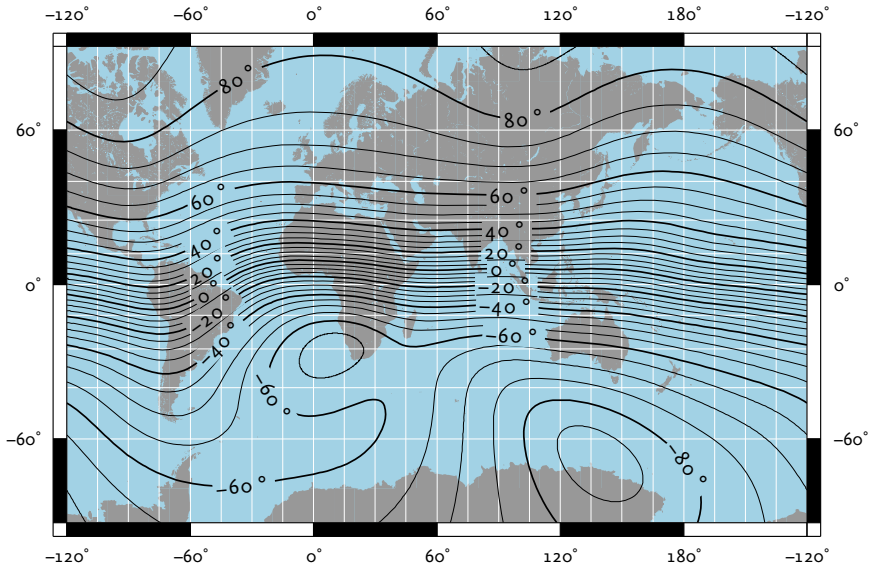

Figure 2.3.: Inclination of the magnetic field according to the International Geomagnetic Reference Field (IGRF). Map generated using IGRF-11 data (Finlay et al., 2010).

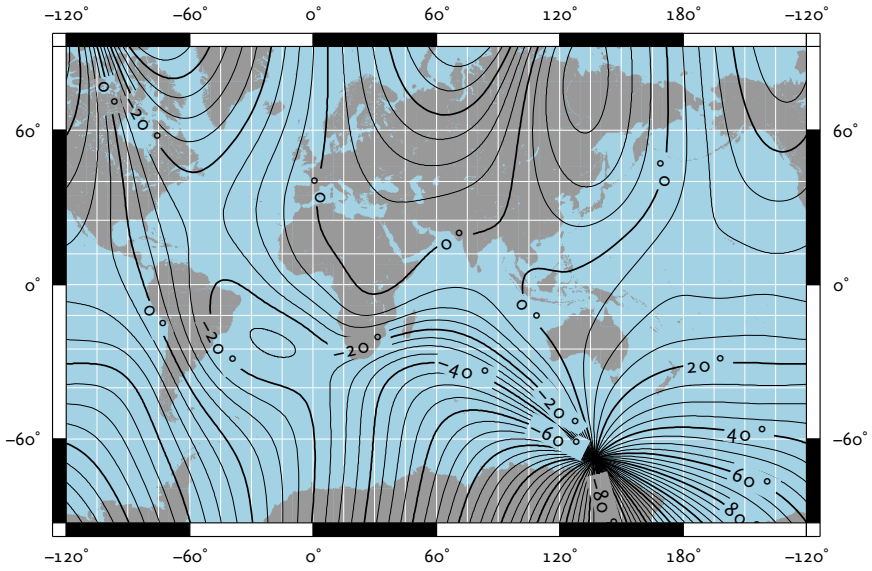

Figure 2.4.: Declination of the magnetic field according to the International Geomagnetic Reference Field (IGRF). Map generated using IGRF-11 data (Finlay et al., 2010).

2.2. Palaeomagnetism and Plate Tectonics

2.2.1. Magnetic Properties of Rocks

In order that be able to learn about the tectonic and magnetic history of Earth by sampling rocks and sediments, we need to understand how the physical properties of different materials influence their suitability for paleomagnetic studies. Depending on their magnetic properties, materials can be divided into several categories:

Diamagnetic: In diamagnetic materials, the induced magnetization opposes the inducing field, that is they have a negative magnetic susceptibility. All materials are, at least in parts, diamagnetic, but this is often masked by other effects. Examples of diamagnetic materials are salt, quartz and calcite. Their susceptibilities are low, mostly in the order of -10^{-6} (Lowrie, 1997).

Paramagnetic: In paramagnetic materials, existing magnetic moments of atoms are aligned in parallel to an external field. They have small positive temperature dependent susceptibilities in the order of 10^{-4} and lose their magnetization as soon as the external field is turned off. Examples are amphibole and olivine (Lowrie, 1997).

Ferromagnetic: In these materials, existing magnetic moments of atoms strongly interact and form so called magnetic domains of uniform magnetization, even without an external magnetic field. Ferromagnetic materials have high positive susceptibilities, which depend non-linearly on the external magnetic field and on their history of magnetization.When an external field is applied to a ferromagnetic material, the magnetization increases until all atomic moments are aligned in parallel to the external field. After the so-called saturation magnetization M_s is reached, an increase

in the external field does not cause the magnetization to increase any longer. Even when the external field is reduced to zero, the material remains partly magnetized and carries a remanent magnetization. The remanent magnetization can only be removed by applying an external field of a certain strength (called coercive strength H_c) in the opposite direction. This behaviour is named hysteresis. Iron, nickel and cobalt are ferromagnetic (Meschede, 2015).

Antiferromagnetic / Ferrimagnetic: In contrast to ferromagnetic materials, magnetic moments of adjacent atoms are aligned antiparallel. In antiferromagnetic materials, the opposing magnetic moments cancel each other, which causes a zero net magnetization and a low, positive susceptibility. In ferrimagnetic materials, the opposing magnetic moments are of unequal strength, and remanent magnetism can occur. This is also possible in antiferromagnetic materials, if lattice defects and impurities cause a non-zero net magnetization. An example for antiferromagnetic materials is Ilmenite. Magnetite is ferrimagnetic and Hematite is an example for a antiferromagnetic material that exhibits ferromagnetic behaviour due to lattice imperfections and opposing magnetic moments that are not exactly antiparallel (Lowrie, 1997). An important property of ferromagnetic materials is their Curie temperature, above which magnetic ordering and magnetization disappears. The Curie temperature of magnetite is 580 °C (Gubbins and Herrero-Bervera, 2007).

Minerals that are able to retain a stable remanent magnetization are of primary interest for paleomagnetic studies, as the remanent magnetization can carry information about the direction of the paleomagnetic field and thus the history of movement of a rock sample. There are several types of the so-called natural remanent magnetization (NRM) of a rock sample, the most important being the thermoremanent magnetization. It is acquired when an igneous rock cools down below the Curie temperature of the respective minerals and is magnetized in the direction of the external field. Other types of remanent magnetization that can occur in igneous rocks are chemical remanent magnetization, for example caused by weathering of minerals, and viscous remanent magnetization, acquired when minerals are exposed to a constant magnetic field for extended periods of time (Merrill, 1996).

The stability of thermoremanent magnetization in a rock sample depends on various parameters, e.g. the type of minerals present, their size and shape. The most important carriers of remanent magnetization are stable single domain grains, i.e. grains of magnetic minerals that are so small that they consist of a single magnetic domain and thus are homogeneously magnetized. The shape of single domain particles significantly influences the stability of the remanent magnetization; due to the so-called *shape anisotropy*, it is much harder to change the direction of magnetization of elongated grains than of spherical or cubic grains. The saturation magnetization also has an influence on the maximum possible size of single domain grains; a lower saturation magnetization allows for larger single domain grains. Hematite can form single domain grains with diameters of up to 15 µm. In contrast, magnetite, which has a much higher saturation magnetization, can only have elongated single domain grains with a maximum length of up to 1 µm (Butler, 1992).

A typical rock sample will contain single domain grains of varying stability. The stability of a grain can be quantified in terms of its blocking temperature or its magnetic coercivity. The blocking temperature is the temperature below which the magnetization becomes stable; it can be anywhere in the range between room temperature and slightly below the Curie temperature of the respective mineral. The coercivity is the minimum magnetic field necessary to change the orientation of the magnetization of the grain and can be in the range of some mT to up to more than 1 T. Multi-domain grains are a much less effective carrier of remanent magnetization, as they typically have a low coercive force and lose their magnetization over time. (Butler, 1992)

When an igneous rock is reheated or the ambient magnetic field changes, some of the grains will change their direction of magnetization, a process that can also happen during drilling (the so-called drilling overprint). To remove such secondary magnetizations, rock samples routinely undergo stepwise demagnetization, for example by alternating-field demagnetization or thermal demagnetization (Butler, 1992). In alternating-field demagnetization, the sample is exposed to a time varying magnetic field of decreasing amplitude. The idea is that this will randomly orient the magnetization of any grains with coercivity below the initial amplitude of the magnetic field (e.g. 5 mT) and thus these grains statistically cancel out and do not contribute to the total magnetization. Thus, only the magnetization of grains of sufficient stability to give an accurate record of the paleomagnetic field direction remains. Typically, this procedure is conducted multiple times, with constantly increasing initial field values (Butler, 1992; Expedition 330 Scientists, 2012a). Similarly, in thermal demagnetization, the sample is heated to a certain temperature and then cooled down again to ambient temperature in zero magnetic field. Thus, the magnetization of any grains with a blocking temperature below the heating temperature is randomized, and again only sufficiently stable grains contribute to the remaining magnetization (Butler, 1992).

2.2.2. Paleomagnetism

Paleomagnetism is the "field of geophysics concerned with the measurement and interpretation of remanent magnetism or the record of the Earth's past magnetic field" (Allaby, 2008). The record of the paleomagnetic field stored in form of the NRM gives us valuable information about the direction (and, to some extent, the strength) of the magnetic field present during the time of formation of a rock. For example, an igneous rock that has cooled below the Curie temperature near the equator is going to acquire a remanent magnetization that is mainly horizontal and, depending on the polarity of the Earth's magnetic field, pointing either north or south. If this rock is then later transported to a more northerly or southerly latitude by plate tectonics, its latitude of formation is still visible in the direction of magnetization.

Probably the most important assumption when using paleomagnetism to trace the movement of tectonic plates is the assumption of a geocentric axial dipole, i.e. that the magnetic field has no higher order terms and that geographic and magnetic poles coincide. As, due to secular variation and non-dipolar contributions, this assumption is obviously

not correct for all times, which can be seen in the Figures depicting the current inclination and declination of the magnetic field (Fig. 2.3 and Fig. 2.4). It is therefore necessary to average multiple measurements over a period of time, ideally several 10000 of years (Butler, 1992), to even out all variations of the magnetic field. Also, any processes that might have changed the orientation of the sample since it acquired its magnetization, for example tectonic folding, have to to be considered, as they can cause errors in the determination of the original direction of the magnetic field.

After measuring the direction of magnetization, the latitude of formation (paleolatitude) can be determined from the inclination of magnetization. It is not possible to derive the corresponding paleolongitude from a single measurement of the magnetization, as the declination of magnetization carries information about the history of rotation of a rock sample, and not about the longitude of formation. The paleolatitude ϕ can be calculated from the inclination I like so (Butler, 1992):

$$\phi = \arctan\left(\frac{\tan I}{2}\right) \tag{2.3}$$

If azimuthally oriented rock samples are available and the declination of magnetization can be measured, the movement of a tectonic plate in time can be determined by calculating so-called Virtual Geomagnetic Poles (VGP). The VGP is the position a geomagnetic pole would need to have in order to explain the direction of the measured magnetization by a geocentric dipole. Here, the inclination of magnetization gives a distance to the pole and the declination of magnetization gives the direction. The calculations and equations are rather involved and, as they are not of direct use for this thesis, are not included here and I refer to Butler (1992) for more details. Instead, I am giving a graphical overview to present the general idea.Figure 2.5a shows two fictional measurements for rock samples of different age at a common location marked by the black and orange circle. The inclinations of magnetization give a distance to the VGP (black circles) and, in combination with the declinations of magnetization, which give a direction (red lines), allow a calculation of the VGP. Figure 2.5b shows the VGPs for a row of fictional measurements (marked with red crosses), again at the same site but for different ages of the rock. The result is called Apparent Polar Wander Path (APWP), as it appears as if the location of the pole has changed with time. However, it is rather the movement of the tectonic plate than true polar wander that causes this change. For igneous rocks that have formed recently (in a geological sense), the VGP will on average coincide with the geographic pole. The older the rocks, the more both are going to diverge, as the relative positions of location of formation of the rock and the geomagnetic pole have changed with time due to continental drift.

Typically, the APWPs for two continents will differ, as the continents have moved independently. By combining several measurements of multiple continents and locations it is possible to reconstruct the actual movements of the tectonic plates and bring the APWPs into agreement. Using a combination of paleomagnetic and other data, the movement of the continents during more than the last 500 Ma has been determined (Gubbins and Herrero-Bervera, 2007).

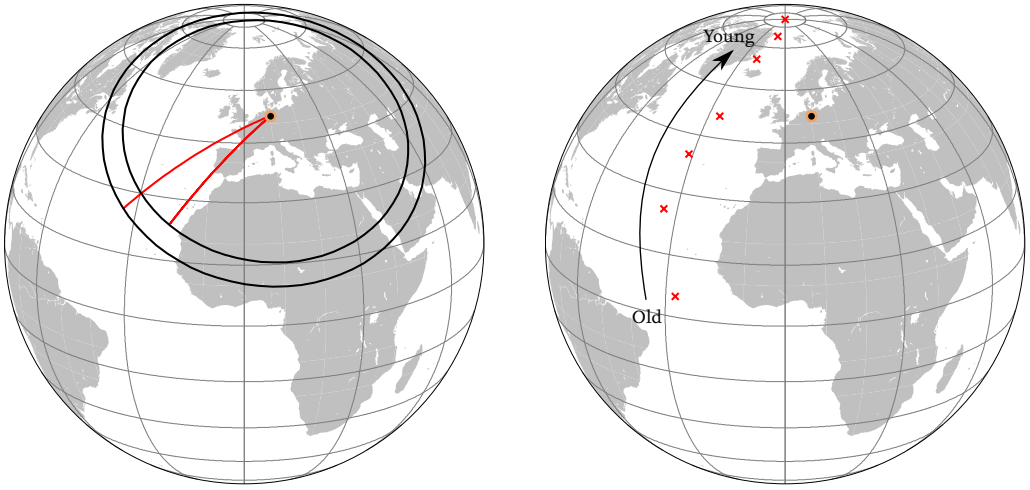

(a) (b)

Figure 2.5.: a) Two fictional measurements for rock samples of different age give two VGPs at the site marked by the black and orange circle. The inclination of magnetization gives a distance (black circles) and the declination of magnetization gives a direction (red lines) to the VGP b) A row of fictional measurements on rock samples of different age gives an Apparent Polar Wander Path, illustrating the movement of the tectonic plate in time. For older measurements, the distance between the VGP and the geographic pole is larger than for younger measurements.

2.3. Potential Field Theory

In this thesis, I am going to use magnetic field measurements to derive estimates for the strength and direction of magnetization of the rocks surrounding a borehole. Therefore it is necessary to understand the relationship between the magnetization of a body and the magnetic field it produces. In the following, I am giving a short introduction in the theory necessary for the calculations within this thesis. Further detail can be found in many excellent textbooks on potential field theory and the theory of electromagnetic fields, for example Kellogg (1929); Stratton (1941); Kaufman (1992); Blakely (1996).

In magnetostatics, that is in the stationary case without electric currents, Maxwell's Equations can be formulated as follows (Blakely, 1996):

$$\nabla \vec{B} = 0 \tag{2.4}$$

$$\nabla \times \vec{H} = 0 \tag{2.5}$$

where, assuming a linear and isotropic material, the magnetic flux $\vec{B}$ is related to the magnetic field $\vec{H}$ by (see e.g. Parasnis, 1997)

$$\vec{B} = \mu \vec{H}. \tag{2.6}$$

Here, μ is the magnetic permeability of the respective material, itself given by:

$$\mu = \mu_0 \cdot \mu_r \tag{2.7}$$

where $\mu_0 = 4\pi \cdot 10^{-7}\,\mathrm{Vs/Am}$ is the vacuum permeability and μ_r is the material dependent relative magnetic permeability. Equation 2.6 can be rewritten (see e.g. Parasnis, 1997):

$$\begin{aligned}\vec{B} &= \mu_r \mu_0 \vec{H} \\ &= \mu_0 \vec{H} + \mu_0(\mu_r - 1)\vec{H} \\ &= \mu_0(\vec{H} + \chi\vec{H}) \\ &= \mu_0(\vec{H} + \vec{M}_i)\end{aligned} \tag{2.8}$$

where $\chi = \mu_r - 1$ is the magnetic susceptibility of a material and the induced magnetization $\vec{M}_i$ is given by

$$\vec{M}_i = \chi\vec{H} \tag{2.9}$$

In the more general case of both induced and remanent magnetization, $\vec{M}_r$, Eq. 2.8 changes to

$$\vec{B} = \mu_0(\vec{H} + \vec{M}_i + \vec{M}_r) \tag{2.10}$$

Looking at Eq. 2.5 we see that the magnetic field $\vec{H}$ can be expressed as the gradient of a scalar field Φ:

$$\vec{H} = -\nabla\Phi \tag{2.11}$$

Applying the divergence operator on Eq. 2.10, using Eq. 2.4 and inserting Eq. 2.11, it follows that:

$$\Delta\Phi = \nabla\vec{M} \tag{2.12}$$

where $\vec{M} = \vec{M}_i + \vec{M}_r$ is the total magnetization of the body. The scalar field can therefore be calculated using (see e.g. Kaufman, 1992):

$$\Phi(\vec{r}) = \frac{1}{4\pi}\int_V \frac{\vec{M}(\vec{r'})(\vec{r} - \vec{r'})}{|\vec{r} - \vec{r'}|^3}\,\mathrm{d}V' \tag{2.13}$$

Which can be rewritten as (see e.g. McFee, 1989):

$$\begin{aligned}\Phi(\vec{r}) &= \frac{1}{4\pi}\int_V \vec{M}(\vec{r'})\nabla'\left(\frac{1}{|\vec{r} - \vec{r'}|}\right)\mathrm{d}V' \\ &= \frac{1}{4\pi}\int_V \nabla'\left(\vec{M}(\vec{r'})\frac{1}{|\vec{r} - \vec{r'}|}\right)\mathrm{d}V' - \frac{1}{4\pi}\int_V \left(\nabla'\vec{M}(\vec{r'})\right)\frac{\mathrm{d}V'}{|\vec{r} - \vec{r'}|}\end{aligned} \tag{2.14}$$

If we assume a homogeneous magnetization of the body, that is $\vec{M}(\vec{r'}) = \vec{M}$, the second term vanishes and we get (Blakely, 1996):

$$\Phi(\vec{r}) = \frac{1}{4\pi}\int_V \nabla'\left(\vec{M}\frac{1}{|\vec{r} - \vec{r'}|}\right)\mathrm{d}V' \tag{2.15}$$

Combining Eq. 2.6, Eq. 2.11 and Eq. 2.15 and using that $\nabla' \frac{1}{|\vec{r}-\vec{r'}|} = -\nabla \frac{1}{|\vec{r}-\vec{r'}|}$, we get (Blakely, 1996):

$$\begin{aligned} \vec{B} &= -\frac{\mu_0}{4\pi} \cdot \nabla \int_V \nabla' \left(\vec{M} \frac{1}{|\vec{r}-\vec{r'}|} \right) \mathrm{d}V' \\ &= \frac{\mu_0}{4\pi} \vec{M} \cdot \nabla^2 \int_V \left(\frac{1}{|\vec{r}-\vec{r'}|} \right) \mathrm{d}V' \end{aligned} \tag{2.16}$$

This means that the magnetic flux and the magnetization are related by a second order tensor

$$B_i = \sum_{k=1}^{3} M_k T_{ik} \tag{2.17}$$

with

$$T_{ik} = \frac{\mu_0}{4\pi} \frac{\partial^2}{\partial x_i \partial x_k} \int_V \left(\frac{1}{|\vec{r}-\vec{r'}|} \right) \mathrm{d}V' \tag{2.18}$$

As the partial derivatives commute, T_{ik} is symmetric, so there are only six independent equations to be calculated.

Applying Gauss's theorem to Eq. 2.15, we can convert the volume integral to a surface integral:

$$\Phi(\vec{r}) = \int_S \frac{\vec{M} \cdot \hat{n}(\vec{r'})}{|\vec{r}-\vec{r'}|} \mathrm{d}S' \tag{2.19}$$

where $\hat{n}$ is the outward normal vector of the surface S bounding the body. Combining Equations 2.11 and 2.19 gives us an equation that can in principle be used to calculate the magnetic field due to homogeneously magnetized bodies of arbitrary shape (Blakely, 1996):

$$\vec{B}(\vec{r}) = -\frac{\mu_0}{4\pi} \nabla \int_S \frac{\vec{M} \cdot \hat{n}(\vec{r'})}{|\vec{r}-\vec{r'}|} \mathrm{d}S' \tag{2.20}$$

Whether Eq. 2.20 has an analytical solution, depends on the shape of the surface bounding the body. Several solutions for different bodies are available in the literature. Bhattacharyya (1964) gives a solution for the magnetic field of a rectangular prism; Hjelt (1972) a solution for dipping prisms; Coggon (1976) gives a solution for more general polyhedra and Emerson et al. (1985) give solutions for 13 different bodies, including many two dimensional sources.

Guptasarma and Singh (1999) give a general solution for the gravitational and magnetic field of arbitrary polyhedra, which is especially interesting as they provide an algorithm that does not need any complicated coordinate transformations. The algorithm reduces the computation to the calculation of line integrals along the edges of the polyhedra and the computation of the solid angles subtended at the origin by the polygons bounding the polyhedron. In Appendix A.5 I am reproducing their calculations and give an efficient implementation of the algorithm in Matlab. In my implementation, I act on an idea given by Bär (2012), who limits the polygons to triangles, which allows for the use of an efficient algorithm to compute the solid angle. Compared to the implementation given in Sing and

Guptasarma (2001) and the run times given in Bär (2012), my implementation significantly reduces the computation time.

Bosum et al. (1988) give equations for the magnetic field at the center of a circular drill hole through a cylindrical layer and Gallet and Courtillot (1989) give a semi-analytical solution for the magnetic field due to a semi-infinite cylinder with an inclined upper surface, a model that can be used to calculate the magnetic field due to drilled inclined layers. Both models are going to be extensively used in this thesis, so they are discussed in more detail in Appendix A.2 and A.3. Additionally, in Appendix A.4, I give expressions for the magnetic field due to an inclined prism, which is going to be used in Section 6.7.2 to calculate the magnetic field inside a rectangular borehole.

An effect not discussed so far is the so-called demagnetization. Demagnetization means that the internal magnetic field of a body opposes the induced magnetization and, in effect, lowers the magnetization (Meschede, 2015). When demagnetization is present, Eq. 2.9 is no longer valid and the relation of the induced magnetization to the inducing field is more complex and depends on the shape of the body. The effect can be accounted for by replacing the susceptibility by an apparent susceptibility χ_a:

$$\vec{M}_i = \chi_a \vec{H} \tag{2.21}$$

where χ_a is defined by:

$$\chi_a = \frac{\chi}{1 + N\chi} \tag{2.22}$$

where N is the so-called demagnetization factor, with $0 < N < 1$ (McFee, 1989; Telford et al., 1990). For spheres, $N = 1/3$, which results in a maximum possible apparent susceptibility of 3. For other shapes of the body, χ_a and N are tensors and depend on the direction and position within the body (Sharma, 1966; Parasnis, 1997; Aharoni, 2001).

Demagnetization is only relevant for materials with magnetic susceptibilities higher than 0.1 SI (Telford et al., 1990). As the susceptibilities encountered during Expedition 330 are lower than 0.02 SI, neglecting demagnetization is appropriate for the igneous bodies discussed here, but might not be appropriate in other cases. For example, overlooking the influence of demagnetization in ore exploration has lead to misplaced boreholes in the past (Anderson and Logan, 1992), and demagnetization is a very pronounced effect in metallic objects, like unexploded ordnance (Sanches et al., 2008).

2.4. Borehole Magnetics

In contrast to surface measurements, measurements in boreholes are limited in so far as they only give a one dimensional view of the magnetic field. There are mainly three different methods of measuring the magnetic field in use, which differ in the amount of information that can be gained from them: total field measurements, measurements of the horizontal and vertical component and, which is the main focus of this thesis, measurements of the oriented magnetic field vector. Other methods include the measurement of the magnetic field tensor (see, for example, Hillan et al., 2012) or measurements of the vertical gradient of the horizontal and/or vertical component. The former is in an early

state of development and the latter methods are almost exclusively used for the detection of unexploded ordnance, so I am not discussing them any further.

Measuring the total magnetic field intensity is a common approach as it is not necessary to know the orientation of the sensor, which reduces the technical complexity of the tool. Additionally, due to the types of sensors that can be used, measuring the total field is possible with a higher accuracy and resolution than measuring individual components of the magnetic field. One tool that has been used extensively in scientific drilling is the Geological High-resolution Magnetic Tool (GHMT), which was in operation in 17 Ocean Drilling Program (ODP) Expeditions. The GHMT was equipped with a proton-precession sensor to measure the total magnetic field as well as an induction sensor to measure the magnetic susceptibility of the rocks surrounding the borehole. Williams (2006) gives an extensive record of its application and the results of the measurements.

Another tool that is routinely used during almost all deep ocean drilling expeditions is the General Purpose Inclinometry Tool (GPIT). It comprises a tri-axial fluxgate magnetic field sensor and three accelerometers, which allows to determine the horizontal and vertical component of the magnetic field as well as the total magnetic intensity. Its main use is to determine the orientation of the tool by assuming an undisturbed magnetic field that is accurately approximated by the IGRF, which allows to orient images of the borehole wall in formations of low magnetization. The GPIT has also been used in the past to identify reversals of the geomagnetic field (see, for example, Tominaga et al., 2012).

2.4.1. Peculiarities of Horizontal and Total Field Anomalies

Both the total field anomaly and the horizontal field anomaly, i.e. the difference between the measured magnetic field and the expected background magnetic field (e.g. given by the IGRF), have in common that they do not represent the true anomaly caused by a magnetized body, but the projection of the anomaly onto the background field. If the background field is given by $\vec{B}_0$ and the magnetic field anomaly by $\vec{B}_A$, then the measured magnetic field $\vec{B}_M$ is the sum of both:

$$\vec{B}_M = \vec{B}_0 + \vec{B}_A \tag{2.23}$$

When the total field intensity is being measured, the difference between measured total field intensity and total field intensity of the background field does not correspond to the total value of the anomalous field (Blakely, 1996):

$$\Delta B = \left|\vec{B}_0 + \vec{B}_A\right| - \left|\vec{B}_0\right| \neq \left|\vec{B}_A\right| \tag{2.24}$$

As the anomalous field $\vec{B}_A$ is usually smaller than the background field $\vec{B}_0$, we can simplify Eq. 2.24:

$$\begin{aligned} \Delta B &= \left|\vec{B}_0 + \vec{B}_A\right| - \left|\vec{B}_0\right| \\ &= \sqrt{B_0^2 + 2 \cdot \vec{B}_0\vec{B}_A + B_A^2} - \sqrt{B_0^2} \\ &\approx \sqrt{B_0^2 + 2 \cdot \vec{B}_0\vec{B}_A} - \sqrt{B_0^2} \end{aligned} \tag{2.25}$$

$$\approx \frac{\vec{B}_0 \vec{B}_A}{B_0}$$

which is, as stated above, the projection of the anomaly on the background field. The same formalism can be applied to the horizontal field anomaly and leads to:

$$\begin{aligned} \Delta B_H &= \left|\vec{B}_{0_H} + \vec{B}_{A_H}\right| - \left|\vec{B}_{A_H}\right| \\ &\approx \frac{\vec{B}_{0_H} \vec{B}_{A_H}}{B_{0_H}} \end{aligned} \tag{2.26}$$

where $\vec{B}_{0_H}$ and $\vec{B}_{A_H}$ correspond to the respective horizontal components of $\vec{B}_0$ and $\vec{B}_A$, i.e. the north and east component of the background field and of the anomaly. This means that measurements of the horizontal field or the total field are unable to resolve anomalies whose magnetic field is perpendicular to the background field.

2.4.2. Three Component Magnetic Field Measurements

Besides the obvious point that more measured components give more information, oriented measurements of all three components of the magnetic field have the additional advantage that they do not share the problem of total and horizontal field measurements discussed in the previous section. Assuming that the background magnetic field is well known, a separation of the background field and the magnetic field anomaly is possible without limitations and the relative direction of both fields has no effect on the detectability and interpretability of the measurements.

When magnetic field measurements in boreholes are used to detect the location of off-borehole bodies, dipolar anomalies can be unambiguously located, which is not possible with other types of magnetic field measurements (Ehmann, 2010). This means that less boreholes are necessary, which can reduce both costs and risks, for example when locating buried unexploded ordnance.

In this thesis, the focus is going to be on the determination of the direction of magnetization of rocks surrounding the borehole. Here, three component measurements can be used to determine the declination of magnetization, which is usually not possible with other methods. For the following discussion as well as throughout this thesis, I am going to use the coordinate system as shown in Fig. 2.6. Figure 2.6a shows a comparison of the geographic reference frame, whose axes are referred to as North, East and Vertical downwards (B_N, B_E and B_V) to the reference frame of a tool, whose geographically unoriented axes are referred to as B_x, B_y and B_z. Figure 2.6b shows the conventions for the angles used to describe the attitude of the tool and angular changes in its orientation. R_x, R_y and R_z correspond to rotations about the respective axes and are positive counterclockwise. The inclinations N_x and N_y are considered positive, when the tool is inclined in direction of the respective axis, which is an intuitive definition, but will sometimes require a negative sign when inclinometer data are compared to gyro data.

There are several technical solutions for measuring the magnetic field vector, but their applicability depends on the types of boreholes to be surveyed. For inclined boreholes,

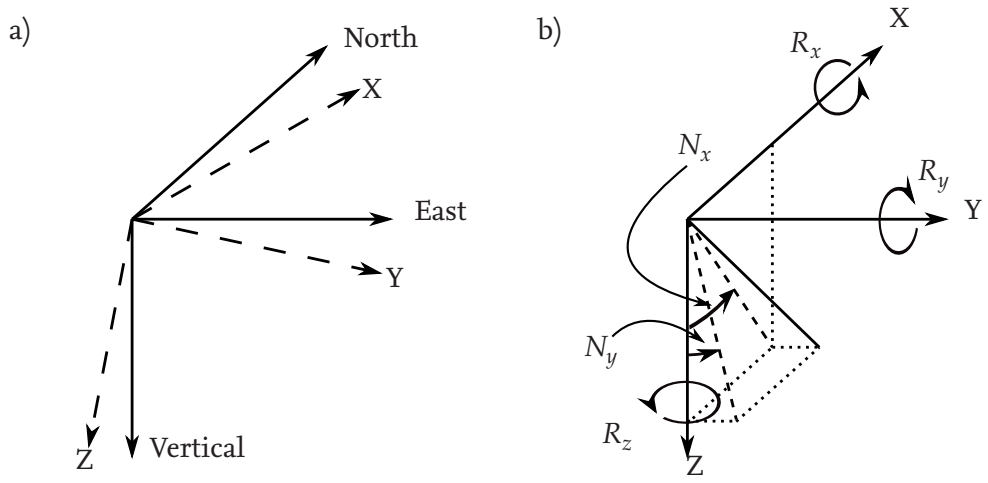

Figure 2.6.: Coordinate systems used in this thesis. a) shows a comparison of the geographic reference frame to the reference frame of a borehole tool. b) shows the convention for the angles used to describe the attitude and changes in orientation of the tool.

it is possible to use inclinometers to determine the orientation of the tool. However, rotations of the tool about the vector of gravity cannot be determined this way, which introduces errors when the azimuth of the borehole, i.e. its orientation relative to geographic north, changes along its path. Errors also grow with increasing inclination of the borehole. The first oriented magnetic field measurements, in which the magnetic field was reoriented using inclinometers, were described by Levanto (1959). Other authors describe similar measurements using different numbers of inclinometers and different technical implementations (Hoschke, 1985; Mueller et al., 1997; Collar et al., 2005).

In order to be able to determine the vector of the magnetic field regardless of the path and inclination of the borehole, it is necessary to use measurements that do not rely on the direction of the vector of gravity. Scott and Olson (1985) as well as Bosum et al. (1988) use mechanical gyros to determine the orientation of their tools. Mechanical gyros rotate with several thousand rotations per minute and, due to the gyroscopic effect, maintain their initial orientation throughout the course of a measurement. Their drawback is, however, that they are susceptible to impacts and vibrations of the tool and that they exhibit an indeterministic drift, both of which affects their long term accuracy.

2.4.3. Göttingen Borehole Magnetometer: History and Assembly

The origins of the Göttingen Borehole Magnetometer (GBM) lie in the German Continental Deep Drilling Project (Kontinentale Tiefbohrung, KTB, Emmermann and Lauterjung, 1997). It was originally developed to measure the vertical gradient of geomagnetic pulsations in all components of the magnetic field, which can be used to determine the transfer functions between surface and borehole tool (Spitzer, 1993; Leven, 1997; Schmucker et al., 2009). This method requires an accurate orientation of the tool in the geographic reference frame. Initially, the tool only comprised two inclinometers and a triaxial fluxgate and was oriented

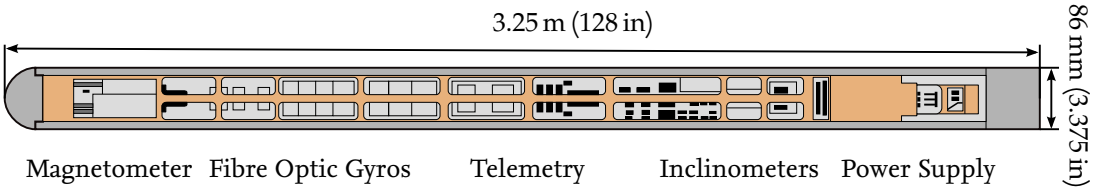

Figure 2.7.: Sketch of the internal structure of the GBM with the approximate locations of its main constituents. Modified from Steveling et al. (2003).

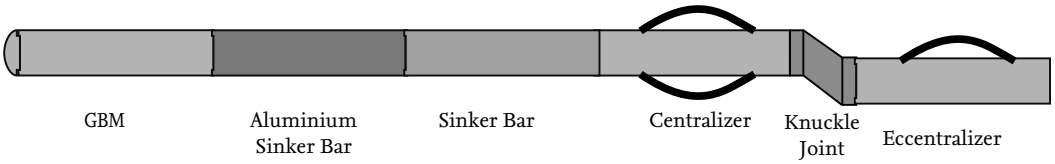

Figure 2.8.: Sketch of the tool string used during Expedition 330 (not to scale).

using Earth's magnetic field. Therefore, only the horizontal and vertical components of the magnetic field could be measured in magnetized formations, as the GBM did not comprise an orientation method that was independent of the magnetic field.

A first fiber optic gyro (FOG) was added to the tool in 2001 in the course of preparations for measurements in the Detroit Seamounts (Ocean Drilling Project Leg 197), where, for example, it was used to assess the accuracy of the orientation algorithms of the GPIT (Gaillot et al., 2004). Two additional FOGs were added after the expedition that now allowed a full three dimensional orientation of the tool without having to rely on inclinometers. In 2003 the tool was used for measurements in Hilo (Hawaii) and the Vogelsberg mountain in Germany. After replacement of one of the FOGs, who exhibited a much larger temperature dependent drift than the other two, further measurements in the drillholes Sichenhausen-Eschwald (Klein, 2009) and in Outokumpu (Finland, Virgil, 2012) followed in 2008 and 2009. In 2010, I conducted measurements in the Cuxhaven-Lüdingworth drillhole for my diploma thesis (Ehmann, 2010).

Figure 2.7 shows the current setup of the GBM. During Expedition 330, the toolstring of the GBM consisted of the GBM, an aluminium sinker bar (custom made for the expedition to limit the magnetic influence of the other parts of the tool string on the GBM, see Ehmann, 2010), a sinker bar, a centralizer, a knuckle joint and a eccentralizer (see Fig. 2.8). The centralizer is necessary to keep the magnetometer in the center of the borehole; the knuckle joints in combination with the eccentralizer are used to press the toolstring against the borehole wall in order to limit rotational movements. The main instruments of the GBM are as follows (Leven, 1997):

Fluxgate Magnetometer The tri-axial fluxgate magnetometer is located at the lower end of the tool. The simplified principle of operation of this kind of magnetometer is shown in

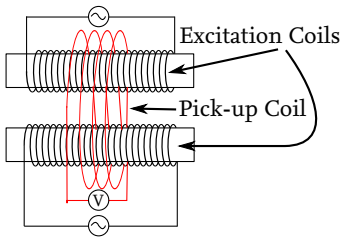

Figure 2.9.: Sketch of a fluxgate magnetometer.

Fig. 2.9: It consists of two excitation coils wound in opposite directions around identical cores made of a permeable material. An additional pick-up coil is wound around the assembly. An alternating current in the excitation coils drives the permeable cores in magnetic saturation. As the windings about the two cores are in opposite directions, the net voltage induced in the sensing coil equals zero in the absence of an external magnetic field. When an external field is present, it is easier to magnetize the cores in the direction of the external field than in the opposite direction. This asymmetry causes a signal in the pick-up coil that can be used to determine both magnitude and direction of the external field. As the measurement is only sensitive to the field component parallel to the long axis of the cores, the magnetometer consists of three sensors, one for each axis of the magnetic field.

The measurement range of the magnetometer of the GBM is $\pm 50000\,\mathrm{nT}$ for the x- and y-sensor and $\pm 70000\,\mathrm{nT}$ for the z-sensor. Depending on the magnetic field expected at a drill site, their ranges can be adjusted. A 14 bit AD converter is used to digitise the magnetometer signals, thus the respective resolution of the sensors is 6.1 nT (x- and y sensor) and 8.5 nT (z-sensor).

A peculiarity of the magnetometer is that its signals are low-pass filtered with a cut-off frequency of 0.35 Hz. It is therefore necessary to assure that the GBM does not experience fast rotations, as this would cause wrong readings of the sensors. During Expedition 330, a combination of a centralizer and a ecentralizer was used to both center the tool in the borehole and to prevent rotations. The low-pass filter is a remnant of the time when the GBM was used to measure low frequency pulsations of the magnetic field.

Fiber Optic Gyros Three orthogonal fiber optic gyros of type µFORS-36M, manufactured by Litef, are used to measure the rotations of the tool about its individual axes. Their principle of measurement is based on the Sagnac effect: A coherent light beam is split into two parts that travel in opposite directions through multiple windings of an optic fiber (Fig. 2.10). The light beam travelling in the direction of rotation experiences a different phase shift than the beam travelling in the opposite direction, which causes an interference pattern in the detector that can be evaluated to determine the rotational rate. The phase difference $\Delta\Phi$ of the light beams is given by

$$\Delta\Phi = \frac{8\pi NA}{c\lambda}\Omega\cos(\theta) \tag{2.27}$$

where A is the area enclosed by the optic fiber, N the number of windings, c the speed of light, λ the wavelength of the light source, Ω the rotational rate and θ the angle between the normal vector of the loop and the axis of rotation (see, for example, Demtröder, 2009).

The measured phase-shift and thus the accuracy of the measurement is directly related to the area enclosed by the loop which in turn is limited by the diameter of the borehole tool.

The FOGs exhibit a temperature dependent drift that is lowest at about 40 °C. Therefore, the sensors are temperature stabilized. Their maximum operational temperature is 70 °C, which would have to be taken into account in geothermal active regions, but was irrelevant during Expedition 330.

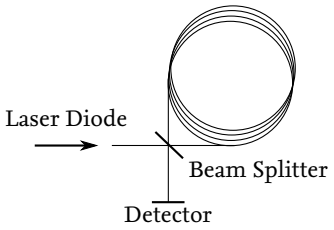

Figure 2.10.: Sketch of a fiber optic gyro. After Lawrence (1998).

Inclinometers The inclination of the GBM is measured by two orthogonal pendulum-type inclinometers. A small permanent magnet is attached to the end of each pendulum which allows for its position to be measured by a magnetoresistor. The movement of the pendulum is dampened by silicon oil, which limits overshoots of the pendulum but also reduces its response time to changes in inclination. The accuracy of the inclinometers is given as 0.3° by the manufacturer, but mostly depends on the conditions of the measurements.

Temperature Sensors The temperature of the FOGs and of the electronics of the GBM is measured by two temperature sensors, approximately located at both ends of the tool. Their data are mostly used for a correction of the temperature dependent drift of the FOGs (see Section 4.2). The sensors use a current source whose current is a linear function of the ambient temperature.

Data Transmission

The GBM does not yet comprise a battery or any means to store sensor data. Therefore, a continuous connection to the computer on the surface is necessary in order for the GBM to operate. During the initial equipment tests for Expedition 330 onboard the JOIDES Resolution, severe signal problems were encountered when the GBM was connected to the wireline. The GBM ran well on a short test cable, but when connected to the wireline, rhythmic signal losses occurred. The signal loss was intermittent and variable with times between loss ranging from a couple of seconds to one or two minutes. Each data loss means that a part of the rotation history is lost, therefore removing the reason of the signal loss is crucial for the data quality. As similar problems might occur during subsequent measurements, I am describing the technical details that are relevant for their removal.

The wireline used on the JOIDES Resolution consists of 7 isolated lines surrounded by a metal armoring. The cable is 9054m (29706 feet) long. Line 7 is in the center of the wireline and has the shortest length; the other lines are wrapped around it. As line 7 has the smallest resistance (282 Ohm) it is used for communication. Lines 1 through 6 are used for the DC power supply and the armoring is used as ground (called line 10). The resistances of line 1 through 6 are about 300 Ohm each, resulting in a parallel resistance of about 50 Ohm. The GBM has a regulated power supply that limits the incoming voltage to

50 V. If the incoming voltage reaches 90 Volts a fuse will blow to prevent damage to the regulatory circuits. A minimum of 25 V is needed for the GBM to power up, after the tool is working the voltage can drop to a minimum of 12 V. As the tool powered up, it was evident that the signal losses were not caused by a lack of power.

As the tool would also power up when using only 5 lines for power supply, one of the first attempts to get the tool working properly was using two lines (6 & 7) for communication. This resulted in total signal loss. As the different lengths of the lines might have caused this, lines 1 & 4 were used for communication in a second attempt. Again, this resulted in a complete signal loss. Several other attempts were made to get a stable signal, but are omitted here.

The final solution of the problem was found with the help of Leven (2011, pers. Comm.) and is related to the transceiver electronics used for communication with the GBM. The computer interrogates the GBM every 0.5 s with a $\pm$12 V signal and the GBM answers with a $\pm$5 V signal. A so-called Manchester 2 code is used for the communication, which is supposed to be very error proof. The upper panel of Fig. 2.11 shows the circuitry and the lower panel of Fig. 2.11 shows a photo of the transceiver used to translate the signal on the cable to a computer readable series of 5 V and 0 V signals.

First, the incoming signal from the GBM is split into two complimentary signals. These are later amplified by the differential amplifier LT 1022 (removing all noise that has entered the signal since its arrival at the communication card). The output signal of the differential amplifier is asymmetric with a maximum positive amplitude of 12 V and a minimum amplitude of -5 V. After amplification, the signal is compared to an adjustable voltage by comparator LT 1011. The threshold for the comparator can be set using the potentiometer R22. The threshold can be measured by connecting a voltmeter to two test pins. When the signal arriving at the comparator is above the set threshold, the exit of the comparator (point 7) goes down to 0 V, without signal the exit is set to a constant 5 V.

To improve the signal quality, the input impedance of the transceiver was increased by replacing resistors R7 and R8 (each 14.7 Ohm) with 59 Ohm resistors. Additionally a bridge resistor (not shown in the circuitry but in the photograph) in parallel to R17* and R18* was changed from 2000 Ohm to 5000 Ohm to reduce the load on the signal line. Also the comparator was set to a value of 0.625 V. This significantly improved the signal quality and reduced the number of data gaps.

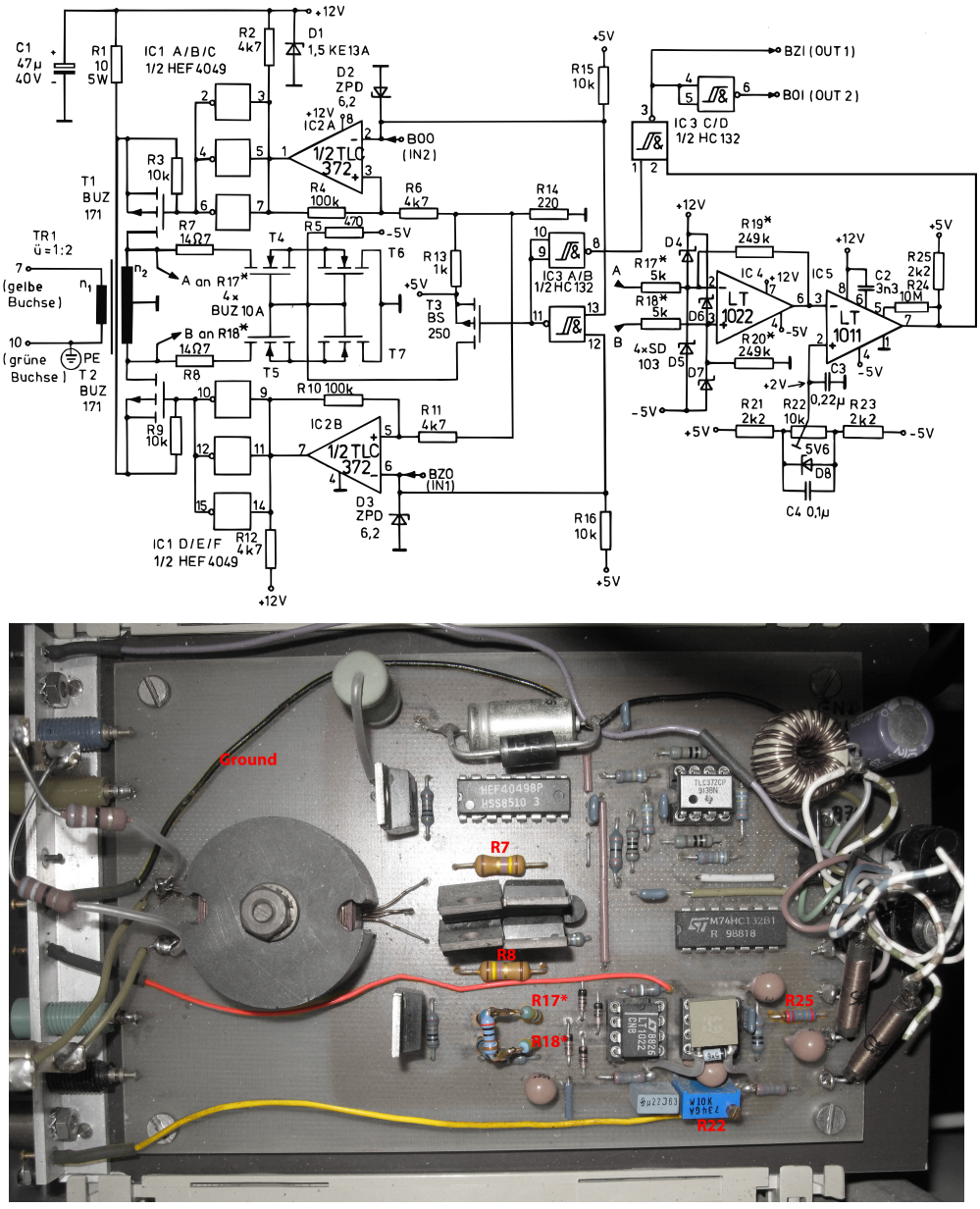

Figure 2.11.: The upper panel shows the schematics of the transceiver electronics (Leven, 1997). The lower panel shows a photograph of the electronics, relevant resistors mentioned in the text are marked.

3 Expedition 330

3.1. The Louisville Seamount Chain

The Louisville seamount chain is believed to have formed during the last 80 Ma, as the Pacific plate moved over hotspot that is currently situated at approximately 52.24° S, 137.12° W. As the hotspot shows no sign of active volcanism , its exact location is not known, but has to be deduced from plate motion modeling (Wessel and Kroenke, 2007). Together with the Hawaiian-Emperor and the Easter seamount trail, the 4300 km long Louisville chain is one of three primary hotspot trails in the Pacific, that is a seamount trail that shows a clear age progression along its extent, which is compatible with the idea that it has been formed by a tectonic plate passing over hotspot situated in Earth's mantle (Courtillot et al., 2003; Koppers et al., 2008).

Tarduno et al. (2003) found that the distinct bend of the Hawaiian-Emperor seamount chain can most likely be explained by a rapid southward motion of the hotspot of $\approx 40\,^{mm}/_{a}$ in the period between 80 and 47 Ma. One of the key questions that lead to IODP Expedition 330 was whether the Louisville Hotspot moves in concordance with the Hawaiian-Emperor Hotspot or whether it is stationary relative to the mantle. Other objectives of the Expedition were to gain more detailed $^{40}Ar/^{39}Ar$ ages of the seamounts as well as the determination of the magmatic evolution of the seamounts. Other interests were to determine whether the formation of the Ontong Java plateau is connected to the Louisville Hotspot, to gain more detailed information about the conditions of formation of the Louisville magmas as well as to provide paleoclimate data from cored pelagic sediments (Koppers et al., 2010).

It should be noted that the hotspot theory, first brought forward by Wilson (1963), is not undisputed. Specifically, the hypothesis that the volcanism is driven by deep mantle convection is questioned. Other theories suggest that the origin of the intraplate volcanism is to be found much shallower and related to plate tectonics. For example, Puchkov (2009) gives an overview of the arguments of both proponents and opponents of the mantle plume hypothesis, but concludes that the mantle plume model in general is more convincing. Also, a recent seismic tomography study by French and Romanowicz (2015) provides evidence for plumes originating from Earth's mantle. A collection of literature with more arguments against deep mantle plumes can be found on the webpage `http://www.mantleplumes.org`. However, the question about the depth of origin of the Louisville magmas is out of the scope of this thesis as it likely can not be answered based on magnetic field measurements.

Figure 3.1 gives an overview of the drill sites of Expedition 330, that took place from December 2010 to February 2011; a total of eight holes were drilled at six sites. Due to various technical difficulties, downhole logging was only possible at Sites U1374 (Rigil Guyot, 28° 35.7513' S, 173° 22.8924' W) and U1376 (Burton Guyot, 32° 13.0429' S, 171° 52.8396' W), with

total depths of penetration of 522.0 m and 182.8 m (Expedition 330 Scientists, 2011). The sites where logging was possible are marked with orange circles in the Figure.

The drilling program was designed to mimic ODP Leg 197 that explored the Hawaiian-Emperor seamount chain, by drilling seamounts of similar ages in order to have a direct comparison of the movement of both hotspots. The seamounts in the north of the chain are of older age of formation than those at the southern end of the chain; the approximate age of Rigil Guyot (Site U1374) is between 69.5±0.4 Ma and 70.7±0.6 Ma and the minimum age of formation for Burton Guyot (Site U1376) is 64.1±0.5 Ma, which are ages comparable to those of Detroit Seamount (ODP Leg 197, ≈ 71-76 Ma) and Nintoku Seamount (ODP Leg 197, ≈ 56 Ma) (Duncan et al., 2006; Koppers et al., 2012). The youngest seamount drilled is Hadar guyout (Site U1377) with an age of approximately 50 Ma (Koppers et al., 2012). At its northern end, the Louisville Seamount Chain is subducted along with the rest of the Pacific Plate under the Indo-Australian Plate at the Kermandec Trench.

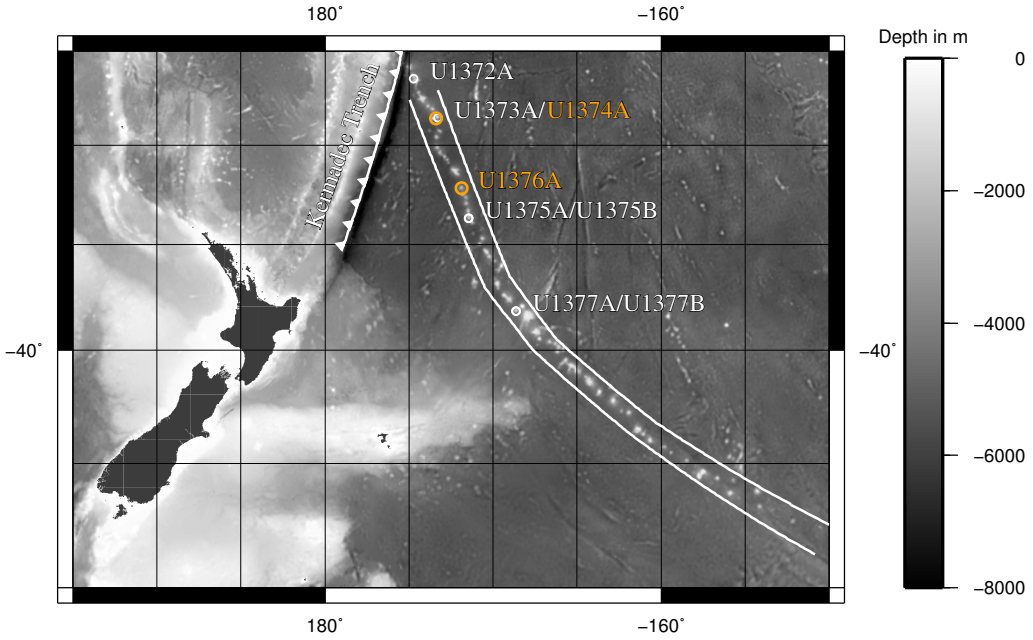

Figure 3.1.: Overview over the Louisville Seamount Chain and the drillsites of Expedition 330. Sites where downhole logging was possible are marked in orange. At its northern end, the Louisville Seamount Chain is subducted at the Kermandec Trench. Adapted from Ehmann et al. (2015).

In order to complement the core data and to give information where no core could be recovered, several downhole logging tools besides the GBM were used during Expedition 330: the triple combination tool string, the Formation MicroScanner (FMS) and the Ultrasonic Borehole Imager (UBI). The triple combination tool string consists of several individual tools that measure different physical properties of the rocks surrounding the borehole: natural gamma radiation, formation porosity via an active neutron source, as well as the resistivity via a dual induction tool. The FMS and the UBI give an image of the borehole

wall, using microresistivity and acoustics, respectively. These images are going to be used in Section 6.6 to aid with the interpretation of the GBM data, where more detail about these tools will be provided.

3.2. Data Acquisition and Operations

The Joides Resolution left Auckland harbor on 18 December 2011 and the first site of the Expedition, Site U1372, was reached on 21 December. The borehole had reached a depth of 232.9 m below seafloor on 29 December, when the drill string got stuck. As the drill string could not be freed again, it had to be severed by an explosive charge at a depth of 83 m below seafloor and no downhole measurements could be conducted (Expedition 330 Scientists, 2012b). After transit to Site U1373 and successfully drilling to a depth of 65.7 m, the drill bit had to be replaced. After the replacement, the drill could not be reentered into the drill hole, and the site was abandoned after several hours of unsuccessful reentry attempts (Expedition 330 Scientists, 2012c).

The first site were downhole logging was possible was Site U1374. Drilling operations on Site U1374 were finished on 18 January 2011 at a depth of 522 m below seafloor, but first downhole logging attempts were impeded by rock bridges in the borehole. As circulating mud and lowering the drill pipe did not improve the borehole, a drill bit was reattached to the drill pipe and the hole was cleared on 21 January 2011. The first tool string deployed was the triple combo toolstring, followed by the first run of the GBM between 15:50 and 23:30. After aligning the tool with the axis of the ship to obtain a geographic reference for the data (northing of the tool, see Section 5.2), the tool was lowered within the drill pipe. During the measurements, 9 gaps in the data occurred, which require special attention during data processing (Section 4.1). After downlog and uplog of the open hole were completed, the tool was brought back to the surface. At 22:40, while the tool was still in the drill pipe, the signal of the tool was lost completely. During a subsequent inspection of the tool, it was found that a connection within the tool had loosened. The connection was restored and secured, afterwards the GBM functioned normally again (Expedition 330 Scientists, 2012d; Grout, 2010-2011).

Subsequent to measurement runs of the FMS and UBI toolstrings, the GBM was deployed a second time on 22 January 2011 between 15:00 and 21:00. The connection within the tool held, but a total of 43 data gaps occurred. An adjustment of the transceiver electronics (see Section 2.4.3) during the logging run did not improve the signal. Both at the start and the end of the measurement, the tool was aligned with the axis of the ship to obtain a geographic reference (Expedition 330 Scientists, 2012d).

When downhole logging operations were finished, the drill string was found to be stuck in the formation and could not be pulled out. It therefore was severed near the bottom of the seafloor using an explosive charge on 23 January to allow for a transit to the next drill site. (Grout, 2010-2011) At Site U1375, the surface of the seamount was found to consist of loosely bound sedimentary breccia and two attempts to advance a drill hole failed after drilling 11.5 m and 8.5 m into the formation. Therefore, Site U1375 was abandoned and the

JOIDES started transit to Site U1376 on 26 January (Expedition 330 Scientists, 2012e). In order to improve the signal quality, further tests of the GBM were run during transit and drilling operations, and an adjustment to the transceiver was made that prevented further gaps in the data (see Section 2.4.3).

Drilling operations on Site U1376 started on 27 January and finished on 2 February at a depth of 182.8 m below seafloor. Logging started with the triple combo toolstring at 21:00. A first deployment of the GBM at 05:50 had to be aborted, as there were signs that the formation closed onto the drill string. After freeing the pipe and a re-northing of the GBM (Section 5.2), the magnetometer was deployed at 08:00 on 3 February. No errors occurred during the measurement, and the GBM was back on the surface at 13:30. After a run of the FMS toolstring, the drill pipe was recovered and the JOIDES departed to Site U1377 (Expedition 330 Scientists, 2012f; Grout, 2010-2011). Two holes were drilled at Site U1377, but due to unstable rock formations and with depths of only 53.3 m and 37.0 m, both holes were unsuitable for downhole logging (Expedition 330 Scientists, 2012g).

4 Data Processing

Several processing steps are necessary before the data recorded by the GBM can be used for further interpretation. Basic processing has already been described in several publications (e.g. Klein, 2009; Ehmann, 2010; Virgil, 2012; Ehmann et al., 2015; Virgil et al., 2015), but as an understanding of every step is fundamental for an accurate calculation of an oriented magnetic field vector, the necessary details are provided in the following. A new step included in this thesis is the determination of the offset of the inclinometers from measured data (Section 4.4).

Table 4.1 shows an excerpt of a raw GBM data file. Depth information is missing, as it was recorded separately during Expedition 330 and is added via time stamp comparison and then corrected for differences between downlog and uplog (Section 4.6). All data are given in raw readings of the AD converters inside the tool and have to be multiplied by appropriate conversion factors to be converted into the right units. The file header gives basic information about these conversion factors and other information, like the location of the measurement. However, the conversion factor for the B_z component of the magnetic field given here is incorrect, as the range of B_z was increased for the measurements during Expedition 330, and has to be multiplied by 1.4.

The sampling rate of the magnetometer channels, the inclinometers and of R_z is 2 Hz; as the data rate of the GBM is limited and as R_x and R_y are less crucial for the reorientation of the magnetic field, they are transmitted alternately and recorded at 1 Hz, as can be easily seen in Table 4.1. Temperature information is sent once a minute instead of inclinometer data and can be identified by the status bit in the second column of the data file. A status bit value of 128 denotes inclinometer data, a value of 0 denotes temperature data.

4.1. Treatment of Data Errors

During Expedition 330, there were significant difficulties with adjusting the signal recording electronics of the GBM to the electromagnetic properties of the wireline. As the right settings were not found yet during the measurements at Site U1374, some data gaps of 0.5 s each occurred. There were 9 gaps during the first and 43 gaps during the second measurement. The measurement conducted at Site U1376 had no data gaps, as the underlying problem with the electronics of the GBM could be fixed (see Section 2.4.3). An additional problem occurred during the first measurement: a connection within the tool loosened while the tool was on its way back to the surface, which resulted in a complete signal loss. But as the tool already was back in the drill pipe, no important magnetic field data were lost.

Data gaps are disadvantageous in so far that they cause errors in the determination of the azimuthal orientation of the GBM. A loss of magnetic field, inclinometer or temperature

```
!  Longitude:  137.38049deg Lattitude:  -28.59590deg Site:  U1374A
!  Date:  21.01.2011 Sampling:  2.00Hz FOG: 24 Bit
!  sBx= 0.163830Bit/nT sBy= 0.163830Bit/nT sBz= 0.163830Bit/nT
!  sRx= 46603.375Bit/deg sRy= 46603.375Bit/deg sRz= 11650.844Bit/deg
!  sNx= 163.830Bit/deg sNy= 163.830Bit/deg
!  sT1= 54.605Bit/K sT2= 54.605Bit/K
!  Time       Sts   Bx     By     Bz      Rx      Ry      Rz      Nx,T1   Ny,T2   Depth
02:28:22.04   128   5546   8482   11088   0       0       0       8316    8085
02:28:22.54   128   5579   8456   11114   0       0       0       8280    7958
02:28:23.03   128   5593   8446   11145   0       -1347   -1733   8403    8000
02:28:23.53   128   5602   8445   11170   4172    0       -1813   8295    8053
02:28:24.02   128   5600   8449   11186   0       -3391   -1842   8467    8054
02:28:24.52   128   5602   8469   11224   -4177   0       -1507   8433    8169
...
02:28:59.50   128   5490   8793   11215   -4585   0       1512    8487    7902
02:29:00.00   0     5560   8748   11242   0       538     1413    10689   9607
02:29:00.55   128   5608   8615   11215   -3778   0       851     8378    7973
```

Table 4.1.: Excerpt of a raw GBM recording. Depth information is recorded separately and is added during processing via time stamp comparison.

data is not crucial, as later recordings and calculations do not depend on the previous measurements. But as the gyros do not measure the absolute orientation, but only changes in orientation, a loss of information about the rotational rate in one data point directly causes an error in orientation. As there are usually only small changes in the deviation of the tool from vertical, gaps in R_x or R_y are less important than gaps in R_z, as the latter is used to calculate the azimuthal orientation.

A correction of the data gaps, i.e. an educated guess of the missing values of R_z, is possible in regions of low magnetic field gradients. Here, a comparison of the reoriented magnetic field of downlog and uplog can be made and the missing values can be iteratively adjusted until both magnetic field recordings exhibit the same characteristics, i.e. no sharp steps occur in the reoriented data (Ehmann, 2010). The magnitude of the local magnetic field gradient determines if and to which amount a correction is possible, as any true change of the magnetic field masks errors due to an incorrect guess of the missing value for R_z.

All data gaps in the first measurement occurred while the GBM was within the drill pipe, as well as most data gaps of the second measurement. As the magnetic field within the drill pipe is heavily distorted, no corrections were possible here and the missing values of R_z were set to zero.

Four data gaps of the second measurement lie within the open hole, but due to the large magnetization of the igneous basement, no corrections were possible here either, and the missing values of R_z were set to zero as well. However, these data gaps will only cause a small error in orientation, as the average rotational rate of the GBM in the open hole is only about 0.036 °/s due to the use of a eccentralizer in the tool string.

Regardless of the possibility of a correction for R_z, missing values for the magnetic field and the inclination of the tool are estimated by the mean value of neighbouring measurements. This helps to avoid problems during reorientation, for example ringing artifacts in the reoriented magnetic field due to the correction of the transfer function of the magnetometers (see Section 4.3).

4.2. Fiber Optic Gyro Corrections

4.2.1. Temperature Drift

After converting the raw sensor readings to degrees, several corrections have to be applied to the fiber optic gyros. The first correction performed is the removal of a temperature dependent drift that has been determined in calibration measurements (Steveling et al., 2005; Klein, 2009). The drift has been measured for different temperatures between 0 °C and 75 °C and is minimal in all gyros at about 40 °C (Fig. 4.1), which is the reason that the gyros are actively heated to this temperature. The measured drift is subtracted from the readings of the gyro; for temperature values in between the measured nodes, a linear behaviour with temperature is assumed.

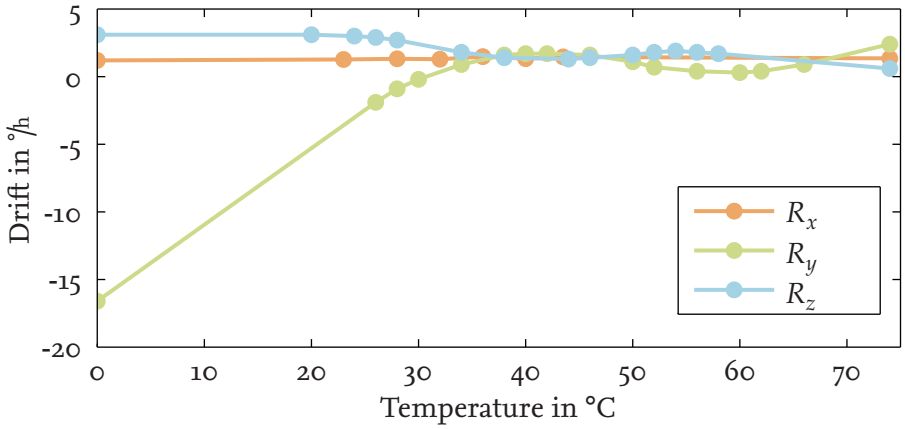

Figure 4.1.: Temperature dependent drift of the fiber optic gyros

Figure 4.2 shows the temperature progression during the measurements of Expedition 330. The left panel shows the temperature measured by the sensor close to the FOGs, which is the temperature used for the correction of the gyros. The right panel shows the temperature measured by the second sensor closer to the upper end of the tool, which, with some lag, corresponds to the temperature of the sea water. Even though the gyros are heated, their temperature got as low as 28.5 °C, due to the limited power of the heating system.

Also shown are the water depths of the respective sites, indicated by dashed vertical lines. The influence of the geothermal gradient inside the seamounts can be seen best in the right panel. While the GBM is descending through the water column, its temperature drops from ambient temperature down to 2.2 °C. As soon as the tool enters the seamount, the temperature starts to rise again. The hysteresis-like behaviour of the temperature is caused by the temperature sensors not being in direct contact with the seawater, but being insulated by the housing of the tool. Therefore, the temperature data can only be used for a qualitative interpretation of the temperature regime of the seamount.

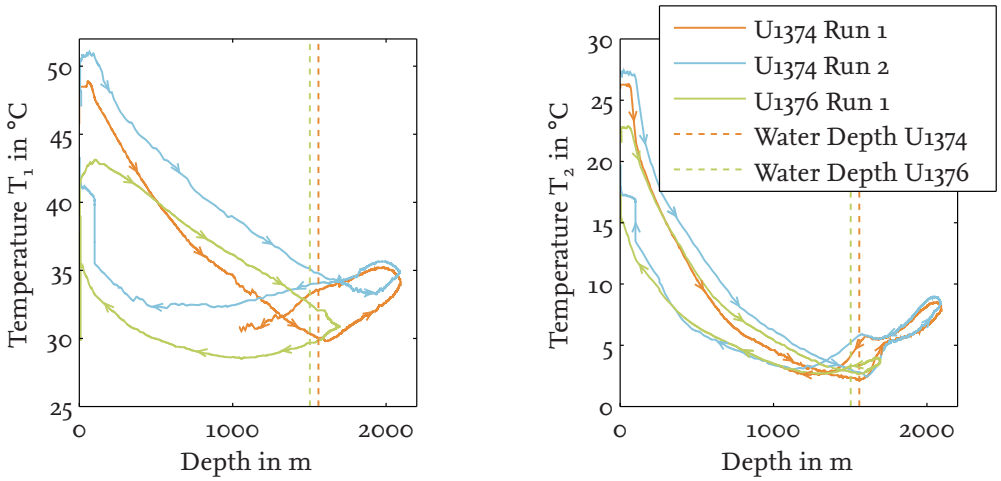

Figure 4.2.: Temperature progression during the measurements of Expedition 330. The left panel shows the temperature measured close to the FOGs. The right panel shows the temperature of the electronics, which, with some lag, corresponds to the temperature of the sea water. Arrows indicate the temporal progression of the measurements.

4.2.2. Errors in Orthogonality

After subtracting the known temperature drift, errors in orthogonality between the different gyros are corrected for. As the sensors are not perfectly orthogonal to each other, a rotation about one axis of the tool also affects the readings of the other sensors. To determine the deviations from orthogonality, the GBM is placed on the ground, supported by roller bearings, and rotated about its vertical axis. The errors in orthogonality between R_z and R_x as well as R_z and R_y can then be determined by finding values that remove the influence of the rotation about the z-axis from the other two axes (Klein, 2009). The correction is straightforward:

$$\tilde{\omega}_x = \omega_x + \omega_z \sin \eta_{xz} \tag{4.1}$$

$$\tilde{\omega}_y = \omega_y + \omega_z \sin \eta_{xy} \tag{4.2}$$

where $\tilde{\omega}_x$ and $\tilde{\omega}_y$ are the corrected values and η_{xz} and η_{yz} are the deviation angles.

Here, we have to consider that the data rate of R_z is twice the data rate of R_x and R_y, and that the values of R_x and R_y are transmitted alternately; therefore, in each case the sum of both preceding values of ω_z has to be used for the actual correction. The errors in orthogonality are small, with η_{xz} = 0.19° and η_{yz} = 0.02°. However, even small errors accumulate; for every rotation of the GBM about its vertical axis, 0.126° would be projected into R_y. As, for example, the GBM rotated about 25 times before it reached the open hole at Site U1376, this can have a huge impact.

A determination of the error in orthogonality between R_x and R_y would require to stably rotate the tool about its x or y axis, which cannot be performed easily. But as the tool is mainly rotating about the vertical axis, this error is negligible.

4.3. Magnetometer Calibration

4.3.1. Magnetometer Transfer Function

The electronics of the magnetometer of the GBM comprises a low pass filter with a cut-off frequency of about 0.3 Hz. It was originally implemented when the GBM was used to measure low frequency pulsations of Earth's magnetic field where the filter was supposed to minimize aliasing effects in the data (Virgil, 2012). The filter has the disadvantage that fast changes in the magnetic field, for example caused by a rotation of the tool, are not recorded correctly. By applying magnetic field step functions to the sensors, Virgil (2012) experimentally determined parameters for a combination of a Gauss filter and an optimal Wiener filter that reduces the effect of the low pass filter on the data. Nevertheless, it is still necessary to limit the amplitude of changes in the magnetic field, that is ultimately the amount of rotations the tool experiences. Therefore, the GBM was run in combination with a centralizer and a eccentralizer (see Fig. 2.8), to keep it centered within the borehole and to limit rotations.

4.3.2. Sensor Errors

Like the three fibre optic gyros, the three axes of the magnetometer are not perfectly orthogonal to each other. In addition, they have different scale factors and offsets. These errors have to be corrected before the data can be used for interpretation.

Currently, two different methods are used to determine the calibration factors. In the first method, the GBM is placed inside a Braunbek coil system at the TU Braunschweig calibration facility Magnetsrode (Glaßmeier et al., 2007). An additional fluxgate magnetometer and an Overhauser magnetometer measure Earth's background magnetic field. The coil system is then used to cancel the known background field and to generate arbitrary magnetic fields. By applying a known magnetic field of varying strength and direction, all sensor calibration parameters can be determined.

For the second method, only an additional total field magnetometer is necessary. The total field magnetometer is constantly measuring the background field, while the sensor that is to be calibrated is put into different orientations relative to the background field (Auster, 2000). In theory, a rotation about two axes is sufficient to determine all calibration factors, but ideally, every sensor axis is at least once oriented roughly parallel and antiparallel to the background field and once in a direction of minimal magnetic field. The calibration factors are then determined using a least-squares algorithm.

Using parameters determined from either of the methods, the calibrated magnetic field B_c is given by

$$\vec{B}_c = \boldsymbol{\omega} \cdot \boldsymbol{\sigma}(\vec{B}_m - \vec{B}_{off}) \tag{4.3}$$

with

$$\boldsymbol{\omega} = \begin{pmatrix} 1 & \cos\xi_{xy} & \cos\xi_{xz} \\ 0 & \sin\xi_{xy} & \frac{\cos\xi_{yz} - \cos\xi_{xy}\cos\xi_{xz}}{\sin\xi_{xy}} \\ 0 & 0 & \sqrt{\sin^2\xi_{xz} - \left(\frac{\cos\xi_{yz} - \cos\xi_{xy}\cos\xi_{xz}}{\sin\xi_{xy}}\right)^2} \end{pmatrix}, \tag{4.4}$$

and

$$\boldsymbol{\sigma} = \begin{pmatrix} \sigma_x & 0 & 0 \\ 0 & \sigma_y & 0 \\ 0 & 0 & \sigma_z \end{pmatrix}, \tag{4.5}$$

where $\boldsymbol{\omega}$ is a matrix containing the misalignment angles ξ_{ij}, $\boldsymbol{\sigma}$ is a matrix containing the scale factors σ_i and $\vec{B}_{off}$ is a vector containing the offsets (Kügler, 2004; Richter, 2012).

The calibration factors used for processing the data from Expedition 330 are given in Table 4.2.

Scale Factors:		Offsets:		Errors in Orthogonality:	
σ_x:	0.9982	Off_x:	98.85	ξ_{xy}:	-0.001352
σ_y:	1.0068	Off_y:	316.73	ξ_{xz}:	0.0001863
σ_z:	0.9940	Off_z:	187.48	ξ_{yz}:	0.000178

Table 4.2.: Calibration factors for the magnetometer as used for processing Expedition 330 data.

4.3.3. Effect of the Calibration

Figure 4.3 shows the effect of the different magnetometer calibration steps on a data set recorded while the GBM was rotated about its vertical axis in a constant background field of 22913 nT in the Braunbek coil system (20000 nT north, 10000 nT east, 5000 nT vertical). The upper panel shows total magnetic field data; the lower panel shows the rotation about the vertical axis of the GBM. Uncorrected magnetic field data are shown in blue. Data corrected for sensor offsets, scale factors and misalignment are shown in red. Data that are both corrected for sensor errors as well as the system transfer function are shown in green. The applied background field is shown in black.

During the measurement, the GBM was rotated several times with a mean rate of rotation of 33.6 °/s. If no sensor errors were present, the rotation should not influence the magnetic field measurements. But as they are present, the raw, uncorrected magnetic field data (B_r, blue line) does not coincide with the background field applied by the Braunbek coil system (B_0, black line). The difference between raw magnetic field and background field is not constant, but depends both on sensor orientation and rate of rotation. After correcting for sensor offsets, scale factors and sensor misalignment, the total magnetic field (B_c, red line) now coincides with the background magnetic field as long as the tool does not rotate. However, due to the high rate of rotation and the influence of the low pass filter of the magnetometer, there are rotation induced artefacts in the data: as soon as the tool starts to rotate, the measured magnetic field deviates from the background field (for example data points 25 through 100). When the data are additionally corrected for the system transfer function ($B_{c,s}$, green line), these artefacts are still present, but their magnitude has decreased. The correction works best for slower rates of rotation, as the influence of the low pass filter is smaller. As the average rate of rotation in the open hole was below 1° during Expedition 330, errors due to the low pass filter are insignificant.

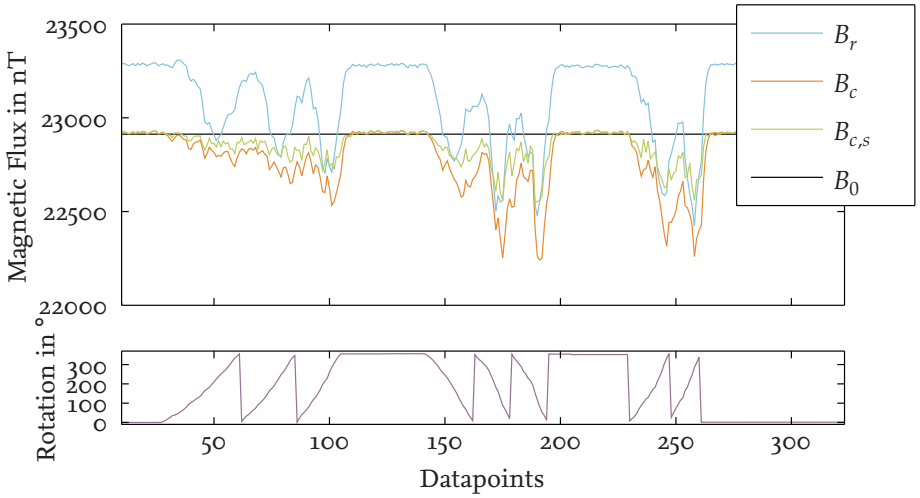

Figure 4.3.: Effect of the different magnetometer calibration steps on a data set recorded while the GBM was rotated about its vertical axis in a constant background field. The upper panel shows total magnetic field data for several correction steps: B_r: raw, uncorrected data. B_c: data calibrated for sensor errors, but not for the system transfer function. $B_{c,s}$: data corrected for both sensor errors and the system transfer function. B_0: background field applied in the coil system. The lower panel shows the rotation of the GBM about the vertical axis.

4.3.4. Unoriented Data

Figure 4.4 (Ehmann et al., 2015, modified) shows the magnetic field data of the first run at Site U1374 after all sensor errors are accounted for. The data are shown in the reference frame of the tool and are not corrected for the rotation of the tool, that is they are not yet reoriented to the geographic reference frame. Blue lines denote the downlog and orange lines denote the uplog. The depth scale shows meters below drillfloor. The data shown in the Figure start at the depth of the seafloor and end at the bottom of the hole. In order to stabilize the drill hole, a part of the drill pipe protruded into the formation; therefore the upper 140 m of the data are not usable for interpretation. The influence of the drill pipe on the magnetic field extends several meters into the open borehole and decays in a monopole-like fashion, which can be seen in the B_z component at a depth of approximately 1700 m.

In general, the B_z component is the only component where downlog and uplog agree, as it is much less influenced by the rotation of the tool than B_x and B_y. Besides not being corrected for the inclination of the borehole, B_z mostly corresponds to the vertical component of the magnetic field. Due to the uncorrected rotation of the tool, none of the structures visible in B_z can be identified in either of the other components. In combination, B_x and B_y could be used to approximately give the horizontal component of the magnetic field (not shown here), which could give some more information.

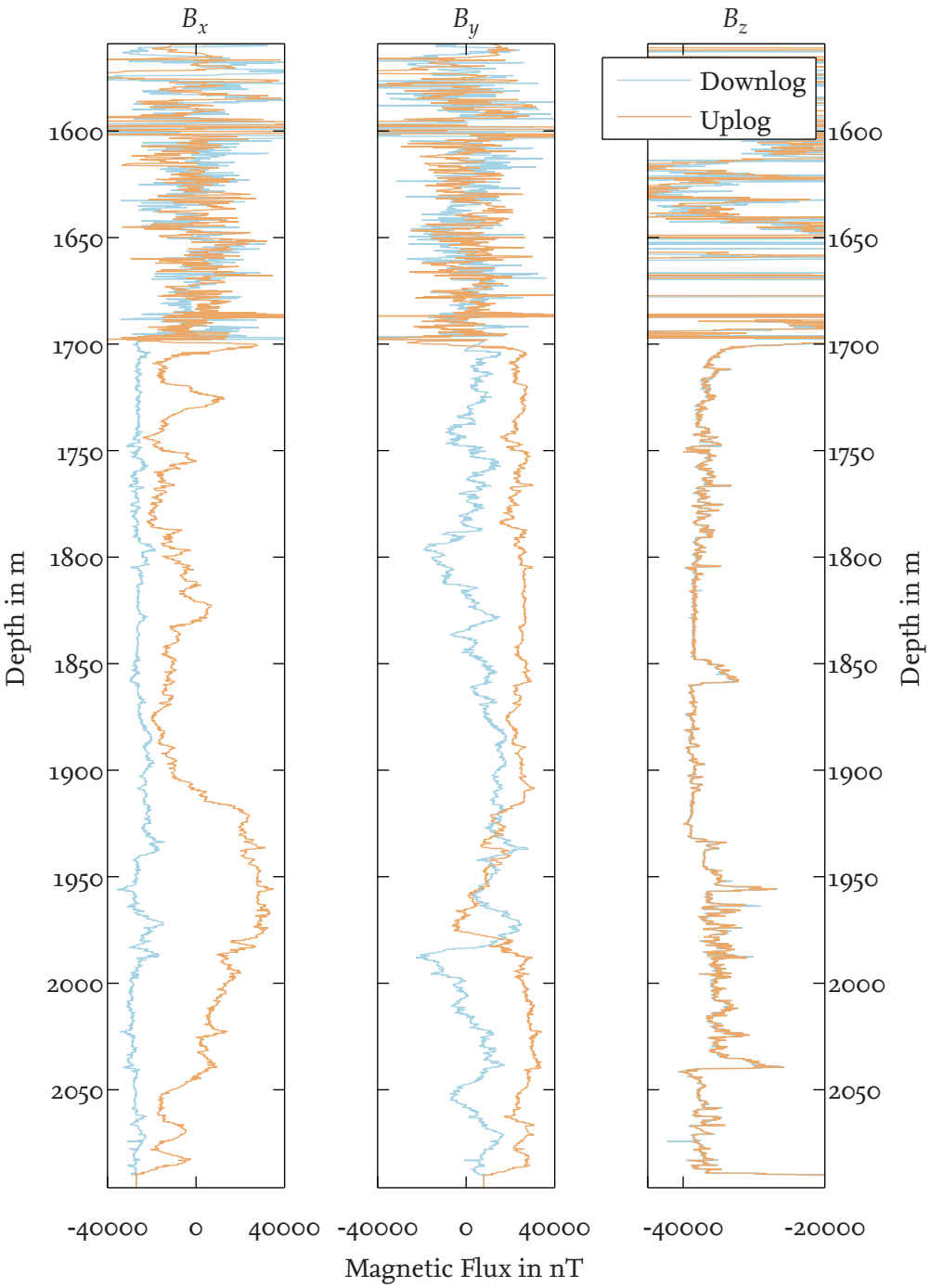

Figure 4.4.: Unoriented magnetic field data of the first run at Site U1374, corrected for sensor errors but not for tool orientation. Blue lines denote the downlog, orange lines the uplog. Modified from Ehmann et al. (2015)

4.4. Determination of Inclinometer Offsets

The inclinometers of the GBM also do have offsets, that is an output of zero degree does not have to coincide with a vertical orientation of the GBM. On land, the offsets can be calibrated by freely hanging the GBM, thus aligning the tool with the direction of gravity. Any non-zero reading of the inclinometers can then be corrected by subtracting appropriate offsets (Virgil, 2012).

On a ship, the situation is more complex, as the constant movements of the ship prevent the static calibration described above, so I am using a different approach. As long as the tool is within the drill pipe during a measurement, we can assume that its absolute inclination is only varying slowly. If the inclinometer data are then plotted versus the cumulated rotation of the tool about the vertical axis, we should see a sine wave with a mean value of zero for each inclinometer. Offsets in the inclinometer data are going to cause mean values that differ from zero and can thus be corrected. Figure 4.5 shows the data of Site U1374 (first measurement, data points 33000 through 37000) and Site U1376 (data points 5000 through 14000) plotted accordingly. The respective upper panels of Fig. 4.5 show the inclinometer data before the correction is applied, the respective lower panels show the inclinometer data after correction. Especially N_x for Site U1376 is clearly offset from zero. After an offset of -0.25° has been removed from N_x and an offset of -0.04° has been removed from N_y, both sine waves are centered. For Site U1374, an offset of -0.15° was removed from N_x and an offset of -0.05° was removed from N_y.

The data of both sites show very different noise characteristics: while the data of Site U1374 are almost free of noise, there is significant noise in the data of Site U1376. Therefore, in addition to the unsmoothed data shown in pale colors, data smoothed using a moving average of 40 data points are shown using dark colors. The reason for the differing amount of noise is most likely that the data shown for Site U1374 were recorded during the uplog of the measurement, whereas the data shown for Site U1376 were recorded during downlog. As more tension is on the wireline during uplog, this causes a more stable rotation of the tool. Additionally, the total inclination of the tool was larger at Site U1374, which, to some extent, reduces the visible influence of vibrations on the inclinometer data. The average logging speed in the intervals shown is similar for both data sets, with approximately 0.25 m/s at Site U1374 and -0.3 m/s at Site U1376.

As the offsets are likely to change during transport of the tool, they should be calibrated before or during each measurement.

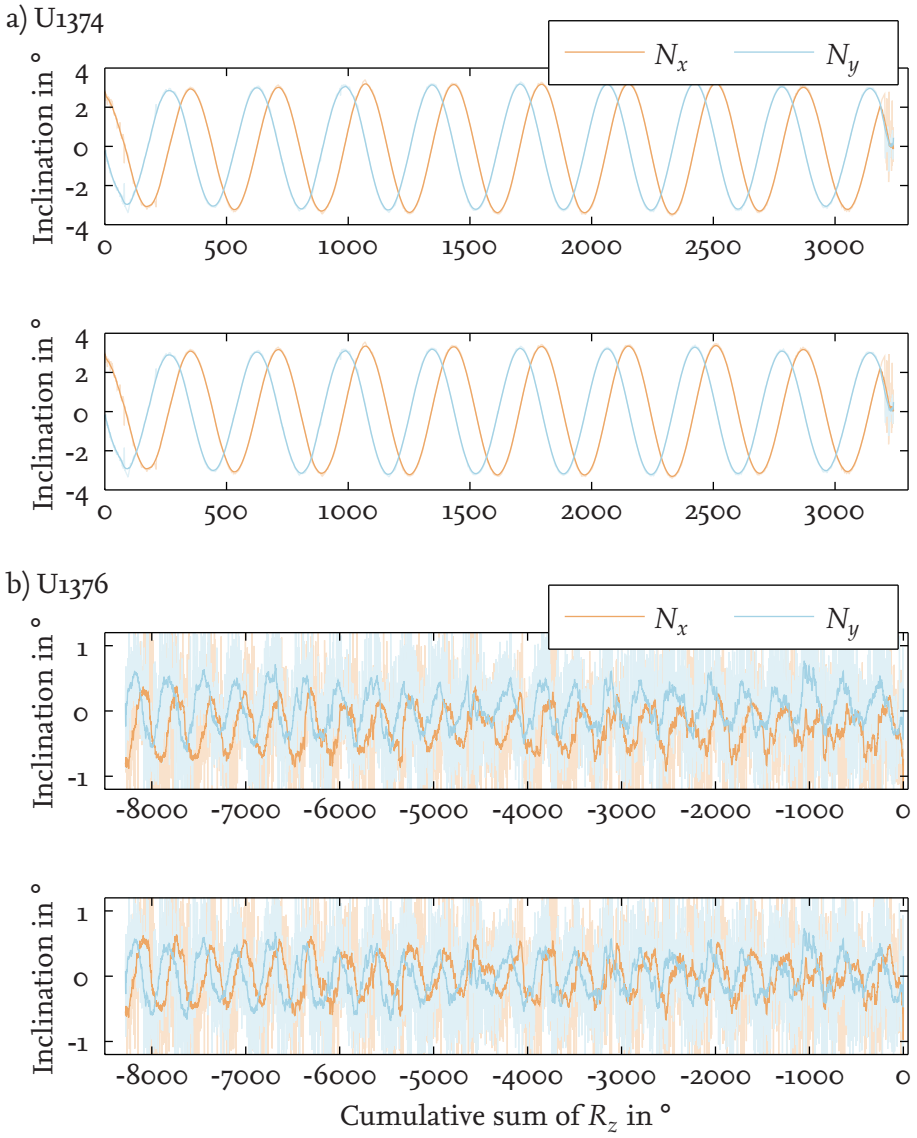

Figure 4.5.: Offset correction of the inclinometer data for Site U1374 (a) and Site U1376 (b). The respective upper panels show the data before correction of the offsets, the respective lower panels show the data after the correction has been applied. Data smoothed using a moving average of 40 data points are shown using dark colors. Unsmoothed data are shown using pale colors.

4.5. Misalignments between Sensor Systems

So far we have treated every sensor system individually, but for a complete calibration of the GBM as a platform of multiple sensors, we have to consider potential misalignments.

Figure 4.6 shows a visual representation of all relevant coordinate systems. The only coordinate system visible from the outside of the tool is its housing (denoted in black). Its z axis is given by the axis of symmetry of the tool, its x axis by a marking on the housing, used to align the tool with geographic north (see Section 5.2). The y axis is implicitly defined by the other two axes.

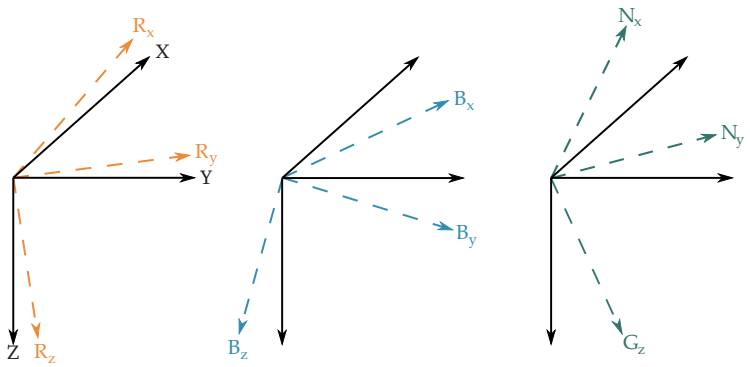

Figure 4.6.: Schematic of the misalignments between the different sensor systems and the housing of the tool. The housing is denoted in black (X, Y, Z), the FOGs in orange (R_x, R_y, R_z), the magnetometer in blue (B_x, B_y, B_z). The inclinometers (N_x, N_y) as well as the vector of gravity (G_z) are shown in green.

The sensors most relevant for the reorientation of the data are the FOGs. Their coordinate system is supposed to be aligned with the housing, but small errors are inevitable; especially as the inner workings of the GBM can be completely removed from the housing. The same is valid for the magnetometers, the coordinate system of which is not necessarily completely aligned with either the housing or the fibre optic gyros. These potential misalignments are evident, as each of the sensor systems has small errors in orthogonality between its individual sensors. Due to asymmetries in the weight distribution within the GBM, the vertical axis of the tool also potentially does not coincide with the vector of gravity and therefore the vertical axis of the coordinate system of the inclinometers, even if the tool is hanging freely.

Fortunately, not all potential misalignments are equally relevant for the quality of the reoriented magnetic field data. But also not all of them can be easily determined.

For example, during the initial northing of the tool (see Section 5.2), it is assumed that the sensitive axis of the gyro R_z coincides with the sensitive axis of the inclinometers, that is the vector of gravity, and that the sensitive axis of R_x coincides with the marker on the housing used for alignment of the housing with geographic north. If either of the assumptions is not right, this is going to cause an error in the determination of the initial orientation of the tool and therefore an error in the removal of the effect of Earth's rotation

on the FOGs. In theory, a misalignment that corresponds to a mutual rotation about the z axis of the respective sensor systems could be determined by a precise orientation of the tool, a long time measurement of the rotation of the Earth as well as controlled rotations of the tool. In practice, the requirements in accuracy for such an experiment likely exceed the capabilities of the gyros and the experimental possibilities.

Misalignments that can be determined experimentally are mutual rotations about the respective x and y axis of the coordinate system of the magnetometer and either the FOGs and the inclinometers. As a result, the equivalent misalignments between the FOGs and the inclinometers can be deduced.

To do so, we either need an experimental setup in a magnetically noise free environment or a real measurement in weakly magnetized sediments. In both cases, data have to be recorded with the GBM rotating about its vertical axis as smoothly and often as possible. Then, the recorded data is reoriented using both an algorithm that relies on FOG data (Section 5.4) and an algorithm that relies on R_z and inclinometer data (Section 5.3).

If the reoriented data shows sinusoidal structures correlating with the rotations of the GBM, this means that the coordinate system of the magnetometer and the coordinate system of the sensors used for reorientation are inclined relative to each other. These misalignments then can be determined and corrected for. The correction takes place during the reorientation of the data and is performed by multiplying each magnetic field vector with an appropriate rotation matrix.

The misalignment between FOGs and magnetometer can be removed by a rotation of 0.165° about the x axis and of -0.028° about the y axis, which has been determined from measurements in the test well Cuxhaven Lüdingworth CAT LUD 1A (Ehmann, 2010). Determined using the same data set, the misalignment between inclinometers and magnetometers can be removed by a rotation of 0.10° about the x axis and -0.07° about the y axis.

If data from both types of sensors are to be used, for example in a Kalman filter (Section 5.6), it is easiest to first correct the inclinometers to the coordinate system of the FOGs, by adding -0.07°+0.028° to N_x and -0.1°+0.165° to N_y, to allow for an error-free fusion of both data sets. In the final reorientation step, the magnetic field vector then has to be rotated according to the values given above for the misalignment of the FOGs. Note that a misalignment of FOGs and inclinometers can not be easily separated from a wrong offset of the inclinometers, as both can be corrected by adding an offset to the inclinometers. Additionally, the possible misalignment determined here is below the accuracy of the inclinometers given by their manufacturer (≈0.3°); however, the true accuracy depends on the noise level during the measurement and was likely higher during the measurements at Lüdingworth (Ehmann, 2010).

Also note that, due to the nature of the ship-based measurements in highly magnetized formations during Expedition 330, no new calibration of these misalignments could be performed and it is therefore likely that the values given above are not necessarily accurate.

4.6. Depth Corrections

The depth data for the magnetic field logs are recorded separately using a counter on the winch of the drill cable and are than added to the GBM datasets in post-processing via a time stamp comparison. Besides possible inaccuracies in the time stamps due to drifting clocks, there are several other things that affect the quality of the depth data and impede a comparison of downlog and uplog, as well as the comparison of data from different tools. As the depth is recorded indirectly by measuring the length of the wireline, any factor that affects the tension of the wireline can also cause a difference between the depth given by the counter on the winch and the actual depth of the tool. Some of the factors that affect the depth measurement are different logging speeds, hole conditions and the weight of the tool string. An additional complication on board of a ship is the movement of the waves that can cause vertical and horizontal movements of the ship and thus can cause movement and oscillations of the tool position that are not recorded by the winch. Wave induced motion of the tools is reduced on average 60% by the use of a so-called wireline heave compensator (Iturrino et al., 2013), but, in combination with other effects, some vertical displacement remains between different logging runs and between downlog and uplog.

In order to compensate for these inaccuracies in the determination of the depth of the tool, depth data is adjusted during processing of the data. Virgil (2012) chooses a combination of a manual adjustment of the depths and an algorithm that calculates correlations between different logs. For the data presented here, I am manually correcting the depths, as I found this to be sufficient for the data of Expedition 330, which show a maximum depth offset of 1 m between the two measurements at Site U1374 and typical offsets of about 0.5 m between downlog and uplog of each measurement.

Figure 4.7 demonstrates the process of the correction. The upper panel shows the downlog (blue line) and uplog (orange line) of the total magnetic field measured at Site U1376 using the uncorrected depth data obtained from the time stamp comparison. A depth shift between the two logs is clearly visible. The middle panel shows a section of both logs with prominent features of the magnetic field that were picked by hand marked with black crosses. Based on these selections, the depth of the datapoint of the uplog is set to the depth of the associated points of the downlog, which are connected by dashed lines in the Figure; the intervals between two selections are then compressed or elongated accordingly.

The effect of the correction is shown in the lower panel of Fig. 4.7 : the depth shift between the downlog and uplog has been reduced. The same procedure demonstrated here is used to correct for the data of Site U1374: first, the depths of the uplog of the first measurement are adjusted to the depths of the downlog. Then, downlog and uplog of the second measurement are adjusted to the depths of the first measurement.

One important criterion for the quality of the reorientation of the magnetic field is the agreement between downlog and uplog in all three components of the magnetic field vector. In order to be able to calculate a difference between the magnetic field values of the different logs, the corrected depth data are further interpolated to fixed depth values,

which allows for a subtraction of the magnetic field of the different logs. Some differences between downlog and uplog always remain, as the horizontal position of the tool within the borehole can differ between both logs, which causes a true change in the recorded magnetic field. Therefore, one cannot use the mean value of the differences as an objective universal criterion for the quality of reorientation; but it can be used to compare the relative accuracy of different reorientation algorithms for a given data set.

On several occasions I am going to compare data from drill core samples to logging data. Here, I used constant depth shifts for the different sites in order to achieve a match between prominent features of the magnetic field logs and the magnetization data of the samples.

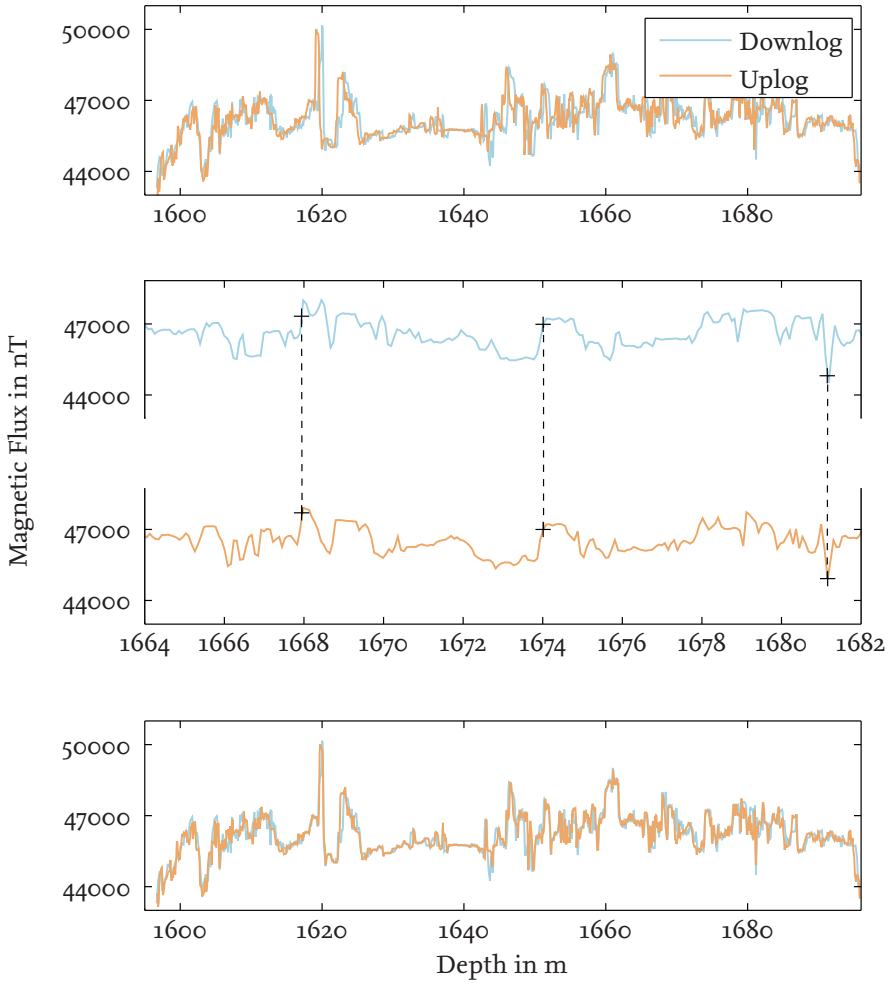

Figure 4.7.: Depth correction of the data at Site U1376. Shown is the total magnetic field of the downlog (blue lines) and uplog (orange lines). Upper panel: Total field displayed using uncorrected depths. Middle panel: manually picked features of the magnetic field visible in both downlog and uplog are marked by crosses, associated points are connected by dashed lines. Lower panel: Total field displayed using corrected depths.

5 Data Reorientation

The main point that distinguishes the GBM from other tools is its capability to determine the vector of the magnetic field. There are several possible methods to reorient the magnetic field data from the tool's reference frame into the geographic reference frame using the available sensor data from inclinometers and gyros. The decision about which algorithm is to be used in a specific case depends on the availability and quality of the data. In all methods that are going to be presented in the following sections, data of the R_z gyro are used to determine the rotation about the vertical axis of the tool. Any method that relies on inclinometers to determine the rotation about the vertical axis is limited to measurements in inclined boreholes with a constant azimuth, as rotations about the vector of gravity cannot be determined from inclinometer data.

5.1. Orientation in Three Dimensions

There are several ways to represent rotations and orientation in a three dimensional space, for example Euler angles, quaternions and rotation matrices. In this thesis, I am going to use rotation matrices throughout all algorithms, as they can be easily used in combination with the readings of the fiber optic gyros.

The fiber optic gyros of the GBM measure the rotation about their sensitive axis integrated over a period of 0.5 s (R_z), respectively 1 s (R_x and R_y). They do not give information about whether the rotations about the individual axes occurred simultaneously, sequentially or in any other form. When one wants to calculate the orientation from the recorded angular change, a decision has to be made about the order of rotations, as matrix multiplication is not commutative, and therefore the outcome of any calculation involving multiple rotation matrices depends on the order of operations. Only for infinitesimally small rotations, the order of rotations becomes unimportant. Without further information, it is sensible to assume that the individual rotations occurred more or less simultaneously. Then we can use a direct cosine matrix (DCM) approach (Virgil, 2012) to calculate a rotation matrix $\mathbf{A}_{DCM}$:

$$\mathbf{A}_{DCM}(\omega_x, \omega_y, \omega_z) = \mathbf{I} + \frac{\sin\omega}{\omega} \cdot \boldsymbol{\omega} + \frac{1 - \cos\omega}{\omega^2} \cdot \boldsymbol{\omega}^2 \tag{5.1}$$

where

$$\omega = \sqrt{\omega_x^2 + \omega_y^2 + \omega_z^2} \tag{5.2}$$

and

$$\boldsymbol{\omega} = \begin{pmatrix} 0 & -\omega_z & \omega_y \\ \omega_z & 0 & -\omega_x \\ -\omega_y & \omega_x & 0 \end{pmatrix} \tag{5.3}$$

and ω_x, ω_y and ω_z are the rotations about the respective axis. The orientation of the GBM at a time t_i can then be represented by the product of all rotations matrices up to that point in time:

$$\mathbf{A}_{t_i}^{tot} = \mathbf{A}_{t_0} \cdot \mathbf{A}_{t_1} \cdot \ldots \cdot \mathbf{A}_{t_i} \tag{5.4}$$

$\mathbf{A}_{DCM}$ contains information about the attitude viewed from the internal reference frame of the GBM. To transform any measured vectorial quantity to the geographic reference frame, it has to be multiplied by the inverse matrix, i.e. the transposed matrix $(\mathbf{A}_{t_i}^{tot})^T$.

To be able to compare the information about the orientation contained in the rotation matrix with the output of the inclinometers, whose angular measurements give more descriptive values for the orientation, a simple approach can be used. The orientation of the geographic reference frame with respect to the GBM in the beginning of the measurement can be represented by two vectors, $T_1 = (\ 0 \quad 0 \quad 1\ )^T$ and $T_2 = (\ 1 \quad 0 \quad 0\ )^T$, where T_1 represents the direction of gravity and T_2 the orientation with respect to geographic north. Using two vectors is necessary, as for example T_1 is insensitive to pure rotations about the vertical axis and cannot be reliably used to determine the azimuth of the tool. Multiplying these vectors with the accumulated rotational matrices gives the orientation of the geographic reference frame as viewed from within the tool. The orientation of the tool can then be calculated as follows (see Fig. 5.1 for a graphical representation of the quantities used in the calculations):

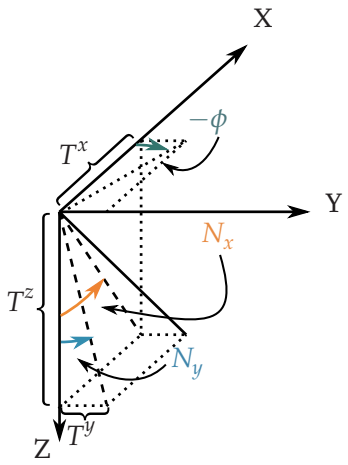

Figure 5.1.: Calculation of orientation angles from vector components.

$$N_x = \arctan\left(\frac{T_1^x}{T_1^z}\right) \tag{5.5}$$

$$N_y = \arctan\left(\frac{T_1^y}{T_1^z}\right) \tag{5.6}$$

$$\phi = -\arctan\left(\frac{T_2^y}{T_2^x}\right) \tag{5.7}$$

The negative sign in the calculation of the azimuth ϕ is necessary, as the azimuth is defined in the geographic reference frame, whereas the inclinations N_x and N_y are defined in the coordinate system of the GBM. To obtain the right quadrant of the azimuth, most programming languages offer an *atan*2 function that takes the sign of the arguments into account.

The total inclination of the tool, $|N|$, can be calculated from inclinometer data like so:

$$|N| = \arctan\left(\sqrt{\tan\left(N_x\right)^2 + \tan\left(N_y\right)^2}\right) \tag{5.8}$$

5.2. Northing

In order to be able to reorient the magnetic field data with respect to geographic north and to remove the influence of the rotation of the Earth from the gyro data, it is necessary to determine the orientation of the GBM relative to the geographic coordinate system in the beginning of each measurement as accurately as possible On land, the orientation is determined by positioning several markers around the borehole, forming baselines whose orientations relative to geographic north are determined by differential GPS measurements. Thus, in the beginning and in the end of each measurement, the GBM can be aligned to one of these baselines using a scope mounted on its housing and the known orientation can be used to correct the data. This procedure is referred to as *northing*.

When running measurements at sea, northing is complicated by the movements of the ship. During Expedition 330, we put a marker on the helipad at the aft of the ship, on the symmetry axis of the ship. As the drill rig is located above the center of the vessel, the orientation of the line of sight from drill rig to the marker equals the orientation of the ship. The orientation relative to geographic north of the ship itself is continuously monitored for navigation purposes by several mechanical gyros. The output of these gyros is regularly compared with the orientation derived from celestial navigation and from known landmarks, with a mean deviation of about $\pm$ 0.2°. An excerpt from the navigation log of the Joides Resolution can be found in Table 5.1.

In order to obtain a second data source for the orientation of the ship, we recorded the GPS signals of two antennas. One is regularly mounted at the aft of the ship, the second one was set up in a distance of 97.3 m further mid-ship with an offset of one degree towards the port side. With their known positions relative to the ship, it is possible to calculate the bearing and to compare it with the output of the gyros. However, the signal of the second antenna was distorted; most likely due to interferences caused by the superstructure of the ship. Figure 5.2a shows a comparison of the bearing computed using the GPS antennas and the gyro data, Fig. 5.2b shows the distance of the two GPS antennas computed using the GPS signals. What seems like noise combined with a more or less constant offset in Fig. 5.2a becomes more obvious in Fig. 5.2b: The computed distance of the two GPS sensors varies significantly around the true value, and it is therefore very likely that the GPS bearing also does not coincide with the true bearing of the ship. Thus, the output of the ship's gyro is being used for the determination of the orientation of the GBM in the beginning of the measurements.

Figure 5.3 shows an example of the data of the first run at Site U1374 used for northing. The Figure shows the cumulative rotation about the vertical axis of the tool in the beginning of the measurement. Data are not yet corrected for the rotation of the Earth (see Section 5.2.2). Several strong rotations of the tool are visible that occurred during the initial setup and the preparations for northing. The zoom-in figure shows the interval used for the determination of initial orientation. Visible are small oscillations as the GBM is aligned with the marker positioned at the end of the ship. The data point marked with the circle is used as the first data point during reorientation of the magnetic field; its initial value is

Date	Time	Position		Bearing		Object	Error
		Lon	Lat	True	Gyro		
19 Dec '10	0715	S 31-59	E 179-52	042.1	042	☾	0.1L
20 Dec '10	0655	S 29-08	E 176-51	052.4	053	☾	0.4H
21 Dec '10	1607	S 26-29	W 174-44	303	303.4	☾	0.4L
22 Dec '10	1538	S 26-29	W 174-44	315	315.2	☾	0.2L
23 Dec '10	1530	S 26-29	W 174-44	326	326.6	☾	0.6L
26 Dec '10	1508	S 26-29	W 174-44	085.5	085	♀	0.5L
28 Dec '10	0625	S 26-29	W 174-44	243	243	☉	-
28 Dec '10	1606	S 26-29	W 174-44	092.8	093	♀	0.2H
29 Dec '10	0825	S 26-29	W 174-44	286.3	286	♃	0.3L
31 Dec '10	1555	S 28-34	W 173-17	049.9	050	Antares	0.1H
01 Jan '10	1500	S 28-34	W 173-17	058.7	059	Antares	0.3H
02 Jan '10	1600	S 28-34	W 173-17	092.8	093	♀	0.2H
04 Jan '11	0602	S 28-34	W 173-17	247	247	☉	-
07 Jan '11	1551	S 28-36	W 173-23	108.4	108	Antares	0.4L
12 Jan '11	1445	S 28-36	W 173-23	103.3	103	♀	0.3L
19 Jan '11	1600	S 28-36	W 173-23	297.5	297	☽	0.5L
20 Jan '11	1622	S 28-36	W 173-23	298.6	298	☽	0.6L
24 Jan '11	0520	S 32-31	W 172-35	256.3	256	☉	0.3L
26 Jan '11	0515	S 32-57	W 171-40	257.3	257	☉	0.3L
31 Jan '11	1602	S 32-13	W 171-53	218.4	218	Canopus	0.4L
03 Feb '11	1342	S 33-02	W 171-27	113.8	114	♀	0.2H
08 Feb '11	1504	S 37-44	W 172-54	306.8	307	Regulus	0.2H
09 Feb '11	0621	S 37-12	W 175-02	254.2	254	☉	0.2L

Table 5.1.: Excerpt from the navigation log of the Joides Resolution. The bearing given by the ship's gyro is compared with the bearing derived from astronomical observations. The mean error of the bearing is 0.2 °
L: Gyro bearing is low, H: Gyro bearing is high
☾ , ☽: Moon, ☉: Sun, ♀: Venus, ♃: Jupiter

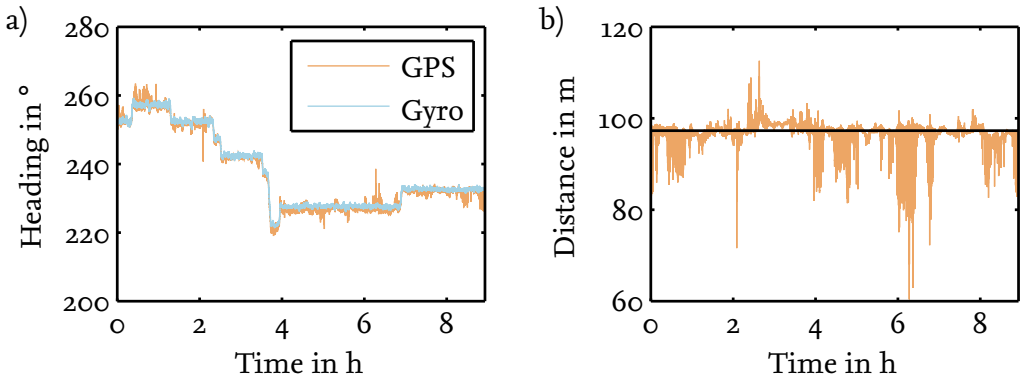

Figure 5.2.: (a) Comparison of the bearing measured by the ship's gyro and the bearing computed from two GPS antennas. The latter one shows larger noise. (b) Comparison of the computed distance of two GPS antennas to their true distance. Due to a disturbed signal of the antenna closer midship, the distance varies significantly. Thus, the bearing given by the gyro is used for further data processing.

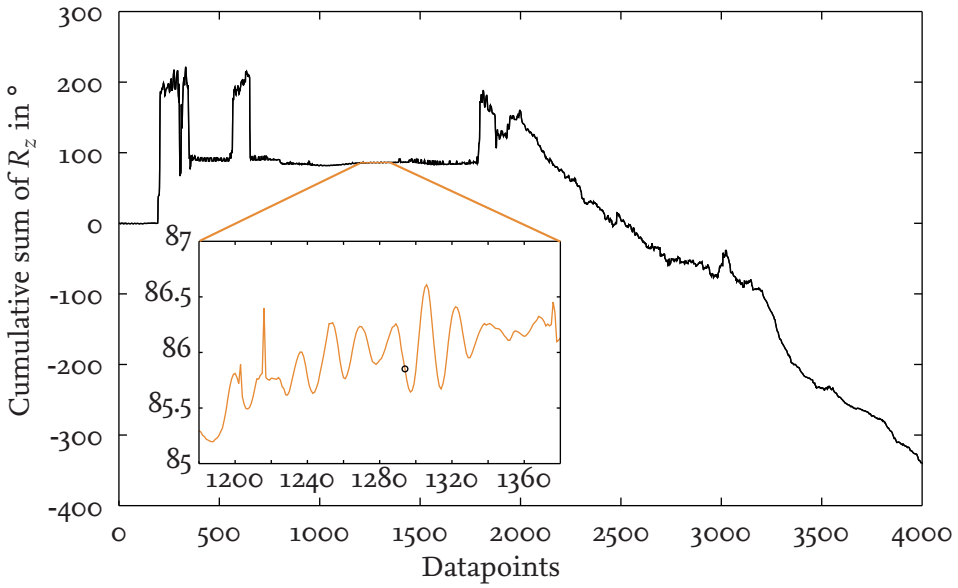

Figure 5.3.: Example for the data used to determine the orientation of the tool during northing. Shown is the cumulative rotation about the vertical axis of the tool. The data point later used for the start of the reorientation algorithm for the magnetic field is marked with a circle.

later set to the azimuth determined from the ship's gyro. The data point is chosen based on its time stamp: whenever the scope mounted to the GBM was aligned with the marker, the time was recorded. Out of several readings, the one with the smallest oscillations was chosen at each site.

For the first measurement run at Site U1374 (shown in Fig. 5.3), data point 1294 was chosen as the start point for the reorientation algorithms and the orientation of the tool was determined as 53.70° relative to geographic north. For the second run at Site U1374, data point 2725 was chosen and the orientation was determined as 51.07°. For the measurement at Site U1376, data point 3027 was chosen, with an azimuth of the tool of 227.35°. The initial values for the inclination of the tool are directly taken from the inclinometer readings at the respective data points.

5.2.1. Quality Control

Inaccuracies in the determination of the orientation of the GBM (bearing and tilt) can lead to errors accumulating in the course of the measurement. The signal of the ship's gyro, which is used to orient the GBM in the horizontal plane, is only accurate within about 0.2°; also, due to the heave of the ship during northing, it is not as easy to align the sight mounted on the GBM with the marker on the back of the ship as accurately as this is possible on land. The inclinometers that are used to determine the other two angles are susceptible to vibrations and mechanical shocks, which can cause further inaccuracies during northing.

To assess the impact of these inaccuracies, one can use the signal of the inclinometers that, on average, still coincides with the true inclination of the tool. Using Eq. 5.5 and Eq. 5.6, the signal of the FOGs can be used to compute a second set of inclinations, $N_{x,y}^{FOG}$, that should on average coincide with the inclination given by the inclinometers, $N_{x,y}$. Due to the noise of the inclinometers, some difference is always going to be present. However, any error in the determination of the start angles or an uncorrected drift of the FOGs (e.g. due to not completely corrected temperature offsets) is going to cause an increased difference between both datasets. The residual between both sets of inclinations, normalized by the number of datapoints, can be calculated as follows:

$$residual = \sqrt{\sum_{i=a}^{b} \frac{(N_{x_i}^{FOG} - N_{x_i})^2 + (N_{y_i}^{FOG} - N_{y_i})^2}{b-a}} \tag{5.9}$$

where the sum is taken over an interval of datapoints extending from index a to b. To reduce the influence of other possible offsets to the gyros, only the first third of each measurement is used, starting from the datapoint of the initial northing. Note that the quality control is conducted before any further corrections (e.g. offset corrections, see Section 5.5) are made to the data.

By adding some offsets δN_x, δN_y and δR_z to the angles determined in the initial northing, and by using Eq. 5.9 to calculate the residual for a range of combinations of offsets, one can find whether the difference between those two sets of inclinations are minimal for the original angles or can be minimized by choosing different start angles.

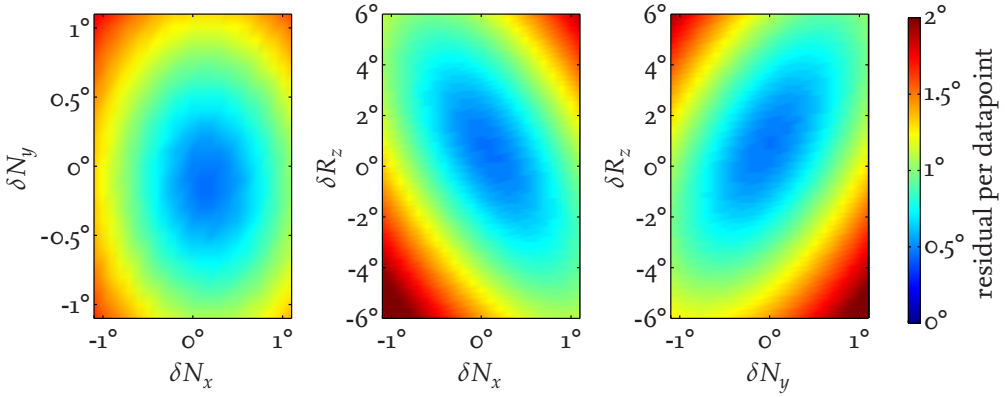

Figure 5.4.: Offset study for the northing angles at Site U1376. The panels show the influence of a variation of the northing parameters by offsets δN_x, δN_y and δR_z on the residual (calculated using Eq. 5.9) between the inclination given by the inclinometers and the inclination calculated from the GBM's gyros. Color coded is the residual per datapoint in three slices through the parameter space. In each slice the third parameter is set to 0°: left panel: δR_z = 0°, middle panel: δN_y = 0°, right panel: δN_x = 0°.

Figure 5.4 shows the result of a offset study for Site U1376. Here, the northing angles were determined to be R_z = 227.35°, N_x = -0.70° and N_y = -0.43°. Shown are three slices through the parameter space; in each slice the third parameter is set to 0° (left panel: δR_z = 0°, middle panel: δN_y = 0°, right panel: δN_x = 0° . The residual between the inclination given by the inclinometers and the inclination calculated from gyro data is color coded. An algorithm that uses the data of all three FOGs (see Section 5.4) was used for the reorientation necessary to calculate inclination angles from gyro data. The residual was calculated for a total of 287288 offset combinations, which took about 48 hours to complete, which corresponds to approximately 0.6 s per reorientation.

The Figure shows that the minimum of the residual is found close to the parameters determined during initial northing; the absolute minimum lies at δN_x = 0.16°, δN_y = -0.11° and δR_z = 0.08°; these values would have to be added to the northing angles to reduce the residual to 0.45° per datapoint. The results for Site U1374 are not shown here, but are comparable, with minimum residuals found within 0.5° of the parameters determined during northing. As other error sources besides a possibly imprecise northing are present, the optimum offsets determined by the parameter search described here cannot directly be used for a correction of the northing angles. But as the optimum offsets are close to the northing angles and as any large change in the northing parameters would cause an increase in the residuals, the parameter study is an indication that northing was conducted with an acceptable accuracy.

5.2.2. Correction for the Rotation of the Earth

During the course of a measurement, Earth (astronomical symbol ♁) is both rotating about its axis as well as about the sun. This rotation is also measured by the fiber optic gyros

and has to be accounted for, as it will otherwise cause a significant artificial drift in the magnetic field data (see also Section 5.2). The rotation amounts to 360° per sidereal day, that is per 23.934 h, which equals a rotation of 15.041°/h. The amount of Earth's rotation contributing to the individual gyro depends on the latitude of the site of the measurement as well as the current orientation of the tool. If A_i is a rotational matrix giving the tool's orientation at a time i and with Φ being the latitude, the effective rotation of the Earth for each gyro is given by:

$$\vec{E}_{\oplus} = \mathbf{A}_{t_i}^{tot} \cdot \begin{pmatrix} 15.041\,^{\circ}/\mathrm{h} \cdot \cos\Phi \\ 0 \\ -15.041\,^{\circ}/\mathrm{h} \cdot \sin\Phi \end{pmatrix} \cdot \delta t \tag{5.10}$$

where δt is the time passed since measurement $i-1$. The elements of $\vec{E}_{\oplus}$ can then be subtracted from the appropriate gyro measurements at time t_{i+1}. This correction is included in all of the following algorithms used for the reorientation of the magnetic field data. The correction is one of the possible sources for errors during reorientation: if, at any data point, the orientation of the tool with respect to the geographic coordinate system is erroneous, the rotation of the Earth is not going to be correctly accounted for, which can give rise to accumulating errors in orientation.

Figure 5.5 demonstrates the effect of correction. Shown is the cumulative sum of the data of all three gyros, recorded while the GBM was hanging vertically with a fixed and known orientation. The uncorrected data are shown in blue and the data corrected for Earth's rotation are shown in orange; the temperature dependent offset of the gyros has been removed from both datasets. If there was no rotation recorded by the gyros, the cumulative sum should remain zero. The linear trend visible in the uncorrected data is caused by Earth's rotation and is removed by the correction.

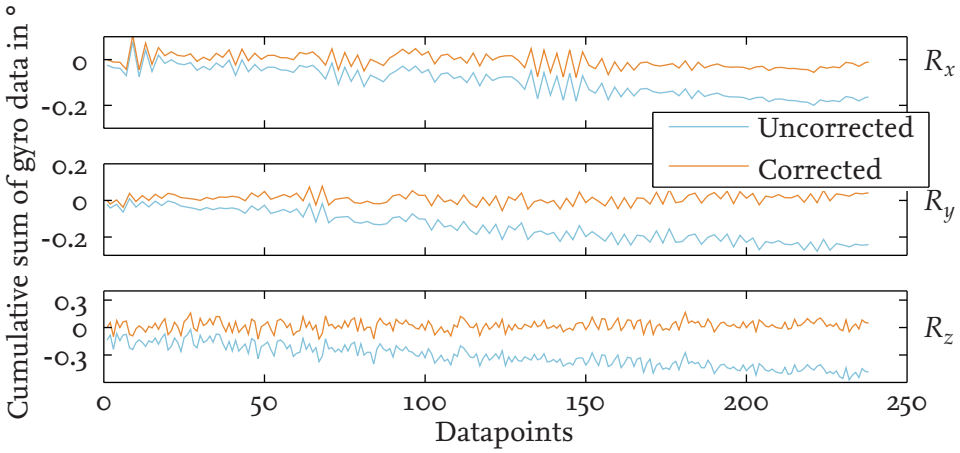

Figure 5.5.: Effect of the correction for the rotation of the Earth on gyro data. Uncorrected data are shown in blue, corrected data are shown in orange. Upper panel: cumulative sum of R_x. Middle panel: cumulative sum of R_y. Lower panel: cumulative sum of R_z.

5.3. Reorientation using one Gyro and two Inclinometers

The minimal setup necessary to obtain oriented three component magnetic field data in a vertical or near-vertical borehole is a combination of a gyro measuring the rotation about the vertical axis and two inclinometers measuring the inclination of the tool about the other two axes. Using the inclinometers for reorientation will always result in some motion induced noise in the magnetic field data. Here it is important to notice that simply filtering the inclinometer data, e.g. by a moving average, can introduce rotation dependent artifacts in the magnetic field data if the filtered inclinometer data are used for reorientation: the inclination given by the inclinometers varies depending on their orientation relative to the path of the borehole. For a rotating tool in an inclined borehole, even a completely noise free measurement is going to give a variation in the inclinometer data, which would incorrectly be removed by a simple moving average (see Fig. 4.5 and Section 4.4). In the following two implementations, I am therefore abstaining from filtering the inclinometer data. A Kalman filter that incorporates gyro and inclinometer data and is effectively smoothing the inclinometer data is described in Section 5.6. Please note that even though using a moving average of the inclinometer data is not appropriate for reorientation purposes, I am nevertheless going to use it for illustration purposes in some figures of this thesis, as it makes it easier to visually compare the datasets of gyros and inclinometers.

The reason for including algorithms that do not use all of the available gyro data are the data gaps that occurred at the measurements at Site U1374: a data gap in the gyro data causes a loss of information about the history of rotation of the tool and therefore also affects all subsequent data. In contrast, a gap in the inclinometer data causes only a temporary loss of information. By using the inclinometers instead of R_x and R_y, the influence of the data gaps can be reduced, at the cost of introducing inclinometer noise to the magnetic field data.

5.3.1. Implementation A - Separate Treatment of Inclination and Rotation

In the first implementation of a reorientation algorithm, we treat the rotation about the vertical axis separately from rotations about the other two axes. By doing so, the inclination of the tool is treated as a temporary disturbance from the vertical. In every data point t, the measured valued for ω_{z_t} is corrected for the rotation of the Earth. Then, it is added to all previously recorded (and corrected) values of ω_z and a rotational matrix is calculated:

$$\mathbf{A}_t^z = \begin{pmatrix} \cos\omega_z^{tot} & \sin\omega_z^{tot} & 0 \\ -\sin\omega_z^{tot} & \cos\omega_z^{tot} & 0 \\ 0 & 0 & 1 \end{pmatrix} \tag{5.11}$$

where

$$\omega_z^{tot} = \omega_{z_{t_0}} + \omega_{z_{t_1}} + \ldots + \omega_{z_{t_i}} \tag{5.12}$$

A second rotation matrix is calculated for the inclinometers, using the DCM approach (Eq. 5.1), that is assuming that the rotations they measure occur simultaneously:

$$\mathbf{A}_t^N = \mathbf{A}_{DCM}(N_y, -N_x, 0) \tag{5.13}$$

The final orientation matrix is then calculated using the product of both matrices:

$$\mathbf{A}_t^{tot} = \mathbf{A}_t^N \cdot \mathbf{A}_t^z \tag{5.14}$$

The advantages of this method are that it is easy to understand and robust against noise of the inclinometers. As the calculated orientation at time t only depends on the inclinometer measurements of time t and not on any previous measurements, temporary noise in the inclinometer data is only going to affect the corresponding data points and none of the subsequent and possibly less noisy data points.

The disadvantage is that, as inclination of the tool is not considered in the calculation of the change of azimuth of the tool, any deviation of the borehole from the vertical will, cause the computed azimuth of the tool to differ from the true azimuth. The error in azimuth made in each step i, $\delta\phi_{t_i}$, depends on the rotation about the vertical axis and the total inclination of the borehole, $|N|$:

$$\delta\phi_{t_i} = \omega_{z_{t_i}} \cdot |N| \tag{5.15}$$

The maximum error in azimuth of this method, $\delta\phi_{max} = \sum_i \delta\phi_{t_i}$, depends on the history of rotation of the tool. However, if the error of the calculated azimuth becomes too big, this will be visible in a difference between the downlog and the uplog of the reoriented magnetic field. As long as this difference is within an acceptable range, the algorithm can be used nevertheless.

5.3.2. Implementation B - Inclinometers as Rate Sensors

In order to avoid the disadvantages of Implementation A, the rotation of the tool about its horizontal axes can be derived from inclinometer data and, in conjunction with the rotation about its vertical axis recorded by the R_z FOG, used with the DCM approach (Eq. 5.1). By calculating the change in orientation about the horizontal axes from the inclinometers and treating the inclinometers as rate sensors like the FOGs, we lose the advantage of the absolute measurement of the inclinometers, but now correctly take a change of inclination into account when calculating the azimuth of the tool.

Here, the readings of the inclinometers cannot be used directly, as they measure orientation and not change in orientation. As noted previously, if a borehole has a constant inclination and the tool is only rotating about its vertical axis, the readings of the inclinometers will change as their sensitive axis points in a different direction. The new angles after a rotation about the vertical axis by an angle ω_z are given by (see Fig. 5.1 for a sketch of the geometry):

$$\begin{pmatrix} \tan N_x' \\ \tan N_y' \end{pmatrix} = \begin{pmatrix} \cos\omega_z & \sin\omega_z \\ \sin\omega_z & \cos\omega_z \end{pmatrix} \cdot \begin{pmatrix} \tan N_x \\ \tan N_y \end{pmatrix} \tag{5.16}$$

To derive the true rotation of the tool about its two horizontal axes, this has to be taken into account and the apparent change in inclination that is caused by the rotation about the vertical axis has to be subtracted:

$$\omega_{x_t}^N = N_{y_t} - \arctan\left(\cos(\omega_{z_{t_i}}) \cdot \tan(N_{y_{t_{i-1}}}) - \sin(\omega_{z_{t_i}}) \cdot \tan(N_{x_{t_{i-1}}})\right) \tag{5.17}$$

$$\omega_{y_t}^N = -N_{x_t} + \arctan\left(\sin(\omega_{z_{t_i}}) \cdot \tan(N_{y_{t_{i-1}}}) + \cos(\omega_{z_{t_i}}) \cdot \tan(N_{x_{t_{i-1}}})\right) \tag{5.18}$$

Here, $\omega_{x_t}^N$ and $\omega_{y_t}^N$ are the angles of rotation about the respective axes estimated from the inclinometer readings. The total rotation matrix can then be calculated with the DCM approach (Eq. 5.1) as follows:

$$\mathbf{A}_t^{tot} = \mathbf{A}_{DCM}(\omega_{x_t}^N, \omega_{y_t}^N, \omega_{z_t}) \tag{5.19}$$

where ω_{z_t} is the change in orientation measured by the vertical FOG. A disadvantage of this method is that the calculation of the azimuth is influenced by noise in the inclinometers and that noise in one part of the measurement is propagated into later parts of the measurement by the algorithm.

5.3.3. Comparison of both Implementations

Which of both implementations can or should be used depends on the general conditions of the measurement and has to be decided based on the advantages and disadvantages of each implementation. As neither of both algorithms takes significant time to compute, the choice of algorithm can be based on a comparison of the reoriented data.

Figure 5.6 shows a comparison of the east component of the reoriented magnetic field for the first measurement at Site U1374. The left panel shows implementation A and the right panel shows implementation B. Both reoriented data sets show the influence of the noise of the inclinometers.

Down- and uplog for implementation B agree better than down- and uplog of implementation A and therefore implementation B should be preferred for reorientation in this case. The north and the vertical component of the reoriented magnetic field data do not show visible differences between down- and uplog in both implementations, so they are not shown here.

In addition to the two implementations presented here, other implementations are possible. For example, in implementation A, one could use Eq. 5.15 and the inclination measured by the inclinometers to correct the calculation of the azimuth for tool inclination. However, this would introduce the noise of the inclinometers into the calculation of the azimuth and thus also cause errors, albeit different ones, in the reorientation. Especially as the implementation presented here suffice for the reorientation of the magnetic field data at hand, I am therefore not going into further detail of additional methods.

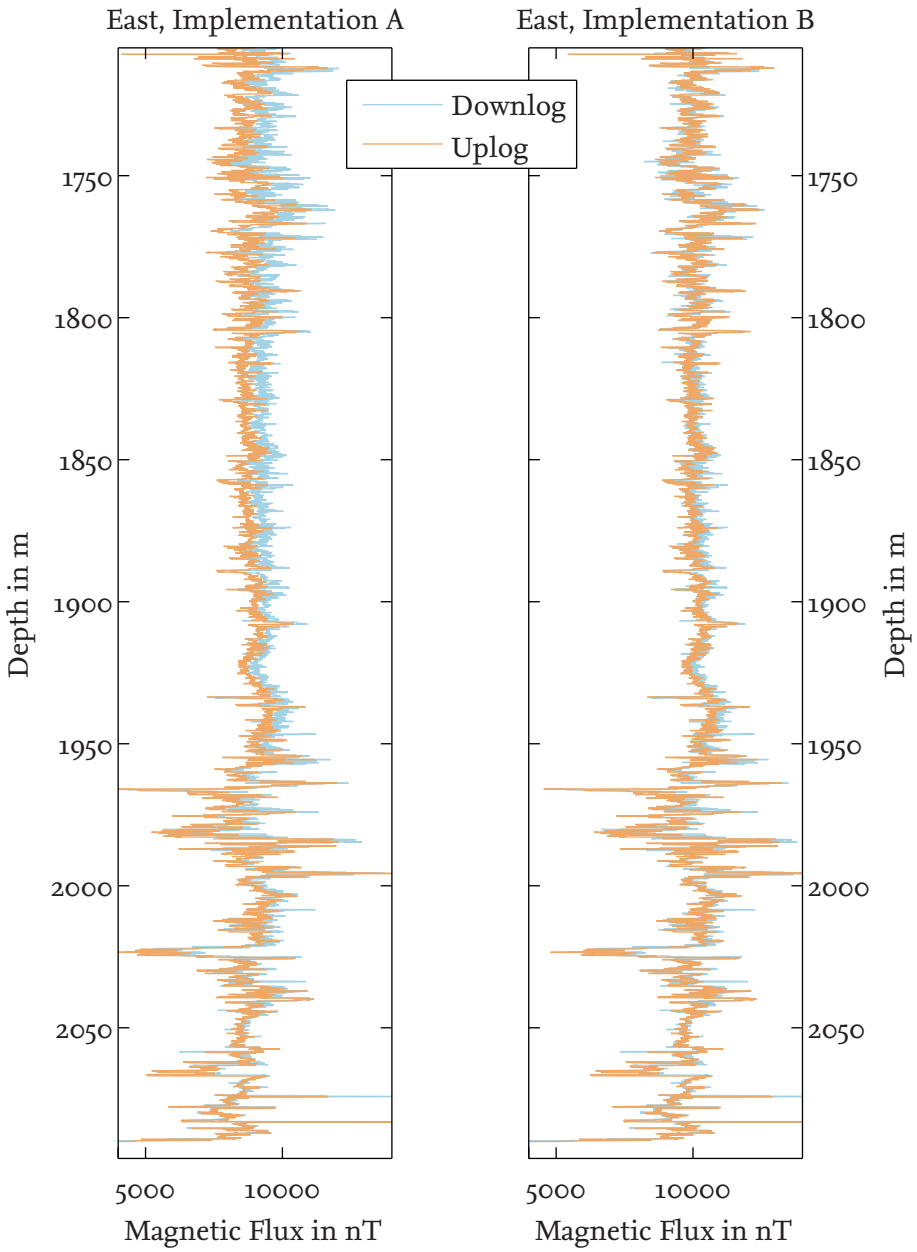

Figure 5.6.: Comparison of both implementations of the reorientation using one gyro and both inclinometers. Shown is the down and uplog of the east component of the reoriented magnetic field for implementation A (left panel) and implementation B (right panel).

5.4. Reorientation using three Fibre Optic Gyros

The preferred method of reorientation of the GBM data developed during recent years is one that uses the data of all three fiber optic gyros. Using Eq. 5.1, the calculation of the rotation matrix for every data point is straight forward:

$$\mathbf{A}_t^{tot} = \mathbf{A}_{DCM}(\omega_x, \omega_y, \omega_z) \tag{5.20}$$

The advantage of this method is that the gyros are not susceptible to shocks and vibrations and that the rotation matrix derived from gyro data is therefore the most accurate description of the true motion of the tool. The disadvantage is that drifts and offsets of the gyros in the order of millidegrees, that are negligible in the short term, accumulate in the course of a measurement and therefore cause a drift in the reoriented magnetic field. There exist several methods to correct for those errors, which are presented in the following.

5.5. Combining FOGs and Inclinometers: Gyro Offset Correction

Even though all care is taken to remove all known offsets from the fibre optic gyros during data processing, some offsets can remain that degrade the quality of the reoriented magnetic field. Possible sources for these offsets are errors in the temperature or misalignment correction of the FOGs.

Virgil (2012) suggested a correction for remaining, uncorrected offsets of the fiber optic gyros that is based on the northing process at the end of a measurement. In the first step, the traditional reorientation algorithm that uses FOG data (Section 5.4) is run once, and the orientation of the GBM calculated by the reorientation algorithm is compared to the true orientation of the GBM determined by the northing procedure.

Then, in three subsequent reorientation runs, an offset of 1 °/h is added to the data of each of the fiber optic gyros, and the change in difference between the physical orientation and the calculated orientation is determined. By assuming a linear dependence of the offset and the error in orientation, an optimal constant offset is calculated that should minimize the error.

However, this method could not successfully be used for the data of Expedition 330. Due to a loose connection, communication with the tool was lost at the end of the first measurement at Site U1374, so no northing could be conducted. For the second measurement at Site U1374, as well as for the measurement at Site U1376, northing was possible at the end of the measurement, but the algorithm suggested offsets in the order of several tens of degrees per hour, which resulted in a magnetic field where downlog and uplog did not agree at all and which was unsuitable for any further interpretation.

Therefore, I implemented a new algorithm that uses the difference in tool inclination calculated using the fiber optic gyros (see Eq. 5.5 and Eq. 5.6) to the inclination measured using the inclinometers. Similar to the correction used by Virgil (2012), the assumption is made that any observed difference between the two sets of inclinations is caused by an

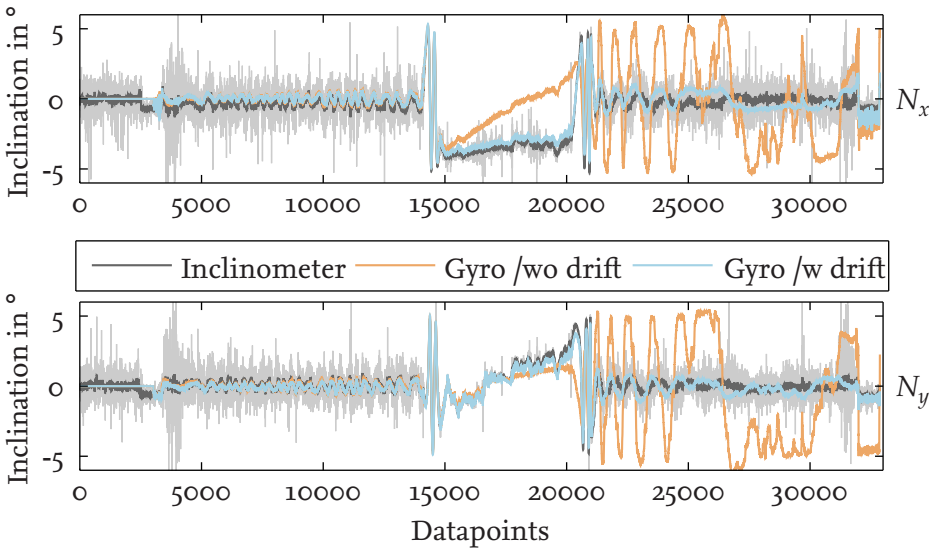

Figure 5.7.: The effect of the FOG offset correction on the calculated inclination of the tool (Site U1376). The upper panel shows N_x, the lower panel N_y. Black lines show the inclination as measured by the inclinometers smoothed by a moving average with a window width of 60 datapoints; unfiltered data are shown in gray. Orange lines show the inclination calculated from FOG data without offset correction; blue lines show the calculated inclination with offset correction. Without correction, the calculated inclination differs from the measured inclination during the course of the measurement.

uncorrected, constant offset of the gyros. Using the reorientation algorithm described in Section 5.4, the difference in inclination can be calculated for every data point and used as input for a least squares algorithm that minimizes the residual. The residual is calculated according to Eq. 5.9 in Section 5.2.1, summing over all datapoints between both northings - or, as no second northing was possible for the first measurement at Site U1374, all datapoints between the first northing and the end of the dataset. The advantage of this method is that it does not rely on the orientation determined in a single point, but, depending on the duration of the measurement, compares several thousand points.

Figure 5.7 demonstrates the necessity for and the effect of the correction for the measurement at site U1376. The upper panel shows the inclination of the tool in x direction and the lower panel shows the inclination in y direction. The inclination of the tool calculated from gyro data is shown in orange; unfiltered inclinometer data are shown in gray and inclinometer data filtered by a moving average with a window size of 60 datapoints are shown in black. Without correction, the inclination of the tool calculated from the gyros is differing from the inclinometer data during the course of the measurement. Applying the constant offset calculated by the least-squares algorithm, this difference is significantly reduced (blue lines). The calculated offsets are 1.6568 °/h to R_x, -5.3142 °/h to R_y and 1.0151 °/h to R_z. These values correlate well with the temperature corrections applied to the gyros

(see Fig. 4.1): The FOGs that require a higher temperature correction also require an higher additional offset to reduce the difference to the inclinometers. This could be a sign that the temperature correction should be repeated in order to see whether any offsets have changed since the last calibration measurements.

In general, the gyro offset correction algorithm should not be used as a substitute of the temperature correction. The algorithm calculates a constant offset for the whole dataset, but the temperature (and the associated corrections) are not constant throughout a measurement, which can, depending on the conditions of the measurement, give rise to errors. However, the offset correction can compensate for a complete lack of temperature correction, which is demonstrated in the following.

Figure 5.8 shows the effect of the correction on the reoriented magnetic field data. All panels show the east component of the magnetic field, as it is the component of the field most influenced by errors in reorientation. Downlogs are shown in blue and uplogs are shown in orange. The left panel shows the magnetic field reoriented after the temperature correction has been applied to the gyros, but no additional offset correction. Here, down- and uplog do not agree well and the magnetic field is drifting apart. The middle panel shows the magnetic field reoriented without temperature correction, but with the gyro offset correction applied. Without temperature correction, the calculated offsets change to 2.7290 °/h (R_x), -5.2744 °/h (R_y) and 2.9214 °/h (R_z). The right panel of Fig. 5.8 shows the reoriented magnetic field, this time with temperature correction and additional offset correction.

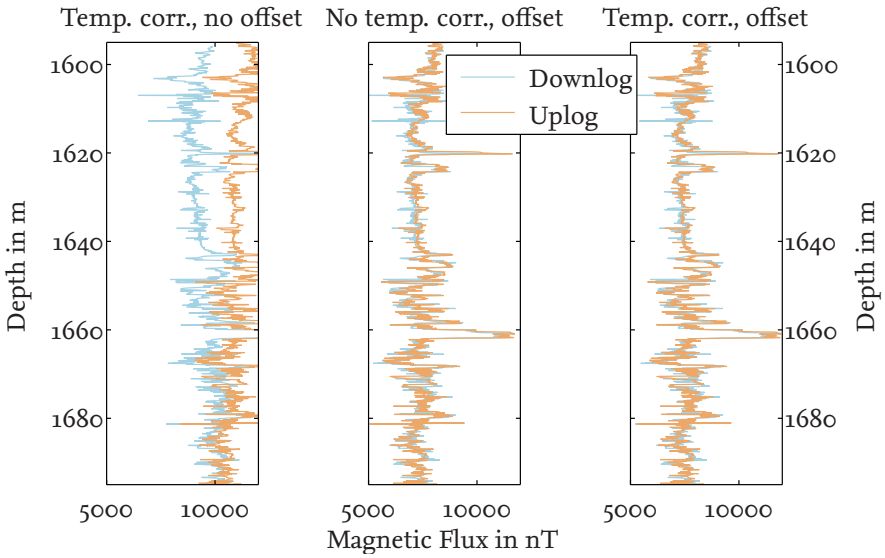

Figure 5.8.: The effect of the FOG offset correction on the reoriented magnetic field (Site U1376). All panels show the east component. Blue lines show the downlog and orange lines the uplog. Left panel: Temperature correction applied, no additional offset correction. Middle panel: No temperature correction, but additional offset correction. Right panel: Both temperature correction and additional offset correction are performed.

In both the middle and the right panel, downlog and uplog agree well, with mean differences of 45 nT (103 nT) north, 86 nT (40 nT) east and 76 nT (107 nT) vertical. Additionally, the middle panel shows almost no difference to the right panel, which means that the gyro offset correction compensated for the lack of temperature correction in the middle panel. The maximum difference in the reoriented magnetic field between the combination of algorithms of the middle panel and the right panel is 150 nT north, 50 nT east and -250 nT vertical, which corresponds to an approximate difference in orientation of 0.4°.

The corrections calculated by the offset correction algorithm are lower when the algorithm is used in combination with a temperature correction of the gyros, which is expectable. Even though the algorithm manages to correct for a lack of temperature correction, the calculated orientation of the tool is more likely to coincide with the true orientation when both temperature correction and additional offset correction are performed. Summing up, Fig. 5.8 demonstrates that the offset correction helps to compensate for gyro errors and succeeds in giving a reoriented magnetic field where downlog and uplog agree.

5.6. Combining FOGs and Inclinometers: Kalman Filtering

Even though the gyro offset correction results in a good agreement of downlog and uplog of the reoriented field and manages to compensate for a lack of temperature correction, it is limited in so far that it does not fully exploit the potential of the complementary inclinometer and gyro data. Its results are offset values that are constant throughout the measurement, but most of the physical reasons for an offset of the gyros are likely to be variable with time, for example if they are temperature dependent. In theory, it is possible to try and split the reorientation into multiple intervals and calculate separate offsets for any of them. However, the result is likely to depend strongly on the choice of intervals and there are no obvious objective parameters for the choice of the interval boundaries.

A Kalman Filter (Kalman, 1960) is an algorithm that can be used to get an optimal linear estimate of the true state of a system using a set of noisy observations. It is an iterative method in which the state of the system is estimated using the previous state and a current observation. Since its discovery in the 1960s, it has been applied to a wide range of problems. There are numerous books and articles available on it, e.g. Maybeck (1979); Brown and Hwang (1997); Grewal and Andrews (2001). For the following short introduction, I am closely going to follow the notation and equations given by Simon (2006).

In order to be able to use a Kalman filter, the state of the system needs to be describable by a set of linear equations:

$$x_i = F_{i-1}x_{i-1} + G_{i-1}u_{i-1} + w_{i-1} \tag{5.21}$$

where x_i is the state of the system at time t_i, x_{i-1} is the previous state and F_{i-1} is the state transition matrix. u_{i-1} is a known input variable, with an associated input model described by matrix G_{i-1}; w_i is the process noise, which is assumed to be Gaussian white noise with

standard deviation σ_w and variance $Q_i = \sigma_w^2$. Here, the state of the GBM can be described by its angular orientation and gyro data can be used as the input variable u_i: the new orientation is given by the previous orientation changed by the measurement of the gyro (more detail is provided in the implementations in Section 5.6.2 and Section 5.6.3).

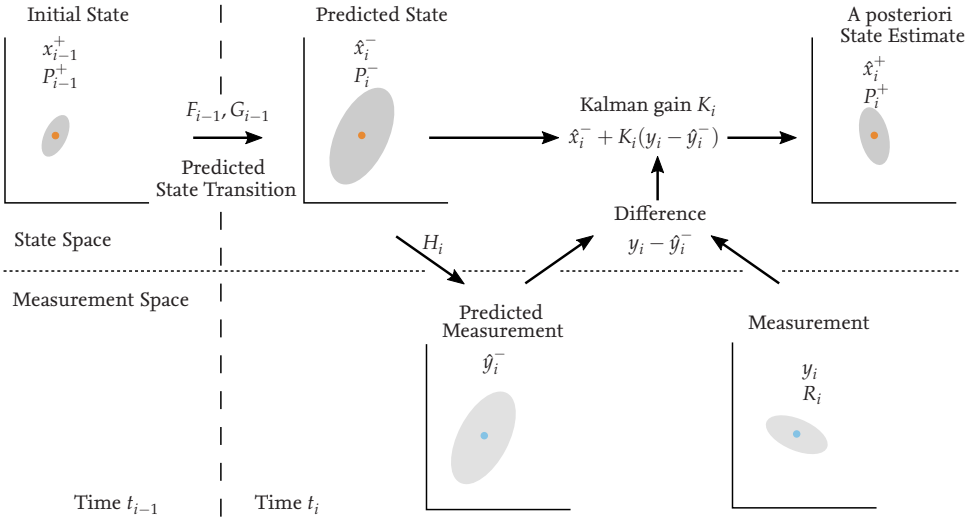

Figure 5.9.: Kalman . Adapted from Winner et al. (2015)

Figure 5.9 shows a schematic overview of the operation of a Kalman filter. The upper half of the Figure (above the dashed line) represents operations in the state space, whereas the lower half of the Figure represents operations in the measurement space. The distinction between state space and measurement space is important, as not necessarily all parameters that are included in the description of the state of the system can also be measured. An example would be the determination of the speed of a car by frequent measurements of its position: state variables would be speed and position, but the only measurement variable is the location of the car (Anderson and Moore, 1979). In our case, a measurable state of the GBM is its angular orientation, whereas an uncorrected offset of the gyros cannot directly be measured, but is included in the state of the GBM in one of the following implementations of the Kalman filter (Section 5.6.3).

Measurements y_i of the state x_i are described by

$$y_i = H_i x_i + v_i \tag{5.22}$$

where H_i is an observation model that connects measurement (inclinometer data) and state (inclination of the tool and possibly gyro offset), v_i is the measurement error with standard deviation σ_v and variance $R_i = \sigma_v^2$.

In the so-called prediction phase of the filter, an initial, *a priori* estimate $\hat{x}_i^-$ of the state of the system and its associated error covariance matrix P_i^- is made. In the following, $\hat{x}$ denotes an estimate of the state, in contrast to the true state x. A superscript minus denotes the *a priori* prediction, in contrast to a refined, *a posteriori* state estimate denoted with a

superscript plus. The *a priori* estimate is based on the previous estimate of the state of the system, the state transition matrix as well as any additional input:

$$\hat{x}_i^- = F_i \hat{x}_{i-1}^+ + G_{i-1} u_{i-1} \tag{5.23}$$

An estimate is also made for the error covariance matrix P_i, using the state transition matrix F and the process noise Q:

$$P_i^- = F_{i-1} P_{i-1}^+ F_{i-1}^T + Q_{i-1} \tag{5.24}$$

In the so-called update phase of the filter, the initial estimate of the state is transformed into the measurement space:

$$\hat{y}_i^- = H_i \hat{x}_i^- \tag{5.25}$$

The difference between the actual measurement y_i and the predicted measurement $\hat{y}_i^-$ is combined with the initial estimate $\hat{x}_i^-$ to obtain a refined, *a posteriori* estimate:

$$\hat{x}_i^+ = \hat{x}_i^- + K_i (y_i - \hat{y}_i^-) \tag{5.26}$$

where K_i is the so-called Kalman gain. The difference between predicted and actual measurement

$$y_i - \hat{y}_i^- \tag{5.27}$$

is often referred to as *innovation*. The innovation is expected to have zero-mean, and a non-zero-mean can indicate problems with the filter (Simon, 2006). In the subsequent chapters about the specific implementations of the Kalman Filter, I am going to refer to the product of Kalman gain and innovation, i.e.

$$K_i (y_i - \hat{y}_i^-) = K_i (y_i - H_i \hat{x}_i^-) \tag{5.28}$$

as the *correction*, as this term describes to which amount the initial data are corrected by the filter. The Kalman gain can be computed using

$$K_i = P_i^- H_i^T (H_i P_i^- H_i^T + R_i)^{-1} \tag{5.29}$$

where, as stated above, P_i^- is the estimate of the error covariance matrix for the state, H_i is the measurement model matrix, and R_i the measurement noise covariance matrix. Then, the error covariance matrix can be updated using

$$P_i^+ = (I - K_i H_i) P_i^- \tag{5.30}$$

where I is an identity matrix of appropriate dimensions.

The Kalman filter works iteratively. Initially, an estimate for the error covariance matrix P and the state of the system has to be made. If a parameter of the initial state is well known, the corresponding entry in P can be made small; if only limited knowledge is available, the corresponding entry can be of a higher value.

In the implementations discussed here, F, G, H, Q and R are time-invariant, as the error estimates and the state and measurement models do not change during the course of a measurement. In such cases, P_i^- and thus K_i can reach a steady state. Assuming $P_i^- = P_{i-1}^-$ and $P_i^+ = P_{i-1}^+$ for $i \to \infty$, we can use Eq. 5.24, Eq. 5.30 and Eq. 5.29 to get:

$$\begin{aligned} P_\infty^- &= FP_\infty^+F_\infty^T + Q \\ &= F(I - K_\infty H)P_\infty^-F^T + Q \\ &= FP_\infty^-F^T - FP_\infty^-H^T[HP_\infty^-H^T + R]^{-1}HP_\infty^-F^T + Q \end{aligned} \tag{5.31}$$

Using P_∞^-, we can then compute the steady state Kalman gain K_∞:

$$K_\infty = P_\infty^-H^T(HP_\infty^-H^T + R)^{-1} \tag{5.32}$$

Finding an analytic expressing for P_∞ using Eq. 5.31 is not necessarily easy. As P_i does not depend on the measurements but only on the parameters of the system, it can be easier in practice to compute the steady state solution iteratively — and possibly also in advance of the measurement, if data are to be processed in real time (Simon, 2006).

5.6.1. Linear Approximation

A complete description of the orientation of the GBM requires the use of non-linear equations (see Eq. 5.1), which have to be linearized in order to be able to use a Kalman filter. To do so, we assume that the order of rotations is irrelevant and that each axis can be treated individually. This is not a strong limitation, as a similar assumption is also made in the regular DCM approach, in which we treat all rotations as if they were occurring simultaneously. As typical changes in orientation between data points are below 0.5° for the x- and y-axis and usually below 5° for the z-axis, this is a valid assumption.

The only information we have about the rotation of the GBM about its vertical axis is gyro data, which only give incremental changes in orientation, but not the absolute value of the azimuth of the tool. Other borehole tools, for example the GPIT (see Section 2.4), as well as many inertial measurement units (Marins et al., 2001, for example) use Earth's magnetic field to determine the azimuth. But as the aim of the GBM measurements is the determination of the magnetic field vector and its deviations from the background field, we cannot use the magnetic field for orientation. Therefore, as we cannot directly measure the azimuth of the tool, which describes the state of the z-axis, we are only using Kalman Filters for the x- and y-axis.

However, as mentioned previously , if an inclined tool is rotated about its vertical axis, the readings of the inclinometers will change, even if there is no change in the total tilt angle, which has to be corrected for (see Eq. 5.17 and Eq. 5.18). The new readings of the inclinometer after a rotation of the tool about the z-axis are given by:

$$\hat{N}_{x_t} = \arctan\left(\cos(\omega_{z_{t_i}}) \cdot \tan(N_{x_{t_{i-1}}}) + \sin(\omega_{z_{t_i}}) \cdot \tan(N_{y_{t_{i-1}}})\right) \tag{5.33}$$

$$\hat{N}_{y_t} = \arctan\left(\cos(\omega_{z_{t_i}}) \cdot \tan(N_{y_{t_{i-1}}}) - \sin(\omega_{z_{t_i}}) \cdot \tan(N_{x_{t_{i-1}}})\right) \tag{5.34}$$

Regardless of the specific implementation of the Kalman filter, the complete correction algorithm involves the following steps:

1. Correction of the inclination measurements for possible rotations about the vertical axis (Eq. 5.33 and Eq. 5.34)
2. Use a Kalman Filter to correct ω_x using N_y to obtain a new estimate for the rotation about the x-axis, $\hat{\omega}_x$
3. Use a Kalman Filter to correct ω_y using N_x to obtain a new estimate for the rotation about the y-axis, $\hat{\omega}_y$
4. Calculate a rotation matrix $\mathbf{A}_{DCM}(\hat{\omega}_x, \hat{\omega}_y, \omega_z)$ using Eq. 5.1.

5.6.2. Implementation A - Estimation of Angle

In our first implementation we are only interested in the angle of the tool and do not include any potential gyro offset in our model of the system. Similar filters are used, for example, for the control of self-balancing robots (see, for example, Li et al., 2012). Here, the state x is given by the angle Ω_i, and the state transition matrix is $F = 1$. Treating the change in angle ω measured by the gyro as a deterministic input u ($G = 1$), the state equation (Eq. 5.21) is given by:

$$\Omega_i = \Omega_{i-1} + \omega_i + w_i \tag{5.35}$$

where the process noise w_i is given by the gyroscope error with variance $Q_i = \sigma_w^2$. Note that, compared to Eq. 5.21, the index of ω is i instead of $i - 1$. The change in index reflects the way data is given in the GBM files: ω_i is the change in angle recorded by the gyro between time t_{i-1} and t_i. Also, due to the choice of coordinate systems (Section 2.4.2), some signs differ between the following equations and the actual implementation of the algorithm. The necessary changes are presented in Appendix A.1.

The measurement equation (Eq. 5.22) for the measured state of the system y_i is given by

$$y_i = \Omega_i^N + v_i \tag{5.36}$$

where Ω_i^N is the angle measured by the inclinometer and v_i the inclinometer error with variance $R_i = \sigma_v^2$. The prediction phase of the filter is thus given by:

$$\hat{\Omega}_i^- = \hat{\Omega}_{i-1}^+ + \omega_i \tag{5.37}$$

$$P_i^- = P_{i-1}^+ + Q_i \tag{5.38}$$

where an initial prediction is made for the angle Ω_i and the associated covariance matrix P_i. In the next phase, these predictions are updated, starting with a measurement of the angle and a calculation of the Kalman gain:

$$y_i = \Omega_i^N \tag{5.39}$$

$$K_i = \frac{P_i^-}{P_i^- + R_i} \tag{5.40}$$

Then, the updated estimate of the angle and covariance matrix are calculated, using the innovation, that is the difference between the prediction for the angle $\hat{\Omega}_i^-$ and the measured angle Ω_i^N, as well as the Kalman gain:

$$\begin{aligned} \hat{\Omega}_i^+ &= \hat{\Omega}_i^- + K_i \cdot (\Omega_i^N - \hat{\Omega}_i^-) \\ &= \hat{\Omega}_{i-1} + \omega_i + K_i \cdot (\Omega_i^N - \hat{\Omega}_{i-1} - \omega_i) \end{aligned} \tag{5.41}$$

$$P_i^+ = (1 - K_i) P_i^- \tag{5.42}$$

In all equations $\hat{\Omega}_{i-1}$ has to be corrected for a possible rotation about the vertical axis of the tool (see Eq. 5.33 and Eq. 5.34). The actual input for our standard algorithm (Eq. 5.1) for the reorientation of magnetic field data is the change of the angle between t_{i-1} and t_i:

$$\begin{aligned} \hat{\omega}_i &= \hat{\Omega}_i^+ - \hat{\Omega}_{i-1}^+ \\ &= \omega_i + K_i \cdot (\Omega_i^N - \hat{\Omega}_{i-1}^+ - \omega_i) \end{aligned} \tag{5.43}$$

The correction (Eq. 5.28) is given by $K_i \cdot (\Omega_i^N - \hat{\Omega}_{i-1}^+ - \omega_i)$ and represents the amount by which inclinometer or gyro data are corrected by the filter.

Here, the steady state covariance matrix can be calculated using Eq. 5.31:

$$P_\infty = P_\infty - \frac{P_\infty}{P_\infty + R} P_\infty + Q \tag{5.44}$$

$$0 = P_\infty^2 - PQ - RQ \tag{5.45}$$

$$P_\infty = \frac{Q \pm \sqrt{Q^2 + 4RQ}}{2} \tag{5.46}$$

which then can be used in conjunction with Eq. 5.32 to calculate the steady state Kalman gain. In order to apply the filter, a choice has to be made for the variances Q and R of gyro and inclinometer data. The noise of the gyros has been determined in calibration measurements (Steveling et al., 2005 and Klein, 2009, see also the discussion in Virgil, 2012). It is highest for lower temperatures and has a standard deviation in the order of 0.002 °/0.5s, giving a variance Q of $4 \cdot 10^{-6}\,{}^{\circ 2}/(0.5\mathrm{s})^2$. The variance R of the inclinometers depends on the circumstances of the specific measurement. As approximation, I calculated the variance of the difference between the inclination given by the inclinometers and the inclination calculated from FOG data after application of the FOG offset correction (Section 5.5), which is $0.44\,{}^{\circ 2}/(0.5\mathrm{s})^2$ for N_x and $0.59\,{}^{\circ 2}/(0.5\mathrm{s})^2$ for N_y. Thus I decided to use $R = 0.5\,{}^{\circ 2}/(0.5\mathrm{s})^2$ for the Kalman filter. As the filter only operates on R_x and R_y, any offset of R_z remains uncorrected, which can result in a drift between downlog and uplog of the reoriented magnetic fields. To correct for this, the offset of R_z estimated by the FOG offset correction (Section 5.5) is used. Using Eq. 5.46 and Eq. 5.32, this gives a steady state Kalman gain of 0.0028, which is in practice reached after approximately 1000 iterations. Rearranging Eq.5.43 gives:

$$\hat{\omega}_i = (1 - K_i)\omega_i + K_i(\Omega_i^N - \hat{\Omega}_{i-1}^+) \tag{5.47}$$

which shows that the output of the Kalman filter in its steady corresponds to a weighted average of inclinometer and gyro data. This type of steady state Kalman filter is referred to as a *complementary filter* (Higgins, 1975).

Figure 5.10 shows the effect of the Kalman filter on the inclination data. The unfiltered inclinometer data are shown in gray and a moving average with a window width of 40 points (approximately 4 m) is shown in black. The inclination given by the Kalman filter is shown in orange.

The Kalman filter has a similar effect as the gyro-offset correction: by combining the long time accuracy of the inclinometers with the vibration-unaffected data of the fiber optic gyros, both noise and time dependent drifts can be effectively removed from the inclination data.

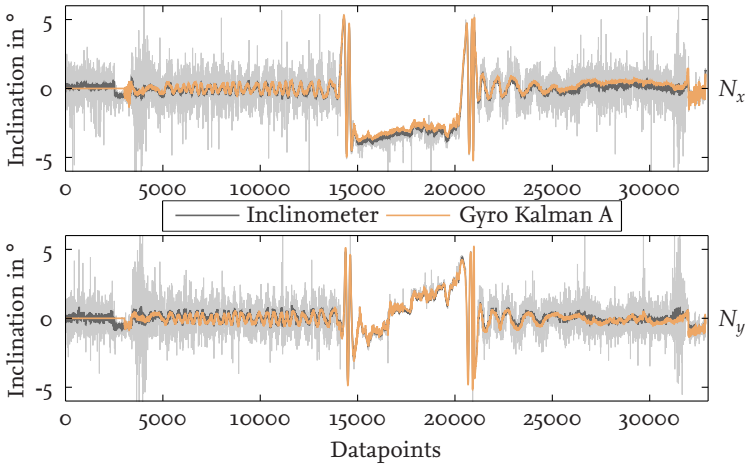

Figure 5.10.: Comparison of inclinometer data to the inclination calculated using a Kalman filter that operates on the angle (Implementation A) for the measurements on Site U1376. The upper panel shows the inclination in x direction, the lower panel shows the inclination in y direction. Unfiltered Inclinometer data are shown in gray, and a moving average with a window width of 40 points is shown in black. The unsmoothed calculated inclination is shown in orange.

The innovations and corrections given by the Kalman filter can also be used to explore potential error sources. Figure 5.11 shows several ways of displaying the filter outputs. Panel a shows the innovations, that is the difference between measured and predicted inclination, for every datapoint. The innovations are highest when the tool was in the drill pipe and lower in the open hole (between data points 14700 and 20300, marked by two black lines), which corresponds to the logging speed and the amount of vibration the tool experiences.

Panel b an panel c of Fig. 5.11 show histograms of the innovation for the x and y angle. As stated previously, the innovation of the Kalman filter is expected to have a zero mean (Simon, 2006), but the means of the data shown here are -0.15° and 0.05°. A non-zero mean suggests that the model used is insufficient or that there are other error sources present

than uncorrelated noise of gyros or inclinometers.

In order to assess the nature of the potential error sources, panel c shows the shows the cumulative sum of the corrections versus the number of data points. The open hole is marked by black lines. Here, I chose to display the corrections, that is the amount by which the estimate of the angles is corrected by the filter, as this allows for a direct comparison with the offset given by the gyro offset correction (Section 5.5). The solid lines show the cumulative sum of the respective axes, the slope of the dashed lines corresponds to the gyro offset correction. Due to the choice of coordinate systems, the correction for Ω^x has to be compared to the negative offset of R_y but the correction for Ω^y can be directly compared to the offset of R_x (see Appendix A.1). The cumulative sum of corrections can be divided into several intervals that are mostly linear with time. The offset given by the gyro offset correction matches the corrections given by the Kalman filter in the section of the open borehole , but not in the other sections. This might be caused by the least squares fitting algorithm of the gyro offset correction: a change in parameters has a higher effect on the residual in regions of low noise (open borehole) compared to regions of higher noise (drillpipe), and therefore the algorithm optimizes the offset for the low noise regions.

There are several potential sources of error that could cause the non-zero mean of the innovations and therefore also the trend in the cumulative sum of corrections. Panel e of Fig. 5.11 suggests that both an offset correlated with time as well as a misalignment of the sensor systems is present: the panel shows the cumulated sum of the corrections versus the cumulated rotation about the vertical axis of the tool (corrected for the effect of the rotation of the Earth). For the biggest part of the measurement, the corrections performed by the Kalman filter are linearly correlated to the amount of rotation about the vertical axis of the tool.

The linear dependence of the corrections on the rotational rate can be explained by the coordinate system of the gyros not being completely aligned with the coordinate system of the inclinometers (see Section 4.5). However, this potential error in alignment is very small, as the average correction applied to the rotational rate per data point is $-4.1 \cdot 10^{-4}$ ° in x direction and $1.6 \cdot 10^{-4}$ ° in y direction.

In theory, the misalignment between the sensor systems could be evaluated by varying misalignment angles until the linear dependence of the corrections on the rotation about the vertical axis is removed. In practice, it is hard to differentiate between a misalignment of the sensor systems and an offset of the inclinometers, especially as the latter can only be determined with limited accuracy (see Section 4.4 and Section 4.5).

While the tool was in the open hole, it rotated with a much lower rotational rate than within the drill pipe, with a total rotation of about 100°. This time interval is marked by rectangles in the lower panel of Fig. 5.11 and corresponds to the sections where the cumulative sum of corrections varies without a corresponding change in the rotation about the vertical axis. This shows that the misalignment of the sensor systems cannot be the only source for errors, but that another error source is present as well. The behaviour found here could be both explained by an incomplete removal of temperature dependent offsets

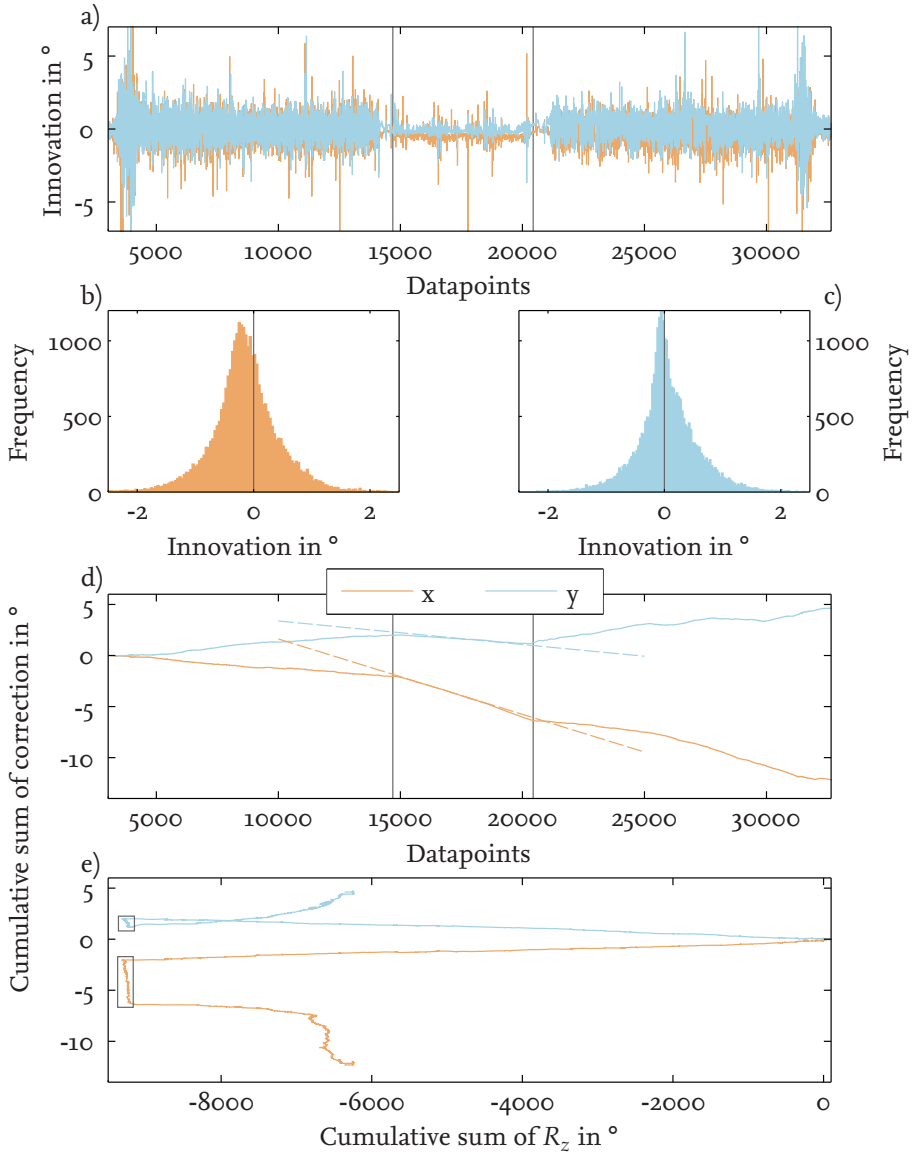

Figure 5.11.: Innovation and Corrections of a Kalman filter that operates on the angle. Data for the inclination in direction of N_x are shown in orange, data for the inclination in direction of N_y are shown in blue. All data are from Site U1376. a) Innovation of the filter. The open hole is marked by two black lines. b) and c) Histograms of the innovations, bin width 0.038° d) Cumulative sum of corrections versus the number of datapoints. Dashed lines indicate the offset given by the gyro offset correction. The open hole is marked by two black lines. e) Cumulative sum of corrections versus the cumulative rotation about the vertical axis of the tool. Data recorded within the open hole are marked by rectangles.

or by an incomplete removal of the rotation of the Earth. The latter would be present, if the orientation of the tool is calculated wrongly, possibly due to an uncorrected offset on R_z, and therefore R_x and R_y experience a different fraction of Earth's rotation than the algorithm assumes. Regardless of the origin of these errors, the Kalman filter corrects R_x and R_y for them using the inclinometer data.

Figure 5.12 shows the magnetic field reoriented using this implementation of the Kalman filter. In all components, downlog and uplog agree well, which demonstrates the quality of the reorientation algorithm. Only a small offset between both logs of approximately 130 nT is visible in the north component of the magnetic field at a depth between 1620 m and 1640 m. The quality of reorientation is comparable to that of the simpler offset correction described in Section 5.5: the mean difference between uplog and downlog for the gyro offset correction is 103 nT in the north, 39 nT in the east and 107 nT in the vertical component, whereas the mean difference for this implementation of the Kalman filter is -94 nT, -46 nT and -48 nT, respectively. The Kalman filter is more flexible in so far that it makes assumptions about the nature of a possible offset to the gyros and can also correct for non-constant offsets. However, the Kalman filter is not able to determine corrections for R_z, and in that respect I resorted to the result of the simple offset correction. Using the Kalman filter would also be possible without using the offset for R_z, but that would lead to a slightly worse agreement between downlog and uplog of ≈170 nT in the north and east component and ≈50 nT in the vertical component (see also Table 5.4 in Section 5.8 for a comparison of the different algorithms).

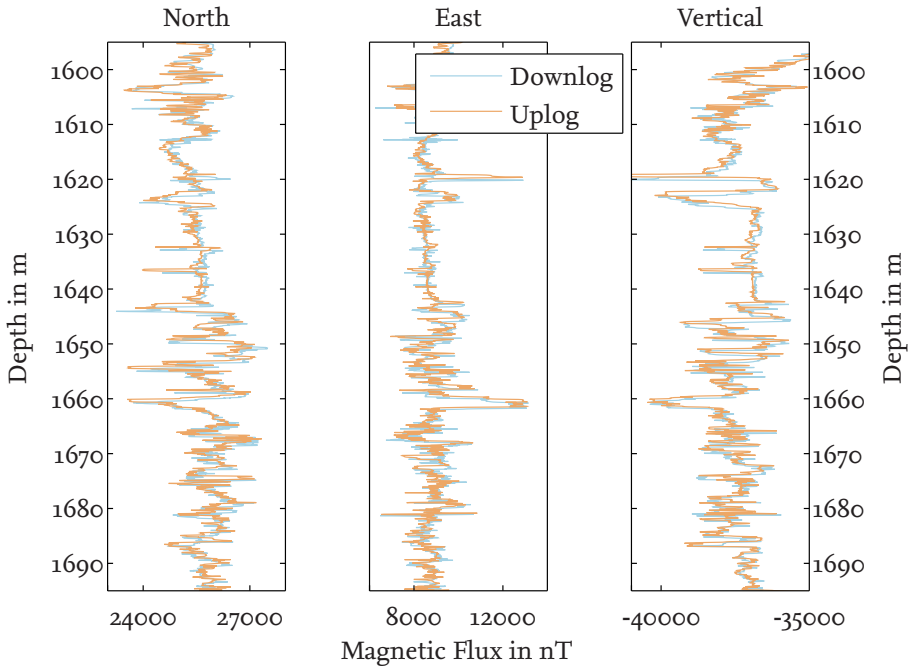

Figure 5.12.: The magnetic field of Site U1376 shown in the geographic reference frame, reoriented using implementation A of a Kalman filter.

5.6.3. Implementation B - Estimation of Angle and Gyro Offset

The non-zero mean of the innovation in implementation A of the Kalman filter is evidence that the gyro data are influenced by uncorrected offsets. Therefore, these offsets are included in the second implementation of the filter. Here, we assume that the gyro is affected by an offset g_i, which might be due to small errors in the temperature correction or accumulating errors in the correction for the rotation of the Earth. This offset is part of the state of the system, but cannot be measured directly. A similar filter is, for example, described by Teruyama and Watanabe (2013), where they use the filter to determine lower limb angles of the human body and by Paina et al. (2011), who discuss the attitude estimation for a small unmanned aerial vehicle. The angle Ω_i at time t_i is given by:

$$\Omega_i = \Omega_{i-1} + \omega_i - g_{i-1} + w_i^{\omega} \tag{5.48}$$

where ω_i are gyro data. Assuming that the offset is constant, g_i is given by:

$$g_i = g_{i-1} + w_i^{g} \tag{5.49}$$

where w_i^{ω} and w_i^{g} are gyro and gyro offset noise with respective variances of $Q_i^{\omega} = \sigma_{\omega}^2$ and $Q_i^{g} = \sigma_{g}^2$. Equation 5.48 and Eq. 5.49 can be written in matrix form:

$$\underbrace{\begin{bmatrix} \Omega_i \\ g_i \end{bmatrix}}_{x_i} = \underbrace{\begin{bmatrix} 1 & -1 \\ 0 & 1 \end{bmatrix}}_{F} \cdot \underbrace{\begin{bmatrix} \Omega_{i-1} \\ g_{i-1} \end{bmatrix}}_{x_{i-1}} + \underbrace{\begin{bmatrix} \omega_i \\ 0 \end{bmatrix}}_{u} + \begin{bmatrix} w_i^{\omega} & 0 \\ 0 & w_i^{g} \end{bmatrix} \tag{5.50}$$

with the current and previous states x_i and x_{i-1}, the state transition matrix F and the input variable u; the input model is $G = 1$ (see Eq. 5.21). The model covariance matrix is given by:

$$Q_i = \begin{bmatrix} Q_i^{\omega} & 0 \\ 0 & Q_i^{g} \end{bmatrix} \tag{5.51}$$

The measurement equation (Eq. 5.22) is given by:

$$\begin{aligned} y_i &= \underbrace{\begin{bmatrix} 1 & 0 \end{bmatrix}}_{H} \cdot \begin{bmatrix} \Omega_i \\ g_i \end{bmatrix} \\ &= \Omega_i \end{aligned} \tag{5.52}$$

where H is the measurement model. As the gyro offset cannot be measured directly, the measurement equation is the same as for implementation A (Eq. 5.36).

The initial predictions for the state vector and the covariance matrix P_i are thus given by:

$$\begin{bmatrix} \hat{\Omega}_i^{-} \\ \hat{g}_i^{-} \end{bmatrix} = \underbrace{\begin{bmatrix} 1 & -1 \\ 0 & 1 \end{bmatrix}}_{F} \cdot \begin{bmatrix} \hat{\Omega}_{i-1}^{+} \\ \hat{g}_{i-1}^{+} \end{bmatrix} + \begin{bmatrix} \omega_i \\ 0 \end{bmatrix} \tag{5.53}$$

$$P_i^- = \underbrace{\begin{bmatrix} 1 & -1 \\ 0 & 1 \end{bmatrix}}_{F} \cdot P_{i-1}^+ \cdot \underbrace{\begin{bmatrix} 1 & 0 \\ -1 & 1 \end{bmatrix}}_{F^T} + Q \tag{5.54}$$

where the predicted value for angle now includes the gyro offset. The prediction for the gyro offset equals the previous value of the offset, as there is no external data source present that either influences the offset or allows for its prediction.

In the update phase of the filter, the angle of the tool is measured and the Kalman gain is calculated using the state covariance matrix P, the inclinometer variance R and the measurement model matrix H:

$$y_i = \underbrace{\begin{bmatrix} 1 & 0 \end{bmatrix}}_{H} \cdot \begin{bmatrix} \Omega_i^N \\ g_i \end{bmatrix} = \Omega_i^N \tag{5.55}$$

$$K_i = \begin{bmatrix} K_i^\Omega \\ K_i^g \end{bmatrix} = P_i^- \cdot H^T \cdot \left(H \cdot P_i^- \cdot H^T + R_i \right)^{-1} \tag{5.56}$$

Here, the Kalman gain K_i is comprised of a gain for the angle, K_i^Ω, and a gain for the offset K_i^g. The following update of the initial prediction of angle, offset and covariance matrix P_i^- is given by:

$$\begin{bmatrix} \hat{\Omega}_i^+ \\ \hat{g}_i^+ \end{bmatrix} = \begin{bmatrix} \hat{\Omega}_i^- \\ \hat{g}_i^- \end{bmatrix} + \begin{bmatrix} K_i^\Omega \\ K_i^g \end{bmatrix} \cdot (\Omega_i^N - \hat{\Omega}_i^-) \tag{5.57}$$

$$P_i^+ = \left(\begin{bmatrix} 1 & 0 \\ 0 & 1 \end{bmatrix} - K_i \cdot \begin{bmatrix} 1 \\ 0 \end{bmatrix} \right) \cdot P_i^- \tag{5.58}$$

As in the previous implementation, Ω_i^N has to be corrected for a possible rotation about the vertical axis of the tool (see Eq. 5.33 and Eq. 5.34). We can see that, although initially assumed to be constant, the gyro offset is modified according to its Kalman gain and the difference between the predicted angle $\hat{\Omega}_i^-$ and the measured angle Ω_i^N, that is the innovation. Again, I am going to refer to the product of the Kalman gain for the angle and the innovation

$$K_i^\Omega \cdot (\Omega_i^N - \hat{\Omega}_i^-) \tag{5.59}$$

as correction of the filter. Using Eq. 5.53, the input to the reorientation algorithm is given by:

$$\begin{aligned} \hat{\omega}_i &= \hat{\Omega}_i^+ - \hat{\Omega}_{i-1}^+ \\ &= \omega_i - \hat{g}_{i-1}^+ + K_i^\Omega \cdot (\Omega_i^N - \hat{\Omega}_{i-1}^+ - (\omega_i - \hat{g}_{i-1}^+)) \end{aligned} \tag{5.60}$$

The variance of the offset necessary in this implementation of the Kalman filter can only be estimated. Choosing a a value comparable to the variance of the inclinometers would result in an offset that is strongly variable, which does not reflect the possible physical

reasons for such an offset, for example a temperature dependent behaviour. Thus, it is sensible to choose a value lower than the variance of the FOG noise, as this will result in an offset that is only slowly varying with time and, as a result, varying with a rate comparable to changes in physical parameters that could be the underlying reason for the offset.

Figure 5.13 shows the effect of three different values for the variance of the offset on the output of the Kalman filter for the data of Site U1376. The upper panel shows the computed inclination N_x after application of the filter. Some variation in the order of fractions of a degree are visible, but the overall quality for all values is similar. The maximum differences in inclination N_x between the different values for Q_g is 0.2°, but for 95% of the datapoints, the differences are below 0.08°. Panel b and c show the histogram of the innovations for $Q_g = 5 \cdot 10^{-8}$; here, the mean values are $-0.46 \cdot 10^{-3}$° for the x-axis and $-0.004 \cdot 10^{-3}$° for the y-axis, which is much closer to the expected zero mean than the means of the innovations of implementation A of the Kalman filter.

Panel d of Fig. 5.13 shows the cumulative sum of the correction for N_x and panel e shows the computed gyro offset for the corresponding axis for the different values of the variance Q_g versus the number of datapoints. The lower the variance, the smoother and less variable is the computed offset, which corresponds to its possible physical reasons, which are not expected to vary rapidly with time. For higher variances, the corrections are smaller, but at the cost of a stronger variation of the offset. The offsets have mean values in the order of -2.5°/h, with minimum values of down to -50°/h.

In this implementation, it is easier to calculate the Kalman gains numerically using the filter. For $Q_g = 5 \cdot 10^{-8}$, the steady state is reached after about 500 iterations with $K^{\Omega} = 0.016$ and $K^{g} = -0.126 \cdot 10^{-3}$.

Figure 5.14 shows the magnetic field of Site U1376 reoriented using implementation B of the Kalman filter, using a value of $8 \cdot 10^{-9}\,{}^{\circ 2}/(0.5\mathrm{s})^2$ for the variance of the offset. In general, the quality of the reorientation is good. The downlog and uplog agree better than in the implementation A of the Kalman filter, with mean differences of 31 nT in the north, -30 nT east and 42 nT in the vertical component of the magnetic field. Using the other two values for the variance of the offset gives similar results for the reoriented magnetic field (see Table 5.4 in Section 5.8 for a comparison of the different algorithms). The exact value chosen for the variance of the gyro offset therefore plays no crucial part in the reorientation of the magnetic field.

As the agreement of downlog and uplog of the magnetic field is one of the most important quality criteria, this means that at least in this case the second implementation of the Kalman filter is to be preferred. However, even though an implementation that includes a possible gyro offset more appropriately describes the physics of the system, it cannot always be expected to give a better result if the input parameters, in this case the estimate of the variance of the gyro offset, are not sufficiently well known.

A possible improvement for both implementations could be to adjust the variance of the inclinometers according to some criteria for vibration induced noise, possibly varying throughout the course of the measurement.

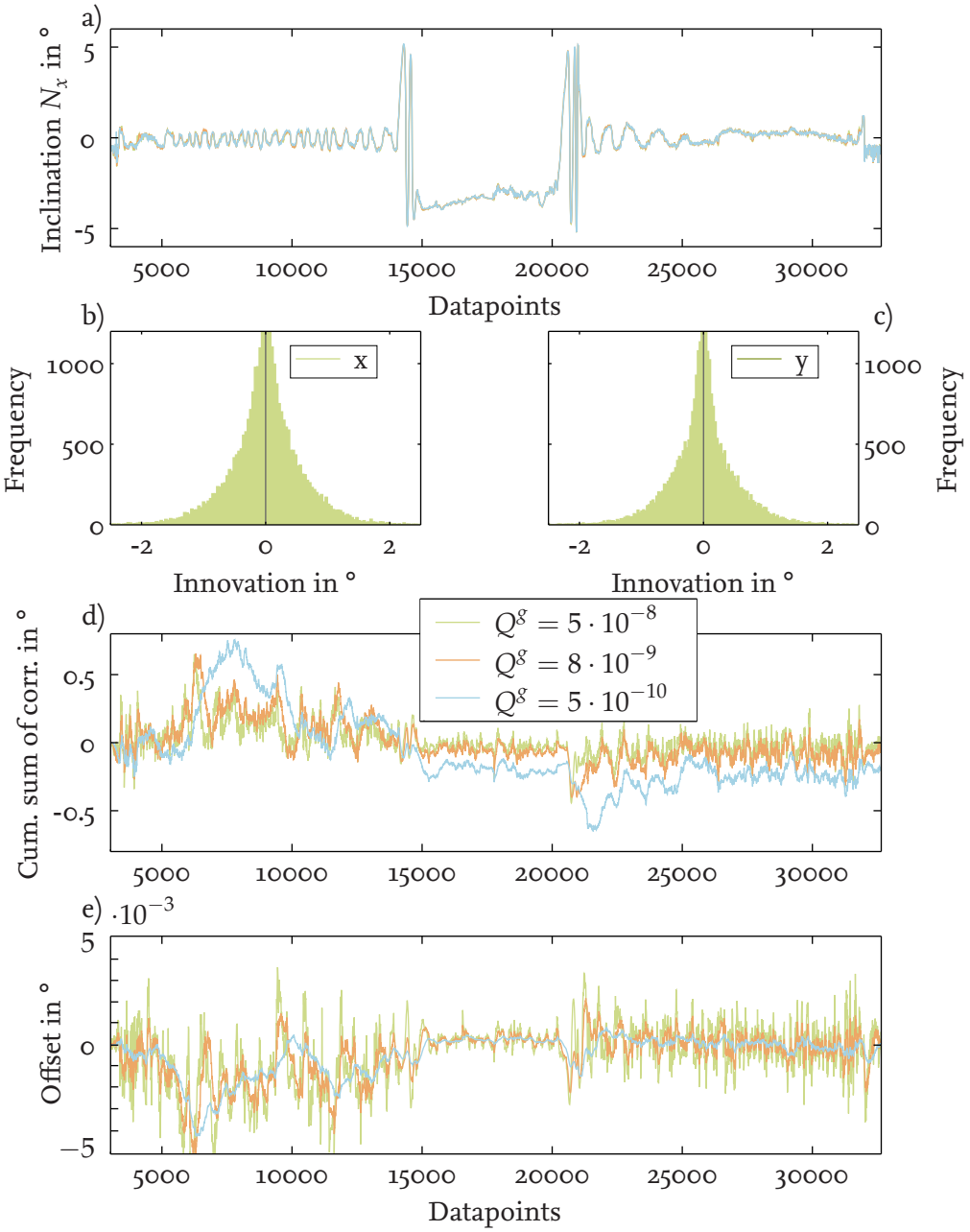

Figure 5.13.: Comparison of the effect of different values for the variance Q of the gyro offset on the output of implementation B of the Kalman filter for the inclination N_x and the data of Site U1376. a) Inclination N_x. Maximum difference between datasets is 0.2°. b) and c) Histograms of the innovations, bin width 0.038° d) Cumulative sum of corrections versus the number of datapoints. e) Gyro offset in degree per datapoint versus the number of datapoints. $5 \cdot 10^{-3}$° per datapoint correspond to 36°/h.

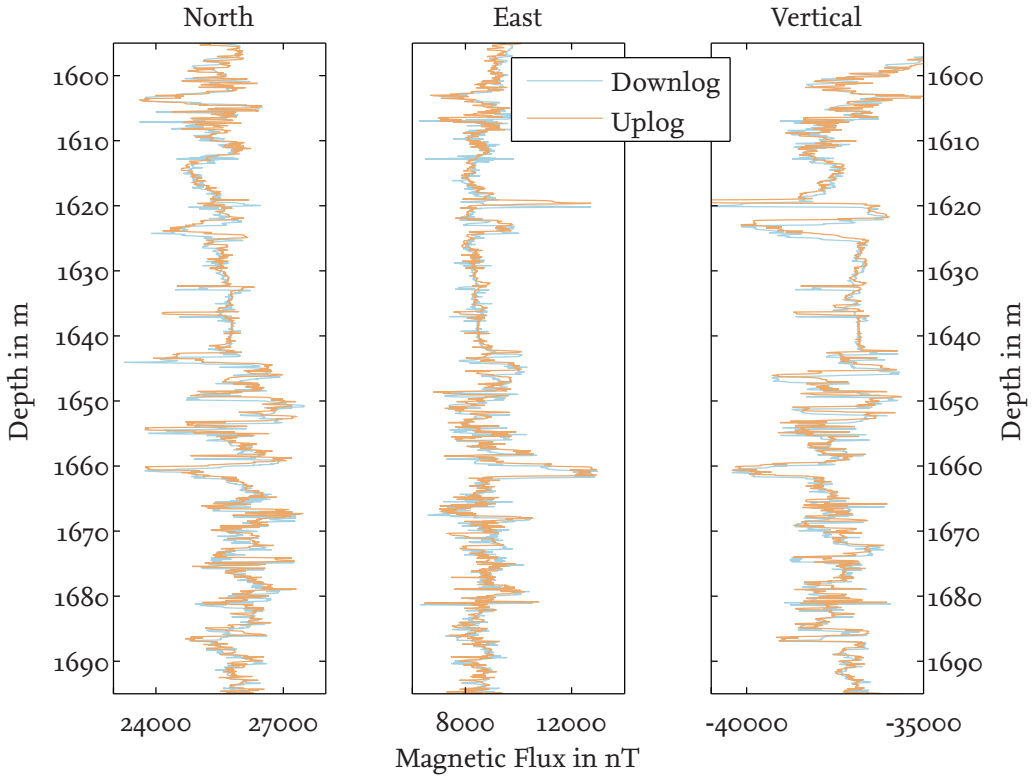

Figure 5.14.: The magnetic field of Site U1376 shown in the geographic reference frame, reoriented using implementation B of a Kalman filter that includes an offset of the gyro.

5.7. Site U1374: Comparison of Algorithms

The most significant challenge for this data set are the data gaps that occurred in both measurement runs at this site. The first measurement at this site has less data gaps than the second measurement and, in addition, the gaps only occur in the cased part of the borehole, so I am going to focus on the first run.

The occurrence of data gaps has an impact on the choice of the reorientation algorithm: the standard algorithm (Section 5.4) is going to propagate errors due to the data gaps through the course of the reorientation. As these errors do not accumulate gradually, as for example if they were due to a erroneous temperature correction, but emerge at specific points in time, they are unlikely to be sufficiently corrected by a constant correction as, for example, the gyro offset correction described in Section 5.5.

I am using two methods to compare the different algorithms. Table 5.2 shows a comparison of the mean difference of downlog and uplog of the magnetic field in the open hole (1699 m through 2095 m, interpolated to steps of 0.1 m). Table 5.3 shows a comparison of the mean declination of the reoriented magnetic field at a depth of 1916.7±0.5 m. This particular depth was chosen for comparison, as here the magnetic field is relatively quiet and the magnetization of core samples from the corresponding depth are only weakly magnetized (Expedition 330 Scientists, 2012d).

Both the mean difference between downlog and uplog, which has already been used in the previous section, as well as the declination of the magnetic field reveal uncorrected trends in the reoriented magnetic field and can be used to assess the relative accuracy of the different reorientation algorithms. The declination also allows to evaluate the general accuracy of the reorientation algorithms in respect to the geographic reference frame.

As can be seen in Table 5.2, the smallest difference between downlog and uplog occur for the data reoriented using the reorientation algorithm that uses the vertical gyro and treats the inclinometers as rate sensors (Inclinometer B, Section 5.3.2). This algorithm also shows the least spread in the declination of the magnetic field between downlog and uplog, with a difference of 0.8° (Table 5.3).

It is somewhat surprising that both Implementation A of the FOG/Inclinometer algorithm (Section 5.3.2, see also the comparison between Implementation A and B in Section 5.3.3) and the Kalman filters (Section 5.6) give worse results, as they would be expected to be more stable and less susceptible to data errors. The constant gyro offset correction (Section 5.5) is comparable to the Kalman filters both in the mean difference as well as the spread in declination between downlog and uplog.

Algorithm	Difference North	Difference East	Difference Vertical
Inclinometer A	107 nT	-470 nT	-40 nT
Inclinometer B	-133 nT	-124 nT	-135 nT
Gyro Offset Correction	190 nT	-564 nT	11 nT
Kalman A, with R_z Offset	327 nT	-504 nT	119 nT
Kalman B, $Q_g = 8 \cdot 10^{-9}$	251 nT	-482 nT	68 nT

Table 5.2.: Mean difference between downlog and uplog of the reoriented magnetic field for different reorientation algorithms for Site U1374. The algorithm chosen for further processing of the data is bolded.

Algorithm	Declination Downlog	Declination Uplog
Inclinometer A	18.93°	19.64°
Inclinometer B	21.82°	22.02°
Gyro Offset Correction	17.67°	18.65°
Kalman A, with R_z Offset	19.23°	20.19°
Kalman B, $Q_g = 8 \cdot 10^{-9}$	19.27°	20.23°

Table 5.3.: Mean declination of the reoriented magnetic field at a depth of 1916.7±0.5 m for different algorithms for the data of Site U1374. The algorithm chosen for further processing of the data is bolded.

The declination data shown in Table 5.3 demonstrates the influence of the choice of algorithm on the declination of the reoriented magnetic field: there is a difference in declination of 4.35° between the downlog of the magnetic field given by the gyro offset correction and the uplog of the magnetic field given by implementation B of the inclinometer algorithm. Even though this is not necessarily representative for the actual error in orientation, it shows that some error in orientation can remain after a reorientation of the magnetic field. As will be shown in Section 6.3, this potential source of error in the absolute orientation of the magnetic field data can be addressed by a suitable choice of the background field.

As a connection within the tool loosened and communication with the tool was lost during the uplog of the first measurement at Site U1374, a second northing could not be conducted at the end of the measurement. Thus, a comparison of the true orientation of the tool and its computed orientation can not be made to further assess the quality of reorientation.

Based on these comparisons, I chose Implementation B of the reorientation algorithm using the vertical gyro and both inclinometers (Section 5.3.2) in combination with the data of the first measurement (Ehmann et al., 2015) for further processing of the data of Site U1374. The magnetic field given by, for example, the Kalman filters, would be smoother, as it is not as much influenced by the noise of the inclinometers, but as the agreement of downlog and uplog is likely to be the most objective quality criterion, using the algorithm that leads to the best agreement is sensible.

5.8. Site U1376: Comparison of Algorithms

Table 5.4 shows the comparisons of the mean difference of downlog and uplog for the different reorientation algorithms for the data of Site U1376. Here, I again used data from the open, uncased hole for the comparison, that is from a depth of 1595 m through a depth of 1695 m, interpolated to steps of 0.1 m.

Table 5.5 shows the comparison of the mean declination of the magnetic field, calculated at a depth of 1628.2±0.5 m, which is region of the borehole where the magnetic field is relatively quiet and core samples indicate a low magnetization (Expedition 330 Scientists, 2012f).

For the data of this site, the best result is obtained using the Kalman filters that include a potential offset of the gyros, with typical differences of 30 nT between downlog and uplog and a maximum difference in declination of the magnetic field of 0.07°. In general, the differences are smaller than at Site U1374, with the most likely reason being the lack of data errors at Site U1376, which benefits all reorientation algorithms. Here, the offset to R_z determined by the gyro offset correction was used in all Kalman filters, except where marked. Without the additional offset, the performance of the Kalman filter is worse than when the offset is included, as the Kalman filters itself do not correct for errors of R_z. It therefore seems advisable to combine the gyro offset correction and the Kalman filter for the reorientation of the data.

Algorithm	Difference North	Difference East	Difference Vertical
Inclinometer A	174 nT	-156 nT	120 nT
Inclinometer B	41 nT	335 nT	136 nT
Gyro Offset Correction	103 nT	39 nT	107 nT
Kalman A, with R_z Offset	-94 nT	-46 nT	-48 nT
Kalman A, no R_z Offset	-171 nT	145.5 nT	-50 nT
Kalman B, $Q_g = 5 \cdot 10^{-8}$	28 nT	-30 nT	40 nT
Kalman B, $Q_g = 8 \cdot 10^{-9}$	31 nT	-30 nT	42 nT
Kalman B, $Q_g = 5 \cdot 10^{-10}$	27 nT	-29 nT	39 nT

Table 5.4.: Mean difference between downlog and uplog of the reoriented magnetic field for different reorientation algorithms for Site U1376. The algorithm chosen for further processing of the data is bolded.

Algorithm	Declination Downlog	Declination Uplog
Inclinometer A	14.66°	15.09°
Inclinometer B	18.57°	17.56°
Gyro Offset Correction	16.08°	16.08°
Kalman A, with R_z Offset	18.52°	18.60°
Kalman A, no R_z Offset	20.87°	20.38°
Kalman B, $Q_g = 5 \cdot 10^{-8}$	18.17°	18.24°
Kalman B, $Q_g = 8 \cdot 10^{-9}$	18.16°	18.21°
Kalman B, $Q_g = 5 \cdot 10^{-10}$	18.23°	18.24°

Table 5.5.: Mean declination of the reoriented magnetic field at a depth of 1628.2±0.5 m for different algorithms for the data of Site U1376. The algorithm chosen for further processing of the data is bolded.

The algorithms that use the inclinometer data instead of R_x and R_y perform worse than the other algorithms for the data of Site U1376, and they should therefore not be used here, especially as the inclinometers introduce additional noise to the magnetic field data.

Even though the Kalman filters give the best results in terms of the comparisons presented here, I am going to use the reoriented magnetic field obtained using the gyro offset correction for further processing. The main reason is to stay consistent with the work presented in Ehmann et al. (2015). The differences between downlog and uplog are larger by approximately 50 nT for the gyro offset correction, but are still acceptable with a maximum of 107 nT.

As shown in Section 5.5, the offsets determined by the FOG offset correction algorithm are 1.66 °/h for R_x , -5.31 °/h for R_y and 1.02 °/h for R_z, which correlates well with the temperature drift of the gyros (Section 4.2, Fig. 4.1). After applying these offsets to the gyros, the difference

between the computed azimuth of the tool and its physical orientation determined in a second northing at the end of the measurement, is 1.5°. Thus, the approximate error in orientation of the magnetic field measurements at the bottom of the borehole is 0.75°.

The absolute difference in orientation between Kalman filters and offset correction, judged from the declination of the magnetic field at a depth of 1628.2 m (Table 5.5), is 2.52° (excluding the Kalman filter without offset to R_z), which suggests a slightly larger error in orientation than given by the second northing. However, it cannot be guaranteed that either of the algorithms gives a better absolute accuracy in orientation, and any potential error in orientation is going to be mitigated by an appropriate choice of the background field (Section 6.3).

6 Modeling Magnetostratigraphy

In order to determine the magnetization from measurements of the magnetic field, a suitable model has to be found for the subsurface. If the chosen model differs too much from reality, the calculated magnetization is not going to be meaningful.

There is little information available about the structure of the seamounts drilled during Expedition 330. Even though seismic data has been collected during previous cruises in preparation for Expedition 330, these datasets are not of sufficient quality to deduce structural information of satisfactory spatial resolution to aid in the interpretation of the magnetic field measurements. Images of the borehole wall and structural information from drill cores are thus the only sources of information that can, to some extent, reduce the inherent ambiguity of the measurements.

The evolution of a seamount is a complicated process that can give rise to a multitude of geological formations. Staudigel and Clague (2010) describe the evolution of seamounts and define their typical stages. They give the depth of eruption as an important factor for the lithology; for water depths above 700 m, due to the associated lower hydrostatic pressure combined with water vapor, the eruptions are likely to become explosive in nature, which results in volcanic breccia that is a less suitable target for paleomagnetic studies than massive flow units. Staudigel and Clague (2010) also state that the more the seamount is elevated above the oceanic crust, they more likely it is that intrusions are beginning to form. As intrusions intersect previously deposited units, they make both structure and magnetic history of the seamount more complex. All seamounts studied during Expedition 330 are elevated by several thousand meters above the surrounding crust and there is evidence in the core samples that suggests both submarine and subaerial episodes of volcanism. Abundant volcanic breccia, interbedded by pillow lavas and lava flows, resedimented breccias and sandstone as well as an algal boundstone reef were found in core samples (Expedition 330 Scientists, 2011; Koppers et al., 2013).

Figure 6.1 shows several photographs taken on the island of La Palma (Canary Islands), that was formed by a hotspot underneath the African plate. La Palma is therefore comparable to the seamounts examined during Expedition 330, and it can be expected that the drilled lithology is similar to what can be seen in the photographs. Panel a in Fig. 6.1 shows a steep section of the coast of La Palma, where multiple subhorizontal layers can be identified. Panel b in Fig. 6.1 shows a photograph taken on the rim of the Caldera de Taburiente, a crater-shaped mountain that dominates the northern part of La Palma, where we can see several steeply dipping layers.

The inner wall of the Caldera shown in panel c in Fig. 6.1, as well as the close-up photograph shown in panel d of Fig. 6.1, which was taken at the bottom of the Caldera, show a more complicated geology; in general, the Caldera wall is composed of multiple layers,

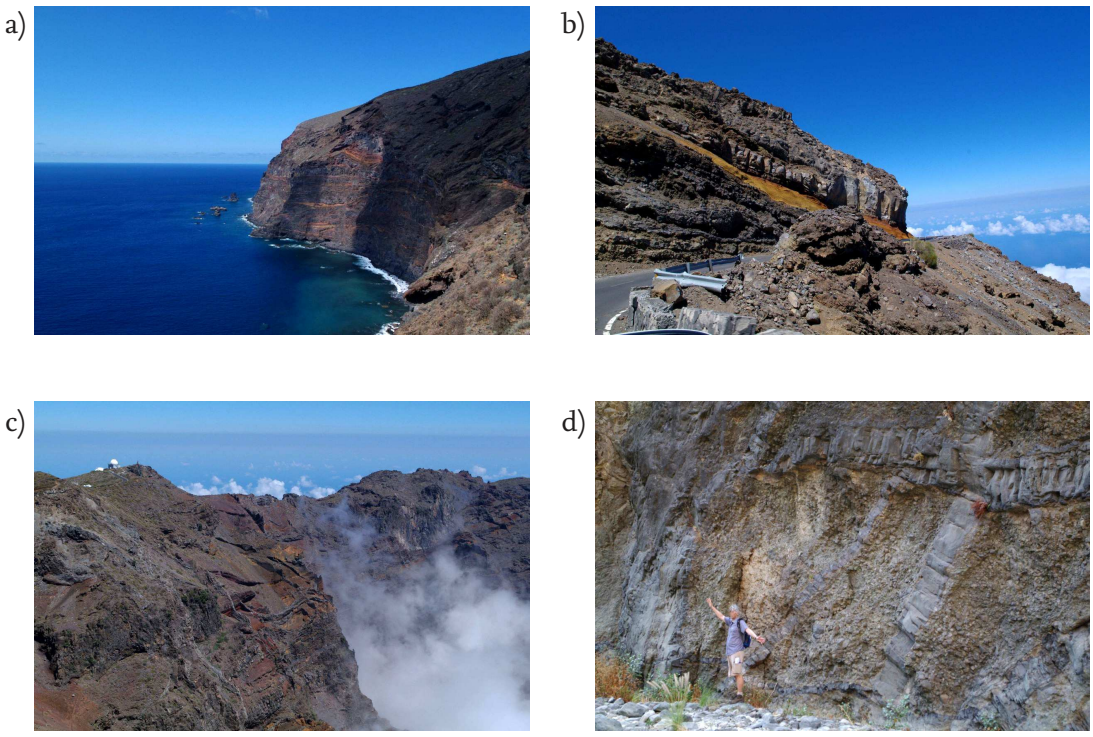

Figure 6.1.: Geological structures of La Palma and the Caldera de Taburiente.

which are intersected by multiple sills and dykes, some of them crossing.

As the lithology of the drill sites of Expedition 330 can only be described based on the one-dimensional view of core samples of a single borehole, we can not be sure whether the structures surrounding the boreholes are closer to panels a and b in Fig. 6.1, which would be preferable, or closer to panels c and d in Fig. 6.1, which would require more complicated models. Intrusions which are close to the boreholes, but are not intersected by them, will have an influence on the magnetic field that can not be corrected for.

In the following sections, I am going to use horizontal layer models and inclined layer models of infinite lateral extent to derive the direction and magnitude of magnetization from magnetic field data, as, without further information about the true structure of the subsurface, this is the most plausible assumption for the potential structure of seamounts of volcanic origin.

6.1. Reoriented Data and Lithology: Site U1374

Figure 6.2 (Ehmann et al., 2015) shows a comparison of the final reoriented magnetic field data set of Site U1374 to the lithology as found in drill core samples (Expedition 330 Scientists, 2011). Here, the depth scale has been adjusted to show the depth below seafloor to facilitate a comparison to the drill core data. The downlog of the magnetic field is shown in light gray, the uplog in black. The magnetic background field as expected according to the IGRF is shown in dark gray. The average difference between downlog and

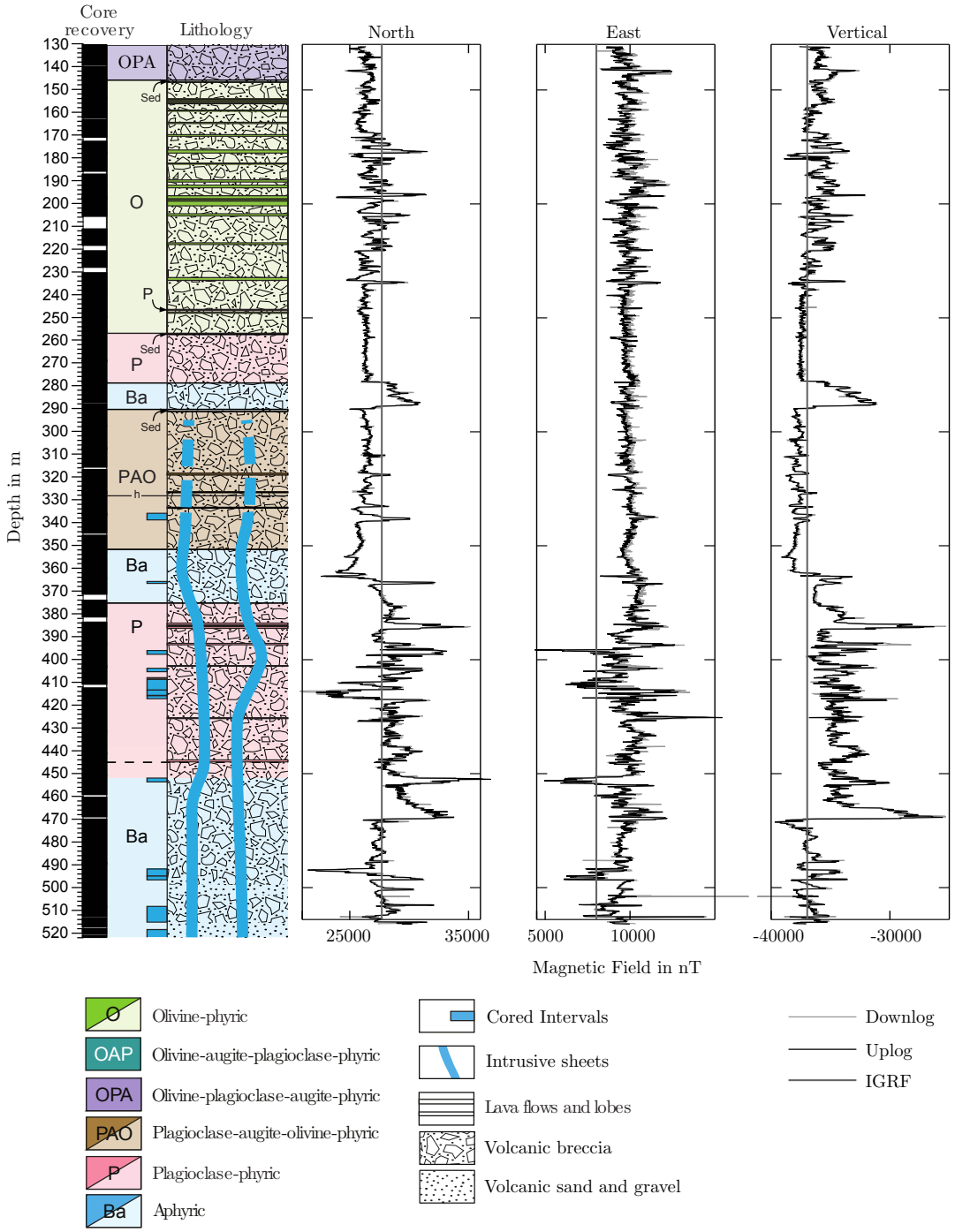

Figure 6.2.: Comparison of the lithology of Site U1374 (Expedition 330 Scientists (2011), modified) to the reoriented magnetic field data. Light gray lines denote the downlog, black lines the uplog of the reoriented magnetic field and dark gray lines the magnetic field as expected according to the IGRF. Adapted from Ehmann et al. (2015)

uplog is 130 nT (Section 5.7), which can be attributed to errors in reorientation, but also to small depth offsets between the logs, remaining magnetometer errors, inclinometer noise and true differences in the recorded magnetic field, e.g. due to lateral movement of the tool within the borehole. Due to several possible reasons, the IGRF values do not coincide with the general trend of the magnetic field data; therefore different values for the background magnetic field are going to be used during further interpretation of the data (see Section 6.3). At this Site, 88 % of the drill core could be recovered, which is unusual for igneous basement (Expedition 330 Scientists, 2012d). This provides a good foundation for the comparison of drill core and logging data.

As part of the drill pipe had to remain in the borehole for stability reasons, the magnetic field data of the upper 130 m is strongly distorted and can not be used for interpretation. A remaining influence of the drill pipe on the upper meters of the vertical component of the magnetic field that was visible in the unoriented data (see Fig. 4.4) has been removed by subtracting a best-fit monopole. A linear trend remains in the vertical component, down to a depth of approximately 300 m. As the trend is visible in both downlog and uplog, as well as in the total magnetic field (not shown here) it is not an artefact of the reorientation, but is of geological origin (Ehmann et al., 2015).

The magnetic field shows some correlation with the lithology; most strikingly visible is the aphyric basalt breccia between 280 m and 290 m. The prominent step of the north and vertical component of the magnetic field between 365 m and 470 m, however, has no corresponding change in lithology. In general, the lithology consists of basaltic breccias with 13 intrusive sheets that, according to the drill cores, are most likely steeply dipping. The intrusive sheets, as well as some lava lobes and pillow lavas intersected by the borehole, are most likely in-situ, i.e. have not been moved since the material cooled down below its Curie temperature, which makes these units the most promising target for paleomagnetic studies (Expedition 330 Scientists, 2012a). The brecciated units are unlikely to be in-situ, except the olivine-phyric breccia between 145 m and 260 m, whose core samples show several intervals with consistent inclination of magnetization. A possible explanation for this is that a lava flow was fragmented in a subaqueous environment, with fragments large enough to only acquire a remanent magnetization after the end of their movement. (Expedition 330 Scientists, 2012d; Ehmann et al., 2015).

6.2. Reoriented Data and Lithology: Site U1376

Figure 6.3 (Ehmann et al., 2015) shows the reoriented magnetic field of Site U1376, starting with the end of the drill pipe at a depth of 90 m, in comparison to the lithology (Expedition 330 Scientists, 2012f). As in Section 6.1, the depth below seafloor is used to facilitate a comparison to drill core data.

Here, the average difference between downlog and uplog of the reoriented magnetic field is 100 nT (Section 5.7). As for Site U1374, the IGRF values differ from the average magnetic field, most notably in the east and vertical component of the reoriented data. Therefore adjusted values are going to be used for further modeling of the data (see Section 6.3).

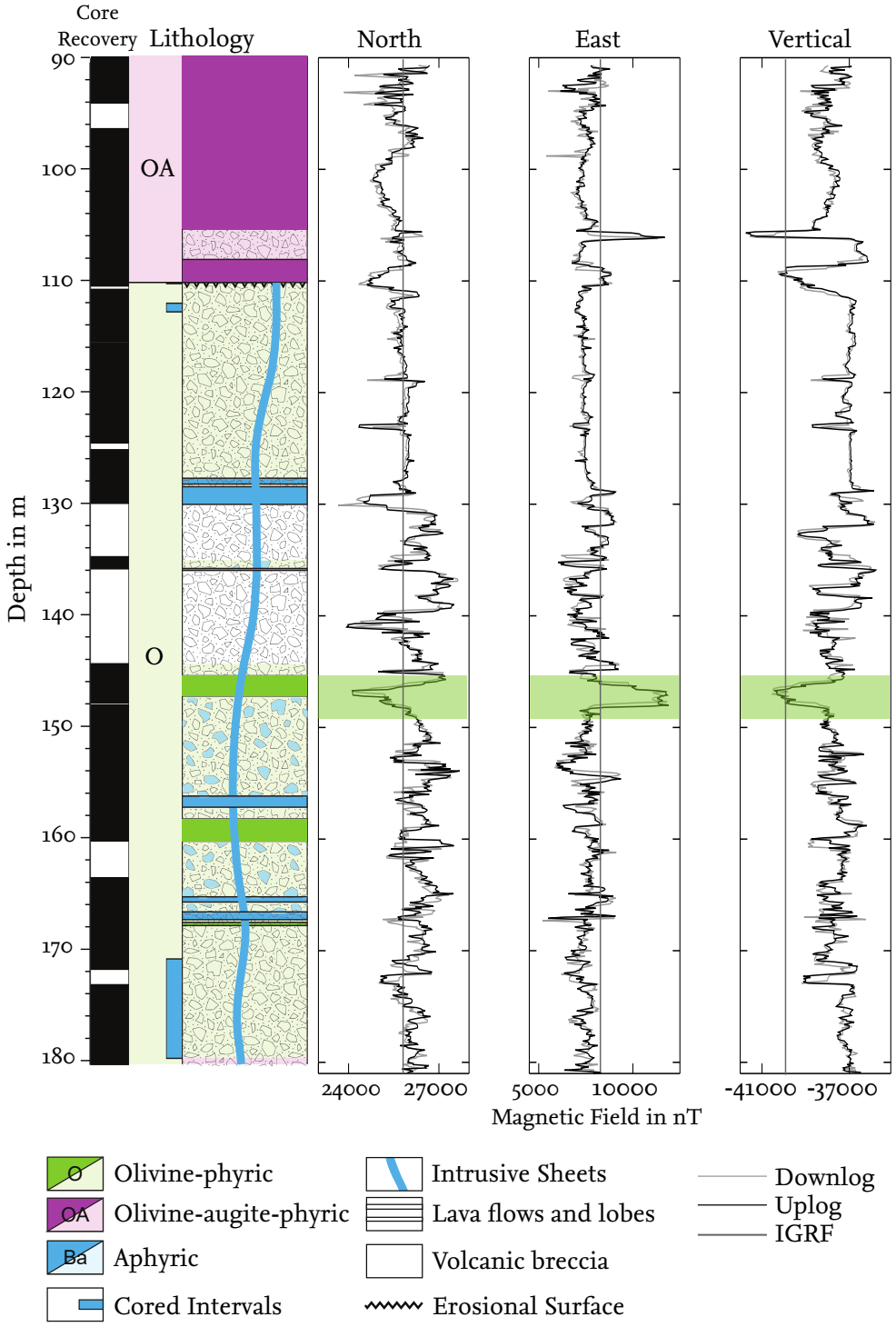

Figure 6.3.: Comparison of the lithology of Site U1376 (Expedition 330 Scientists (2011), modified) to the reoriented magnetic field data. Light gray lines denote the downlog, black lines the uplog of the reoriented magnetic field and dark gray lines the magnetic field as expected according to the IGRF. The layer marked in green is interpreted in more detail in Section 6.7.8. Adapted from Ehmann et al. (2015)

Like at Site U1374, the lithology is mostly composed of volcanic breccia, interlayered by several flow units and intrusive sheets. Albeit the drill hole intersects a massive, 33.1 m thick olivine-augite-phyric lava flow at the top of the open hole, there is no corresponding signature in the data. The following flow unit at a depth of approximately 110 m as well as the flow units at 130 m and 146 m clearly show in the magnetic field.

With an average core recovery rate of 76 % (Expedition 330 Scientists, 2012f), recovery is not as large as at Site U1374, but downhole logging data can help to fill some of the gaps. For example, the large gap between approximately 136 m and 144 m shows magnetic activity comparable to other sections that consist mainly of volcanic breccia. In contrast, the small gap at 172 m has a spike in both the north and the vertical component of the magnetic field; thus it is likely that the unrecovered section is a flow unit that is more strongly and more homogeneously magnetized than the surrounding breccia (Expedition 330 Scientists, 2012f; Ehmann et al., 2015).

The layer marked in green in the magnetic field data of Fig. 6.3 is going to be interpreted in more detail in Section 6.7.8.

6.3. Importance of the Background Field

An important factor in the modeling of magnetic field data is the background field assumed at the site of the measurement, which has to be subtracted from the reoriented data before any further steps can be taken. One possible choice is the value of the magnetic field given by the IGRF. However, as was shown in Section 6.1 and Section 6.2, the IGRF values do not coincide with the magnetic field measured in regions of low magnetization. There are several possible reasons for this (Ehmann et al., 2015):

Low density of observatories There are only very few magnetic observatories close to the sites of the measurements, which limits the accuracy of the IGRF in the region (see also Fig. 6.4 for a map of nearby observatories).

Magnetic influence of the tool string There are several magnetized parts in the tool string, e.g. the centralizer and the sinker bar (Ehmann, 2010). Even though a non-magnetic sinker bar was used as a spacer between the GBM and the rest of the tool string, there is going to be a remaining influence. This affects mainly the vertical component of the measured magnetic field, as high-permeable cylindrical objects are mainly magnetized along their long axis.

Regional scale variations Large off-borehole bodies can cause long wavelength anomalies in the borehole that overprint the magnetic influence of drilled structures. As the IGRF is based on observatory and satellite data, there is a limit to the wavelength of the magnetic field that it can resolve.

Errors in orientation Even though considerable effort is put into the reorientation of the magnetic field data, some errors in orientation can remain. The comparison of the different reorientation algorithms in Section 5.7 and Section 5.7 shows that the choice of the reorientation algorithm already can have an effect on the declination of the magnetic

field in the order of 1°. As the anomalies in the magnetic field are typically smaller than the background field, an error in orientation can lead to a non-linear increase in the error of the determination of the magnitude and direction of magnetization, if the IGRF values are used as background field. The measured field $\vec{B}$ is composed of the background field $\vec{B}_0$ and the anomaly $\vec{B}_A$ (Ehmann et al., 2015):

$$\vec{B} = \vec{B}_0 + \vec{B}_A \tag{6.1}$$

By expressing an error in orientation in terms of a rotation matrix $\mathbf{R}$, the measured field is given by

$$\mathbf{R}\vec{B} = \mathbf{R} \cdot (\vec{B}_0 + \vec{B}_A) \tag{6.2}$$

If a possible error in orientation is not considered, that is when for example the IGRF values are used directly, the assumed anomalous field $\vec{B}'_A$ is given by:

$$\begin{aligned} \vec{B}'_A &= \mathbf{R} \cdot (\vec{B}_0 + \vec{B}_A) - \vec{B}_0 \\ &= \mathbf{R}\vec{B}_A + (\mathbf{R} - \mathbf{I})\vec{B}_0 \end{aligned} \tag{6.3}$$

as $\vec{B}_0$ is typically much larger than $\vec{B}_A$, even with small errors in orientation $(\mathbf{R} - \mathbf{I})\vec{B}_0$ can be of similar size as $\vec{B}_A$ and thus the choice of the background field can significantly affect the interpretation of the magnetic field. To prevent this, one can choose an alternative background field B'_0 from known regions of low magnetization (for example identified in core samples). With

$$B'_0 \approx (\mathbf{R} - \mathbf{I})\vec{B}_0 \tag{6.4}$$

the anomaly is approximately given by

$$\vec{B}'_A = \mathbf{R}\vec{B}_A \tag{6.5}$$

an therefore the error in the direction of the anomalous field corresponds to the error in orientation (Ehmann, 2010).

By choosing the background field from regions of low magnetization, one does not only appropriately consider errors in orientation, but also corrects for toolstring influence and long wavelength crustal anomalies. For Site U1374, the magnetic field expected according to the IGRF (Finlay et al., 2010) is 27628 nT north, 8037 nT east and -36865 nT vertical, which does not coincide with the general trend of the magnetic field (see Section 6.1). Therefore, I am using the magnetic field from a lowly magnetized region at a depth of about 350 m, which is 25980 nT north, 9532 nT east, and -38050 nT vertical. For Site U1376, the IGRF gives values of 25,932 nT north, 8398 nT east, and -39949 nT vertical. Here I considered the magnetic field at a depth of about 120 m as more appropriate choice for further modeling, which is 25990 nT (north), 7456 nt (east) and -36949 nT vertical (Ehmann et al., 2015).

Another important point is the temporal variability of the background field, as true changes in the background magnetic field might occur during a measurement which generally reduce the quality of the data, or even could wrongfully be interpreted as magnetic anomalies. In order to avoid such errors, one can run a dedicated magnetometer to monitor fluctuations in the background field but this was not possible during IODP Expedition 330. To make up for that one can use data from nearby geomagnetic observatories.

The observatories closest to the drillsites of Expedition 330 are Apia (API), Eyrewell (EYR) and Macquarie Island (MCQ); all of which are still a considerable distance away: the maximum distance is between Macquarie Island and Site U1374, with 3642 km; the minimum distances are between Site U1374 and Apia, with 1652 km, and between Site U1376 and Eyrewell, with 1857 km (see Fig. 6.4).

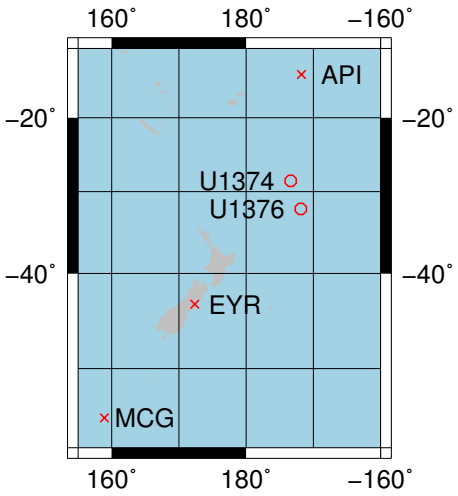

Figure 6.4.: Map of drillsites (o) and observatories (x)

Even though the distances are too large if the observatory data was to be used to correct the magnetic field, the data can still serve as an indication whether fluctuations of the background field might have an adverse effect on the measured downhole data. This luckily does not seem to be the case: for both Apia and Eyrewell, the variations of the magnetic field are smooth and in the order of some 10 nT. Variations at Macquarie Island are larger, with a maximum variation of 150 nT within half an hour on the day of the measurement at Site U1376 . However, as Macquarie Island is the most distant observatory, it is likely safe to assume that variations of the background field during all measurements were lower than the typical differences between downlog and uplog ($\approx$ 100 nT) of the magnetic field and thus can be safely neglected (all observatory data were acquired via `http://intermagnet.org/`).

6.4. Induced and Remanent Magnetization

Besides being an additive contribution to the measured magnetic field, the background field has the additional effect of contributing to the magnetic field by causing an induced magnetization in the rocks surrounding the borehole. Thus, if values for the magnetization are calculated from magnetic field measurements, they are comprised of both the induced and the remanent magnetization (see Eq. 2.10), of which the latter is the main objective of paleomagnetic studies. Using the background field and the susceptibility measured on drill core samples, one could calculate the induced magnetization and correct for it.

As described in Ehmann et al. (2015), I am going to neglect the influence of the induced magnetization. According to measurements on drill core samples, the ratio of the remanent magnetization to the induced magnetization, the so-called Königsberger ratio, is typically above 10 for Site U1376 and above 5 for Site U1374 for lavas and intrusive sheets (Expedition 330 Scientists, 2012d,f). The Königsberger ratio is lower for the brecciated units, but as they are unlikely to be in situ, including the induced magnetization would not improve the paleomagnetic analysis. The values of the induced magnetization form a skewed distribution, with a maximum value of the induced magnetization for Site U1374 of approximately 0.9 A/m, a mean of 0.1 A/m and a median of 0.08 A/m. The maximum

for Site U1376 is 0.7 A/m, with a mean of 0.07 A/m and a median of 0.05 A/m. Calculating the influence of the induced magnetization on the measured magnetic field is more complicated, as it depends on the structure assumed for the subsurface. Assuming layers of arbitrary orientation, I am going to show the maximum influence on the magnetic field in Section 6.7.5.

In the following interpretations of the magnetic field, I am frequently going to compare drill core magnetization data to magnetization data calculated from magnetic field measurements. As mentioned in Section 2.2.1, core samples routinely undergo demagnetization treatment in order to separate different types of magnetization and to gain a reliable record of the direction of magnetization. The demagnetization process is likely to give a more reliable record of the direction of magnetization, for example by removing drilling overprint, but is also likely to reduce the total strength of magnetization. In the case at hand, core samples were demagnetized by applying an alternating magnetic field of increasing peak strength. When using data from these samples for comparison, one has to decide about which data from which of the different demagnetization steps are used. As the remanent magnetization is relatively strong at Site U1374 (up to $\approx$ 20 A/m, I chose data from a demagnetization field of 10 mT, which has to be considered when comparing relative strengths of magnetization. As the magnetization is lower in general at Site U1376 (up to $\approx$ 10 A/m), I decided to use data from undemagnetized samples (see Ehmann et al., 2015).

6.5. Interpretation using Horizontal Layers

6.5.1. Bosum Model

For a first interpretation and without additional knowledge about the drilled geology, it is sensible to assume a horizontal layering of the subsurface. Bosum et al. (1988) give an analytical solution for the magnetic field of a horizontal circular layer intersected by a circular borehole (see Appendix A.2 for a simplified calculation of the model). For a layer with an outer radius R_o that extends from $+h$ to $-h$ on the vertical axis, with a borehole radius R_b and magnetization M_i (see Fig. 6.5), the magnetic field on the axis of the borehole ($x = y = 0$) is given by:

$$\begin{aligned} B_i = M_i \cdot a_i \cdot \mu_0 \cdot \Bigg(& \frac{z+h}{\sqrt{R_o^2 + (z+h)^2}} - \frac{z+h}{\sqrt{R_b^2 + (z+h)^2}} \\ & + \frac{z-h}{\sqrt{R_b^2 + (z-h)^2}} - \frac{z-h}{\sqrt{R_o^2 + (z-h)^2}} \Bigg) \end{aligned} \tag{6.6}$$

where

$$\begin{aligned} a_x = a_y &= \frac{1}{4} \\ a_z &= -\frac{1}{2}. \end{aligned} \tag{6.7}$$

For a layer of infinite extent ($R_o \to \infty$), the magnetic field is given by

$$\begin{aligned} B_i &= M_i \cdot a_i \cdot \mu_0 \left(\frac{z+h}{\sqrt{R_b^2 + (z+h)^2}} - \frac{z-h}{\sqrt{R_b^2 + (z-h)^2}} \right) \\ &= M_i \cdot a_i \cdot c \end{aligned} \tag{6.8}$$

where c is defined by:

$$c = \mu_0 \cdot \left(\frac{z+h}{\sqrt{R_b^2 + (z+h)^2}} - \frac{z-h}{\sqrt{R_b^2 + (z-h)^2}} \right) \tag{6.9}$$

Figure 6.5 shows an exemplary calculation for a horizontal layer as well as the geometry used in the Bosum model. No background field is present and the layer has a magnetization of 1 A/m in x direction. All other components of magnetization are zero and therefore only the x component of the magnetic field is shown. As all components share the same c (Eq. 6.9), all components of the magnetic field exhibit the same symmetries, so there is no loss of generality. The radius of the borehole, R_b, is 0.1 m, and the half-height h of the layer is 1.5 m. The outer radius of the layer, R_a is either 10 m (blue line) or infinite (orange line).

For the finite layer, the the maximum amplitude of the magnetic field inside the layer is lower and the magnetic field does not almost immediately return to zero outside of the

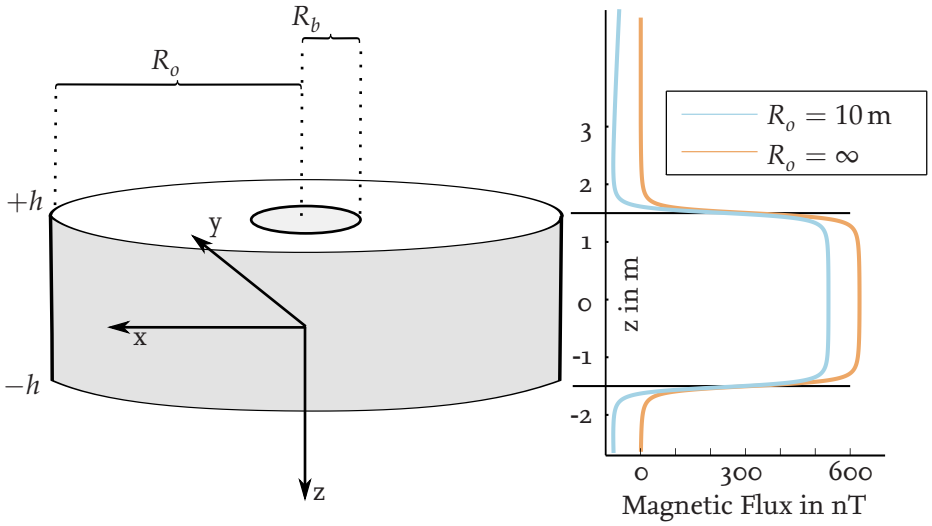

Figure 6.5.: Geometry of the Bosum model and an example of the effect of the finiteness of the layer on the magnetic field. Shown is the x component of the magnetic field for a layer with a magnetization of 1 A/m in x direction, for an outer radius of the layer of 10 m (blue line) and an infinite outer radius (orange line).

body, but becomes negative and increases slowly afterwards. This is understandable, as the magnetic far field of a finite body decays like that of a dipole, respectively the near field of a magnetized cylinder decays like that of a monopole, whereas the magnetic field above an infinite layer is zero. A borehole, which is small compared to the body it intersects, should not significantly affect the expected behaviour of the magnetic field outside of the body.

One can also identify a transition zone inside the layer, where the magnetic field is constantly increasing until it reaches a maximum amplitude. The depth extent of the transition zone depends on the ratio of the borehole radius and the height of the layer and is smaller for smaller radii. If the outer radius is similar to or smaller than the height of the layer, the magnetic field would, after reaching a maximum, decrease again until the center of the layer (Virgil, 2012).

For the data analysis presented here, the properties of finite layers are less important, as we do not have information about the lateral extent of the drilled structures. Here, it is of greater importance to know in which cases the assumption of infinite layers is justified, which errors are made if the assumption is not justified and which effect the ratio of layer height to borehole radius has on the maximum value of the magnetic field inside an infinite layer. Therefore, these two points are discussed in the following. The interested reader should refer to Virgil (2012) for a detailed discussion of the influence of the shape and orientation of finite layers on the magnetic field.

When is a layer of infinite extent?

In order to assess under which conditions a model comprising infinite layers can be used to interpret the magnetic field data of a borehole, we start with the properties of a single

layer. Whether we can treat a layer as being of infinite lateral extent, depends on its height, outer radius and the radius of the borehole. The magnetic field at the center of a layer ($z = 0$) is given by:

$$B_i = M_i \cdot a_i \cdot \mu_0 \cdot \left(\frac{2h}{\sqrt{R_b^2 + h^2}} - \frac{2h}{\sqrt{R_o^2 + h^2}} \right) \tag{6.10}$$

and reaches its maximum value for an infinite outer radius:

$$B_i^{max} = M_i \cdot a_i \cdot \mu_0 \cdot \left(\frac{2h}{\sqrt{R_b^2 + h^2}} \right) \tag{6.11}$$

The ratio of the magnetic field at the center and the maximum possible value is given by

$$\frac{B_i}{B_i^{max}} = 1 - \frac{\sqrt{R_b^2 + h^2}}{\sqrt{R_o^2 + h^2}} \tag{6.12}$$

By setting a minimum ratio of b (for example, 99%), above which we assume the layer to be infinite, we can solve Eq. 6.12 for the outer radius of the layer:

$$R_o = \sqrt{\frac{R_b^2 + h^2}{(b-1)^2} - h^2} \tag{6.13}$$

which gives the minimum outer radius a layer has to have to count, within some margin of error, as infinite.

Figure 6.6 shows the minimum outer radius versus the half-height h of the layer for different inner radii and accepted margins of error. For $R_b << h$, the minimum outer radius is linearly dependent on h, the half-height of the layer. For a maximum error in the magnetic field of 1% (b=0.99), the constant of proportionality is approximately 100; for a maximum error of 5% (b=0.95) it is 20.

Now we imagine a borehole drilled through a homogeneously magnetized layer: if the borehole has a depth of 10 m (half-height of 5 m), a layer with an outer radius of 100 m can be treated as infinite (within an error of 5%, see Fig. 6.6). If the borehole extends to a depth of 20 m, the outer radius of the layer needs to be at least 200 m to stay within the same error margin.

The results for a single layer can be generalized to a borehole intersecting several differently magnetized layers: regardless of whether a single, homogeneous layer or multiple differently magnetized layers are intersected, the consequences remain the same: the influence of the regions surrounding the borehole grows with the depth of the borehole. The requirements on the lateral extent of the layers increase with the depth of the borehole; the necessary lateral extent of multiple layers, so that they are correctly approximated by infinite layers, is a multiple of the depth of the borehole.

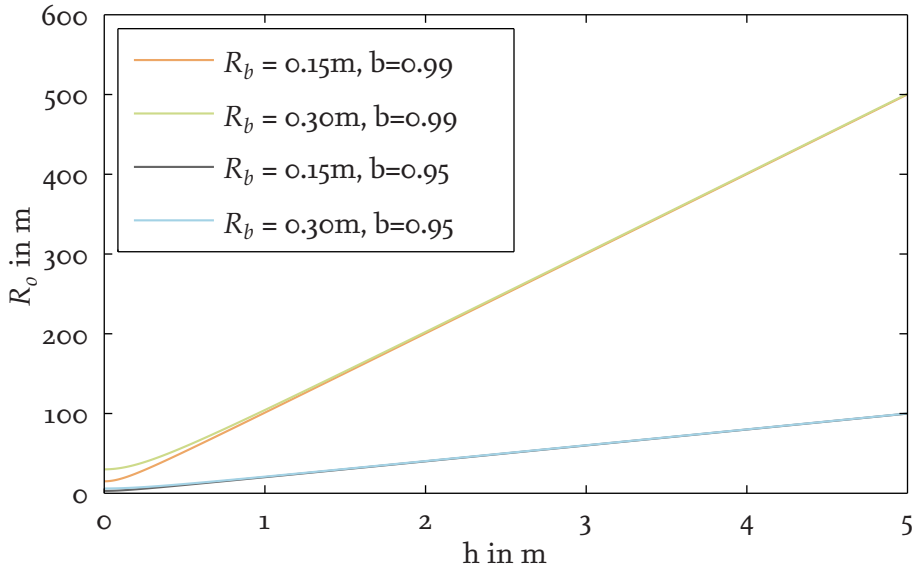

Figure 6.6.: The minimum outer radius a layer has to be approximable by an infinite layer, depending on its half-height h and the radius of the borehole R_b. b is the ratio of the magnetic field at the center of the finite layer to the maximum possible value of the infinite layer.

Figure 6.7 demonstrates the effect of a finite outer radius on one component of the magnetic field. The left panel shows a schematic view of the boreholes discussed in the graphs of the middle and right panel. The middle panel shows magnetic field data for a homogeneously magnetized layer, the right panel shows magnetic field data for multiple differently magnetized layers. Dashed lines indicate data for an infinite outer radius of the layers, solid lines indicate data with an outer radius of 100 m. Orange lines indicate data for a borehole with a depth of 10 m, red lines data for a borehole with a depth of 20 m. In all cases, the borehole radius is 0.1 m.

The middle panel shows the aforementioned result for a single layer: for an infinite outer radius of the layer (dashed lines), the magnetic field does not depend on the depth of the borehole, that is, in this case, the height of the layer. But if the layer has a finite outer radius (solid lines), the strength of the magnetic field depends on the depth of the borehole (the height of the layer); the magnetic field for the 10 m borehole (solid orange line) is closer to the magnetic field of the infinite layer and higher than that of the 20 m borehole (solid red line).

The right panel demonstrates that the effect discussed for a single layer is also present for multiple layers and that eventually the depth of the borehole is the important parameter when discussing the validity of a model comprising infinite layers: shown is the same combination of borehole depths and outer radii for a random distribution of magnetization. As in the homogeneous layer in the middle panel, the dashed lines (infinite outer radius) coincide and do not depend on the depth of the borehole. Likewise, the magnetic field for a finite radius of the layers depends on the depth of the borehole: the strength of the

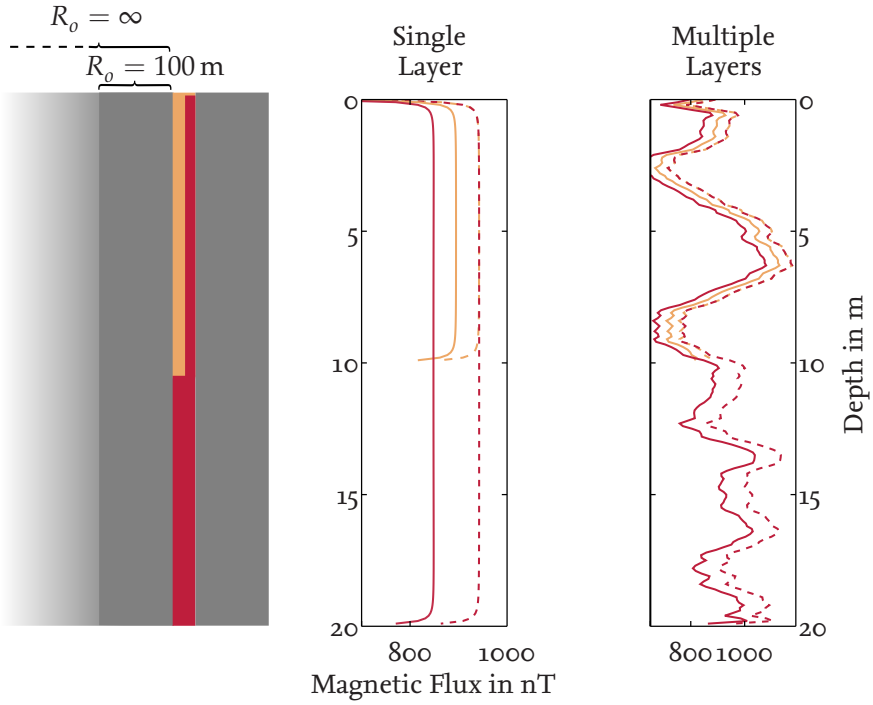

Figure 6.7.: The effect of a finite outer radius on one component of the magnetic field of a layer in dependence of the borehole depth, which corresponds to the layer height. Solid lines show data for an outer radius of 100 m, dotted lines show data for an infinite outer radius. Orange lines show data for a 10 m borehole, red lines show data for a 20 m borehole. The borehole radius is 0.1 m. Left panel: schematic overview of the borehole. Middle panel: data for boreholes through a homogeneous layer. Right panel: data for boreholes through several layers of differing magnetization. For infinite layers, the magnetic field is independent of the depth of the borehole. For finite layers, the magnetic field depends on the depth of the borehole.

magnetic field measured in the shallow borehole (solid orange line) differs from the field measured in the deep borehole (solid red line).

In practice, this means that if the lateral extent of the drilled structures is not known, it would be preferable to measure the magnetic field multiple times during deepening of the borehole, as a limited lateral extent of the drilled layers could sometimes be visible in differences between logs from different stages of the borehole. The strength of the effect is also going to depend on the structure and type of material the finite layered model is embedded in; the data shown assumes that the finite structure is surrounded by nonmagnetic material.

An important point here is that the finiteness of the layers not only influences the strength, but also the direction of the magnetic field. When finite layers are wrongfully interpreted as infinite, this can result in a wrong strength of the calculated magnetization and cause some, albeit probably small, errors in the recovered inclination and declination.

The Influence of the Height of a Layer on its Maximum Magnetic Field

For layers of infinite lateral extent, there is a maximum value that the magnetic field at the center of the layer can reach in dependence on the ratio of the height of the layer and the radius of the borehole. For $h >> R_b$, using Eq. 6.11, we get:

$$\max(B_i^{max}) = 2\mu_0 \cdot M_i a_i \tag{6.14}$$

where M_i is the magnetization of the layer and the constant a_i is given by Eq. 6.7. As we can see, the maximum is independent of the exact values of the borehole radius and the height of the layer. Once this maximum is reached, further increasing the height of the layer has no effect on the measured magnetic field near the center of the layer; an effect that is visible in the middle panel of Fig. 6.7 (dashed lines) in the previous discussion of the influence of the outer radius of the layer. In a realistic borehole, the radius is not going to be constant and the height of the layer cannot be determined exactly; therefore it is helpful to know whether errors in the determination of these parameters are relevant for a given layer or whether the layer is of sufficient height for the magnetic field at its center to have reached the maximum possible value.

To assess for which ratio of layer height to borehole radius the maximum value of the magnetic field is reached, we again calculate the ratio of the actual value of the magnetic field to the maximum possible value and get:

$$\frac{B_i^{max}}{\max(B_i^{max})} = \frac{h}{\sqrt{R_b^2 + h^2}} \tag{6.15}$$

By substituting $h = n \cdot R_b$, choosing a minimum ratio of b and solving for n we get:

$$n = \frac{b}{\sqrt{1 - b^2}} \tag{6.16}$$

For example, if we postulate that the magnetic field at the center of the layer should reach 99% of the maximum possible value (b=0.99), the half-height of the layer has to be at least seven times the radius of the borehole. This result is similar to the conclusion that Virgil (2012) reaches in a numerical parameter study, where he concludes that the height of the layer should be about ten times the radius of the borehole. If we can accept a slightly larger error margin and accept a deviation of the magnetic field of 5% (b=0.95), the half-height of the layer only needs to be three times the radius of the borehole.

With an average borehole radius of approximately 0.14 m for Expedition 330, a layer therefore needs to have a height of approximately one meter for the magnetic field to reach 95% of its maximum value. Many of the igneous layers drilled during the Expedition are close to or above this threshold (see Fig. 6.2 and Fig. 6.3 for information about the lithology). But to avoid errors, it is advisable to include the radius of the borehole in all models for the magnetization of the seamounts, especially as the radius was measured by the Formation Microscanner (FMS) and is readily available.

6.5.2. Inversion for Multiple Horizontal Layers

After subtracting the selected values for the background field from the reoriented magnetic field data, we can make an initial assessment of the magnetization by running an inversion using horizontal layers. I am using an inversion procedure based on Virgil (2012), with some modifications (as described in Ehmann et al., 2015). Figure 6.8 shows a flow chart of the general procedure, which I am going to illustrate in the following paragraphs.

The first step is to interpolate the measurements to equally spaced depths. Here, I am using an interpolation distance of 0.1 m, which corresponds to the average distance between data points. Then, a model is constructed using as many magnetized layers as data points. Using Eq. 6.8, the magnetic field can be written in the following form:

$$\begin{pmatrix} B_k^1 \\ B_k^2 \\ B_k^3 \\ \dots \\ B_k^m \end{pmatrix} = a_k \begin{pmatrix} c^{1,1} & c^{1,2} & \dots & \dots \\ c^{2,1} & c^{2,2} & \dots & \dots \\ c^{3,1} & c^{3,2} & \dots & \dots \\ \dots & \dots & \dots & \dots \\ \dots & \dots & \dots & c^{m,n} \end{pmatrix} \cdot \begin{pmatrix} M_k^1 \\ M_k^2 \\ M_k^3 \\ \dots \\ M_k^n \end{pmatrix} \tag{6.17}$$
$$\rightarrow \vec{B}_k = a_k \cdot \mathbf{C}_k \cdot \vec{M}_k$$

Here, B_k^i and M_k^i are the magnetic field and magnetization component k at the position of layer i; a_k is defined as in Eq. 6.7 and $c_k^{m,n}$ is given by:

$$\begin{aligned} c^{m,n} = \mu_0 \Bigg(& \frac{z^{m,n} + h_n}{\sqrt{R_{b_n}^2 + (z^{m,n} + h_n)^2}} - \frac{z^{m,n} + h_n}{\sqrt{R_{o_n}^2 + (z^{m,n} + h_n)^2}} \\ & + \frac{z^{m,n} - h_n}{\sqrt{R_{o_n}^2 + (z^{m,n} - h_n)^2}} - \frac{z^{m,n} - h_n}{\sqrt{R_{b_n}^2 + (z^{m,n} - h_n)^2}} \Bigg) \end{aligned} \tag{6.18}$$

where R_{b_n} is the radius of the borehole and R_{o_n} is the outer radius of layer n. The half-height of the layer is denoted by h_n, and equals half the interpolation distance of the magnetic field data. $z^{m,n}$ is the vertical distance between the location of the magnetic field measurements B_k^m and the layer with magnetizations M_k^n. As we do not have information about the true extent of the layer, we are usually going to use infinite layers, so $c^{m,n}$ can be simplified as in Eq. 6.8.

As the magnetic field of a layer is quickly decaying outside of the layer, the diagonal elements of matrix $\mathbf{C}_k$ are much larger than the off-diagonal elements. For example, an element four positions off the diagonal is typically only a hundredth of the diagonal element. For similar reasons, Virgil (2012) suggests to only include the neighbouring layers with 15 m of each data point for the calculation of elements of the matrix. However, as $\mathbf{C}_k$ only has to be calculated once during an inversion, including all neighbouring layers does not significantly decrease the speed of the inversion, which has typical runtimes of less than 5 s (5000 layers, Intel Core i5-4300U, 8 GB RAM, 10 iterations).

A direct inversion of the sparse matrices $\mathbf{C}_k$ is not stable and leads to unphysical models with a magnetization oscillating over several orders of magnitude between neighbouring

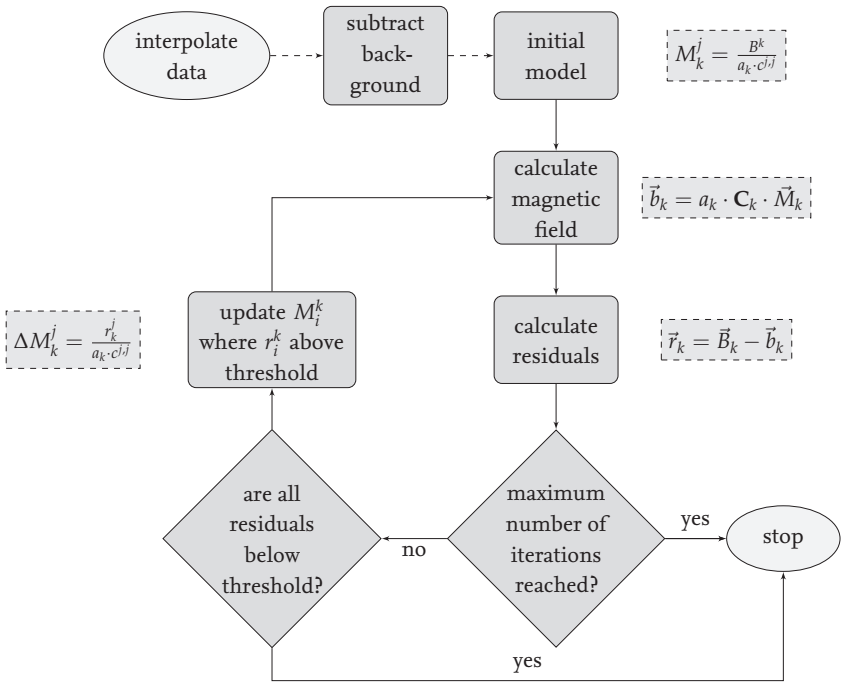

Figure 6.8.: Flow chart for an inversion using multiple horizontal layers.

layers. Therefore, I am using an iterative approach. First, an initial magnetization model is calculated for all three components of the magnetic field using

$$M_k^j = \frac{B^k}{a_k \cdot c^{j,j}} \tag{6.19}$$

thereby neglecting the influence of nearby layers/data points. The minimum possible value for M_k^j is given for the maximum possible value of $c^{j,j}$, which is reached for $R_o \to \infty$ and $R_b >> h$ (see also Eq. 6.14):

$$c^{j,j} = 2\mu_0 \tag{6.20}$$

By using this value for the initial guess of the magnetization, the magnetization of layer of sufficient height is guessed right immediately; for any other layer the initial guess is too low and is going to be increased during further iterations of the algorithm.

Then, the complete matrix $\mathbf{C}_k$ is used to calculate a model of the magnetic field, $\vec{b}_k$, including the mutual influence between the different layers:

$$\vec{b}_k = a_k \cdot \mathbf{C}_k \cdot \vec{M}_k \tag{6.21}$$

After calculating the residuals $\vec{r}_k$ via a comparison of the measured magnetic field and the model via

$$\vec{r}_k = \vec{B}_k - \vec{b}_k\,, \tag{6.22}$$

two checks are made: if either a preset maximum number of iterations of the algorithm is reached or if all residuals in all components of the magnetic field are below a specific

threshold, the algorithm stops. Otherwise, the algorithm continues by updating those M_i where the absolute value of the residual is above the predefined threshold. Any M_i^k whose corresponding magnetic field value b_i^k differ from the measurement by less than the threshold remain unchanged in the next iteration; however, if at any time the residual should rises above the threshold, the magnetization is updated again. Listing A.2 in Appendix A.6 gives an implementation of the algorithm in Matlab.

By using (a) a minimal plausible update of the magnetization, (b) a threshold for the individual residuals and (c) a maximum number of iterations, it can be ensured that the measured data are not overfitted and oscillations in the calculated magnetization are reduced. I am typically using 10 iterations and a threshold of 100 nT.

In the following, I am going to refer to the magnetization derived from a horizontal layer inversion of magnetic field data as *measured apparent magnetization*, similar to the definition of the apparent resistivity measured in geoelectric surveys (Ehmann et al., 2015). Any other model for the magnetization of the subsurface can then be explained in terms of the apparent magnetization it produces. The use of this definition is going to become more evident in the later chapters that deal with inclined layers.

6.5.3. Horizontal Layers: U1374

Figure 6.9 (Ehmann et al., 2015) shows the result of the horizontal layer inversion (i.e. the measured apparent magnetization) for the data of the uplog of the first measurement at Site U1374 (red lines). The natural remanent magnetization data measured on core samples are shown in black. As the core data are unoriented, the (apparent) declination of magnetization is only shown for the horizontal layer model calculated using the oriented magnetic field data of the GBM.

For the data of Site U1374, the measured apparent inclination differs from the inclination measured on core samples, which also expresses itself in a horizontal apparent magnetisation that is in general higher than the respective core data and a vertical apparent magnetization that is in general lower than the respective core data. The total apparent magnetization is higher than the total magnetization of the core samples, which could in part be caused by the fact that I am using data from partly demagnetized core samples for comparison (see Section 6.4).

The linear trend that is visible in the magnetic field data up to a depth of 300 nT, as well as the sudden increase in the north and vertical magnetic field component between 365 m and 470 m (see Fig. 6.2 in Section 6.1) cause correspondent features in the apparent magnetization. However, there are no correspondent changes in the core data, which supports the assumption that those features of the magnetic field are caused by geological features not intersected by the borehole.

These differences between the horizontal layer model and the core data indicate that the apparent declination shown in Fig. 6.9 is to be treated with caution, as it is very likely that the horizontal layer model does not represent the true geometry of the subsurface within an acceptable level of accuracy.

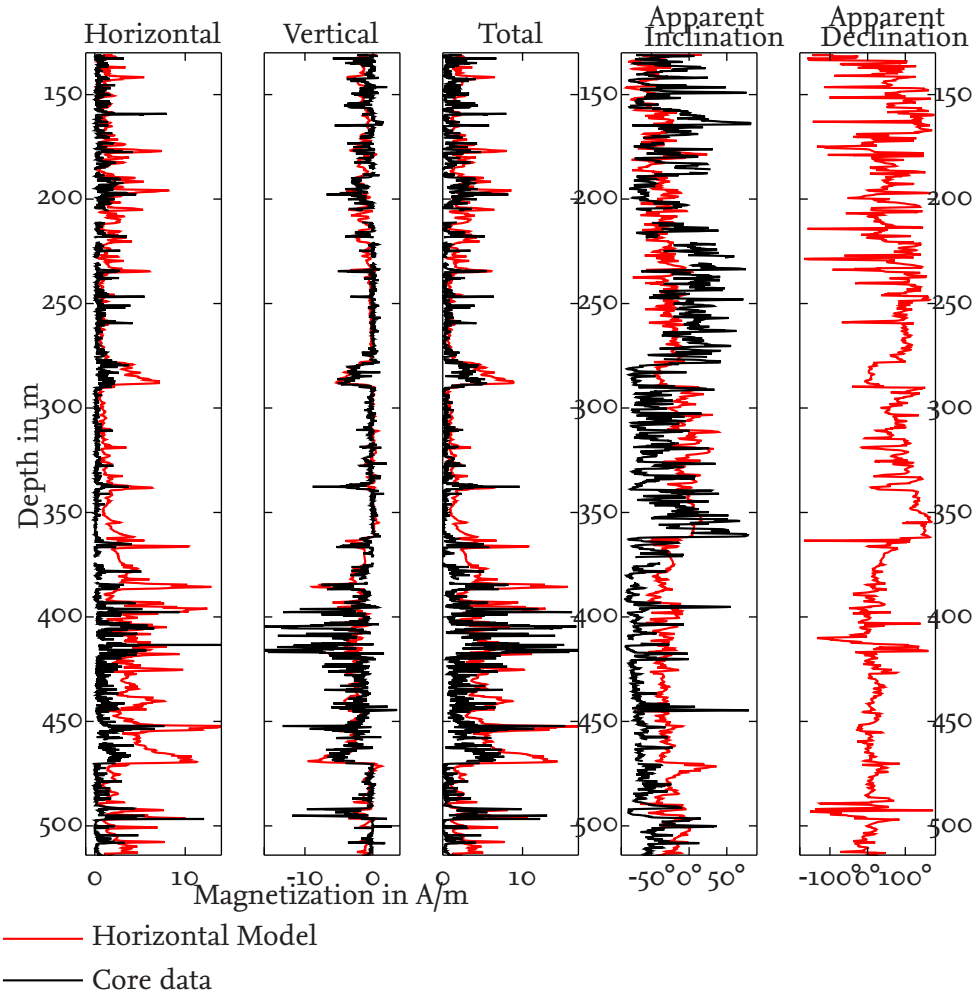

Figure 6.9.: Comparison of the measured apparent magnetization data (red lines) of Site U1374 to the natural remanent magnetization (NRM) measured on drill core samples (black lines). (from left to right: first to third panel) Horizontal, vertical, and total magnetizations. (fourth panel) Measured apparent inclination and inclination measured on drill core samples. (fifth panel) Measured apparent declination and no core data. Adapted from Ehmann et al. (2015).

6.5.4. Horizontal Layers: U1376

Figure 6.10 (Ehmann et al., 2015) shows a comparison of the measured apparent magnetization to drill core data for the uplog of the measurement at Site U1376. As some of the core could not be retrieved during drilling, there are some gaps in the magnetization data, mainly in the section between 130 m and 145 m.

Here, the situation is largely the opposite of Site U1374, which is particularly well visible at a depth of 145 m: The horizontal apparent magnetization is lower than the core data, whereas the vertical apparent magnetization is higher, which results in an apparent inclination that

is in general lower than the inclination measured on core samples. The total measured apparent magnetization is in good agreement with the NRM data.

At a depth of 110 m, the differences between vertical and horizontal apparent magnetization and core data are smaller than at 145 m, but the high apparent declination of ≈ 100° as well as the differences between apparent inclination and core sample inclination suggest that the model is insufficient. In general, the measured apparent declination is highly variable and, as for Site U1374, likely unreliable.

This means that, as at the other drill site, a horizontal layer model does not adequately represent the lithology of the seamount and that we have to allow for more complicated layer geometries in order to bring magnetic field data and core data into agreement.

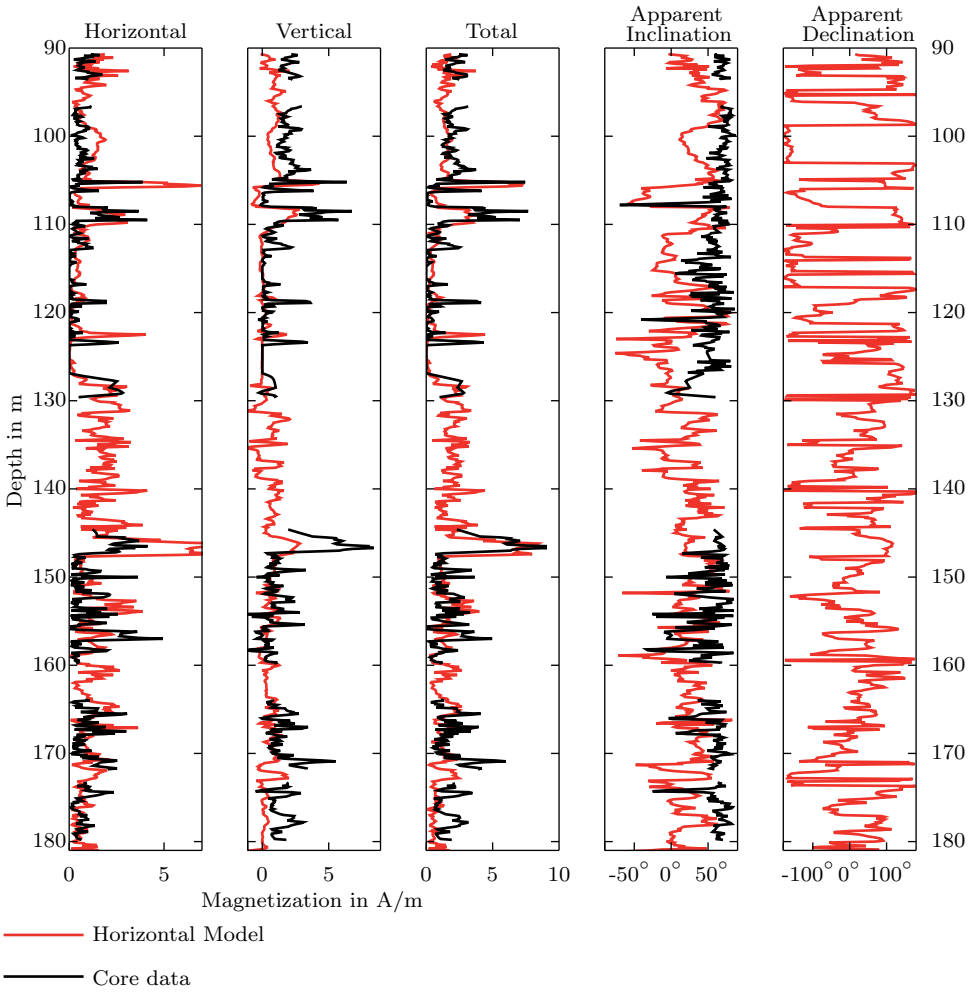

Figure 6.10.: Comparison of the measured apparent magnetization data (red lines) of Site U1376 to the natural remanent magnetization (NRM) measured on drill core samples (black lines). (from left to right: first to third panel) Horizontal, vertical, and total magnetizations. (fourth panel) Measured apparent inclination and inclination measured on drill core samples. (fifth panel) Measured apparent declination and no core data. Adapted from Ehmann et al. (2015).

6.6. Incorporating Structural Information

In order to improve the model for the magnetization of the seamounts, we need to incorporate additional information about the geometry of the lithologic units, i.e. possible dips and azimuths of drilled layers. Several seismic surveys have been conducted in the forefront of Expedition 330; the igneous basement, however, is mostly opaque to seismic waves (Koppers et al., 2010), so this data give no further information for the modelling of the magnetization.

A remaining option is provided by images of the borehole wall. Two downhole logging tools were used during the expedition that can help with putting limits on the possible geometry of drilled layers: the Ultrasound Borehole Imager (UBI) and the Formation Micro Scanner (FMS) (Expedition 330 Scientists, 2012a). Gaillot et al. (2007) give their technical details as follows:

The UBI comprises a rapidly rotating dual-frequency ultrasound transducer that emits pulses that are reflected by the borehole wall. The amplitude and travel times of the reflected waves allow to draw conclusions about the radius of the borehole and the structure of the borehole wall.

The FMS comprises four orthogonal arms, each featuring a pad with 16 micro-electrodes that are pressed against the borehole wall. These electrodes are arranged in two rows with a horizontal spacing of 0.51 cm (0.2 ”) and a vertical spacing of 0.76 cm (0.3 ”). A current is sent through the electrodes and the resulting voltage is measured, which gives a high-resolution image of the micro-resistivity of the borehole wall. The variable extension of the arms is measured and gives the diameter (*caliper*) of the borehole.

The spatial resolution and dynamic range of the electrical images is higher than that of the acoustic images; in contrast, the UBI covers the whole borehole wall whereas the FMS image only covers the part of the borehole wall that is in contact with the four pads. During Expedition 330, due to time constraints the UBI was only run at Site U1374; the FMS was run at both Site U1374 and Site U1376. As electrical images are available for both sites, and as their quality in general was higher than the UBI images, I am going to focus on the electrical images for the determination of geometrical parameters.

Both the FMS and the UBI use the General Purpose Inclinometry Tool (GPIT) for orientation. The GPIT itself uses a triaxial accelerometer in combination with a tri-axial fluxgate magnetometer to determine the direction to north. The basic assumption for this method of orientation is that the magnetic field is undisturbed and points in the direction given by a magnetic field model, for example the IGRF. This works well in sediments but becomes more erroneous in magnetized formations like the igneous rocks drilled during the Louisville expedition. Gaillot et al. (2004) give a review of the orientation algorithms applied within the GPIT and compare their accuracy with the orientation calculated using oriented GBM data instead of a fixed value for the background field. They find that, for their data, the differences are typically in the order of 5° to 10° in tool azimuth.

For the data discussed here, the error of the azimuth of a layer determined using FMS images can, depending on the strength of the local magnetic field, be in the order of 10°,

Correcting these errors is not easily possible, as the available borehole image processing software packages do not allow the implementation of a non-constant background field. Thus, no further corrections are made to the data. However, as we are going to see later in this thesis, other error sources like the inexact determination of layer parameters from images are dominant (Section 6.7.4).

Figure 6.11 shows how images of the borehole wall can be used to derive geometrical information about the subsurface: when a borehole is drilled through an inclined layer, the layer boundary shows up as a sinusoidal feature when the image is projected on a two-dimensional plane. The azimuth ϕ of the layer is given by the angular location of the minimum of the sinusoid. The dip δ of the layer can be calculated from the amplitude A of the sinusoid:

$$\delta = \arctan \frac{A}{2R_b} \tag{6.23}$$

where R_b is the radius of the borehole. As a borehole is rarely circular, the value for the dip depends on which of the two caliper values given by the FMS is chosen for the calculations. For Expedition 330, maximum differences between both sets of dips are in the order of 2°.

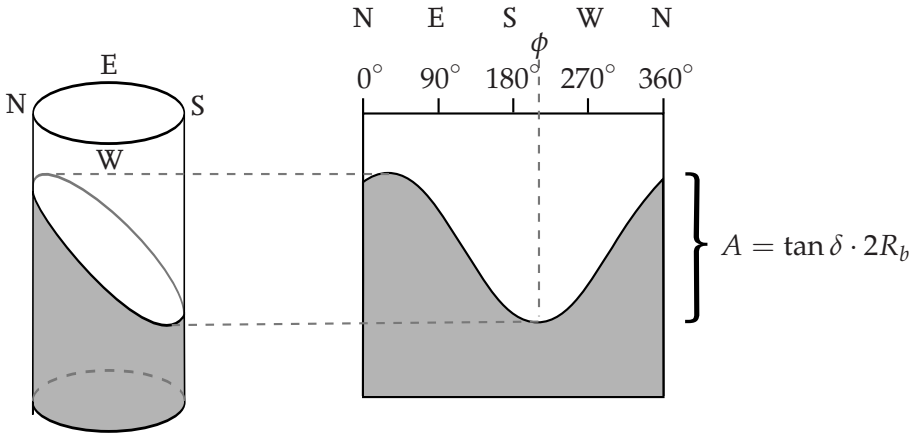

Figure 6.11.: The left panel shows a borehole intersecting the upper surface of an inclined layer. The right panel shows an unrolled image of the borehole wall, where the inclined layer interface shows up as sinusoidal structure. A measurement of the amplitude A of the sinusoid and knowledge of the borehole radius R_b allows for a calculation of the inclination δ of the layer. The layer azimuth ϕ is given by the location of the minimum of the sinusoid.

Figure 6.12 shows an example of an FMS image recorded at Site U1376 during Expedition 330. Shown are the four traces of the FMS pads as raw data and in two different color normalizations: For the static normalization, a histogram of all measured data is calculated and color values are assigned so that each color represents the same number of data points. For the dynamic normalization, the same procedure is performed for moving windows of the data, which can result in a more detailed image in regions of strongly variable resistivity (Advanced Logic Technology, 2014). Using different data normalizations aids

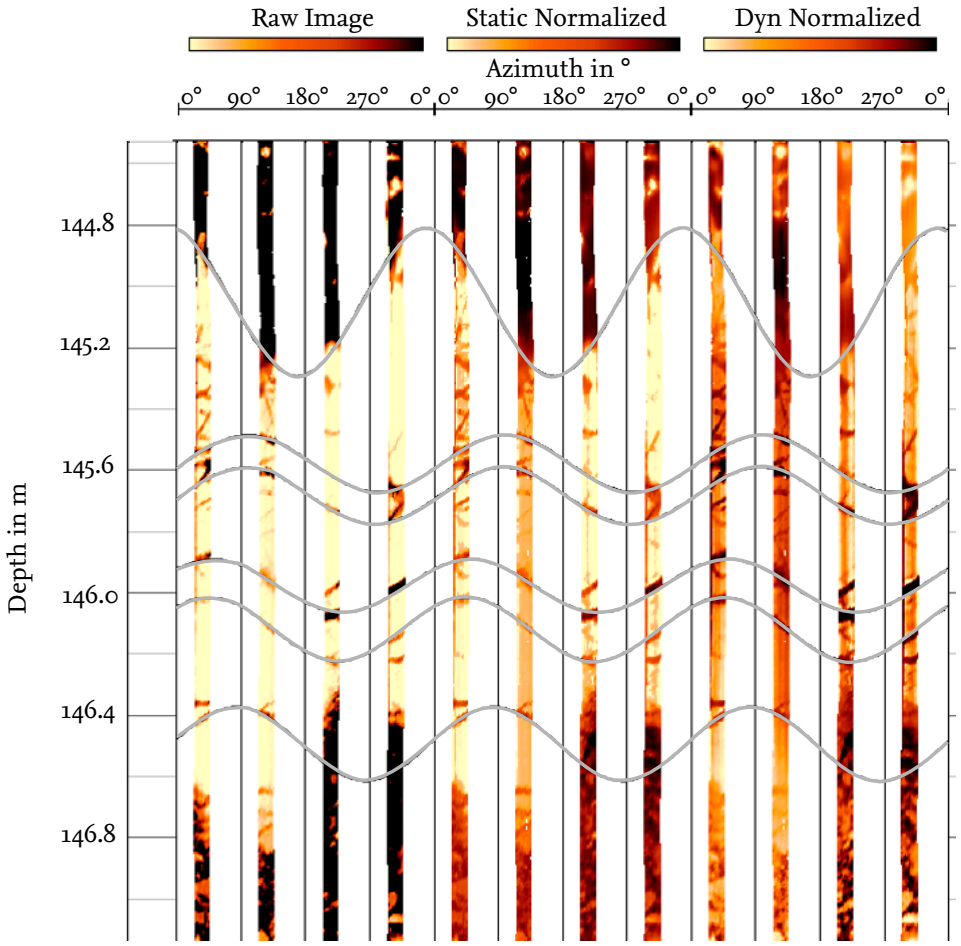

Figure 6.12.: Example of an FMS image recorded at Site U1376 during Expedition 330. Shown is an image of the microresistivity of the borehole wall given by the four pads of the FMS. The left four traces show raw data, the middle four traces show statically normalized data and the right four traces show dynamically normalized data. The Gray lines represent sinusoidal structures identified during data processing. See text for details.

with the visual interpretation of the data. All data are displayed using a linear color scale with light colors representing low resistivity and dark colors representing high resistivity values.

A lava flow identified in drill core samples can be clearly distinguished from the surrounding breccia. Several sinusoidal features are visible in the data; the topmost is likely to be associated with the top boundary of a lava flow or dike, the lower ones are more likely to be associated with fractures in the borehole wall. The bottom boundary of the lava flow is also visible in the data, but not marked in the figure.

The images of the borehole wall show that the layers encountered at Sites U1374 and U1376 are not likely to be horizontal and therefore the magnetization model has to be extended to inclined layers.

6.7. Interpretation using Inclined Layers

6.7.1. Gallet and Courtillot Model

In many cases, as for the data presented in this thesis, horizontal layers do not sufficiently describe the subsurface. The next logical step here is to extend the model to the more general case of inclined layers. The model closest to the horizontal layer model used so far is given by Gallet and Courtillot (1989), where they describe a semi-analytical solution for the magnetic field of a cylinder with an inclined upper surface, which they use to calculate the magnetic field of inclined layers intersected by a circular borehole. Figure 6.13 shows the general geometry used for inclined layers: a circular layer, inclined by an angle δ in direction of the azimuth ϕ with an outer radius R_o is intersected by a borehole with radius R_b. The azimuth is considered positive clockwise and measured relative to geographic north.

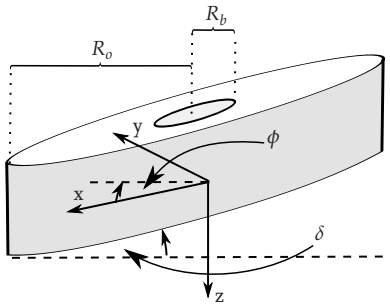

Figure 6.13.: Inclined layer with outer radius R_o intersected by a borehole with radius R_i. The layer is inclined by an angle δ. The direction of inclination relative to geographic north is given by the azimuth ϕ.

The model relates the magnetization to the magnetic field via a second order tensor C_{ij}:

$$\begin{pmatrix} B_x \\ B_y \\ B_z \end{pmatrix} = \begin{pmatrix} C_{xx} & C_{xy} & C_{xz} \\ C_{yx} & C_{yy} & C_{yz} \\ C_{zx} & C_{zy} & C_{zz} \end{pmatrix} \begin{pmatrix} M_x \\ M_y \\ M_z \end{pmatrix} \tag{6.24}$$

As C_{ij} is symmetric (see Section 2.3), it has only six independent coefficients. Gallet and Courtillot (1989) give solutions for all coefficients and do not explicitly mention the symmetry, so this has to be kept in mind when implementing their results. As there seem to be some typographic errors in some of the equations of the original publication, Appendix A.3 gives an overview of the calculations of the coefficients (see also Ehmann et al., 2015).

The main issue of the model is that it involves integrals that can only be solved numerically. If the geometry of the layer is known, this does not considerably affect an inversion, as the coefficients only have to be computed once for each position within the borehole and can be reused when inverting for the magnetization alone. But as soon as one inverts for multiple layers or a layer with unknown geometry, this significantly increases the computation time.

6.7.2. Rectangular Layers

A possible solution to overcome the shortcomings of the accurate but slow model by Gallet and Courtillot (1989) is to use rectangular layers intersected by a rectangular borehole. Compared to circular boreholes, a model using rectangular layers has the advantage that the geometry of the layer can be adapted much more easily; for example, elliptical boreholes can be approximated by changing the extent of the prisms, which would not be possible with the model by Gallet and Courtillot. Hamano and Kinoshita (1990) use a rectangular borehole model to give the magnetic field at the contact of two differently magnetized layers; however they do not include the derivation of the model, but refer to an article that was supposed to be published subsequent to their original publication, but which I was unable to find.

Therefore I am using my own model based on the magnetic field of an inclined prism, that is a parallelepiped. The calculations, which are similar to the ones given in Hjelt (1972), can be found in Appendix A.4. In order to calculate the magnetic field inside a rectangular borehole through a rectangular layer, I am using a model composed of four prisms. Theoretically, it is possible to use two prisms by subtracting the magnetic field of one prism representing the borehole from another prism that represents the layer (Fig. 6.14a); nevertheless, I found that this can give rise to numerical instabilities near the surface of the layer which can be avoided by a four prism model (Fig. 6.14b). Using double the amount of prisms also doubles the calculation time; however, as the magnetic field of a prism can be expressed analytically, this is no significant limitation. Figure 6.14c shows how an inclined layer can be represented by prisms. The length of the sides of each prism can be adjusted independently, allowing for the aforementioned approximation of elliptical boreholes, with the limitation that the main axes of the shape of the borehole and of the layer always coincide.

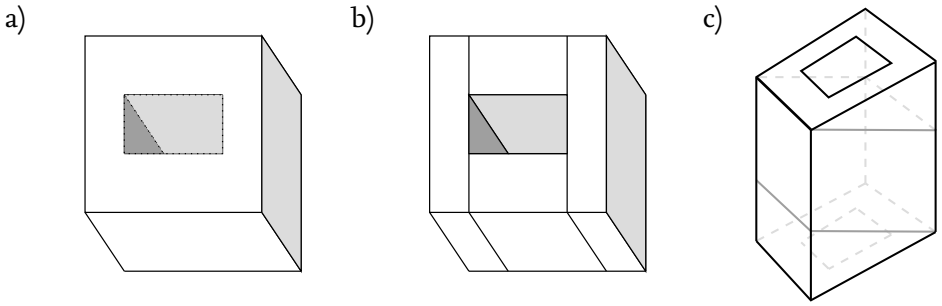

Figure 6.14.: a) Rectangular layer and rectangular borehole represented by one prism for the layer and one for the borehole b) Rectangular layer and rectangular borehole represented by four prisms c) Inclined rectangular layer with a rectangular borehole represented by two prisms (parallelepipeds).

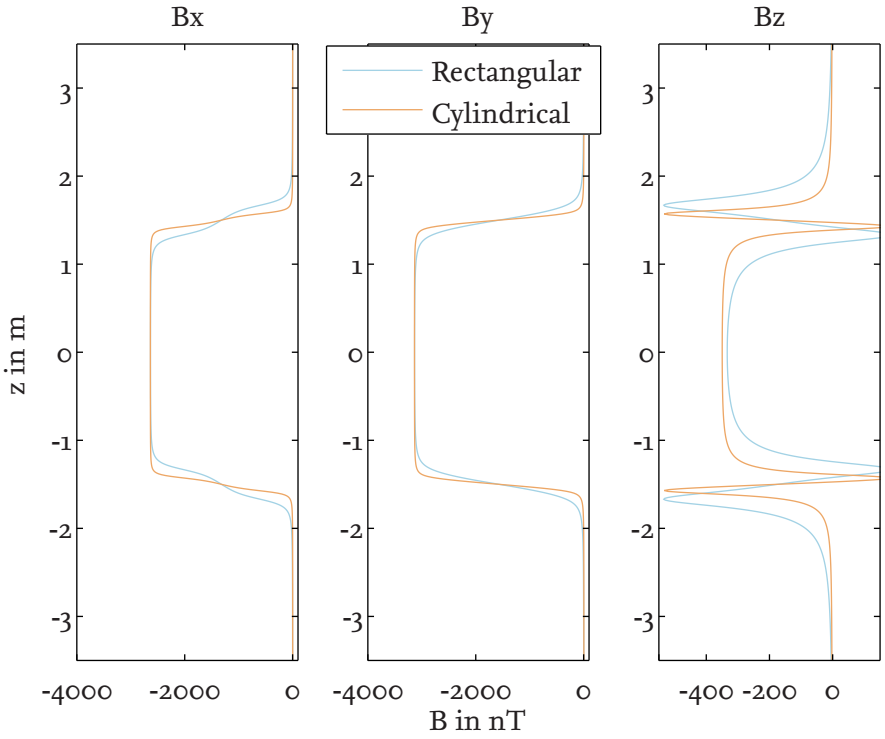

Figure 6.15.: Comparison of the magnetic field of a circular layer and borehole to a rectangular layer and borehole. Parameters are M = 9.9 A/m, I=53.9°, D=-121.0°, ϕ=180.0°, δ=65.0°, R_b = 0.04 m, R_o = 500 m. See Fig. 6.13 for a definition of the quantities used.

Figure 6.15 shows a comparison of the magnetic field of a rectangular model to a circular model for a layer with a intensity of magnetization of 9.9 A/m, declination of magnetization of 121°, inclination of magnetization of 53.9°, inclined by 65° in southerly direction (azimuth of 180°). The diameter of the borehole is 0.08 m, and the diameter of the layer is 1000 m in both cases; which means that both the area of the borehole and the area of the layer are larger for the rectangular layer than for the circular layer. In both cases, the layer has a height of 3 m.

The Figure shows that both models are basically equivalent. Only the magnetic fields at the boundary of the layer differ; here, the rectangular layer has a larger transition zone. The choice of the layer parameters was made to show an effect sometimes visible in the magnetic field, in this case in the vertical component: for some combination of parameters, the magnetic field overshoots at the boundary of the layer. As the effect is visible in two different models and can also be reproduced by numerical simulations (not shown here), it is not a result of numerical inaccuracies, but the true behaviour of the magnetic field.

In practice, the remaining differences between both models would not be distinguishable from geological noise, as a realistic borehole is neither perfectly circular nor rectangular. So if speed of computation is critical and the borehole is not believed to be perfectly circular, a rectangular layer can likely be preferred.

6.7.3. Approximation using the Bosum Model

Even though both the Gallet-Courtillot-Model and rectangular layers can be used to correctly describe inclined layers, both models have some shortcomings. The main disadvantages of the former are that solving integrals numerically is computationally expensive and that there is no obvious way to combine it with the existing inversion for horizontal layers. The rectangular layer model has a significantly improved speed of calculation; nonetheless it shares the disadvantage that it cannot be used with the horizontal layer inversion. Additionally, even though the rectangular case can be completely solved analytically, the equations are rather involved and it is hard to get an intuitive understanding.

Therefore, I developed an approximation for the magnetic field of inclined layers that is based on the Bosum model (Ehmann et al., 2015). It uses the equations of the Bosum model in combination with an *apparent magnetization* (see Section 6.5.2) that depends on the true magnetization of a layer and its geometrical properties.

We start with a layer that is inclined by an angle δ in direction of the x-axis of the coordinate system. If the layer is inclined in a different direction, i.e. has a non-zero azimuth ϕ, we first transform the magnetization from the geographic reference frame (M_N, M_E, M_V) into a corresponding local coordinate system (M_x, M_y, M_z) by means of a rotation:

$$\begin{pmatrix} M_x \\ M_y \\ M_z \end{pmatrix} = \begin{pmatrix} \cos(\phi) & \sin(\phi) & 0 \\ -\sin(\phi) & \cos(\phi) & 0 \\ 0 & 0 & 1 \end{pmatrix} \cdot \begin{pmatrix} M_N \\ M_E \\ M_V \end{pmatrix} \tag{6.25}$$

Following the Bosum model, the magnetization component perpendicular to the surfaces of borehole and layer give rise to a corresponding magnetic field component (see Fig. 6.16a). The component of magnetization perpendicular to the surface of the layer, M'_V (see Fig. 6.16b) is composed of the x and z component of the magnetization:

$$M'_V = -\sin(\delta)M_x + \cos(\delta)M_z \tag{6.26}$$

which, according to the Bosum model, gives rise to a magnetic field B'_V:

$$B'_V = -\frac{c}{2} \cdot M'_V = -\frac{c}{2}\left(-\sin(\delta)M_x + \cos(\delta)M_z\right) \tag{6.27}$$

using c as defined in Eq. 6.8. As this contribution to the magnetic field is still perpendicular to the surface of the layer (see Fig. 6.16c), it has to be transformed back into the reference frame of the layer:

$$\vec{B} = \begin{pmatrix} \cos(\delta) & 0 & -\sin(\delta) \\ 0 & 1 & 0 \\ \sin(\delta) & 0 & \cos(\delta) \end{pmatrix} \cdot \begin{pmatrix} 0 \\ 0 \\ B'_V \end{pmatrix} \tag{6.28}$$

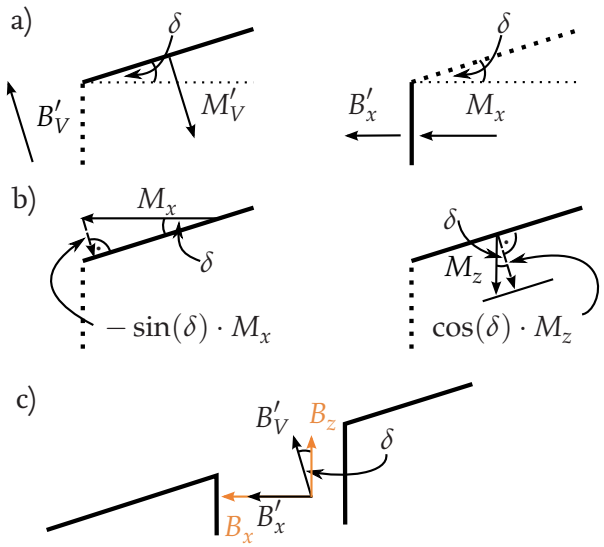

Figure 6.16.: Visual representation of the approximation for inclined layers: a) The component of magnetization perpendicular to the borehole wall, M_x, and the component of magnetization perpendicular to the borehole surface, M'_V contribute to the magnetic field. b) M'_V is composed of M_x and M_z. c) B'_x and B'_V contribute to the magnetic field components B_x and B_V. (modified from Ehmann et al. (2015))

Additionally, both M_x and M_y contribute to the magnetic field caused by the borehole wall:

$$\vec{B}_{x,y} = \frac{c}{4}\vec{M}_{x,y} \tag{6.29}$$

As the inclined upper surface of the layer also contributes to B_x (see Eq. 6.28), the contribution of M_x to B_x is denoted as B'_x in Fig. 6.16. In total, this results in a magnetic field on the axis of the borehole given by:

$$\begin{aligned}\vec{B} &= \begin{pmatrix} \frac{c}{4}M_x - \frac{c}{2}M_x \cdot \sin^2(\delta) + \frac{c}{2}M_z \sin(\delta)\cos(\delta) \\ \frac{c}{4}M_y \\ -\frac{c}{2}M_z \cdot \cos^2(\delta) + \frac{c}{2}M_x \sin(\delta)\cos(\delta) \end{pmatrix} \\ &= \begin{pmatrix} \frac{c}{4}M_x \cos(2\delta) + \frac{c}{4}M_z \sin(2\delta) \\ \frac{c}{4}M_y \\ -\frac{c}{2}M_z \cdot \cos^2(\delta) + \frac{c}{2}M_x \sin(\delta)\cos(\delta) \end{pmatrix}\end{aligned} \tag{6.30}$$

Comparing Eq. 6.30 to Eq. 6.6 and Eq. 6.8, we now define an *apparent magnetization* $\vec{M}_a$:

$$\begin{aligned}\vec{M}_a &= \begin{pmatrix} \frac{4}{c}\cdot B_x \\ \frac{4}{c}\cdot B_y \\ -\frac{2}{c}\cdot B_z \end{pmatrix} \\ &= \begin{pmatrix} M_x\cos(2\delta) + M_z\sin(2\delta) \\ M_y \\ M_z\cos^2\delta - M_x\sin\delta\cos\delta \end{pmatrix}\end{aligned} \tag{6.31}$$

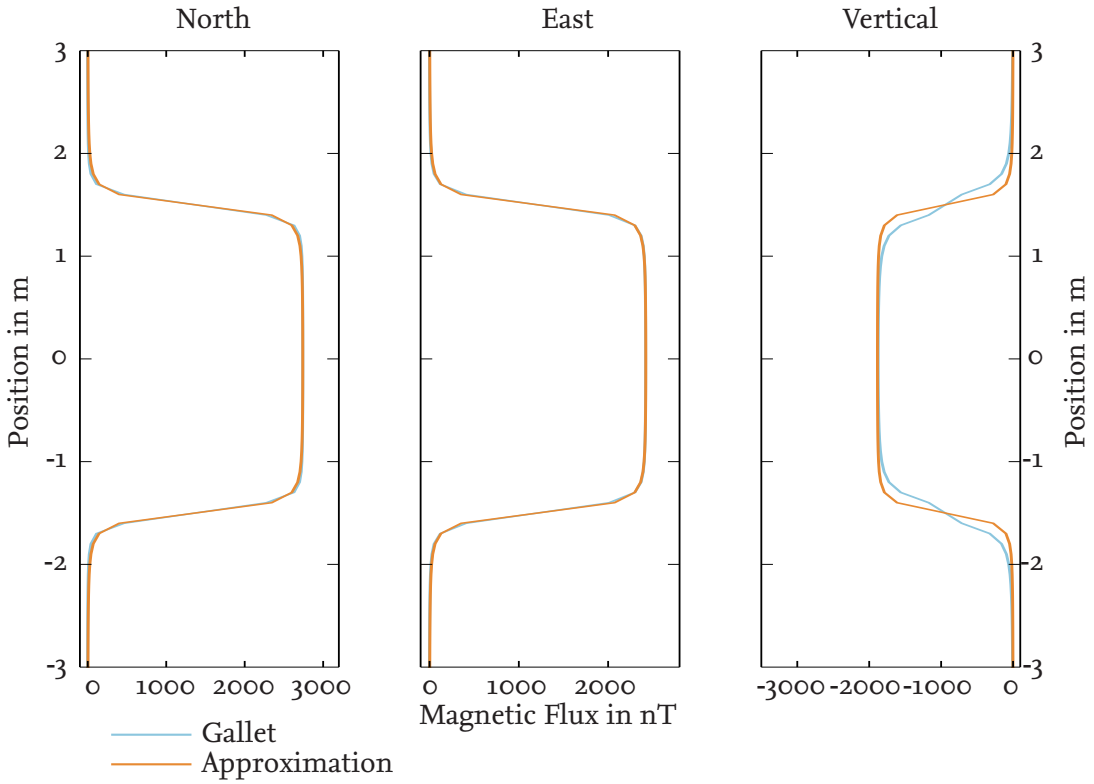

Figure 6.17.: Comparison of the approximation based on the Bosum model to an exact calculation using the Gallet-Courtillot model. Modified from Ehmann et al. (2015)

I am calling it apparent magnetization, as it is the magnetization an inclined layer appears to have when it is interpreted using a horizontal layer model. It can be used in conjunction with the regular Bosum model (Eq. 6.6 and Eq. 6.8) to approximate the magnetic field of inclined layers.

The approximation has significant advantages: Besides being of a much simpler form than the other models, it allows to separate the inversion for the apparent magnetization from the interpretation with different layer geometries. A disadvantage is that it can only be used to calculate the magnetic field on the axis of the borehole, so it cannot be used to, for example, assess the influence of decentralizations of the tool in the borehole. However, this is not a significant limitation, as we do neither know the exact geometry of the borehole nor the exact position of the tool relative to the borehole walls, so we always assume a centered tool anyway.

Figure 6.17 shows a comparison of the approximation to an exact calculation using the Gallet-Courtillot model for a layer with a total magnetization of 6.16 $^{A}/_{m}$, an inclination of magnetization of 54.2°, declination of magnetization of 56.3°, dip of 40° and azimuth of 20°. Differences mostly occur at the edges of a layer and are dependent on the geometry of both borehole and layer. For cases as shown in Fig. 6.15, the approximation is not reproducing the edge effects. But as realistic layers are likely to exhibit no sharp boundaries but to have

uneven surfaces – which might be, as in the case of intrusions, reheated and remagnetized – this does not limit the applicability of the approximation, as the edge effects are either not visible in an actual measurement or indistinguishable from variations in the geometry or magnetization of a layer.

6.7.4. Potential Ambiguities in the Determination of the Direction of Magnetization

In theory, for a noise free measurement of ideal data, three component magnetic field data are sufficient to resolve both dip and azimuth of a layer, as well as the vector of magnetization. However, in a realistic measurement, this is not going to be the case as subtle differences between models, as the edge effects mentioned in Section 6.7.2, are going to be indistinguishable from other effects. Therefore, it is no significant disadvantage that my approximation does not reproduce these differences. On the contrary, the approximation is ideal to study potential ambiguities of magnetic field measurements in inclined layers as it can be used to quickly search the parameter space.

At first, I am going to use the approximation to illustrate the influence of layer dip and azimuth on the apparent inclination. The left panel of Fig. 6.18 (Ehmann et al., 2015) shows the apparent inclination of layer with a true inclination of magnetization of -68°, the expected current day inclination of the Louisville Hotspot (Koppers et al., 2012), and a declination of 0°, in dependence of its dip and azimuth. The middle panel shows the apparent inclination for a layer with the same inclination of magnetization, but a declination of 40°. The right panel shows a layer with a inclination of magnetization of 30° and a declination of 0°. Grey contours denote the regions where the apparent inclination is within ± 5° of the true inclination. Listing A.3 in Appendix A.6 gives the Matlab code used to generate the Figure.

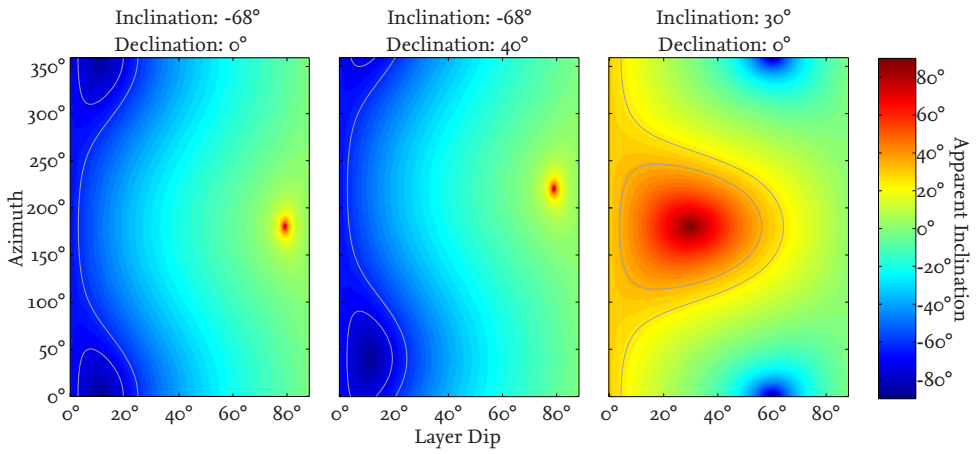

Figure 6.18.: Apparent inclination of a layer for different combinations of true inclination and declination of magnetization. Grey contours denote the regions where the apparent inclination is within ± 5° of the true inclination. Left panel modified from Ehmann et al. (2015).

For zero dip, the apparent inclination matches the true inclination of the layer. For a non-zero dip, the apparent inclination becomes dependent on the azimuth and therefore also on the declination of magnetization. A comparison of the left and middle panel shows that the axis of symmetry of the figure is shifted along the azimuth axis by the value of the declination.

Depending on the true inclination, declination and azimuth, there can be regions where the apparent inclination still corresponds to the true inclination even for high dips. For example, in the right panel, for layer dip of 60° and an azimuth of 184°, the apparent inclination is 30°. But in general, already layer dips of 3° to 4° cause the apparent inclination to differ by more than 5° from the true inclination. Small dips like this are likely to occur in reality, especially as the borehole itself might be inclined. Figure 6.18 also shows that, depending on the parameters of the layer, all apparent inclinations are possible, regardless of the sign of the true inclination. In the left and middle panel, there is only a small region of parameter values that allow for a high positive inclination (dip of 79°; azimuth of 180°, respectively 220°). In the right panel, a high positive apparent inclination of 90° is already possible for a dip of 30°; a high negative apparent inclination of -90° can occur at a dip of 60°. As high layer dips can easily occur in magmatic intrusions, which are most likely prevalent in the data of Expedition 330, this apparent inclination effect has to be considered in the interpretation of the data to avoid potentially large errors.

Another important result is shown in Fig. 6.19. The example shows which parameter combinations reproduce the apparent magnetization of two different layers. Figure 6.19a (Ehmann et al., 2015) shows the equivalent parameters for a layer with an inclination of -68°, a declination and azimuth of 0° and a dip of 15°, Fig. 6.19b shows the equivalent parameters for a layer with an inclination of 40°, a declination of 40°, an azimuth of 0° and a dip of 15°. The images have been generated by calculating the apparent magnetization for a broad range of dips, azimuths and declinations, keeping only the inclination of magnetization fixed. Shown are all combinations that, within some tolerance, give the same apparent magnetization as the original layer. Accepting a small tolerance simplifies the brute-force calculations, as the number of parameter combinations for which the apparent magnetization is calculated can be reduced (Ehmann et al., 2015).

For example, as can be seen in Fig. 6.19a, a layer with a tilt of 11°, a declination of 90° and an azimuth of 69.6°, will result in the same magnetic field as the initial set of parameters. This might seem counter-intuitive, as the initial magnetization has no east component, whereas the magnetization of the equivalent layer has no north component. What one has to keep in mind is that the origin of the apparent magnetization is the magnetic field and that the vertical component of the magnetization can, depending on layer tilt and azimuth, cause a contribution to the magnetic field in any direction in the horizontal plane. This projected magnetic field component interacts with and sometimes cancels out the contributions of the horizontal components of magnetization to the magnetic field.

This means that in general it is not possible to resolve the direction of magnetization without knowledge of the dip and azimuth of a layer. Especially declination and azimuth are

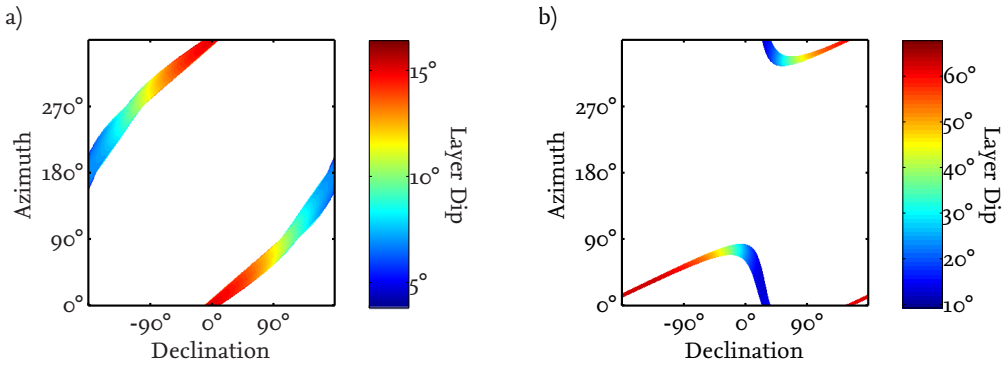

Figure 6.19.: Layer parameters that give the same apparent magnetization like a layer with a) an inclination of -68°, a declination and azimuth of 0° and a dip of 15° (adapted from Ehmann et al., 2015) and b) an inclination of 40°, a declination of 40°, an azimuth of 0° and a dip of 15°.

strongly coupled; for an initial error estimate one can assume at least a linear dependence of the error in the determination of the declination on the error in determination of the azimuth of a layer. For a specific layer, a more realistic error estimate can be made by recalculating Fig. 6.19 with an appropriate set of parameters.

Figure 6.19b shows that not all azimuths have to be possible; and a comparison of Fig. 6.19a and Fig. 6.19b shows that the range of possible dips highly depends on the layer parameters, mainly the inclination of magnetization. This can be used to assess the validity of measurements: if, for example, a measured apparent inclination would require an unlikely high layer dip, then it could be that either the initially assumed true inclination of magnetization is wrong, that there might be uncorrected offsets in the magnetic field or that a layered model is insufficient to explain the data.

6.7.5. Maximum Influence of the Induced Magnetization

As discussed in Section 6.4, I am neglecting the influence of the induced magnetization, as it is in general much lower than the remanent magnetization. In order to motivate this decision, we can use the approximation to quickly estimate the influence of the induced magnetization on the magnetic field (see Ehmann et al., 2015). Even though the induced magnetization can be easily calculated from the susceptibility measured on drill core samples and the background magnetic field, the influence of the induced magnetization on the measured magnetic field is more complex, as it depends on the structure of the subsurface.

Assuming that the azimuth ϕ of a layer is zero, i.e. that the layer is inclined by δ in direction of geographic north, and further assuming that the declination of magnetization equals zero as well, using Eq. 6.31, the apparent magnetization of the layer is given by:

$$\vec{M}_a = \begin{pmatrix} M\cos(I)\cos(2\delta) + M\sin(I)\sin(2\delta) \\ 0 \\ M\sin(I)\cos^2\delta - M\cos(I)\sin\delta\cos\delta \end{pmatrix} \tag{6.32}$$

Table 6.1.: Maximum Induced Apparent Magnetization[a]

	M_{max}	δ_{max}	ϕ_{max}	M_{min}	δ_{min}	ϕ_{min}
North	M_i[b]	29.8°	159.6°	$-M_i$	62.8°	5.9°
East	M_i	51.3°	304.0°	$-M_i$	57.9°	64.1°
Vertical	$0.1M_i$	72.0°	196.0°	$-0.9M_i$	16.0°	20.0°

[a] List of layer parameters that lead to a maximum induced apparent magnetization for an inducing magnetic field with inclination of -54° and declination of 16°.

[b] $M_i = \chi \cdot {}^{B_0}/_{\mu_0}$ is the total induced magnetization of a layer with magnetic susceptibility χ in a background field B_0.

Adapted from Ehmann et al. (2015).

where M is the total magnetization of the layer and I is the inclination of magnetization. In order to derive the maximum and minimum possible induced apparent magnetization, we calculate the derivatives of M_a^x and M_a^z with respect to δ (Ehmann et al., 2015):

$$\begin{aligned} \max(M_a^x) &= M, \qquad \text{for } \delta = \frac{1}{2}I \\ \min(M_a^x) &= -M, \quad \text{for } \delta = \begin{cases} \frac{1}{2}(I-\pi), & \text{if } I > 0 \\ \frac{1}{2}(I+\pi), & \text{if } I < 0 \end{cases} \end{aligned} \tag{6.33}$$

$$\begin{aligned} \max(M_a^z) &= \frac{1}{2}M(\sin(I)-1), \quad \text{for } \delta = \frac{1}{2}(I+\frac{\pi}{2}) \\ \min(M_a^z) &= \frac{1}{2}M(\sin(I)+1), \quad \text{for } \delta = \frac{1}{2}(I-\frac{\pi}{2}) \end{aligned} \tag{6.34}$$

This means that the maximum and minimum apparent magnetization cannot exceed the magnetization of the layer in any component of the magnetic field, a result which can be generalized to layers of arbitrary azimuth and declination of magnetization. As it is difficult to find a closed form solution similar to Eq. 6.33 and Eq. 6.34 for the general case of arbitrary azimuth and declination, it is easier in practice to do a brute force calculation of the apparent magnetization for a large parameter space. Table 6.1 (Ehmann et al., 2015) shows which values for δ and ϕ give the maximum and minimum induced apparent magnetization, assuming an inclination of the background magnetic field of -54° and a declination of magnetization of 16°, which are the values of the background field assumed to be present at Site U1376 (see Section 6.3). Assuming the worst case scenario for each component of the magnetic field, we can now calculate the maximum possible contribution of the induced magnetization. The results are shown in Fig. 6.20 (Ehmann et al., 2015): the minimum possible induced magnetic field is shown in green, the maximum possible field is shown in red. Black lines show the induced magnetic field if the drilled layers were horizontal. Note that due to the negative sign in a_z in Eq. 6.7, the maximum magnetic field values for the vertical component are associated with the minimum value of the apparent magnetization and vice versa.

At large, the magnetic field due to the induced magnetization is within the range of differences between the downlog and uplog of the magnetic field; thus the induced magnetization can safely be neglected. The same is true for the data of Site U1374 (not shown here): though the influence of the induced magnetization is slightly higher, the remanent magnetization is also higher in general.

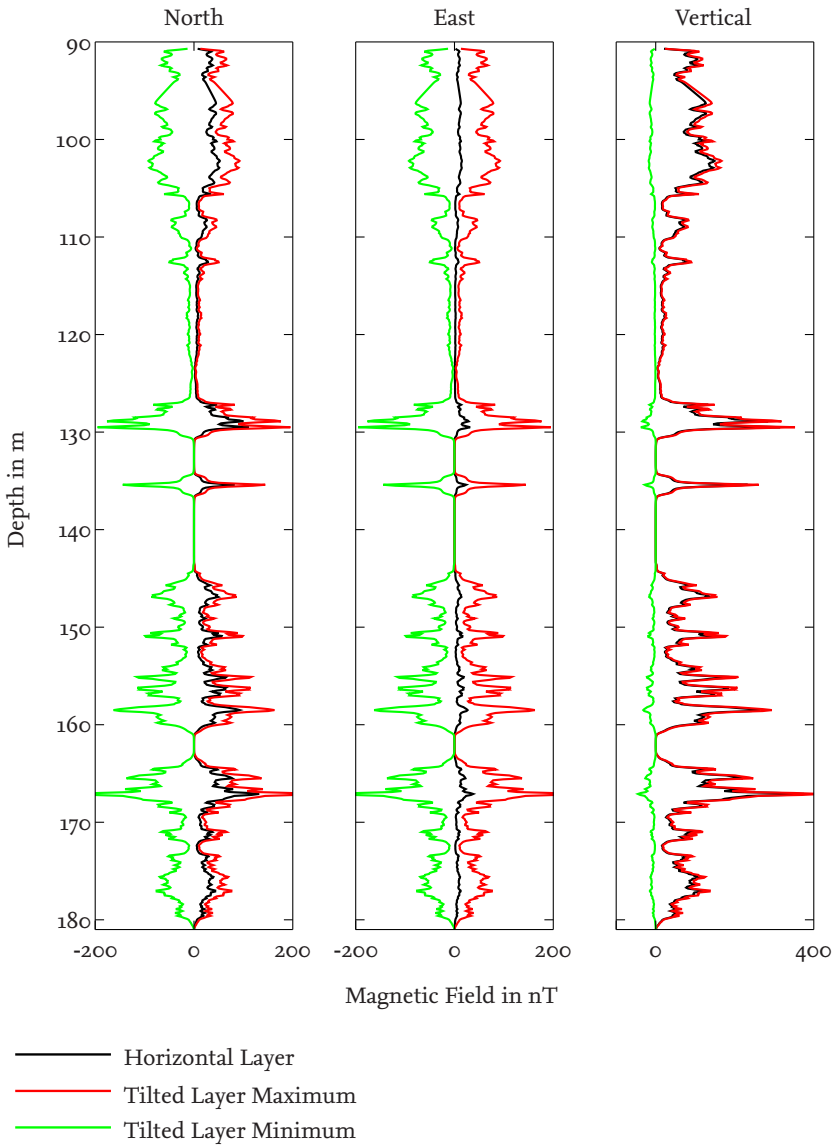

Figure 6.20.: Estimate of the maximum contribution of the induced magnetization on the measured magnetic field for Site U1376. Green lines show the minimal magnetic field possible for tilted layers, red lines the maximum possible values, calculated using the values given in Table 1. For comparison, the magnetic field for the case of horizontal layers is shown in black. Adapted from Ehmann et al. (2015)

6.7.6. Inclined Layers: Site U1374

In order to test whether inclined layers can be used to model the magnetic field data, we can use the inclined layer approximation to determine whether the natural remanent magnetization measured on drill core samples can be brought into agreement with the measured apparent magnetization derived from the GBM data (see Ehmann et al., 2015).

To do so, we first make a brute-force calculation of the apparent magnetization produced by a layer with a true magnetization as given by the drill core samples (which only give us a horizontal and a vertical magnetization) for the full range of possible dips (0° to 90°), declinations and azimuths (0° to 360°) in steps of 3°. The result which gives the minimum difference between the measured apparent magnetization and the thus calculated apparent magnetization is then refined in a second step using a least-squares optimization algorithm.

For the whole procedure, the datasets are interpolated to a fixed depth step of 0.1 m and each datapoint is treated as an individual layer. Thus, the resulting set of layer parameters does not necessarily have to be geometrically plausible; i.e. neighbouring layers are allowed to intersect. The reason for not introducing geometric constraints lies within the ambiguity of the magnetic field of inclined layers: as shown in Section 6.7.4, there are several sets of parameters that can give the same apparent inclination. As it is not possible to distinguish between the different solutions without additional information, limiting the procedure to geological sensible sets of layers might give a result that looks more plausible, but is in no way more correct.

Figure 6.21 compares the optimal calculated apparent magnetization to the measured apparent magnetization for the data of Site U1374 (Ehmann et al., 2015). The calculated apparent magnetization is lower than the measured apparent magnetization, which might be a result of the demagnetization treatment of the core samples which lowers the remanent magnetization (see Section 6.4). The linear trend which is visible in the magnetic field data of site U1374 and thus is also present in the measured apparent magnetization is not visible in the drill core data and can also not be reproduced by the calculated apparent magnetization. The offset in the magnetic field in the section between 365 m and 470 m can also not be reproduced. These magnetic field structures might be caused by larger off-borehole bodies or could mean that the lithologic units intersected by the borehole are embedded in larger geological structures and that the assumption of infinite layers is not justified (Ehmann et al., 2015).

Another method to check the whether an inclined layer model can be used to assess the data is to determine which layer dips would be necessary to explain the measured magnetic field under the assumption of a given inclination of magnetization (see Section 6.7.4 and Ehmann et al., 2015).

Figure 6.22 (Ehmann et al., 2015) shows the range of layer dips that are possible if the inclination of magnetization is assumed to be -64.9°, which is the expected stable inclination determined from measurements on core samples (Koppers et al., 2012). For the calculations, each layer is again treated individually and a brute-fore calculation of the apparent inclination is conducted for the whole range of dips and azimuths. Here, if

the calculated apparent inclination and the measured apparent inclination are within a tolerance of 3°, a solution is is accepted and contributes to the dip interval.

In the Figure, dashed lines show the corresponding dip range for an assumed reversed inclination of +64.9°. A moving average with a 1.8 m window has been applied to the dip data. Other data that are shown are dips of potential layer boundaries from FMS images, dips of chilled contacts and margins as well as of magmatic foliations identified in core samples (Expedition 330 Scientists, 2012d). For orientation, the total apparent magnetization as well as the lithology (see also Fig. 6.2) of the borehole are shown in the upper panel.

Chilled contacts and margins should give the most accurate information about the true dip of a layer; magmatic foliations are often in parallel to the flow direction of the magma and thus can be a proxy for the dip. FMS images have the advantage that they do not depend on the recovery of a drill core and can give information where no core samples are available, but are sometimes hard to interpret (Ehmann et al., 2015).

In general, the necessary dips are high (≈30°) but still plausible for the negative inclination, and are implausibly high for the positive inclination, which means that a reversal would be identifiable. For the most likely correct negative inclination, most implausibly high dips are in regions of low magnetization, which are less reliable as they are more influenced by errors in orientation and the choice of the background field.

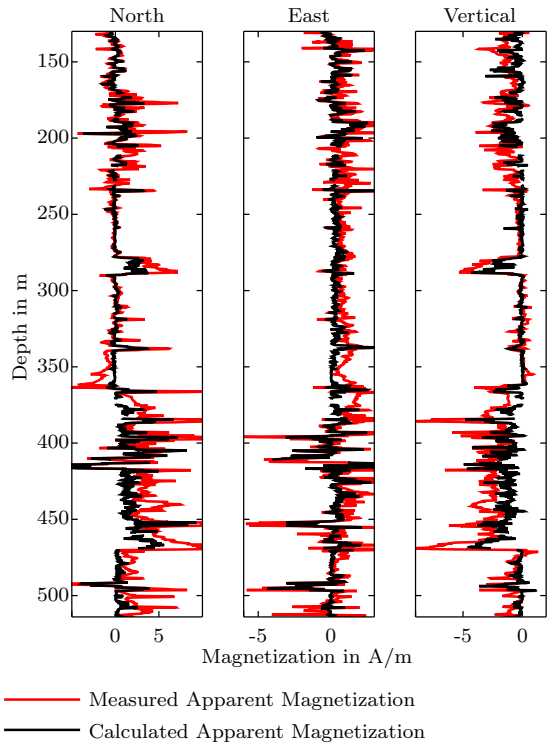

Figure 6.21.: U1374: Comparison of the best fit calculated apparent magnetization (derived from NRM data) assuming inclined layers to the measured apparent magnetization. Adapted from Ehmann et al. (2015).

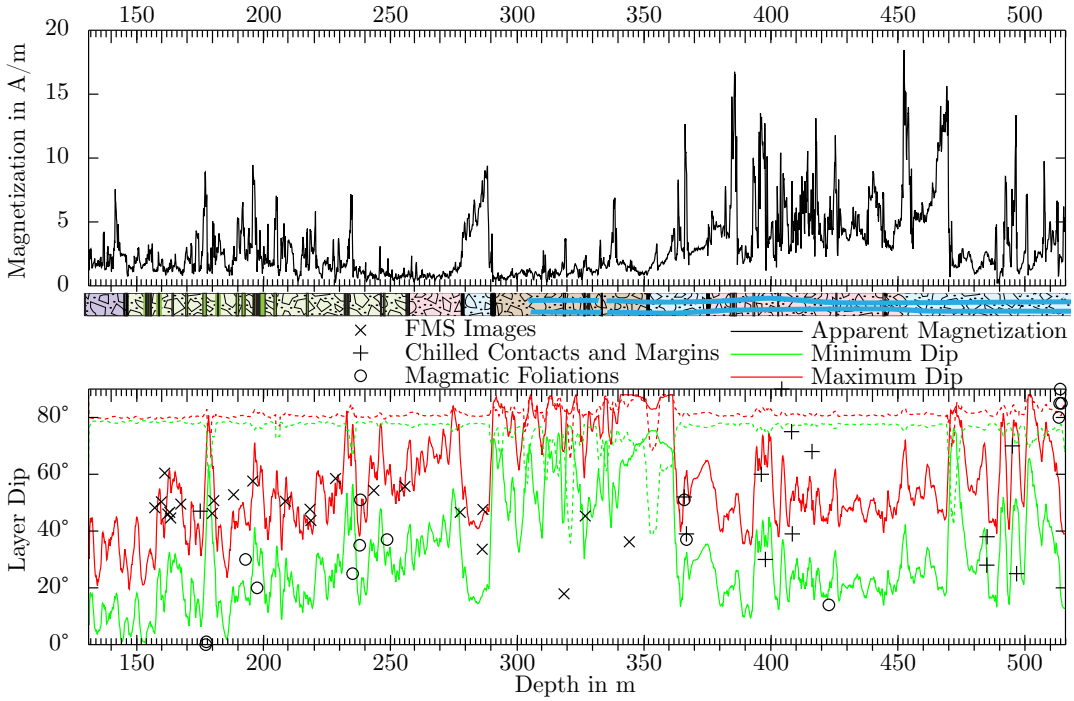

Figure 6.22.: (top) The absolute value of the apparent magnetization for Site U1374 as well as the lithology (Expedition 330 Scientists (2011), modified. See Fig. 6.2 for details). (bottom) The possible range for layer dips. Solid lines are calculated assuming an inclination of magnetization of -64.9° and a maximum error of 3° in apparent inclination. Dashed lines are calculated assuming a reversed inclination of magnetization of +64.9°. Also shown are dips of potential layer boundaries picked from FMS images (crosses), dips measured on drill core samples of chilled contacts and margins (plus symbols), and of magmatic foliations (open circles). Adapted from Ehmann et al. (2015).

6.7.7. Inclined Layers: Site U1376

Figure 6.23 shows the best-fit calculated apparent magnetization (using drill core data) and the measured apparent magnetization for Site U1376. Both datasets can be brought into agreement, which is a sign that a model using inclined layers can be used to determine the direction of magnetization of the drilled rocks.

To further assess the validity of the layered model, Fig. 6.24 (Ehmann et al., 2015) shows in which range the dips of layers would need to lie if the measured apparent magnetization was to be explained by inclined layers with a true inclination of magnetization of +68.3° (the expected stable inclination determined from measurements on core samples, Koppers et al., 2012), with an accepted tolerance of $\pm$ 3° in the apparent inclinations. A moving average with a 0.6 m window has been applied to the dip data. Again, the absolute value of the apparent magnetization and the lithology are shown for orientation (refer to Fig. 6.3 for details of the lithology), and additional information about possible dips is given from FMS images and from dips measured on drill core samples of chilled contacts and margins (Expedition 330 Scientists, 2012f).

For the intervals with reasonably strong magnetization, the calculations give sensible ranges for the dip. The flow units at depths of 130 m and 145 m are likely to be strongly dipping intrusive sheets. In general, the dip range given by the horizontal layer approximation and the dips given by the other data sources agree, but are highly variable (Ehmann et al., 2015).

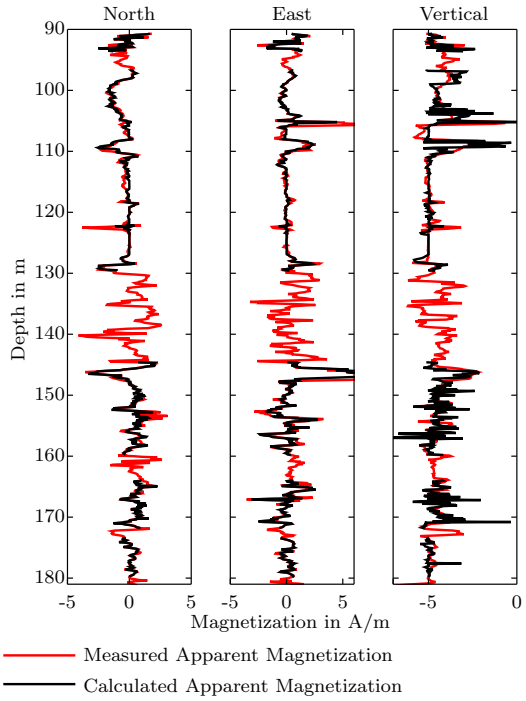

Figure 6.23.: U1376: Comparison of the best fit calculated apparent magnetization (derived from NRM data) assuming inclined layers to the measured apparent magnetization. Adapted from Ehmann et al. (2015).

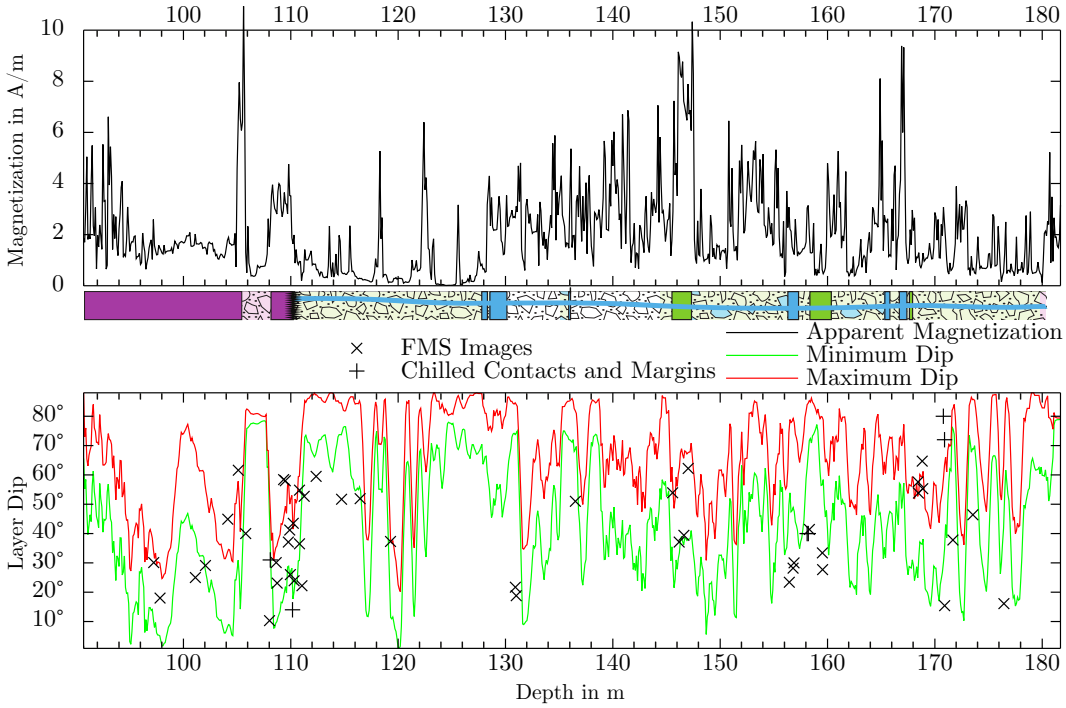

Figure 6.24.: (top) The absolute value of the apparent magnetization for Site U1376 as well as the lithology (Expedition 330 Scientists (2011), modified. See Fig. 6.3 for details). (bottom) The possible range for layer dips calculated assuming an inclination of magnetization of +68.3° and a maximum error of 3° in apparent inclination. Also shown are dips of potential layer boundaries picked from FMS images (crosses), dips measured on drill core samples of chilled contacts and margins (plus symbols), and of magmatic foliations (open circles). Adapted from Ehmann et al. (2015).

6.7.8. Interpretation of a Single Layer

As the data of Site U1376 suggest that it is better suited for an interpretation using inclined layers than the data of Site U1374, I chose a layer at a depth of 146 m for an exemplary detailed interpretation (Ehmann et al., 2015). The layer is both prominently visible in the magnetic field data and the natural remanent magnetization data; additionally, the potential layer dips determined from FMS images are in the range estimated using the inclined layer approximation (see Fig. 6.24).

According to the FMS images, the upper boundary of the layer has a dip of 53.9° (53.0° using the second caliper measurement) and an azimuth of 168.9°, the lower boundary has a dip of 62.2° (60.8°) and an azimuth of 90.9°. Especially the large spread of the azimuth is detrimental for the results, as this causes a comparable uncertainty in the declination of magnetization. For the following interpretation, I use an average dip of 60° and an azimuth of 130° (Ehmann et al., 2015).

Figure 6.25 shows the result of the modeling. Black lines show the magnetic anomaly after subtraction of the background field. Green lines show the magnetic field model. After

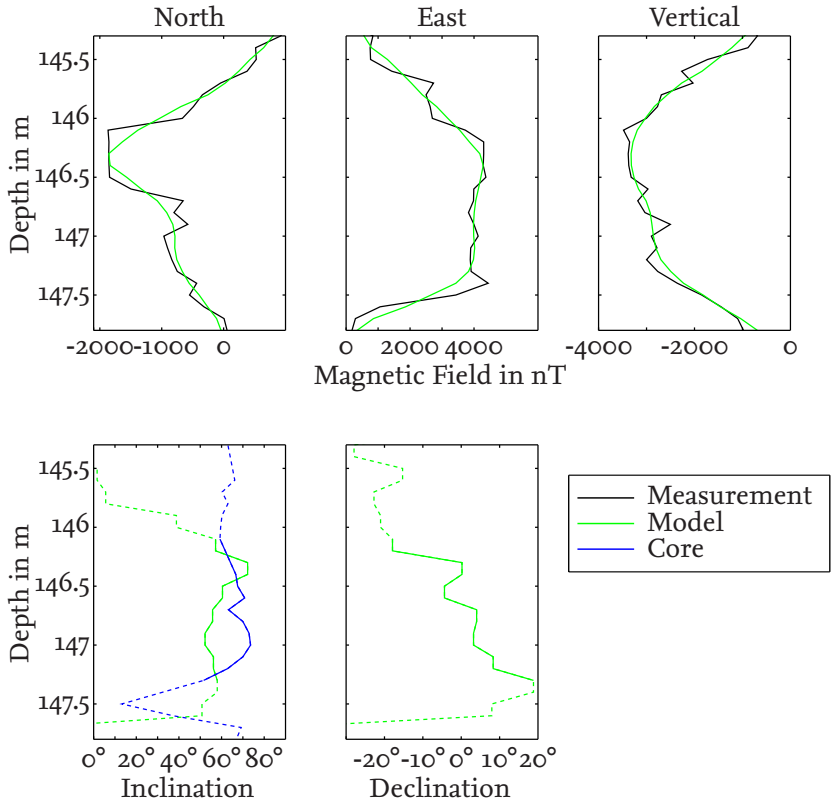

Figure 6.25.: Detailed interpretation of a layer from Site U1376. (top) The magnetic field anomaly in the geographic reference frame (black lines) and the magnetic field model used for further interpretation (green lines). (bottom left) A comparison of the inclination of magnetization calculated from the model, assuming a dip of 60° and an azimuth of 130°, to the inclination of magnetization of core samples. (bottom right) The calculated declination of magnetization. Modified from Ehmann et al. (2015).)

conducting a horizontal layer inversion and averaging the magnetization over intervals of 0.2 m, the inclined layer approximation was used to invert for declination and inclination of magnetization.

The model gives an average inclination of 58.9° (±6.4°) and an average declination of 0.4° (±10.1°). Here, only the data in the interval between 146.1 m and 147.3 m are used to calculate the average values in order to avoid the influence of neighbouring layers on the results. Including the induced magnetization in the model would change the mean inclination to 59.7° (±6.2°) and the mean declination to 0.2° (±10.1°), which again shows that the induced magnetization can be safely neglected (see Section 6.4).

The result agrees well with the mean inclination of the undemagnetized core samples in the same interval, which is 65.7° (±6.2°). It is also compatible with existing ideas of a predominantly stationary Louisville Hotspot (Koppers et al., 2012); in addition, a declination of 0° suggests that Site U1376 has not been rotated since its formation (Ehmann et al., 2015).

However, we have to consider both the relatively large statistical variations in the results as well as the additional error given by our limited knowledge about the azimuth of the layer. A more reliable result could be obtained by an interpretation of multiple layers or if additional constraints could be put on the layer geometry.

6.8. Comparison of Unoriented and Oriented Measurements of the Magnetic Field

So far, I have focussed on the interpretation of oriented magnetic field data and used drill core data mostly for comparison. In the following I am going to demonstrate that, given sufficient information about the geometry and magnetization of a drilled layer, some information about possible values for the declination of magnetization can also be derived from unoriented measurements of the magnetic field. In order to do so, I am assuming a knowledge of the dip and azimuth of a layer, as well as of the horizontal and vertical magnetization M_h and M_v, derived from borehole images and drillcore measurements. I also assume that the background magnetic field is known and therefore the declination of magnetization is the only free parameter left.

Figure 6.26 shows the magnetic field anomaly in all three components, as well as the horizontal and total field anomaly at the center of a layer with a dip δ of 20°, azimuth Φ of 0°, a vertical magnetization M_z of -1 A/m and a horizontal magnetization M_h of 2 A/m in a background field $\vec{B}_0$ of 10000 nT north, 5000 nT east and 30000 nT vertical for different values of the declination of magnetization. The anomalies were calculated using the approximation for the magnetic field of an inclined layer.

If, for example, we assume that the true declination of the magnetization is 19.5°, we would measure the magnetic field anomalies marked by circles. In an ideal measurement, there would only be two values for the declination that give the same values for the magnetic field anomalies on each of the black curves and therefore the true value of the declination could be determined by a joint interpretation of measurements of different components. In a real measurement, however, we only know the layer parameters with some uncertainties: the gray area denotes the error range for the magnetic field, if an error of $\pm$5° is assumed for dip and azimuth and an error of $\pm$0.1 A/m is assumed for the vertical and horizontal magnetization.

These uncertainties in the layer parameters cause that we now get an interval of possible declinations for each curve (marked in orange). Depending on which kind of measurements is conducted, we can take the intersecting set of the different declination intervals to obtain a combined solution. If we conduct oriented magnetic field measurements, that is if we measure ΔB_N, ΔB_E and ΔB_V, we get a small set of possible values between 15° and 25°, mostly due to the small interval of possible declinations in ΔB_E.

However, if we only measure the total field anomaly ΔB (see Section 2.4.1 for a definition and discussion), the declination can only be limited to the interval between 336° and 45.5°. If we additionally have separate measurements of the horizontal and vertical field anomalies, ΔB_H and ΔB_V, the situation is a bit better: combining all information, possible

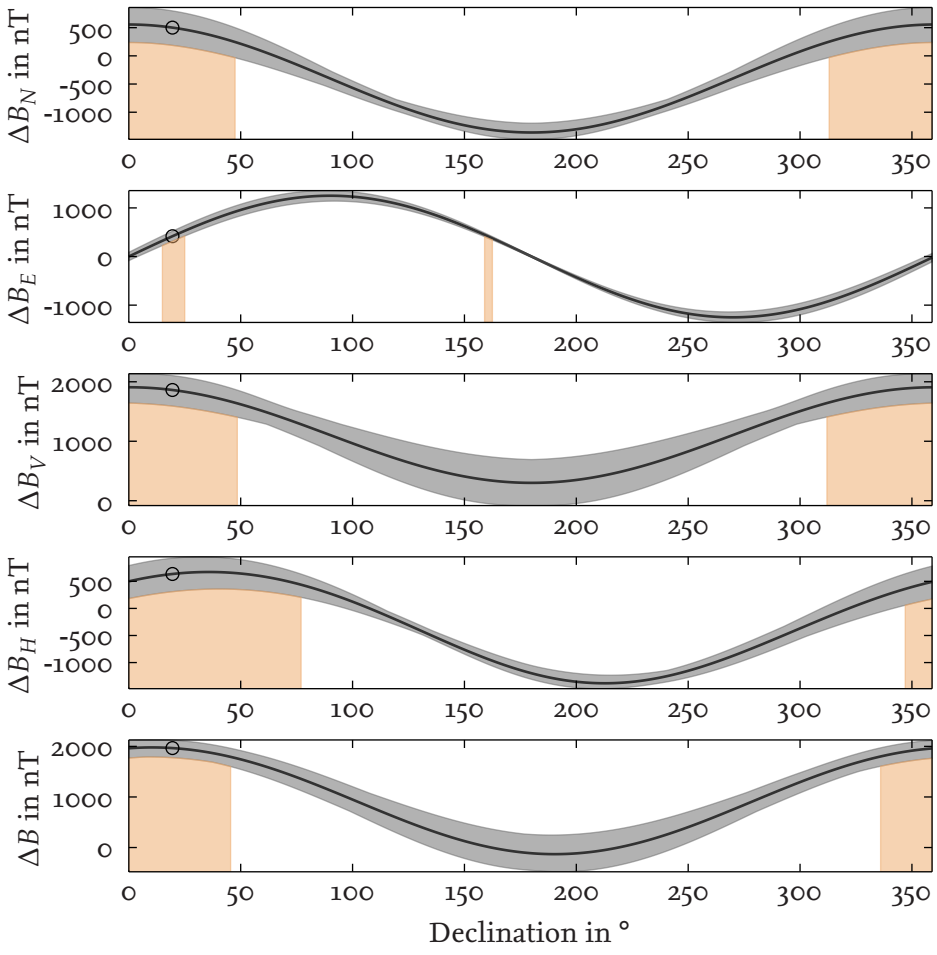

Figure 6.26.: The anomaly at the center of a layer with a dip of 20°, azimuth of 0°, a vertical magnetization of -1 A/m and a horizontal magnetization of 2 A/m, in a background field of 10000 nT north, 5000 nT east and 30000 nT vertical, for different values of the declination of magnetization. Given is the magnetic field anomaly for all three components as well as the horizontal and total anomaly. The gray area denotes the error range for the magnetic field if an error of ±5° is assumed for dip and azimuth and an error of ±0.1 A/m is assumed for the vertical and horizontal magnetization. The orange area denotes the possible intervals for the declination, assuming aforementioned errors and that the true declination of magnetization is 19.5° (marked by circles)

declinations lie between 347° and 45.5°, which is still an uncertainty of 58.5°. This means that even though it might be possible in theory to put limits on possible values of the declination using unoriented measurements of the magnetic field, this is severely limited in practice, unless the constraints that can be put on the geology and the magnetization are very strict or the change in declination to be detected is high.

There are also two cases where a combined measurement of horizontal and vertical anomaly does not give additional information compared to a measurement of the horizontal component alone: the trivial case is a horizontal layer, where the vertical anomaly is independent of the declination of magnetization. The second case is when maxima and minima of horizontal and vertical anomaly are at the same declination of magnetization. Assuming a layer with azimuth $\Phi = 0°$, the approximate horizontal anomaly, that is the projection of the horizontal field of the anomaly onto the background field (see Section 2.4.1), is given by:

$$\Delta B_h = \frac{\frac{1}{4} c B_{0_x} \cdot (M_h \cos(2\delta)\cos(D) + M_v \sin(2\delta)) + \frac{1}{4} c B_{0_y} M_h \sin(D)}{\sqrt{B_{0_x}^2 + B_{0_y}^2}} \tag{6.35}$$

Its extreme points can be found by differentiating Eq. 6.35 with respect to the declination D:

$$\begin{aligned} \frac{\partial \Delta B_h}{\partial D} &= \frac{c \cdot M_h}{4\sqrt{B_{0_x}^2 + B_{0_y}^2}} \cdot \left(B_{0_x} \cdot \cos(2\delta)(-\sin(D)) + B_{0_y} \cdot \cos(D) \right) \\ \frac{\partial \Delta B_h}{\partial D} &\stackrel{!}{=} 0 \\ \rightarrow D &= \arctan\left(\frac{B_{0_y}}{B_{0_x} \cos(2\delta)} \right) \end{aligned} \tag{6.36}$$

The same can be done for the vertical component:

$$\begin{aligned} \frac{\partial \Delta B_z}{\partial D} &= \frac{-c}{2} \sin(D) \cdot M_h \sin(\delta)\cos(\delta) \\ \frac{\partial \Delta B_z}{\partial D} &\stackrel{!}{=} 0 \\ \rightarrow D &= 0°, 180°, \ldots \end{aligned} \tag{6.37}$$

The extrema thus are at the same position if

$$\frac{B_{0_y}}{B_{0_x} \cos(2\delta)} = 0 \tag{6.38}$$

and therefore if $B_y = 0$; respectively, if we allow for a non-zero azimuth of the layer, if its azimuth corresponds to the declination of the background field and thus there is no component of the background magnetic field perpendicular to the layer. This might seem unlikely, but if we consider a real measurement with some error in the determination of the layer parameters, it is sufficient for the azimuth to be within some degrees of the

declination of the background field to cause both horizontal and vertical anomaly to give essentially the same information about the declination of magnetization.

An advantage of this kind of analysis using unoriented measurements of the magnetic field would be that it could be used to reevaluate some of the legacy datasets of ODP/IODP, but so far I was not able to identify a dataset of sufficient quality to attempt a closer investigation. Most of the high-quality total field measurements made with the Geological High-Resolution Magnetic Tool (GHMT) were run in sediments of low magnetization (see the review article of Williams, 2006), and some of the GPIT datasets that can be found in the IODP Logging Database, which comprise horizontal, vertical and total field measurements, are of mixed quality, i.e. the data from multiple runs within the same hole differ.

As only limited constraints can be put on the geometry of the layers found in Expedition 330, an evaluation of the horizontal and vertical component of the GBM data at hand also would not be productive, as the dependence of the results on the geometry of the layer is even higher than in an evaluation of fully oriented magnetic vector data.

7 Conclusion and Outlook

In this thesis, I have demonstrated the limits and possibilities of geographically oriented measurements of the magnetic field vector. By applying both newly developed and existing algorithms to the reorientation of the magnetic field data, I was able to generate high quality data sets for both drill sites of Expedition 330. Using a new approximation for the magnetic field of inclined layers, I showed that it is necessary to include additional information about the dip and azimuth of drilled layers in order to allow for an unambiguous determination of the direction of magnetization. By incorporating geometrical information from resistivity images of the borehole wall into the analysis of an igneous layer, I demonstrated that the magnetic field data recorded at Site U1376 is likely to be compatible with the existing idea of a Louisville Hotspot that is stationary within the mantle and a seamount that has not been rotated since its formation. However, there are considerable errors associated with the estimate of the direction of magnetization and it would have been preferable if more constraints could have been put on the geometry of the layer. As I could not identify layers with better agreeing upper and lower interfaces, additional layers could not be used to increase the statistical accuracy.

I also showed that if high accuracy information about the geometry and magnetization of drilled layers is available, unoriented measurements of the magnetic field could also be used to gain more information about the direction of magnetization; but this yet remains to be proven for real measured data.

Considering the reorientation of the magnetic field data, I expect that the simple implementations of the Kalman filter I presented can be further refined and are going to form the basis for any future interpretation of the magnetic field data, as they combine gyro and inclinometer data in an almost ideal way. The potential of the Kalman filter in the analysis and determination of possible calibration errors also likely can be exploited further.

Considering the analysis of downhole magnetic field measurements, the take-home message of this thesis is that the structure of drilled layers has to be taken into account, as it is otherwise likely that errors are made even in the qualitative determination of the inclination of magnetization, which affects the identification of polarity reversals, and also in the determination of the declination of magnetization, where an error in the azimuth of a layer likely leads to an error in the determination of the declination of comparable magnitude.

The models used for the calculation of magnetization in this thesis are limited to layers of constant height, and differences in the layer parameters determined from the upper and lower end of the layers are assumed to be attributable to uneven surfaces. However, some of the drilled structures might in fact be wedge-shaped and cannot be sufficiently described by constant layers. It is worth exploring this possibility in order to assess the influence of

such a shape on the magnetic field and the recovered magnetization. Ultimately, I expect similar ambiguities as in the constant layer case and a strong dependence on the assumed dips and azimuths of the layer interfaces. Possibly the only way to overcome these problems and to reduce the uncertainty in the structure of the subsurface would be the drilling of multiple holes at one drill site, which is common in sediments but much more costly and time-consuming in igneous rocks.

In order to enhance the quality of the measured data and of the reoriented data sets, I hope that it is possible to acquire funding for an improved rebuilt of the GBM. New generations of all sensors included in the GBM are available. The noise levels of the fibre optic gyros has decreased, more accurate magnetometers can be produced. A redesign would facilitate the implementation of non-volatile memory, a new data transmission unit (likely based on DSL technology) and batteries, which could significantly reduce data transmission errors and related issues. Depending on the pressure tolerance required for the housing, new sensors would enable a smaller diameter version of the GBM, which would allow for a use of the tool in a much greater number of drill holes than possible today.

Bibliography

Advanced Logic Technology. *Well CAD v5 User Manual, Document Version TK141016*, 2014. (Cited once on page 100)

A. Aharoni. *Introduction to the Theory of Ferromagnetism*. The International Series of Monographs on Physics. Oxford University Press, 2nd edition, 2001. (Cited once on page 18)

M. Allaby, editor. *A Dictionary of Earth Sciences*. Oxford University Press, 3rd edition, 2008. (Cited once on page 13)

S. Allerton and M. A. Tivey. Magnetic polarity structure of the lower crust. *Geophysical Research Letters*, 28(3): 423–426, 2001. doi: 10.1029/2000GL008493. (Cited once on page 2)

B. D. O. Anderson and J. B. Moore. *Optimal Filtering*. Prentice Hall, 1979. (Cited once on page 61)

C. G. Anderson and K. J. Logan. The history and current status of geophysical exploration at the Osborne Cu & Au deposit, Mt. Isa. *Exploration Geophysics*, 23: 1–8, 1992. doi: 10.1071/EG992001. (Cited once on page 18)

H.-U. Auster. *Kalibrierung von Fluxgate-Magnetometern mittels Relativbewegung zwischen Sensor und Magnetfeld*. PhD thesis, Institut für Geophysik und Extraterrestrische Physik, TU Braunschweig, 2000. (Cited once on page 35)

H.-U. Auster, I. Apathy, G. Berghofer, K.-H. Fornacon, A. Remizov, C. Carr, C. Güttler, G. Haerendel, P. Heinisch, D. Hercik, M. Hilchenbach, E. Kührt, W. Magnes, U. Motschmann, I. Richter, C. T. Russell, A. Przyklenk, K. Schwingenschuh, H. Sierks, and K.-H. Glassmeier. The nonmagnetic nucleus of comet 67P/Churyumov-Gerasimenko. *Science*, 349(6247), 2015. doi: 10.1126/science.aaa5102. (Cited once on page 156)

M. Beaman, W. W. Sager, G. D. Acton, L. Lanci, and J. Pares. Improved late cretaceous and early cenozoic paleomagnetic apparent polar wander path for the pacific plate. *Earth and Planetary Science Letters*, 262(1-2): 1–20, 2007. doi: 10.1016/j.epsl.2007.05.036. (Cited once on page 1)

B. Bhattacharyya. Magnetic anomalies due to prism-shaped bodies with arbitrary polarization. *Geophysics*, XXIX, No.4: 517–531, 1964. (Cited once on page 17)

R. J. Blakely. *Potential Theory in Gravity and Magnetic Applications*. Cambridge University Press, 1996. (Cited 4 times on pages 15, 16, 17, and 19)

L. Boschi, B. Fry, G. Ekström, and D. Giardini. The european upper mantle as seen by surface waves. *Surveys in Geophysics*, 30(4), 2009. doi: 10.1007/s10712-009-9066-2. (Cited once on page 1)

W. Bosum and J. H. Scott. Interpretation of magnetic logs in basalt, Hole 418A. In *Proceedings of the Ocean Drilling Program, Scientific Results*, volume 102, pages 77–95, 1988. doi: 10.2973/odp.proc.sr.102.112.1988. (Cited once on page 2)

W. Bosum, D. Eberle, and H.-J. Rehli. A gyro-oriented 3-component borehole magnetometer for mineral prospecting, with examples of its application. *Geophysical Prospecting*, 36: 933–961, 1988. (Cited 6 times on pages 2, 3, 18, 21, 88, and 141)

W. Bosum and J. Kopietz. 29. BGR magnetometer logging in Hole 395A, Leg 109. In R. Detrick, J. Honnorez, W. Bryan, and T. Juteau, editors, *Proceedings of the Ocean Drilling Program, Scientific Results*, volume 106/109, 1990. doi: 10.2973/odp.proc.sr.106109.163.1990. (Cited once on page 2)

M. Bär. Entwicklung und Implementierung eines Algorithmus zur Berechnung der gravimetrischen und magnetischen Anomalie von homogenen Körpern mit beliebiger Oberfläche. Master's thesis, Technische Universität Bergakademie Freiberg, 2012. (Cited 3 times on pages 17, 18, and 155)

R. Brown and P. Hwang. *Introduction to Random Signals and Applied Kalman Filtering*. John Wiley & Sons, 1997. (Cited once on page 60)

R. F. Butler. *Paleomagnetism: Magnetic Domains to Geologic Terranes*. Blackwell Science, 1992. (Cited 3 times on pages 12, 13, and 14)

A. Carr and P. J. Coleman. Seafloor spreading theory and the odyssey of the green turtle. *Nature*, 249: 128–130, 1974. doi: 10.1038/249128a0. (Cited once on page 1)

J. Coggon. Magnetic and gravity anomalies of polyhedra. *Geoexploration*, 14: 93–105, 1976. (Cited once on page 17)

F. Collar, P. Fenning, and C. Mora. Application of drillhole vector magnetic measurements to resolve the position of existing underground structures. *NDT&E International*, 38: 231–236, 2005. (Cited once on page 21)

V. Courtillot, A. Davaille, J. Besse, and J. Stock. Three distinct types of hotspots in the earth's mantle. *Earth and Planetary Science Letters*, 205: 295–308, 2003. doi: 10.1016/S0012-821X(02)01048-8. (Cited once on page 27)

N. de Lange. *Geoinformatik in Theorie und Praxis*. Springer, 3rd edition, 2013. (Cited once on page 8)

W. Demtröder. *Experimentalphysik 2, Elektrizität und Optik*. Springer Berlin Heidelberg, 2009. (Cited once on page 23)

R. Duncan, J. Tarduno, and D. Scholl. Leg 197 synthesis: Southward motion and geochemical variability of the Hawaiian hotspot. In R. Duncan, J. Tarduno, T. Davies, and D. Scholl, editors, *Proc. ODP, Sci. Results, 197, 1-39*, 2006. URL `http://www-odp.tamu.edu/publications/197_SR/VOLUME/SYNTH/SYNTH.PDF`. (Cited once on page 28)

S. Ehmann. Messung und Simulation der Signale metallischer Störkörper in dreikomponentiger Bohrlochmagnetik. Master's thesis, Technische Universität Braunschweig, 2010. (Cited 9 times on pages 2, 3, 20, 22, 31, 32, 42, 84, and 85)

S. Ehmann, A. Hördt, M. Leven, and C. Virgil. Paleomagnetic inclination and declination from three-component borehole magnetometer data—New insights from logging in the Louisville seamounts. *Journal of Geophysical Research - Solid Earth*, 120: 18–41, 2015. doi: 10.1002/2014JB011531. (Cited 35 times on pages 3, 28, 31, 37, 38, 76, 77, 80, 81, 82, 83, 84, 85, 86, 87, 94, 96, 97, 98, 102, 105, 106, 107, 108, 109, 110, 111, 112, 113, 114, 115, 116, 117, 118, and 144)

D. W. Emerson, D. A. Clark, and S. J. Saul. Magnetic exploration models incorporating remanence, demagnetization and anisotropy: HP 41C handheld computer algorithms. *Exploration Geophysics*, 16: 1–122, 1985. (Cited once on page 17)

R. Emmermann and J. Lauterjung. The german continental deep drilling program KTB: Overview and major results. *Journal of Geophysical Research*, 102: 18179–18201, 1997. doi: 10.1029/96JB03945. (Cited once on page 21)

Expedition 330 Scientists. Louisville seamount trail: implications for geodynamic mantle flow models and the geochemical evolution of primary hotspots. *IODP Prel. Rept., 330*, 2011. doi: 10.2204/iodp.pr.330.2011. (Cited 7 times on pages 28, 79, 80, 81, 83, 115, and 117)

Expedition 330 Scientists. Methods. In A. Koppers, T. Yamazaki, J. Geldmacher, and the Expedition 330 Scientists, editors, *Proc. IODP, 330*. Integrated Ocean Drilling Program Management International, Inc., Tokyo, 2012a. doi: 10.2204/iodp.proc.330.102.2012. (Cited 3 times on pages 13, 82, and 99)

Expedition 330 Scientists. Site U1372. In A. Koppers, T. Yamazaki, J. Geldmacher, and the Expedition 330 Scientists, editors, *Proc. IODP, 330*. Integrated Ocean Drilling Program Management International, Inc., Tokyo, 2012b. doi: 10.2204/iodp.proc.330.103.2012. (Cited once on page 29)

Expedition 330 Scientists. Site U1373. In A. Koppers, T. Yamazaki, J. Geldmacher, and the Expedition 330 Scientists, editors, *Proc. IODP, 330*. Integrated Ocean Drilling Program Management International, Inc., Tokyo, 2012c. doi: 10.2204/iodp.proc.330.104.2012. (Cited once on page 29)

Expedition 330 Scientists. Site U1374. In A. Koppers, T. Yamazaki, J. Geldmacher, and the Expedition 330 Scientists, editors, *Proc. IODP, 330*. Integrated Ocean Drilling Program Management International, Inc., Tokyo, 2012d. doi: 10.2204/iodp.proc.330.105.2012. (Cited 5 times on pages 29, 74, 82, 86, and 114)

Expedition 330 Scientists. Site U1375. In A. Koppers, T. Yamazaki, J. Geldmacher, and the Expedition 330 Scientists, editors, *Proc. IODP, 330*. Integrated Ocean Drilling Program Management International, Inc., Tokyo, 2012e. doi: 10.2204/iodp.proc.330.106.2012. (Cited once on page 30)

Expedition 330 Scientists. Site U1376. In A. Koppers, T. Yamazaki, J. Geldmacher, and the Expedition 330 Scientists, editors, *Proc. IODP, 330*. Integrated Ocean Drilling Program Management International, Inc., Tokyo, 2012f. doi: 10.2204/iodp.proc.330.107.2012. (Cited 6 times on pages 30, 76, 82, 84, 86, and 116)

Expedition 330 Scientists. Site U1377. In A. Koppers, T. Yamazaki, J. Geldmacher, and the Expedition 330 Scientists, editors, *Proc. IODP, 330*. Integrated Ocean Drilling Program Management International, Inc., Tokyo, 2012g. doi: 10.2204/iodp.proc.330.108.2012. (Cited once on page 30)

Expedition 304/305 Scientists. Site U1309. In D. Blackman, B. Ildefonse, B. John, Y. Ohara, D. Miller, C. MacLeod, and the Expedition 304/305 Scientists, editors, *Proceedings of the Integrated Ocean Drilling Program*, volume 304/305, 2006. doi: 120.2204/iodp.proc.304305.2006. (Cited once on page 3)

F. Fieberg. *Messungen mit einem neuen Drei-Achs-Bohrlochmagnetometer in der Kontinentalen Tiefbohrung (KTB)*. PhD thesis, TU Braunschweig, 1994. (Cited once on page 3)

C. C. Finlay, S. Maus, C. D. Beggan, T. N. Bondar, A. Chambodut, T. Chernova, A. Chulliat, V. P. Golovkov, B. Hamilton, M. Hamoudi, R. Holme, G. Hulot, W. Kuang, B. Langlais, V. Lesur, F. J. Lowes, H. Luhr, S. Macmillan, M. Mandea, S. McLean, C. Manoj, M. Menvielle, I. Michaelis, N. Olsen, J. Rauberg, M. Rother, T. J. Sabaka, A. Tangborn, L. Toffner-Clausen, E. Thebault, A. W. P. Thomson, I. Wardinski, Z. Wei, and T. I. Zvereva. International geomagnetic reference field: the eleventh generation. international association of geomagnetism and aeronomy, working group v-mod. *Geophysical Journal International*, 183: 1216–1230, 2010. doi: 10.1111/j.1365-246X.2010.04804.x. (Cited 5 times on pages 8, 9, 10, 11, and 85)

E. Fontana, G. J. Iturrino, and P. Tartarotti. Depth-shifting and orientation of core data using a core-log integration approach: A case study from ODP-IODP Hole 1256D. *Tectonophysics*, 494: 85–100, 2010. doi: 10.1016/j.tecto.2010.09.006. (Cited once on page 2)

A. C. Fraser-Smith. Centered and eccentric geomagnetic dipoles and their poles, 1600-1985. *Review of Geophysics*, 25(1): 1–16, February 1987. doi: 10.1029/RG025i001p00001. (Cited once on page 8)

S. W. French and B. Romanowicz. Broad plumes rooted at the base of the earth's mantle beneath major hotspots. *Nature*, (525), 2015. doi: 10.1038/nature14876. (Cited 2 times on pages 1 and 27)

P. Gaillot, F. Einaudi, J. Stoll, and M. Leven. General-purpose inclinometry modules in highly magnetized formations: are borehole wall microresistivity images properly

oriented? In R. Duncan, J. Tarduno, T. Davies, and D. Scholl, editors, *Proc. ODP, Sci. Results*, volume 197, pages 1–22, 2004. doi: 10.2973/odp.proc.sr.197.005.2004. (Cited 3 times on pages 3, 22, and 99)

P. Gaillot, T. Brewer, P. Pezard, and E.-C. Yeh. Contribution of borehole digital imagery in core-log-seismic integration. *Scientific Drilling*, 5: 50–53, September 2007. doi: 10.2204/iodp.sd.5.07.2007. (Cited once on page 99)

Y. Gallet and V. Courtillot. Modeling magnetostratigraphy in a borehole. *Geophysics*, 54: 973–983, 1989. (Cited 12 times on pages 3, 4, 18, 102, 103, 141, 142, 144, 145, 146, 147, and 148)

K. Glaßmeier, I. Richter, A. Diedrich, G. Musmann, U. Auster, U. Motschmann, A. Balogh, C. Carr, E. Cupido, A. Coates, M. Rother, K. Schwingenschuh, K. Szegö, and B. Tsurutani. RPC-MAG The fluxgate magnetometer in the ROSETTA plasma consortium. *Space Sci. Rev.*, 128: 649–670, 2007. doi: 10.1007/s11214-006-9114-x. (Cited once on page 35)

M. Grewal and A. Andrews. *Kalman Filtering: Theory and Practice Using MATLAB*. Wiley-Interscience, 2001. (Cited once on page 60)

R. Grout. JOIDES Resolution - Daily Operations Reports, Expedition 330 Louisville Seamount Trail. Technical report, 2010-2011. (Cited 2 times on pages 29 and 30)

D. Gubbins. The distinction between geomagnetic excursions and reversals. *Geophys. J. Int.*, 137(1): F1–F4, April 1999. doi: 10.1046/j.1365-246x.1999.00810.x. (Cited once on page 8)

D. Gubbins and E. Herrero-Bervera, editors. *Encyclopedia of Geomagnetism and Paleomagnetism*. Encyclopedia of Earth Sciences Series. Springer, 2007. (Cited 7 times on pages 1, 2, 7, 8, 9, 12, and 14)

D. Gubbins, D. Alfè, C. Davies, and M. Pozzo. On core convection and the geodynamo: Effects of high electrical and thermal conductivity. *Physics of the Earth and Planetary Interiors*, 2015. doi: 10.1016/j.pepi.2015.04.002. (Cited once on page 8)

D. Guptasarma and B. Singh. New scheme for computing the magnetic field resulting from a uniformly magnetized arbitrary polyhedron. *Geophysics*, 64: 70–74, 1999. (Cited 3 times on pages 17, 153, and 154)

Y. Hamano and H. Kinoshita. Magnetization of the oceanic crust inferred from magnetic logging in Hole 395a. In R. Detrick, J. Honnorez, W. Bryan, and T. Juteau, editors, *Proceedings of the Ocean Drilling Program, Scientific Results*, volume 106/109, pages 223–229, 1990. doi: 10.2973/odp.proc.sr.106109.149.1990. (Cited 3 times on pages 2, 3, and 103)

J. R. Heirtzler, J. H. Allen, and D. C. Wilkinson. Ever-present South Atlantic Anomaly damages spacecraft. *EOS Transactions*, 83(15): 165–172, April 2002. doi: 10.1029/2002EO000105. (Cited once on page 10)

H. H. Hess. History of ocean basins. *Petrologic studies: A Volume in Honor of A. F. Buddington*, pages 599–620, 1962. (Cited once on page 1)

W. T. Higgins. A comparison of complementary and Kalman filtering. *IEEE Transactions on Aerospace and Electronic Systems*, AES-11, No. 3: 321–325, 1975. (Cited once on page 66)

D. Hillan, C. Foss, J. Austin, P. Schmidt, and D. Clark. Direction to magnetic source analysis of single string of down-hole magnetic tensor data. *SEG Annual Meeting*, 2012. (Cited once on page 18)

S.-E. Hjelt. Magnetostatic anomalies of dipping prisms. *Geoexploration*, 10: 239–254, 1972. (Cited 3 times on pages 17, 103, and 148)

T. Hoschke. A new drill hole magnetometer: preliminary results from the Tennant Creek area. *Exploration Geophysics*, 16: 365–374, 1985. (Cited once on page 21)

S. D. Hurst, J. A. Karson, and K. L. Verosub. Paleomagnetism of tilted dikes in fast spread oceanic crust exposed in the hess deep rift: Implications for spreading and rift propagation. *Tectonics*, 13(4): 789–802, 1994. doi: 10.1029/94TC00845. (Cited once on page 2)

E. Irving. Palaeomagnetic and palaeoclimatological aspects of polar wandering. *Geofisica pura e applicata*, 33(1): 23–41, 1956. doi: 10.1007/BF02629944. (Cited once on page 1)

G. Iturrino, T. Liu, D. Goldberg, L. Anderson, H. Evans, A. Fehr, G. Guerin, J. Inwood, J. Lofi, A. Malinverno, S. Morgan, S. Mrozewski, A. Slagle, and T. Williams. Performance of the wireline heave compensation system onboard D/V JOIDES Resolution. *Scientific Drilling*, 15: 46–50, 2013. doi: 10.2204/iodp.sd.15.08.2013. (Cited once on page 43)

R. E. Kalman. A new approach to linear filtering and prediction problems. *Transactions of the ASME–Journal of Basic Engineering*, 82(Series D): 35–45, 1960. (Cited once on page 60)

A. A. Kaufman. *Geophysical Field Theory and Method - Part A - Gravitational, Electric, and Magnetic Fields*. Academic Press, 1992. (Cited 3 times on pages 15, 16, and 154)

O. D. Kellogg. *Foundations of Potential Theory*. Springer, 1929. (Cited once on page 15)

H. Kügler. *Modell eines Saturationskernmagnetometers basierend auf hochgenauen Kalibriermessungen*. PhD thesis, Institut für Geophysik und extraterrestrische Physik, Technische Universität Braunschweig, 2004. http://opus.tu-bs.de/opus/volltexte/2004/591. (Cited once on page 36)

T. Klein. Kalibrierung und Messungen mit der Göttinger Bohrlochmagnetometersonde im Vogelsberg. Master's thesis, TU Braunschweig, 2009. (Cited 6 times on pages 3, 22, 31, 33, 34, and 65)

A. Koppers, J. A. Russell, M. G. Jackson, J. Konter, H. Staudigel, and S. R. Hart. Samoa reinstated as a primary hotspot trail. *Geology*, 36(6): 435–438, 2008. doi: 10.1130/G24630A.1. (Cited once on page 27)

A. A. P. Koppers, T. Yamazaki, J. Geldmacher, J. S. Gee, N. Pressling, H. Hoshi, L. Anderson, C. Beier, D. M. Buchs, L. . Chen, B. E. Cohen, F. Deschamps, M. J. Dorais, D. Ebuna,

S. Ehmann, J. G. Fitton, P. M. Fulton, E. Ganbat, C. Hamelin, T. Hanyu, L. Kalnins, J. Kell, S. MacHida, J. J. Mahoney, K. Moriya, A. R. L. Nichols, S. Rausch, S. . Sano, J. B. Sylvan, and R. Williams. Limited latitudinal mantle plume motion for the Louisville hotspot. *Nature Geoscience*, 5(12): 911–917, 2012. (Cited 5 times on pages 28, 108, 113, 116, and 118)

A. A. P. Koppers, T. Yamazaki, J. Geldmacher, and the IODP Expedition 330 Scientific Party. IODP Expedition 330: Drilling the Louisville Seamount Trail in the SW Pacific. *Scientific Drilling*, (15): 11–22, March 2013. (Cited once on page 79)

A. Koppers, T. Yamazaki, and J. Geldmacher. Louisville seamount trail: implications for geodynamic mantle flow models and the geochemical evolution of primary hotspots. *IODP Sci. Prosp.*, 2010. doi: 10.2204/iodp.sp.330.2010. (Cited 2 times on pages 27 and 99)

A. Lawrence. *Moderin Inerital Technology - Navigation, Guidance, and Control*. Mechanical Engineering Series. Springer, 2nd edition, 1998. (Cited once on page 24)

A. Levanto. A three-component magnetometer for small drill holes and its use in ore prospecting. *Geoph. Prosp.*, VII(2): 183–195, 1959. (Cited 2 times on pages 2 and 21)

M. Leven. *Entwicklung und Aufbau eines triaxialen Bohrlochmagnetometers für den Einsatz in tiefen Bohrungen zur Vertikalen Gradientensondierung*. PhD thesis, Technische Universität Braunschweig, 1997. (Cited 4 times on pages 3, 21, 22, and 26)

B.-B. Li, J.-H. Zhu, and H.-Q. Min. BMP: A self-balancing mobile platform. *International Conference on Machine Learning and Cybernetics*, pages 868–874, 2012. doi: 10.1109/ICMLC.2012.6359467. (Cited once on page 64)

W. Lowrie. *Fundamentals of Geophysics*. Cambridge University Press, 1997. (Cited 4 times on pages 7, 9, 11, and 12)

J. L. Marins, X. Yun, E. R. Bachmann, R. B. McGhee, and M. J. Zyda. An extended Kalman filter for quaternion-based orientation estimation using MARG sensors. In *Proceedings of the IEEE/RSJ International Conference on Intelligent Robots and Systems*, volume 4, pages 2003–2011, 2001. doi: 10.1109/IROS.2001.976367. (Cited once on page 63)

P. Maybeck. *Stochastic Models, Estimation and Control*. Academic Press, 1979. (Cited once on page 60)

M. W. McElhinny and P. L. McFadden. *Paleomagnetism: Continents and Oceans*. Academic Press, 2000. (Cited once on page 1)

J. McFee. *Electromagnetic Remote Sensing: Low Frequency Electromagnetics*. Number 124 in Suffield Special Publication. Defence Research Establishment Suffield, Ralston Alberta (Canada), http://cradpdf.drdc.gc.ca/PDFS/zbc84/p58878.pdf, 1989. (Cited 2 times on pages 16 and 18)

R. Merrill. *Paleomagnetism, the Core, and the Deep Mantle*, volume 63 of *International Geophysics Series*. ACADEMIC PRESS, 1996. (Cited 2 times on pages 8 and 12)

D. Meschede, editor. *Gerthsen Physik*. Springer, 25th edition, 2015. (Cited 2 times on pages 12 and 18)

W. J. Morgan. Convection plumes in the lower mantle. *Nature*, 230: 42–43, 1971. doi: 10.1038/230042a0. (Cited once on page 1)

A. Morris, J. Gee, N. Pressling, B. John, C. MacLeod, C. Grimes, and R. Searle. Footwall rotation in an oceanic core complex quantified using reoriented Integrated Ocean Drilling Program core samples. *Earth and Planetary Science Letters*, 287: 217–228, 2009. doi: 10.1016/j.epsl.2009.08.007. (Cited once on page 2)

E. Mueller, W. Morris, P. Killeen, and S. Balch. Combined 3-D interpretation of airborne, surface and borehole vector magnetics at the McConnel nickel deposit. *Proceedings of Exploration 97: Fourth Decennial International Conference on Mineral Exploration*, pages 657–666, 1997. (Cited once on page 21)

Y. Nogi, J. A. Tarduno, and W. W. Sager. 23. Inferences about the nature and origin of basalt sequences from the Cretaceous Mid-Pacific mountains (Sites 865 and 866), as deduced from downhole magnetometer logs. In E. Winterer, W. Sager, J. Firth, and J. Sinton, editors, *Proceedings of the Ocean Drilling Program, Scientific Results*, volume 143, 1995. doi: 10.2973/odp.proc.sr.143.239.1995. (Cited once on page 3)

A. V. Oosterom and J. Strackee. The solid angle of a plane triangle. *Biomedical Engineering, IEEE Transactions on*, BME-30, Nr. 2: 125–126, 1983. doi: 10.1109/TBME.1983.325207. (Cited once on page 155)

G. P. Paina, D. Gaydou, J. Redolfi, C. Paz, and L. Canali. Experimental comparison of Kalman and complementary filter for attitude estimation. *Argentine Symposium on Technology*, 2011. (Cited once on page 70)

D. Parasnis. *Principles of Applied Geophysics*. Chapman & Hall, 1997. (Cited 3 times on pages 15, 16, and 18)

J. E. Pariso, J. H. Scott, E. Kikawa, and H. P. Johnson. 17. A magnetic logging study of Hole 735b gabbros at the Southwest Indian Ridge. In P. T. Robinson, R. P. Von Herzen, and A. C. Adamson, editors, *Proceedings of the Ocean Drilling Program, Scientific Results*, volume 118, pages 309–321, 1991. doi: 10.2973/odp.proc.sr.118.149.1991. (Cited once on page 2)

S. Pisarevsky. New edition of the global paleomagnetic database. *Eos, Transactions American Geophysical Union*, 86(17): 170, 2005. doi: 10.1029/2005EO170004. (Cited once on page 1)

W. C. Pitman and J. R. Heirtzler. Magnetic anomalies over the Pacific-Antarctic Ridge. *Science*, 154(3753): 1164–1171, 1966. doi: 10.1126/science.154.3753.1164. (Cited once on page 1)

J. P. Pozzi, J. P. Martin, J. Pocachard, H. Feinberg, and A. Galdeano. In-situ magnetostratigraphy: interpretation of magnetic logging in sediments. *Earth and Planetary Science Letters*, 88(3-4): 357–373, 1988. doi: 10.1016/0012-821X(88)90092-1. (Cited once on page 3)

V. N. Puchkov. The controversy over plumes: Who is actually right? *Geotectonics*, 43(1): 1–17, 2009. doi: 10.1134/S0016852109010014. (Cited once on page 27)

I. Richter. Fluxgate magnetometer calibration for PUMA. Technical Report MR—IGEP—TR—0019, IGEP, TU Braunschweig, 2012. (Cited once on page 36)

K. Runcorn. Paleomagnetic comparisons between Europe and North America. *Proc. Geol. Assoc. Canada*, 8: 77–85, 1956. (Cited once on page 1)

W. W. Sager. Cretaceous paleomagnetic apparent polar wander path for the Pacific plate calculated from Deep Sea Drilling Project and Ocean Drilling Program basalt cores. *Physics of the Earth and Planetary Interiors*, 156: 329–349, 2006. doi: 10.1016/j.pepi.2005.09.014. (Cited once on page 1)

V. Sanches, Y. Li, M. N. Nabighian, and D. L. Wright. Numerical modeling of higher order magnetic moments in UXO discrimination. *IEEE Transactions on Geoscience and Remote Sensing*, 46(9): 2568–2583, 2008. doi: 10.1109/TGRS.2008.918090. (Cited once on page 18)

U. Schmucker, K. Spitzer, and E. Steveling. An electromagnetic sounding experiment in Germany using the vertical gradient of geomagnetic variations observed in a deep borehole. *Geophys. J. Int.*, 178: 1273–1288, 2009. doi: 10.1111/j.1365-246.X.2009.04199.x. (Cited once on page 21)

J. H. Scott and G. G. Olson. Three-component borehole magnetometer probe for mineral investigations and geological research. *Transactions of the SPWLA Annual Logging Symposium (Society of Professional Well Log Analysts)*, 1, 1985. (Cited 2 times on pages 2 and 21)

P. V. Sharma. Rapid computation of magnetic anomalies and demagnetization effects caused by bodies of arbitrary shape. *Pure and Applied Geophysics*, 64(1): 89–109, 1966. doi: 10.1007/BF00875535. (Cited once on page 18)

Shipboard Scientific Party. Site 418: Bermuda Rise. In M. Salisbury, J. Scott, and C. Auroux, editors, *Proceedings ODP, Initial Reports*, volume 102, pages 95–149, 1986. doi: 10.2973/odp.proc.ir.102.103.1986. (Cited once on page 2)

Shipboard Scientific Party. Site 395. In R. Detrick, J. Honnorez, W. Bryan, and T. Juteau, editors, *Proceedings of the Ocean Drilling Program, Initial Report*, volume 106/109, 1988. doi: 10.2973/odp.proc.ir.106109.107.1988. (Cited once on page 2)

Shipboard Scientific Party. Site 735. In P. T. Robinson, R. P. Von Herzen, and A. C. Adamson, editors, *Proceedings of the Ocean Drilling Program, Initial Report*, volume 118, pages 89–222, 1989. doi: 10.2973/odp.proc.ir.118.107.1989. (Cited once on page 2)

Shipboard Scientific Party. Explanatory notes. In J. Alt, H. Kinoshita, and L. Stokking, editors, *Proceedings of the Ocean Drilling Program, Initial Report*, volume 148, pages 5–24, 1993. doi: 10.2973/odp.proc.ir.148.101.1993. (Cited once on page 2)

J. B. C. Silva and G. W. Hohmann. Interpretation of three-component borehole magnetometer data. *Geophysics*, 45 No 12: 1721–1731, 1981. (Cited once on page 2)

D. Simon. *Optimal State Estimation.* Wiley-Interscience, 2006. (Cited 4 times on pages 60, 62, 63, and 66)

B. Sing and D. Guptasarma. New method for fast computation of gravity and magnetic anomalies from arbitrary polyhedra geophysics. *Geophysics*, 66(2): 521–526, 2001. (Cited 3 times on pages 17, 155, and 157)

D. Smith, C. Brett, D. Wallis, and J. Derrick. BGS Oriented Seabed Rockdrill (BRIDGE Drill) - Engineering Report for scientific cruise JR63. *British Geological Survey Internal Report*, CR/01/157N, 2001. (Cited once on page 2)

K. Spitzer. Observations of geomagnetic pulsations and variations with a new borehole magnetometer down to depths of 3000m. *Geophys. J. Int.*, 115: 839–848, 1993. (Cited once on page 21)

H. Staudigel and D. Clague. The geological history of deep-sea volcanoes: Biosphere, hydrosphere, and lithosphere interactions. *Oceanography*, 23(1): 58–71, 2010. doi: 10.5670/oceanog.2010.62. (Cited once on page 79)

B. Steinberger and A. R. Calderwood. Models of large-scale visous flow in the Earth's mantle with constraints from mineral physics and surface observations. *Geophys. J. Int.*, 167: 1461–1481, 2006. doi: 10.1111/j.1365-246X.2006.03131.x. (Cited once on page 1)

E. Steveling, J. Stoll, and M. Leven. Quasi-continuous depth profiles of rock magnetization from magnetic logs in the HSDP-2 borehole, Island of Hawaii. *Geochem. Geophys. Geosyst.*, 4(4): 8708, 2003. doi: 10.1029/2002GC000330. (Cited 2 times on pages 4 and 22)

E. Steveling, J. Stoll, and M. Leven. Paläomagnetismus in der Bohrung HSDP (Hilo/Hawaii). *Abschlussbericht zu den Forschungsvorhaben STE 371/6- 2 und STE 371/6-3 im Schwerpunktprogramm International Continental Drilling Program (ICDP),Kontinentales Tiefbohrprogramm der Bundesrepublik Deutschland(KTB), SPP1006*, 2005. (Cited 2 times on pages 33 and 65)

J. Stratton. *Electromagnetic Theory.* McGraw-Hill, New York, 1941. (Cited once on page 15)

J. Tarduno, R. Duncan, D. Scholl, R. Cottrell, B. Steinberger, T. Thordarson, B. Kerr, C. Neal, F. F.A., M. Torii, and C. Carvallo. The Emperor Seamounts: Southward motion of the Hawaiian hotspot plume in Earth's mantle. *Science*, 301: 1064–1069, 2003. (Cited once on page 27)

J. A. Tarduno, M. K. Watkeys, T. N. Huffman, R. D. Cottrell, E. G. Blackman, A. Wendt, C. A. Scribner, and C. L. Wagner. Antiquity of the South Atlantic Anomaly and evidence for top-down control on the geodynamo. *Nature Communications*, 6, 2015. (Cited once on page 10)

W. M. Telford, L. P. Geldart, and R. E. Sheriff. *Applied Geophysics.* Cambridge University Press, 2nd edition, 1990. (Cited 2 times on pages 7 and 18)

Y. Teruyama and T. Watanabe. Effectiveness of variable-gain Kalman filter based on angle error calculated from acceleration signals in lower limb angle measurement with inertial sensors. *Computational and Mathematical Methods in Medicine*, Volume 2013, Article ID 398042, 12 pages, 2013. doi: 10.1155/2013/398042. (Cited once on page 70)

M. Tivey, R. Larson, H. Schouten, and R. Pockalny. Downhole magnetic measurements of ODP Hole 801c: Implications for pacific oceanic crust and magnetic field behavior in the middle jurassic. *Geochemistry, Geophysics, Geosystems*, 6(4), 2005. doi: 10.1029/2004GC000754. (Cited once on page 4)

M. Tominaga, H. F. Evans, and G. Iturrino. "Equator Crossing" of Shatsky Rise?: New insights on Shatsky Rise tectonic motion from the downhole magnetic architecture of the uppermost lava sequences at Tamu Massif. *Geophysical Research Letters*, 39(21), 2012. doi: 10.1029/2012GL052967. (Cited once on page 19)

F. J. Vine and D. H. Matthews. Magnetic anomalies over ocean ridges. *Nature*, 1999: 947–949, 1963. doi: 10.1038/199947a0. (Cited once on page 1)

C. Virgil, A. Hördt, T. Klein, J. Kück, M. Leven, and E. Steveling. High-precision orientation of three-component magnetic downhole logs. *Scientific Drilling*, 9: 37–40, 2010. doi: 10.2204/iodp.sd.9.07.2010. (Cited once on page 3)

C. Virgil, A. Hördt, M. Leven, E. Steveling, J. Kück, and F. Dietze. Three-component magnetic logging in the Outokumpu deep drill hole. *Geological Survey of Finland, Special Paper 51*, pages 119–132, 2011. (Cited once on page 3)

C. Virgil, S. Ehmann, A. Hördt, M. Leven, and E. Steveling. Reorientation of three-component borehole magnetic data. *Geophysical Prospecting*, 63(1): 225–242, 2015. doi: 10.1111/1365-2478.12175. (Cited 2 times on pages 3 and 31)

C. Virgil. *Vorbereitung und Durchführung von dreikomponentigen Magnetfeldmessungen mit dem Göttinger Bohrloch Magnetometer*. PhD thesis, TU Braunschweig, 2012. (Cited 12 times on pages 3, 22, 31, 35, 39, 43, 45, 57, 65, 89, 93, and 94)

A. Wegener. *Die Entstehung der Kontinente und Ozeane.* Number 23. Sammlung Vieweg, 1915. (Cited once on page 1)

P. Wessel and L. W. Kroenke. Pacific absolute plate motion since 145 Ma: An assessment of the fixed hot spot hypothesis. *Journal of Geophysical Research*, 113(B06101), 2007. doi: 10.1029/2007JB005499. (Cited once on page 27)

T. Williams. Magnetostratigraphy from downhole measurements in ODP holes. *Physics of the Earth and Planetary Interiors*, 156: 261–273, 2006. (Cited 3 times on pages 3, 19, and 122)

J. T. Wilson. A possible origin of the Hawaiian Islands. *Canadian Journal of Earth Sciences*, 41 (6): 863–868, 1963. doi: 10.1139/cjes-2014-0036. (Cited once on page 27)

H. Winner, S. Hakuli, F. Lotz, and C. Singer, editors. *Handbuch Fahrerassistenzsysteme*. Springer Vieweg, 3rd edition, 2015. doi: 10.1007/978-3-658-05734-3. (Cited once on page 61)

A Appendix

A.1. Implementation of the Kalman Filters

Due to the choice of coordinate system made for the gyros (Section 2.4.2), the signs in some of the equations given in the discussion in Section 5.6.2 and Section 5.6.3 need to be changed when the algorithms are implemented for use with the GBM data. The main reasons for the changes is that gyro data of R_x corresponds to a change in data of inclinometer N_y, and gyro data of R_y corresponds to a negative change in data of inclinometer N_x. Sign changes and important indices are marked in red in the following equations.

A.1.1. Implementation A - Angle

Inclination N_x

Here, N_x is corrected using ω_y, and some sign changes are present due to the choice of coordinate systems.

Prediction:

$$\hat{\Omega}_i^{x^-} = \hat{\Omega}_{i-1}^{x^+} - \omega_i^{y} \tag{A.1}$$

$$P_i^{x^-} = P_{i-1}^{x^+} + Q_i \tag{A.2}$$

Update:

$$y_i^x = \Omega_i^{N_x} \tag{A.3}$$

$$K_i^x = \frac{P_i^{x^-}}{P_i^{x^-} + R_i} \tag{A.4}$$

$$\begin{aligned} \hat{\Omega}_i^{x^+} &= \hat{\Omega}_i^{x^-} + K_i^x \cdot (\Omega_i^{N_x} - \hat{\Omega}_i^{x^-}) \\ &= \hat{\Omega}_{i-1}^{x^+} - \omega_i^{y} + K_i^x \cdot (\Omega_i^{N_x} - \hat{\Omega}_{i-1}^{x^+} + \omega_i^{y}) \end{aligned} \tag{A.5}$$

$$P_i^{x^+} = (1 - K_i^x) P_i^{x^-} \tag{A.6}$$

Here, the correction (Eq. 5.28) is given by:

$$\text{correction}_x = K_i \cdot (\hat{\Omega}_i^{N_x} - \hat{\Omega}_i^{x^-}) \tag{A.7}$$

and is a correction to the angle, that is the inclinometer data.

The actual input for the standard algorithm (Eq. 5.1) for the reorientation of magnetic field data is the change of the angle between t_{i-1} and t_i:

$$\begin{aligned} \hat{\omega}_i^{y} &= -\left(\hat{\Omega}_i^{x^+} - \hat{\Omega}_{i-1}^{x^+}\right) \\ &= -\left(-\omega_i^{y} + K_i \cdot (\Omega_i^{N_x} - \hat{\Omega}_{i-1}^{x^+} + \omega_i^{y})\right) \end{aligned} \tag{A.8}$$

Using the definition of the correction in Eq. A.7, we can rewrite Eq. A.8:

$$\begin{aligned}\hat{\omega}_i^y &= -\left(\hat{\Omega}_i^{x^-} + \text{correction}_x - \hat{\Omega}_{i-1}^{x^+}\right) \\ &= -\left(\hat{\Omega}_{i-1}^{x^+} - \omega_i^y + \text{correction}_x - \hat{\Omega}_{i-1}^{x^+}\right) \\ &= \omega_i^y - \text{correction}_x\end{aligned} \tag{A.9}$$

which shows that if we want to compare the correction given by the Kalman filter for Ω_x to an offset given by the gyro offset correction (Section 5.5), it has to be compared to the negative offset of R_y.

Inclination N_y

Here, N_y is corrected using ω_x, but no sign changes are present compared to Section 5.6.2.

Prediction:

$$\hat{\Omega}_i^{y^-} = \hat{\Omega}_{i-1}^{y^+} + \omega_i^x \tag{A.10}$$

$$P_i^{y^-} = P_{i-1}^{y^+} + Q_i \tag{A.11}$$

Update:

$$y_i^y = \Omega_i^{N_y} \tag{A.12}$$

$$K_i^y = \frac{P_i^{y^-}}{P_i^{y^-} + R_i} \tag{A.13}$$

$$\begin{aligned}\hat{\Omega}_i^{y^+} &= \hat{\Omega}_i^{y^-} + K_i^y \cdot (\Omega_i^{N_y} - \hat{\Omega}_i^{y^-}) \\ &= \hat{\Omega}_{i-1}^{y^+} + \omega_i^x + K_i^y \cdot (\Omega_i^{N_y} - \hat{\Omega}_{i-1}^{y^+} - \omega_i^x)\end{aligned} \tag{A.14}$$

$$P_i^{y^+} = (1 - K_i^y) P_i^{y^-} \tag{A.15}$$

Here, the correction (Eq. 5.28) is given by:

$$\text{correction}_y = K_i \cdot (\hat{\Omega}_i^{N_y} - \hat{\Omega}_i^{y^-}) \tag{A.16}$$

and is a correction to the angle, that is the inclinometer data.

The actual input for the standard algorithm (Eq. 5.1) for the reorientation of magnetic field data is the change of the angle between t_{i-1} and t_i:

$$\begin{aligned}\hat{\omega}_i^x &= \hat{\Omega}_i^{y^+} - \hat{\Omega}_{i-1}^{y^+} \\ &= \omega_i^x + K_i \cdot (\Omega_i^{N_y} - \hat{\Omega}_{i-1}^{y^+} - \omega_i^x)\end{aligned} \tag{A.17}$$

Using the definition of the correction in Eq. A.16, we can rewrite Eq. A.17:

$$\begin{aligned}\hat{\omega}_i^x &= \hat{\Omega}_i^{y^-} + \text{correction}_y - \hat{\Omega}_{i-1}^{y^+} \\ &= \hat{\Omega}_{i-1}^{y^+} + \omega_i^x + \text{correction}_y - \hat{\Omega}_{i-1}^{y^+} \\ &= \omega_i^x + \text{correction}_y\end{aligned} \tag{A.18}$$

which shows that if we want to compare the correction given by the Kalman filter for Ω_y to an offset given by the gyro offset correction (Section 5.5), it has to be compared to the offset of R_x, and not to the negative offset as for the other axis.

A.1.2. Implementation B - Angle and Gyro Offset

Inclination N_x

Here, N_x is corrected using ω_y, and some sign changes are present compared to Section 5.6.3 due to the choice of coordinate systems.

Prediction:

$$\hat{\Omega}_i^{x^-} = \hat{\Omega}_{i-1}^{x^+} - (\omega_i^y - \hat{g}_{i-1}^{y^+}) \tag{A.19}$$

$$\hat{g}_i^{y^-} = \hat{g}_{i-1}^{y^+} \tag{A.20}$$

$$\tag{A.21}$$

$$P_i^{x^-} = \underbrace{\begin{bmatrix} 1 & -1 \\ 0 & 1 \end{bmatrix}}_{F} \cdot P_{i-1}^{x^+} \cdot \underbrace{\begin{bmatrix} 1 & 0 \\ -1 & 1 \end{bmatrix}}_{F^T} + Q \tag{A.22}$$

Update:

$$y_i^x = \Omega_i^{N_x} \tag{A.23}$$

$$K_i^x = P_i^{x^-} \begin{bmatrix} 1 \\ 0 \end{bmatrix} \cdot \left(\begin{bmatrix} 1 & 0 \end{bmatrix} \cdot P_i^{x^-} \cdot \begin{bmatrix} 1 \\ 0 \end{bmatrix} + R_i \right)^{-1} \tag{A.24}$$

$$\begin{aligned} \hat{\Omega}_i^{x^+} &= \hat{\Omega}_i^{x^-} + K_i^{\Omega_x} \cdot (\Omega_i^{N_x} - \hat{\Omega}_i^{x^-}) \\ &= \hat{\Omega}_{i-1}^{x^+} - (\omega_i^y - \hat{g}_{i-1}^{y^+}) + K_i^{\Omega_x} \cdot (\Omega_i^{N_x} - \hat{\Omega}_{i-1}^{x^+} + (\omega_i^y - \hat{g}_{i-1}^{y^+})) \end{aligned} \tag{A.25}$$

$$\begin{aligned} \hat{g}_i^{y^+} &= \hat{g}^{y^-} + K_i^{g_y} \cdot (\Omega_i^{N_x} - \hat{\Omega}_i^{x^-}) \\ &= \hat{g}^{y^-} + K_i^{g_y} \cdot (\Omega_i^{N_x} - \hat{\Omega}_{i-1}^{x^+} + (\omega_i^y - \hat{g}_{i-1}^{y^+})) \end{aligned} \tag{A.26}$$

$$P_i^{x^+} = \left(\begin{bmatrix} 1 & 0 \\ 0 & 1 \end{bmatrix} - K_i^x \cdot \begin{bmatrix} 1 \\ 0 \end{bmatrix} \right) \cdot P_i^{x^-} \tag{A.27}$$

The input for the reorientation algorithm is the change of the angle between t_{i-1} and t_i:

$$\begin{aligned} \hat{\omega}_i^y &= -\left(\hat{\Omega}_i^{x^+} - \hat{\Omega}_{i-1}^{x^+} \right) \\ &= -(\omega_i^y - \hat{g}_{i-1}^{y^+}) + K_i^{\Omega_x} \cdot (\Omega_i^{N_x} - \hat{\Omega}_{i-1}^{x^+} + (\omega_i^y - \hat{g}_{i-1}^{y^+})) \end{aligned} \tag{A.28}$$

Inclination N_y

Here, N_y is corrected using ω_x, but no sign changes are present compared to Section 5.6.3.

Prediction:

$$\hat{\Omega}_i^{y^-} = \hat{\Omega}_{i-1}^{y^+} + (\omega_i^x - \hat{g}_{i-1}^{x^+}) \tag{A.29}$$

$$\hat{g}_i^{x^-} = \hat{g}_{i-1}^{x^+} \tag{A.30}$$

$$\tag{A.31}$$

$$P_i^{y^-} = \underbrace{\begin{bmatrix} 1 & -1 \\ 0 & 1 \end{bmatrix}}_{F} \cdot P_{i-1}^{y^+} \cdot \underbrace{\begin{bmatrix} 1 & 0 \\ -1 & 1 \end{bmatrix}}_{F^T} + Q \tag{A.32}$$

Update:

$$y_i^y = \Omega_i^{N_y} \tag{A.33}$$

$$K_i^y = P_i^{y^-} \begin{bmatrix} 1 \\ 0 \end{bmatrix} \cdot \left(\begin{bmatrix} 1 & 0 \end{bmatrix} \cdot P_i^{y^-} \cdot \begin{bmatrix} 1 \\ 0 \end{bmatrix} + R_i \right)^{-1} \tag{A.34}$$

$$\begin{aligned} \hat{\Omega}_i^{y^+} &= \hat{\Omega}_i^{y^-} + K_i^{\Omega_y} \cdot (\Omega_i^{N_y} - \hat{\Omega}_i^{y^-}) \\ &= \hat{\Omega}_{i-1}^{y^+} + (\omega_i^x - \hat{g}_{i-1}^{x^+}) + K_i^{\Omega_y} \cdot (\Omega_i^{N_y} - \hat{\Omega}_{i-1}^{y^+} - (\omega_i^x - \hat{g}_{i-1}^{x^+})) \end{aligned} \tag{A.35}$$

$$\begin{aligned} \hat{g}_i^{x^+} &= \hat{g}^{x^-} + K_i^{g_x} \cdot (\Omega_i^{N_y} - \hat{\Omega}_i^{y^-}) \\ &= \hat{g}^{x^-} + K_i^{g_x} \cdot (\Omega_i^{N_y} - \hat{\Omega}_{i-1}^{y^+} - (\omega_i^x - \hat{g}_{i-1}^{x^+})) \end{aligned} \tag{A.36}$$

$$P_i^{y^+} = \left(\begin{bmatrix} 1 & 0 \\ 0 & 1 \end{bmatrix} - K_i^y \cdot \begin{bmatrix} 1 \\ 0 \end{bmatrix} \right) \cdot P_i^{y^-} \tag{A.37}$$

The input for the reorientation algorithm is the change of the angle between t_{i-1} and t_i:

$$\begin{aligned} \hat{\omega}_i^x &= \hat{\Omega}_i^{y^+} - \hat{\Omega}_{i-1}^{y^+} \\ &= \omega_i^x - \hat{g}_{i-1}^{x^+} + K_i^{\Omega_y} \cdot (\Omega_i^{N_y} - \hat{\Omega}_{i-1}^{y^+} - (\omega_i^x - \hat{g}_{i-1}^{x^+})) \end{aligned} \tag{A.38}$$

A.2. Bosum Model

The model given by Bosum et al. (1988) gives a simple formula for the magnetic field on the axis of a circular borehole intersecting a circular cylinder. This model is the foundation for the interpretation of the magnetic field data in this thesis, and is both used in an inversion using horizontal layers and in the approximation derived for inclined layers (Section 6.7.3). However, the derivation of the formulas in the original publication is rather complicated and can be simplified by directly only considering points on the borehole axis and neglecting off-axis points, following the approach taken by Gallet and Courtillot (1989). By doing so, one can avoid the use of Bessel functions and express all intermediary steps in terms of elementary functions.

Using Eq. 2.20, we can split the calculation of the magnetic field into integrations over the cylinder face and the cylinder mantle. We are going to start with the magnetic field of a solid cylinder; the magnetic field on the axis of a borehole can then be found by subtracting the magnetic field of a cylinder with the radius of the borehole, r_1, from the magnetic field of a cylinder with the radius of the layer, r_2.

Figure A.1 shows the geometry used for the calculation of the magnetic field of the cylinder. We are going to calculate the field at point $P(0,0,z)$; $Q(x',y',z')$ is a point on the surface we are integrating over. Where appropriate, we are using cylindrical coordinates $Q(R,\Phi',z')$.

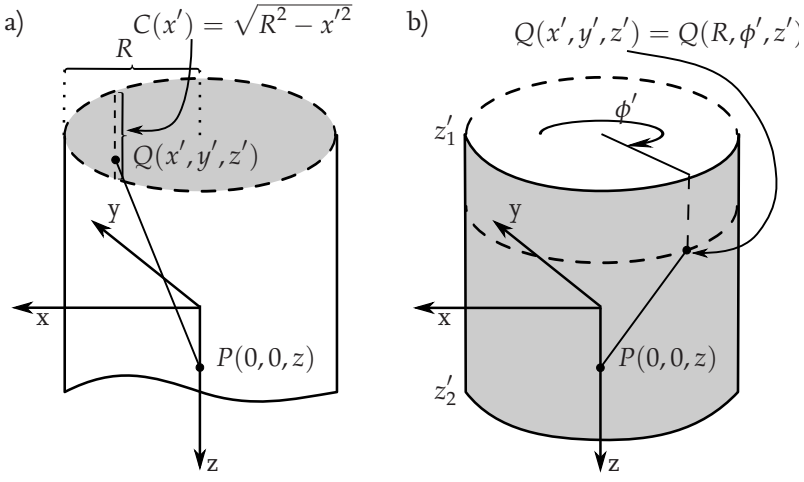

Figure A.1.: Geometry used for the calculation of the magnetic field of a cylinder. a) shows the face of the cylinder, b) shows the cylinder mantle.

A.2.1. Cylinder Face Potential

For the face of the cylinder (Fig. A.1a), $\vec{M} \cdot \hat{n}(\vec{r}) = -M_z$. Due to symmetry reasons, there is only a contribution to the vertical component of the magnetic field on the axis of the cylinder. Like in the more general solution for cylinders with an inclined upper surface

(Gallet and Courtillot (1989), see also Appendix A.3), we integrate in bands parallel to the y-axis. Using $C(x') = \sqrt{R^2 - x'^2}$ we get:

$$\begin{aligned}
B_z(z) &= \frac{\mu_0 \cdot M_z}{4\pi} \frac{\partial}{\partial z} \int_{-R}^{R} \mathrm{d}x' \int_{-C(x')}^{C(x')} \frac{\mathrm{d}y'}{\sqrt{x'^2 + y'^2 + (z - z')^2}} \\
&= -\frac{\mu_0 \cdot M_z}{4\pi} \int_{-R}^{R} \mathrm{d}x' \int_{-C(x')}^{C(x')} \frac{(z - z') \cdot \mathrm{d}y'}{[x'^2 + y'^2 + (z - z')^2]^{3/2}} \\
&= -\frac{\mu_0 \cdot M_z}{4\pi} \int_{-R}^{R} \frac{(z - z')}{x'^2 + (z - z')^2} \frac{\sqrt{R^2 - x'^2}}{\sqrt{R^2 + (z - z')^2}} \mathrm{d}x' \\
&= -\frac{\mu_0 \cdot M_z}{4\pi} \frac{z - z'}{\sqrt{R^2 + (z - z')^2}} \int_{-R}^{R} \frac{\sqrt{R^2 - x'^2}}{x'^2 + ((z - z')^2} \mathrm{d}x' \\
&= -\frac{\mu_0 \cdot M_z}{4\pi} \frac{z - z'}{\sqrt{R^2 + (z - z')^2}} \cdot \\
&\quad \left[\frac{\sqrt{R^2 + (z - z')^2}}{z - z'} \cdot \arctan\left(\frac{x' \sqrt{R^2 + (z - z')^2}}{z \sqrt{R^2 - x'^2}} \right) \right. \\
&\quad \left. - \arctan\left(\frac{x'}{\sqrt{R^2 - x'^2}} \right) \right] \Bigg|_{x'=-R}^{x'=R}
\end{aligned} \tag{A.39}$$

For $x' = \pm R$, the denominator in both arctan becomes zero. Using $\lim_{a \to \pm\infty} \arctan(a) = \pm\frac{\pi}{2}$ we obtain:

$$B_z(z) = -\frac{\mu_0 M_z}{4} \left(1 - \frac{z - z'}{\sqrt{R^2 + (z - z')^2}} \right) \tag{A.40}$$

The magnetic field due to the cylinder face on the axis of a borehole with radius r_1 through a layer with radius r_2 can thus be calculated as follows:

$$\begin{aligned}
B_z &= B_{z'=-h}^{R=r_2} - B_{z'=-h}^{R=r_1} - (B_{z'=h}^{R=r_2} - B_{z'=h}^{R=r_1}) \\
&= -\frac{\mu_0 M_z}{4} \left(\frac{z + h}{\sqrt{r_1^2 + (z + h)^2}} - \frac{z + h}{\sqrt{r_2^2 + (z + h)^2}} \right. \\
&\qquad \left. + \frac{z - h}{\sqrt{r_2^2 + (z - h)^2}} - \frac{z - h}{\sqrt{r_1^2 + (z - h)^2}} \right)
\end{aligned} \tag{A.41}$$

In the case of a layer of infinite horizontal extent, $r_2 \to \infty$, we get:

$$B_z = -\frac{\mu_0}{4} \cdot M_z \left(\frac{z + h}{\sqrt{r_1^2 + (z + h)^2}} - \frac{z - h}{\sqrt{r_1^2 + (z - h)^2}} \right) \tag{A.42}$$

A.2.2. Cylinder Mantle Potential

For the lateral surface of the cylinder (Fig. A.1b), $\vec{M} \cdot \hat{n}(\vec{r}) = M_x \cdot \cos\phi + M_y \cdot \sin\phi$. Starting with the B_x component of the magnetic field we get:

$$\begin{aligned} B_x(z) &= -\frac{\mu_0}{4\pi}\frac{\partial}{\partial x}\int_0^{2\pi} R\mathrm{d}\phi' \int_{z_1}^{z_2} \frac{(M_x \cdot \cos\phi' + M_y \cdot \sin\phi')\mathrm{d}z'}{\sqrt{x'^2 + y'^2 + (z-z')^2}} \\ &= \frac{\mu_0}{4\pi}\int_0^{2\pi} R\mathrm{d}\phi' \int_{z_1}^{z_2} \frac{x' \cdot (M_x \cdot \cos\phi' + M_y \cdot \sin\phi')\mathrm{d}z'}{[x'^2 + y'^2 + (z-z')^2]^{3/2}} \\ &= \frac{\mu_0}{4\pi}\int_0^{2\pi} R\mathrm{d}\phi' \int_{z_1}^{z_2} \frac{R\cos\phi' \cdot (M_x \cdot \cos\phi' + M_y \cdot \sin\phi')\mathrm{d}z'}{[R^2 + (z-z')^2]^{3/2}} \\ &= \frac{\mu_0}{4\pi}\int_0^{2\pi} \frac{R^2\cos\phi' \cdot (M_x \cdot \cos\phi' + M_y \cdot \sin\phi')(z-z)'}{R^2\sqrt{(z-z')^2 + R^2}}\mathrm{d}\phi' \Bigg|_{z'=z_1}^{z'=z_2} \end{aligned} \tag{A.43}$$

With $\int_0^{2\pi}\cos^2\phi'\mathrm{d}\phi' = \pi$ and $\int_0^{2\pi}\cos\phi'\sin\phi'\mathrm{d}\phi' = 0$ we obtain:

$$B_x(0,0,z) = \frac{\mu_0 M_x}{4}\frac{z-z'}{\sqrt{(z-z')^2 + R^2}}\Bigg|_{z'=z_1}^{z'=z_2} \tag{A.44}$$

Similarly, repeating the calculations for B_y yields:

$$B_y(0,0,z) = \frac{\mu_0 M_y}{4}\frac{z-z'}{\sqrt{(z-z')^2 + R^2}}\Bigg|_{z'=z_1}^{z'=z_2} \tag{A.45}$$

On the axis of a borehole through a layer extending from $-h$ to h we thus get:

$$\begin{aligned} B_{x,y}(z) = \frac{\mu_0 M_{x,y}}{4}\Bigg(&\frac{z+h}{\sqrt{r_1^2 + (z+h)^2}} - \frac{z+h}{\sqrt{r_2^2 + (z+h)^2}} \\ &+ \frac{z-h}{\sqrt{r_2^2 + (z-h)^2}} - \frac{z-h}{\sqrt{r_1^2 + (z-h)^2}}\Bigg) \end{aligned} \tag{A.46}$$

For $r_2 \to \infty$, this gives:

$$B_{x,y} = \frac{\mu_0}{4} \cdot M_{x,y}\left(\frac{z+h}{\sqrt{r_1^2 + (z+h)^2}} - \frac{z-h}{\sqrt{r_1^2 + (z-h)^2}}\right) \tag{A.47}$$

A.2.3. Combined Model

Summarized, the magnetic field on the axis of a circular borehole with radius r_1 through a layer of infinite lateral extent and height $2h$ is given by:

$$B_i = M_i \cdot a_i \cdot \left(\frac{z+h}{\sqrt{r_1^2 + (z+h)^2}} - \frac{z-h}{\sqrt{r_1^2 + (z-h)^2}}\right) \tag{A.48}$$

where $a_x = a_y = \frac{mu_0}{4}$ and $a_z = -\frac{mu_0}{2}$.

A.3. Gallet and Courtillot Model

While implementing the results given in Gallet and Courtillot (1989), I discovered some typographic errors in the equations (see Ehmann et al., 2015). In the following part of the appendix, I am recalculating their solution for a semi-infinite cylinder with an inclined surface. In my calculations, I am closely following the original publication but will try to give some more details and highlight in red where my calculations differ. The geometry used for the calculations is shown in Fig. A.2. The figure is a slightly altered version of the original figure.

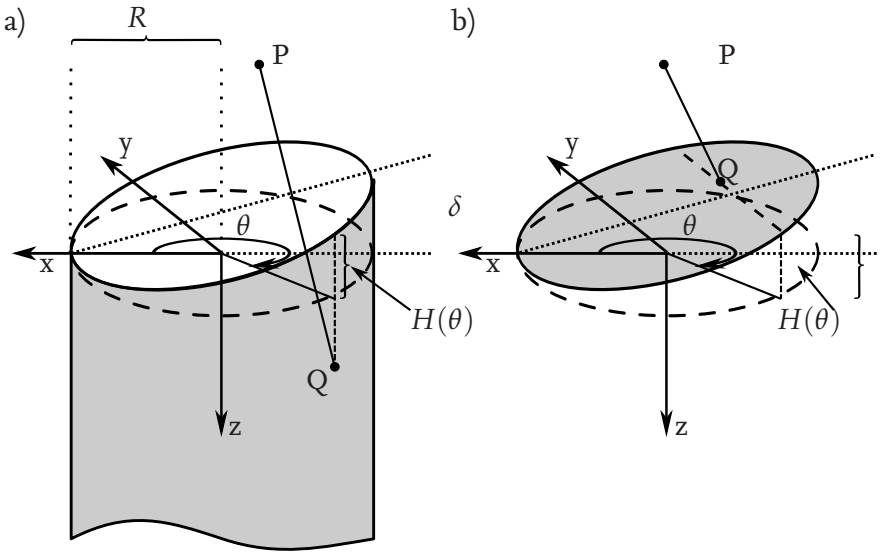

Figure A.2.: The geometry used for the calculations: a) shows the lateral surface of the cylinder, b) shows the upper ellipse. Modified from Gallet and Courtillot (1989)

A.3.1. Recalculating the field coefficients of the lateral surface

First, following Gallet and Courtillot (1989), I calculate the field coefficients for the lateral surface of the cylinder (see Fig. A.2a) by integrating $dV(P) = (\mu_0/4\pi)(dq/r)$, where r is the distance between point P(x,y,z) and point Q($\xi = R\cos\theta$,$\eta = R\sin\theta$,τ). Here, τ gives the vertical position of point Q, with $H(\theta) \leq \tau < -\infty$. In the original publication, $H(\theta)$ is positive. However, as can be seen in Fig. A.2, due to the choice of the coordinate system $H(\theta)$ should actually be negative. Thus I use:

$$H(\theta) = -2R\tan\delta\sin^2(\theta/2) \tag{A.49}$$

where δ is the dip of the ellipse. Figure A.3 illustrates the calculation of $H(\theta)$. Figure A.3a shows a side view of the ellipse. Figure A.3b shows the projection of the ellipse on the horizontal plane, that is a circle with radius R. $H(x)$ can be easily calculated by:

$$H(x) = -\tan\delta(R - x) \tag{A.50}$$

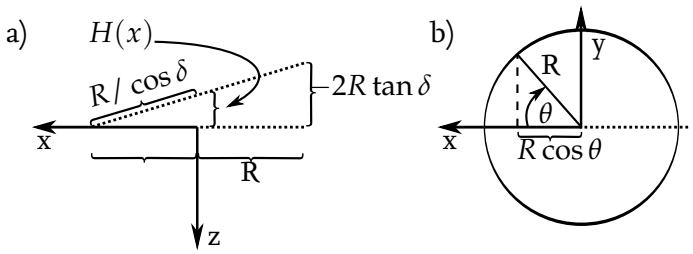

Figure A.3.: Illustration for the calculation of $H(\theta)$. Panel a) shows a side view of the ellipse, Panel b) its projection on the horizontal plane, that is a circle with radius R.

The maximum for $H(x)$ is $-2R\tan\delta$. Using $x = R\cos\theta$ (see Fig. A.3b), $H(\theta)$ can be calculated from $H(x)$:

$$\begin{aligned} H(\theta) &= -\tan\delta(R - R\cos\theta) \\ &= -2R\tan\delta\sin^2(\frac{\theta}{2}) \end{aligned} \tag{A.51}$$

The equivalent magnetic charge dq is given by $dq = \vec{M}\cdot\vec{n}dS$, with the surface element $dS = Rd\tau d\theta$ and the normal vector of the surface element $\vec{n}$. This is correctly given in the original publication, but the radius R is missing in the following calculation of the magnetostatic potential:

$$V(P) = \frac{\mu_0}{4\pi}\int_0^{2\pi}\vec{M}\cdot\vec{n}(\theta)\int_{H(\theta)}^{\infty}\frac{Rd\tau d\theta}{\sqrt{(x - R\cos\theta)^2 + (y - R\sin\theta)^2 + (z-\tau)^2}} \tag{A.52}$$

For the subsequent calculations, Gallet and Courtillot (1989) use that the integration for τ and the derivative for x,y and z can be interchanged when calculating the magnetic field by

$$B_{ij} = -\frac{\partial V(M = M_i)}{\partial j} \tag{A.53}$$

Using

$$\int\frac{1}{(a^2 + (z-\tau)^2)^{3/2}}d\tau = \frac{\tau - z}{a^2\sqrt{a^2 + (z-\tau)^2}} + const \tag{A.54}$$

and

$$\lim_{\tau\to+\infty}\frac{\tau - z}{a^2\sqrt{a^2 + (z-\tau)^2}} = \frac{1}{a^2} \tag{A.55}$$

they define

$$\begin{aligned} A(\theta, x, y, z) &= \int_{H(\theta)}^{\infty}\frac{d\tau}{[(x - R\cos\theta)^2 + (y - R\sin\theta)^2 + (z-\tau)^2]^{3/2}} \\ &= \frac{1}{(x - R\cos\theta)^2 + (y - R\sin\theta)^2} \\ &\cdot\left[1 + \frac{2R\tan\delta\sin^2(\frac{\theta}{2}) + z}{\sqrt{(x - R\cos\theta)^2 + (y - R\sin\theta)^2 + [z + 2R\tan\delta\sin^2(\frac{\theta}{2})]}}\right] \end{aligned} \tag{A.56}$$

Here, all signs are correct, which would not be the case if Gallet and Courtillot (1989) had used the definition of $H(\theta)$ as given in their publication. The signs are also right in their following definition of

$$\begin{aligned} B(\theta,x,y,z) &= \int_{H(\theta)}^{\infty} \frac{(z-\tau)d\tau}{[(x-R\cos)^2+(y-R\sin\theta)^2+(z-\tau)^2]^{3/2}} \\ &= -\frac{1}{\sqrt{(x-R\cos)^2+(y-R\sin\theta)^2+[z+2R\tan\delta\sin^2(\frac{\theta}{2})]^2}} \end{aligned} \tag{A.57}$$

where they used

$$\int \frac{z-\tau}{(a^2+(z-\tau)^2)^{3/2}}d\tau = \frac{1}{\sqrt{a^2+(z-\tau)^2}} + const \tag{A.58}$$

and

$$\lim_{\tau\to+\infty} \frac{1}{a^2\sqrt{a^2+(z-\tau)^2}} = 0 \tag{A.59}$$

They seem to have calculated using the right definition of $H(\theta)$ as given in Eq. A.51. There are no errors in their equations (A-4) through (A-9), and also the previously missing R is included, so I'm only going to recalculate equation (A-4) as an example. Using (Gallet and Courtillot, 1989):

$$\vec{M}\cdot\vec{n}(\theta) = M_x\cos\theta + M_y\sin\theta \tag{A.60}$$

It follows

$$\begin{aligned} B_{xx} &= -\frac{\partial V(M=M_x)}{\partial x} \\ &= -\frac{\mu_0}{4\pi}\frac{\partial}{\partial x}\int_0^{2\pi}\int_{H(\theta)}^{\infty} \frac{M_x\cos\theta R d\tau d\theta}{\sqrt{(x-R\cos\theta)^2+(y-R\sin\theta)^2+(z-\tau)^2}} \\ &= -\frac{\mu_0}{4\pi}M_x R\int_0^{2\pi}\int_{H(\theta)}^{\infty}(-1)\frac{(x-R\cos\theta)\cos\theta d\tau d\theta}{[(x-R\cos\theta)^2+(y-R\sin\theta)^2+(z-\tau)^2]^{3/2}} \\ &= \frac{\mu_0}{4\pi}M_x R\int_0^{2\pi} A(\theta,x,y,z)(x-R\cos\theta)\cos\theta d\theta \end{aligned} \tag{A.61}$$

In the last step, I used $A(\theta,x,y,z)$ as defined in Eq. A.56.

A.3.2. Recalculating the field coefficients of the inclined ellipse

Here, I calculate the magnetostatic potential at point $P(x,y,z)$ by integrating $\mathrm{d}V(P) = (\mu_0/4\pi)\cdot(\mathrm{d}q/r)$, with $\mathrm{d}q = \vec{M}\cdot\vec{n}\mathrm{d}S$ and $\vec{n} = (\sin\delta, 0, -\cos\delta)$. Like in the original publication I integrate along bands parallel to the y-axis. To illustrate the surface element and the boundaries of the integration, Fig. A.4a shows a projection of the ellipse on the horizontal plane and Fig. A.4b shows the ellipse in a coordinate system that coincides with its main axes.

In the coordinate system of the ellipse, the surface element would be given as $\mathrm{d}S = dx'\mathrm{d}\eta$. The surface element in the original coordinate system (ξ,η,τ) is given by $\mathrm{d}S = \mathrm{d}\xi\mathrm{d}\eta/\cos\delta$,

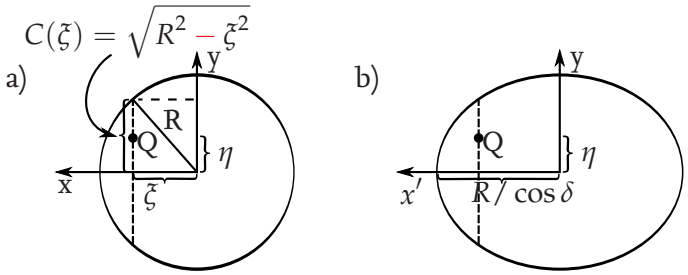

Figure A.4.: Illustration for the calculation of the field coefficients of the inclined ellipse. Panel a) shows a projection of the ellipse on the horizontal plane. Panel b) shows the upper ellipse in a coordinate system that coincides with its main axes.

as $x' = \xi / \cos\delta$, which gives $\mathrm{d}x'/\mathrm{d}\xi = 1/\cos\delta$ and thus $\mathrm{d}x' = \mathrm{d}\xi/\cos\delta$. The boundaries for the integration for $\mathrm{d}\eta$ are $\pm R$ and $\pm C(\xi) = \pm\sqrt{R^2 - \xi^2}$ for $\mathrm{d}\xi$. In the original publication, the definition of $C(\xi)$ erroneously has a $+$ instead of a $-$, but the subsequent calculations use the right definition. There are no errors in equations (B-1) through (B-6) of the original publication, but there are three sign errors in the summary of the results in table 1 of Gallet and Courtillot (1989), namely in C_{xz}, C_{yz} and C_{zz}. To show that we have to look at equations (B-4), (B-5) and (B-6), which are:

$$B_x = -\frac{\partial V}{\partial x} = \frac{\mu_0}{4\pi}\frac{M_x \sin\delta - M_z\cos\delta}{\cos\delta}\int_{-R}^{R} K(\xi,x,y,z)(x-\xi)d\xi \tag{A.62}$$

$$B_y = -\frac{\partial V}{\partial y} = \frac{\mu_0}{4\pi}\frac{M_x \sin\delta - M_z\cos\delta}{\cos\delta}\int_{-R}^{R} L(\xi,x,y,z)d\xi \tag{A.63}$$

$$B_z = -\frac{\partial V}{\partial z} = \frac{\mu_0}{4\pi}\frac{M_x \sin\delta - M_z\cos\delta}{\cos\delta}\int_{-R}^{R} K(\xi,x,y,z)[z + (R-\xi)\tan\delta]d\xi \tag{A.64}$$

These equations are used to determine the coefficients of the matrix C_{ij} that connects the magnetic field and the magnetization:

$$\begin{pmatrix} B_x \\ B_y \\ B_z \end{pmatrix} = \begin{pmatrix} C_{xx} & C_{xy} & C_{xz} \\ C_{yx} & C_{yy} & C_{yz} \\ C_{zx} & C_{zy} & C_{zz} \end{pmatrix} \begin{pmatrix} M_x \\ M_y \\ M_z \end{pmatrix} \tag{A.65}$$

The lateral surface of the cylinder only contributes to the diagonal components of C_{ij}, whereas the upper ellipse contributes to all elements. For example, Eq. A.62 gives a contribution to C_{xx} and C_{xz}:

$$\begin{aligned} B_x &= \frac{\mu_0}{4\pi}\frac{M_x \sin\delta - M_z\cos\delta}{\cos\delta}\int_{-R}^{R} K(\xi,x,y,z)(x-\xi)d\xi \\ &= \frac{\mu_0}{4\pi}(M_x\tan\delta - M_z)\int_{-R}^{R} K(\xi,x,y,z)(x-\xi)d\xi \\ &= \frac{\mu_0}{4\pi}M_x\tan\delta\int_{-R}^{R} K(\xi,x,y,z)(x-\xi)d\xi + M_z C_{xz} \end{aligned} \tag{A.66}$$

with

$$C_{xz} = -\frac{\mu_0}{4\pi}\int_{-R}^{R} K(\xi,x,y,z)(x-\xi)d\xi \tag{A.67}$$

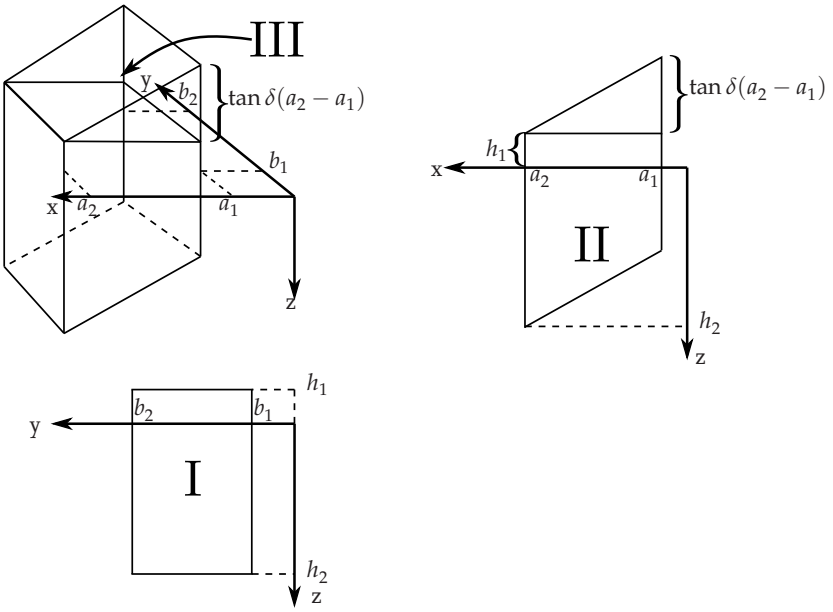

Figure A.5.: Coordinate Systems for the inclined prism.

Here, the sign of the equation given in Gallet and Courtillot (1989) differs. In a similar fashion, the signs of C_{yz} and C_{zz} have to be changed. For C_{xz} and C_{yz}, this can also seen by calculating explicit values for a given cylinder; as partial derivatives commute, C_{ij} needs to be a symmetric tensor, that is $C_{ij} = C_{ji}$. This is not the case when using the signs as given in the original publication.

A.4. Inclined Prism

The calculations presented here are similar to the ones given in Hjelt (1972), but I am going to use a different coordinate system that is more appropriate for a use of the model to calculate magnetic fields in boreholes. I am also going to include more details of the calculation, as Hjelt's publication omits many steps, which makes it quite difficult to follow. The model and the coordinate system used is shown in Fig. A.5. For the calculations, the model is split into the three faces of the prism and each face is integrated over separately.

A.4.1. Face I - YZ

First, I calculate the influence due to the rectangular faces of the prism, using Eq. 2.20. Here, $M^I = \vec{M}(\vec{r}')\hat{n} = \pm M_x$, depending on whether the left or the right face of the prism is considered.

$$\begin{aligned} B_x^I &= -\frac{\mu_0 M^I}{4\pi}\frac{\partial}{\partial x}\int_{h_1}^{h_2}\mathrm{d}z\int_{b_1}^{b_2}\mathrm{d}y\frac{1}{\sqrt{(x-x')^2+(y-y')^2+(z-z')^2}} \\ &= \frac{\mu_0 M^I}{4\pi}\int_{h_1}^{h_2}\mathrm{d}z'\int_{b_1}^{b_2}\mathrm{d}y'\frac{x-x'}{((x-x')^2+(y-y')^2+(z-z')^2)^{3/2}} \end{aligned} \tag{A.68}$$

Now we substitute $x - x' = x_0$, $y - y' = y_0$ and $z - z' = z_0$, which results in $dy' = -dy_0$ and $dz' = -dz_0$ and a corresponding change in the limits of the integration:

$$\begin{aligned}
B_x^I &= \frac{\mu_0 M^I}{4\pi} \int_{z-h_1}^{z-h_2} \mathrm{d}z_0 \int_{y-b_1}^{y-b_2} \mathrm{d}y_0 \frac{x_0}{(x_0^2 + y_0^2 + z_0^2)^{3/2}} \\
&= \frac{\mu_0 M^I}{4\pi} \int_{z-h_1}^{z-h_2} \mathrm{d}z_0 \frac{x_0 y_0}{(x_0^2 + z_0^2)\sqrt{x_0^2 + y_0^2 + z_0^2}} \Bigg|_{y_0=y-b_1}^{y_0=y-b_2} \\
&= \frac{\mu_0 M^I}{4\pi} \arctan\left(\frac{y_0 z_0}{x_0 \sqrt{x_0^2 + y_0^2 + z_0^2}} \right) \Bigg|_{y_0=y-b_1}^{y_0=y-b_2} \Bigg|_{z_0=z-h_1}^{z_0=z-h_2} \\
&= \frac{\mu_0 M^I}{4\pi} \arctan\left(\frac{(y-y')(z-z')}{x_0 \sqrt{x_0^2 + (y-y')^2 + (z-z')^2}} \right) \Bigg|_{y'=b_1}^{y'=b_2} \Bigg|_{z'=h_1}^{z'=h_2}
\end{aligned} \tag{A.69}$$

$$\begin{aligned}
B_y^I &= -\frac{\mu_0 M^I}{4\pi} \frac{\partial}{\partial y} \int_{h_1}^{h_2} \mathrm{d}z \int_{b_1}^{b_2} \mathrm{d}y \frac{1}{\sqrt{(x-x')^2 + (y-y')^2 + (z-z')^2}} \\
&= \frac{\mu_0 M^I}{4\pi} \int_{h_1}^{h_2} \mathrm{d}z' \int_{b_1}^{b_2} \mathrm{d}y' \frac{y - y'}{((x-x')^2 + (y-y')^2 + (z-z')^2)^{3/2}} \\
&= \frac{\mu_0 M^I}{4\pi} \int_{z-h_1}^{z-h_2} \mathrm{d}z_0 \int_{y-b_1}^{y-b_2} \mathrm{d}y_0 \frac{y_0}{(x_0^2 + y_0^2 + z_0^2)^{3/2}} \\
&= -\frac{\mu_0 M^I}{4\pi} \int_{z-h_1}^{z-h_2} \mathrm{d}z_0 \frac{1}{\sqrt{x_0^2 + y_0^2 + z_0^2}} \Bigg|_{y_0=y-b_1}^{y_0=y-b_2} \\
&= -\frac{\mu_0 M^I}{4\pi} \log\left(\sqrt{x_0^2 + y_0^2 + z_0^2} + z_0 \right) \Bigg|_{y_0=y-b_1}^{y_0=y-b_2} \Bigg|_{z_0=z-h_1}^{z_0=z-h_2} \\
&= -\frac{\mu_0 M^I}{4\pi} \log\left(\sqrt{x_0^2 + (y-y')^2 + (z-z')^2} + (z-z') \right) \Bigg|_{y'=b_1}^{y'=b_2} \Bigg|_{z'=h_1}^{z'=h_2}
\end{aligned} \tag{A.70}$$

$$\begin{aligned}
B_z^I &= -\frac{\mu_0 M^I}{4\pi} \frac{\partial}{\partial z} \int_{h_1}^{h_2} \mathrm{d}z \int_{b_1}^{b_2} \mathrm{d}y \frac{1}{\sqrt{(x-x')^2 + (y-y')^2 + (z-z')^2}} \\
&= \frac{\mu_0 M^I}{4\pi} \int_{h_1}^{h_2} \mathrm{d}z' \int_{b_1}^{b_2} \mathrm{d}y' \frac{z - z'}{((x-x')^2 + (y-y')^2 + (z-z')^2)^{3/2}} \\
&= \frac{\mu_0 M^I}{4\pi} \int_{z-h_1}^{z-h_2} \mathrm{d}z_0 \int_{y-b_1}^{y-b_2} dy_0 \frac{z_0}{(x_0^2 + y_0^2 + z_0^2)^{3/2}} \\
&= -\frac{\mu_0 M^I}{4\pi} \log\left(\sqrt{x_0^2 + y_0^2 + z_0^2} + y_0 \right) \Bigg|_{y_0=y-b_1}^{y_0=y-b_2} \Bigg|_{z_0=z-h_1}^{z_0=z-h_2} \\
&= -\frac{\mu_0 M^I}{4\pi} \log\left(\sqrt{x_0^2 + (y-y')^2 + (z-z')^2} + (y-y') \right) \Bigg|_{y'=b_1}^{y'=b_2} \Bigg|_{z'=h_1}^{z'=h_2}
\end{aligned} \tag{A.71}$$

A.4.2. Face II - XZ

Here, z' depends on x'. We define $h_1(x') = h_1 - \tan\delta(a_2 - x')$ and $h_2(x') = h_2 - \tan\delta(a_2 - x')$. Other substitutions that are used if appropriate are $x - x' = x_0$, $y - y' = y_0$ and $z - z' = z_0$, which leads to $h_1(x_0) = z - h_1 + \tan\delta(a_2 + x_0 - x) = m \cdot x_0 + t_1$ and $h_2(x_0) = z - h_2 + \tan\delta(a_2 + x_0 - x) = m \cdot x_0 + t_2$ with $m = \tan\delta$ and $t_{1/2} = z - h_{1/2} + \tan\delta(a_2 - x)$. Here, $M^{II} = \vec{M}(\vec{r}')\hat{n} = \pm M_y$, depending on whether the back or the front face is calculated.

$$
\begin{aligned}
B_x^{II} &= -\frac{\mu_0 M^{II}}{4\pi}\frac{\partial}{\partial x}\int_{a_1}^{a_2}\mathrm{d}x'\int_{h_1(x')}^{h_2(x')}\mathrm{d}z'\frac{1}{\sqrt{(x-x')^2+(y-y')^2+(z-z')^2}} \\
&= -\frac{\mu_0 M^{II}}{4\pi}\int_{a_1}^{a_2}\mathrm{d}x'\int_{h_1(x')}^{h_2(x')}\mathrm{d}z'\frac{x-x'}{[(x-x')^2+(y-y')^2+(z-z')^2]^{3/2}} \\
&= -\frac{\mu_0 M^{II}}{4\pi}\int_{x-a_1}^{x-a_2}\mathrm{d}x_0\int_{h_1(x_0)}^{h_2(x_0)}\mathrm{d}z_0\frac{x_0}{[x_0^2+y_0^2+z_0^2]^{3/2}} \\
&= -\frac{\mu_0 M^{II}}{4\pi}\int_{x-a_1}^{x-a_2}\mathrm{d}x_0\frac{x_0 z_0}{(x_0^2+y_0^2)\sqrt{x_0^2+y_0^2+z_0^2}}\Bigg|_{z_0=h_1(x_0)}^{z_0=h_2(x_0)} \\
&= -\frac{\mu_0 M^{II}}{4\pi}\int_{x-a_1}^{x-a_2}\mathrm{d}x_0\frac{x_0(mx_0+t)}{(x_0^2+y_0^2)\sqrt{x_0^2+y_0^2+(mx_0+t)^2}}\Bigg|_{t=t_1}^{t=t_2} \\
&= -\frac{\mu_0 M^{II}}{4\pi}\int_{x-a_1}^{x-a_2}\mathrm{d}x_0\left(\frac{tx_0 - my_0^2}{x_0^2+y_0^2}+m\right)\frac{1}{\sqrt{x_0^2+y_0^2+(mx_0+t)^2}}\Bigg|_{t=t_1}^{t=t_2} \\
&= -\frac{\mu_0 M^{II}}{4\pi}\frac{1}{2}\log\left(\frac{mx_0+t-\sqrt{x_0^2+y_0^2+(mx_0+t)^2}}{mx_0+t+\sqrt{x_0^2+y_0^2+(mx_0+t)^2}}\right) \\
&\quad + \frac{m\log\left(x_0+m(mx_0+t)+\sqrt{1+m^2}\sqrt{(mx_0+t)^2+x_0^2+y_0^2}\right)}{\sqrt{1+m^2}}\Bigg|_{t=t_1}^{t=t_2}\Bigg|_{x_0=x-a_1}^{x_0=x-a_2}
\end{aligned}
\tag{A.72}
$$

$$
\begin{aligned}
B_y^{II} &= -\frac{\mu_0 M^{II}}{4\pi}\frac{\partial}{\partial y}\int_{a_1}^{a_2}dx'\int_{h_1(x')}^{h_2(x')}dz'\frac{1}{\sqrt{(x-x')^2+(y-y')^2+(z-z')^2}} \\
&= \frac{\mu_0 M^{II}}{4\pi}\int_{a_1}^{a_2}\mathrm{d}x'\int_{h_1(x')}^{h_2(x')}\mathrm{d}z'\frac{y-y'}{((x-x')^2+(y-y')^2+(z-z')^2)^{3/2}} \\
&= \frac{\mu_0 M^{II}}{4\pi}\int_{x-a_1}^{x-a_2}\mathrm{d}x_0\int_{h_1(x_0)}^{h_2(x_0)}\mathrm{d}z_0\frac{y_0}{(x_0^2+y_0^2+z_0^2)^{3/2}} \\
&= \frac{\mu_0 M^{II}}{4\pi}\int_{x-a_1}^{x-a_2}\mathrm{d}x_0\frac{y_0 z_0}{(x_0^2+y_0^2)\sqrt{x_0^2+y_0^2+z_0^2}}\Bigg|_{z_0=mx_0+t_1}^{z_0=mx_0+t_2} \\
&= \frac{\mu_0 M^{II}}{4\pi}\int_{x-a_1}^{x-a_2}\mathrm{d}x_0\frac{y_0(mx_0+t)}{(x_0^2+y_0^2)\sqrt{x_0^2+y_0^2+(mx_0+t)^2}}\Bigg|_{t=t_1}^{t=t_2}
\end{aligned}
\tag{A.73}
$$

$$= -\frac{\mu_0 M^{II}}{4\pi} \arctan\left(\frac{m y_0^2 - t x_0}{y_0\sqrt{(mx_0+t)^2 + x_0^2 + y_0^2}}\right)\Bigg|_{t=t_1}^{t=t_2}\Bigg|_{x_0=x-a_1}^{x_0=x-a_2}$$

$$= -\frac{\mu_0 M^{II}}{4\pi} \arctan\left(\frac{m y_0^2 - (z-h+m(a_2-x))(x-x')}{y_0\sqrt{(m(x-x')+z-h+m(a_2-x))^2+(x-x')^2+y_0^2}}\right)\Bigg|_{h=h_1}^{h=h_2}\Bigg|_{x'=a_1}^{x'=a_2}$$

$$= -\frac{\mu_0 M^{II}}{4\pi} \arctan\left(\frac{m y_0^2 - (z-h+m(a_2-x))(x-x')}{y_0\sqrt{(z-h+m(a_2-x'))^2+(x-x')^2+y_0^2}}\right)\Bigg|_{h=h_1}^{h=h_2}\Bigg|_{x'=a_1}^{x'=a_2}$$

$$\begin{aligned}
B_z^{II} &= -\frac{\mu_0 M^{II}}{4\pi}\frac{\partial}{\partial z}\int_{a_1}^{a_2} \mathrm{d}x' \int_{h_1(x')}^{h_2(x')} \mathrm{d}z' \frac{1}{\sqrt{(x-x')^2+(y-y')^2+(z-z')^2}} \\
&= \frac{\mu_0 M^{II}}{4\pi}\int_{a_1}^{a_2} \mathrm{d}x' \int_{h_1(x')}^{h_2(x')} \mathrm{d}z' \frac{z-z'}{((x-x')^2+(y-y')^2+(z-z')^2)^{3/2}} \\
&= \frac{\mu_0 M^{II}}{4\pi}\int_{a_1}^{a_2} \mathrm{d}x' \frac{1}{\sqrt{(x-x')^2+(y-y')^2+(z-z')^2}}\Bigg|_{z'=h_1(x')}^{z'=h_2(x')} \\
&= -\frac{\mu_0 M^{II}}{4\pi}\int_{x-a_1}^{x-a_2} \mathrm{d}x_0 \frac{1}{\sqrt{x_0^2+y_0^2+(mx_0+t)^2}}\Bigg|_{t=t_1}^{t=t_2} \\
&= -\frac{\mu_0 M^{II}}{4\pi}\frac{\log\left(x_0+m(t+mx_0)+\sqrt{1+m^2}\sqrt{(mx_0+t)^2+x_0^2+y_0^2}\right)}{\sqrt{1+m^2}}\Bigg|_{t=t_1}^{t=t_2}\Bigg|_{x_0=x-a_1}^{x_0=x-a_2} \\
&= -\frac{\mu_0 M^{II}}{4\pi}\frac{1}{\sqrt{1+m^2}}\log\big((x-x')+m(z-h+m(a_2-x)+m(x-x'))+ \\
&\sqrt{1+m^2}\sqrt{(m(x-x')+z-h+m(a_2-x))^2+(x-x')^2+y_0^2}\big)\Big|_{h=h_1}^{h=h_2}\Big|_{x'=a_1}^{x'=a_2} \\
&= -\frac{\mu_0 M^{II}}{4\pi}\frac{1}{\sqrt{1+m^2}}\log\Big((x-x')+m(z-h+m(a_2-x'))+ \\
&\sqrt{1+m^2}\sqrt{(z-h+m(a_2-x'))^2+(x-x')^2+y_0^2}\Big)\Big|_{h=h_1}^{h=h_2}\Big|_{x'=a_1}^{x'=a_2}
\end{aligned} \tag{A.74}$$

A.4.3. Face III - XY

For this face of the prism, several things have to be taken into account. First of all, the same substitutions as for the other faces can be used to simplify the equations. Here, the product of the magnetization vector with the outer normal of the surface gives $M^{III} = \vec{M}(\vec{r}')\hat{n} = \pm\sin(\delta)M_x \mp \cos(\delta)M_z$, depending on whether the lower or the upper face of the prism (in respect to the z coordinate) is calculated. Also, the surface element is given by $dS = dx'dy' / \cos\delta$.

$$B_x^{III} = -\frac{\mu_0}{4\pi}\frac{M^{III}}{\cos\delta}\frac{\partial}{\partial x}\int_{a_1}^{a_2} \mathrm{d}x' \int_{b_1}^{b_2} \mathrm{d}y' \frac{1}{\sqrt{(x-x')^2+(y-y')^2+(z-z')^2}}$$

$$
\begin{aligned}
&= \frac{\mu_0 M^{III}}{4\pi\cos\delta}\int_{a_1}^{a_2}\mathrm{d}x'\int_{b_1}^{b_2}\mathrm{d}y'\frac{x-x'}{((x-x')^2+(y-y')^2+(z-z')^2)^{3/2}}\\
&= \frac{\mu_0 M^{III}}{4\pi\cos\delta}\int_{x-a_1}^{x-a_2}\mathrm{d}x_0\int_{y-b_1}^{y-b_2}\mathrm{d}y_0\frac{x_0}{(x_0^2+y_0^2+z_0^2)^{3/2}}\\
&= \frac{\mu_0 M^{III}}{4\pi\cos\delta}\int_{x-a_1}^{x-a_2}\mathrm{d}x_0\int_{y-b_1}^{y-b_2}\mathrm{d}y_0\frac{x_0}{(x_0^2+y_0^2+(mx_0+t)^2)^{3/2}} \qquad \text{(A.75)}\\
&= -\frac{\mu_0 M^{III}}{4\pi\cos\delta}\int_{y-b_1}^{y-b_2}\mathrm{d}y_0\frac{y_0^2+t(mx_0+t)}{(t^2+(1+m^2)y_0^2)\sqrt{(mx_0+t)^2+x_0^2+y_0^2}}\Bigg|_{x_0=x-a_1}^{x_0=x-a_2}\\
&= -\frac{\mu_0 M^{III}}{4\pi\cos\delta}\frac{1}{1+m^2}\left(m\arctan\left(\frac{(x_0+m(mx_0+t))y_0}{t\sqrt{(mx_0+t)^2+x_0^2+y_0^2}}\right)\right.\\
&\left.+\log\left(y_0+\sqrt{(mx_0+t)^2+x_0^2+y_0^2}\right)\right)\Bigg|_{x_0=x-a_1}^{x_0=x-a_2}\Bigg|_{y_0=y-b_1}^{y_0=y-b_2}
\end{aligned}
$$

$$
\begin{aligned}
B_y^{III} &= -\frac{\mu_0 M^{III}}{4\pi\cos\delta}\frac{\partial}{\partial y}\int_{a_1}^{a_2}\mathrm{d}x'\int_{b_1}^{b_2}\mathrm{d}y'\frac{1}{\sqrt{(x-x')^2+(y-y')^2+(z-z')^2}}\\
&= \frac{\mu_0 M^{III}}{4\pi\cos\delta}\int_{a_1}^{a_2}\mathrm{d}x'\int_{b_1}^{b_2}\mathrm{d}y'\frac{y-y'}{((x-x')^2+(y-y')^2+(z-z')^2)^{3/2}}\\
&= \frac{\mu_0 M^{III}}{4\pi\cos\delta}\int_{x-a_1}^{x-a_2}\mathrm{d}x_0\int_{y-b_1}^{y-b_2}\mathrm{d}y_0\frac{y_0}{(x_0^2+y_0^2+z_0^2)^{3/2}}\\
&= -\frac{\mu_0 M^{III}}{4\pi\cos\delta}\int_{x-a_1}^{x-a_2}\mathrm{d}x_0\frac{1}{\sqrt{x_0^2+y_0^2+z_0^2}}\Bigg|_{y_0=y-b_1}^{y_0=y-b_2} \qquad \text{(A.76)}\\
&= -\frac{\mu_0 M^{III}}{4\pi\cos\delta}\int_{x-a_1}^{x-a_2}\mathrm{d}x_0\frac{1}{\sqrt{x_0^2+y_0^2+(mx_0+t)^2}}\Bigg|_{y_0=y-b_1}^{y_0=y-b_2}\\
&= -\frac{\mu_0 M^{III}}{4\pi\cos\delta}\frac{1}{\sqrt{1+m^2}}\cdot\\
&\log\left(x_0+m(mx_0+t)+\sqrt{1+m^2}\sqrt{(mx_0+t)^2+x_0^2+y_0^2}\right)\Bigg|_{y_0=y-b_1}^{y_0=y-b_2}\Bigg|_{x_0=x-a_1}^{x_0=x-a_2}
\end{aligned}
$$

$$
\begin{aligned}
B_z^{III} &= -\frac{\mu_0 M^{III}}{4\pi\cos\delta}\frac{\partial}{\partial z}\int_{a_1}^{a_2}\mathrm{d}x'\int_{b_1}^{b_2}\mathrm{d}y'\frac{1}{\sqrt{(x-x')^2+(y-y')^2+(z-z')^2}}\\
&= \frac{\mu_0 M^{III}}{4\pi\cos\delta}\int_{a_1}^{a_2}\mathrm{d}x'\int_{b_1}^{b_2}\mathrm{d}y'\frac{z-z'}{((x-x')^2+(y-y')^2+(z-z')^2)^{3/2}}\\
&= \frac{\mu_0 M^{III}}{4\pi\cos\delta}\int_{x-a_1}^{x-a_2}\mathrm{d}x_0\int_{y-b_1}^{y-b_2}\mathrm{d}y_0\frac{z_0}{(x_0^2+y_0^2+z_0^2)^{3/2}}\\
&= \frac{\mu_0 M^{III}}{4\pi\cos\delta}\int_{x-a_1}^{x-a_2}\mathrm{d}x_0\int_{y-b_1}^{y-b_2}\mathrm{d}y_0\frac{mx_0+t}{(x_0^2+y_0^2+(mx_0+t)^2)^{3/2}} \qquad \text{(A.77)}
\end{aligned}
$$

$$= \frac{\mu_0 M^{III}}{4\pi \cos\delta} \int_{y-b_1}^{y-b_2} \frac{tx_0 - my_0^2}{(t^2 + (1+m^2)y_0^2)\sqrt{(mx_0+t)^2 + x_0^2 + y_0^2}} \Bigg|_{x_0=x-a_1}^{x_0=x-a_2}$$

$$= \frac{\mu_0 M^{III}}{4\pi \cos\delta} \frac{1}{1+m^2} \left[\arctan\left(\frac{(x_0 + m(mx_0+t))y_0}{t\sqrt{(mx_0+t)^2 + x_0^2 + y_0^2}} \right) \right.$$

$$\left. - m \log\left(y_0 + \sqrt{(mx_0+t)^2 + x_0^2 + y_0^2} \right) \right] \Bigg|_{x_0=x-a_1}^{x_0=x-a_2} \Bigg|_{y_0=y-b_1}^{y_0=y-b_2}$$

A.5. Arbitrary Polyhedra

Guptasarma and Singh (1999) show an efficient way of calculating the magnetic and gravitational field of arbitrary polyhedrons, which is based on using line integrals along the edges of the surfaces bounding the body and exploiting a relationship between the solid angle subtended by the polygons bounding the polyhedron and their magnetic field.

In the following, I am reproducing their calculations in order to facilitate the understanding of the Matlab implementation given at the end of this section. We are going to consider the magnetic field of a single polygon at the origin of the coordinate system and thus set $\vec{r} = 0$. By multiplying Eq. 2.20 with a unit vector $\hat{e}$ and using $\nabla \frac{1}{r'} = -\frac{\vec{r}'}{r'^3}$, we get

$$B_e = \frac{\mu_0}{4\pi} \int_S \vec{M} \cdot \hat{n} \frac{\vec{r}' \cdot \hat{e}}{r'^3} \, \mathrm{d}S' \tag{A.78}$$

where B_e is the magnetic field component in direction of $\hat{e}$. In order to simplify the equations, I am dropping the superscript ' in the following.

By choosing $\hat{e} = \hat{x}_i$ to be a unit vector in the direction of axis x_i of the coordinate system and defining $\sigma = \vec{M} \cdot \hat{n}$, where $\hat{n}$ is the normal vector of the surface with cartesian components l, m and n, the magnetic field components are given by :

$$\begin{aligned} B_x &= \frac{\mu_0}{4\pi} \sigma \int_S \frac{x}{r^3} \, \mathrm{d}S \\ B_y &= \frac{\mu_0}{4\pi} \sigma \int_S \frac{y}{r^3} \, \mathrm{d}S \\ B_z &= \frac{\mu_0}{4\pi} \sigma \int_S \frac{z}{r^3} \, \mathrm{d}S \end{aligned} \tag{A.79}$$

Guptasarma and Singh (1999) then use that

$$\begin{aligned} \hat{n} \cdot (\nabla \times \frac{\hat{x}}{r}) &= \frac{-mz + ny}{r^3} \\ \hat{n} \cdot (\nabla \times \frac{\hat{y}}{r}) &= \frac{-nx + lz}{r^3} \\ \hat{n} \cdot (\nabla \times \frac{\hat{z}}{r}) &= \frac{mx + ly}{r^3} \end{aligned} \tag{A.80}$$

If we compare Eq. A.79 and Eq. A.80 we see that they share common terms. Guptasarma

and Singh (1999) then integrate Eq. A.80 over the surface of the polygon and get

$$\begin{aligned} P &= \int_S \hat{n} \cdot (\nabla \times \frac{\hat{x}}{r}) = \frac{4\pi}{\sigma\mu_0} \left(-nB_y + mB_z\right) \\ Q &= \int_S \hat{n} \cdot (\nabla \times \frac{\hat{y}}{r}) = \frac{4\pi}{\sigma\mu_0} \left(nB_x - lB_z\right) \\ R &= \int_S \hat{n} \cdot (\nabla \times \frac{\hat{z}}{r}) = \frac{4\pi}{\sigma\mu_0} \left(-mB_x + lB_y\right) \end{aligned} \tag{A.81}$$

According to Stokes' Theorem:

$$\int_S \hat{n} \cdot (\nabla \times \frac{\hat{x}}{r}) \, \mathrm{d}S = \oint \frac{\hat{x}}{r} \, \mathrm{d}r \tag{A.82}$$

Guptasarma and Singh (1999) give the result of the line integral over each edge i of the polygon as

$$\begin{aligned} P_i &= IL_x \\ Q_i &= IL_y \\ R_i &= IL_z \end{aligned} \tag{A.83}$$

with $L_x = x_2 - x_1$, $L_y = y_2 - y_1$ and $L_z = z_2 - z_1$, where (x_1, y_1, z_1) are the coordinates of the beginning and (x_2, y_2, z_2) the coordinates of the end of the edge. With $L = (L_x^2 + L_y^2 + L_z^2)^{1/2}$ being the length of the edge, and $b = 2(x_1 L_x + y_1 L_y + z_1 L_z)$, I is given by:

$$\begin{aligned} I &= \frac{1}{L} \frac{\ln \left[L^2 + b^2 + r_1\right]^{1/2]} + L + \frac{b}{2L}}{r + \frac{b}{2L}}, \text{ for } r + \frac{b}{2L} \neq 0 \\ I &= \frac{1}{L} \ln \left[\frac{|L - r|}{r}\right], \qquad\qquad \text{for } r + \frac{b}{2L} = 0 \end{aligned} \tag{A.84}$$

The solid angle Ω subtended by the polygon at the origin is given by (see e.g. Kaufman, 1992):

$$\Omega = \int_S \frac{\vec{r}\hat{n}}{r^3} \, \mathrm{d}S \tag{A.85}$$

Using Eq. A.78 to calculate the magnetic field at the origin in direction of the normal vector $\hat{n}$ of the polygon, we get:

$$\hat{n} \cdot \vec{B} = \frac{\mu_0}{4\pi} \int_S \sigma \frac{\vec{r} \cdot \hat{n}}{r^3} \, \mathrm{d}S. \tag{A.86}$$

Guptasarma and Singh (1999) exploit that, using Eq. A.85 and Eq. A.86, the solid angle Ω subtended by the polygon at the origin can be written as

$$\Omega = \frac{4\pi}{\sigma\mu_0} (lB_x + mB_y + nB_z) \tag{A.87}$$

Table A.1.: Calculation Time

No. Faces	No. Datapoints	Time (this thesis) [a]	Time (Bär, 2012) [b]
8	1001	-	1.1 s
120	1001	-	15.1 s
180	1001	0.5 s	-
760	1001	1.7 s	-
1224	1001	-	218.6 s
1560	1001	7.2 s	-
4900	1001	11.1 s	-
5040	1001	-	1821.5 s
16020	1001	37.6 s	-

[a] Intel Core-i3 370M with 2 GB of memory
[b] Intel Core-i5 2500k with 8 GB of memory

Then, using $l^2 + m^2 + n^2 = 1$, $P = \sum_i P_i$, $Q = \sum_i Q_i$, $R = \sum_i R_i$, and combining Eq. A.81 and Eq. A.87, they derive a simple solution for the magnetic field of a polygon:

$$\begin{aligned} B_x &= \frac{\mu_0 \sigma}{4\pi}(l\Omega + nQ - mR) \\ B_y &= \frac{\mu_0 \sigma}{4\pi}(m\Omega + lR - nP) \\ B_z &= \frac{\mu_0 \sigma}{4\pi}(n\Omega + mP - lQ). \end{aligned} \tag{A.88}$$

To calculate the magnetic field, one only needs an additional formula to calculate the solid angle. The following code (Listing A.1) is based on Sing and Guptasarma (2001), but uses some of Matlabs vectorization features to significantly increase the speed of calculations. In contrary to the code of the original publication, which is able to use any polygons as boundary surfaces, it requires bodies composed of triangles. By doing so, I am following an idea given by Bär (2012), which allows to use an efficient algorithm to calculate the solid angle subtended by the triangles given by Oosterom and Strackee (1983).

Bär (2012) does not give the detailed implementation of its algorithms and also calculates both gravitational and magnetic fields, so a direct comparison of his and my implementation is not possible. However, a comparison of the calculation times of the following algorithm to the calculation times given in his thesis suggests a 150-fold speedup (see Tab. A.1 for details). To run the calculations, Bär (2012) used an Intel Core-i5 2500k with 8 GB of memory, I am using an Intel Core-i3 370M with 2 GB of memory.

To demonstrate the possibilities of the algorithm, Fig. A.6 shows an irregularly shaped body intersected by a borehole of approximately circular shape with a radius of 0.15 m, which is close to the average value of the borehole radii of Expedition 330. Figure A.7 shows the magnetic field that would be measured along the axis of the borehole if the body was homogeneously magnetized with a magnetization of 1 $^{A}/_{m}$ in x-, 2 $^{A}/_{m}$ in y- and

3 A/m in z-direction. The geometry of the body is based on an early model of the comet Churyumov-Gerasimenko (U. Auster, personal communication), but has been scaled down by a factor of 1000. In contrast to the model displayed here, Churyumov-Gerasimenko was found to be nonmagnetic (Auster et al., 2015). The comet was chosen as an example as the Rosetta mission, whose magnetometer was built at the IGEP in Braunschweig, reached the comet during the writing of this thesis.

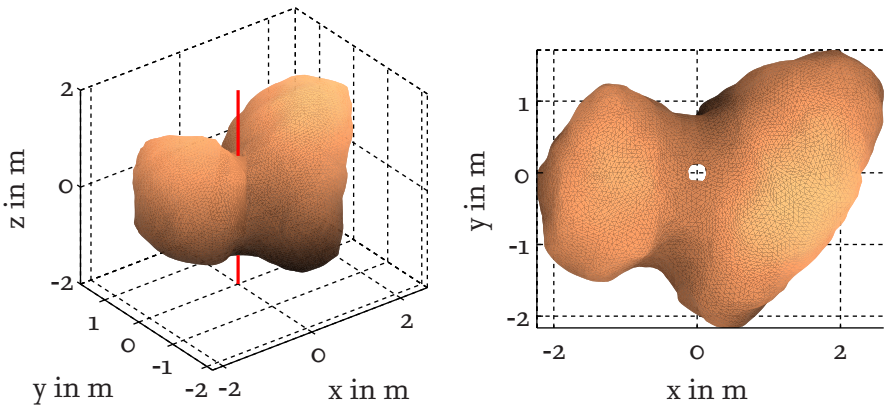

Figure A.6.: Irregularly shaped body intersected by a borehole of 0.15 m radius. Geometry data courtesy of U. Auster, pers. comm.

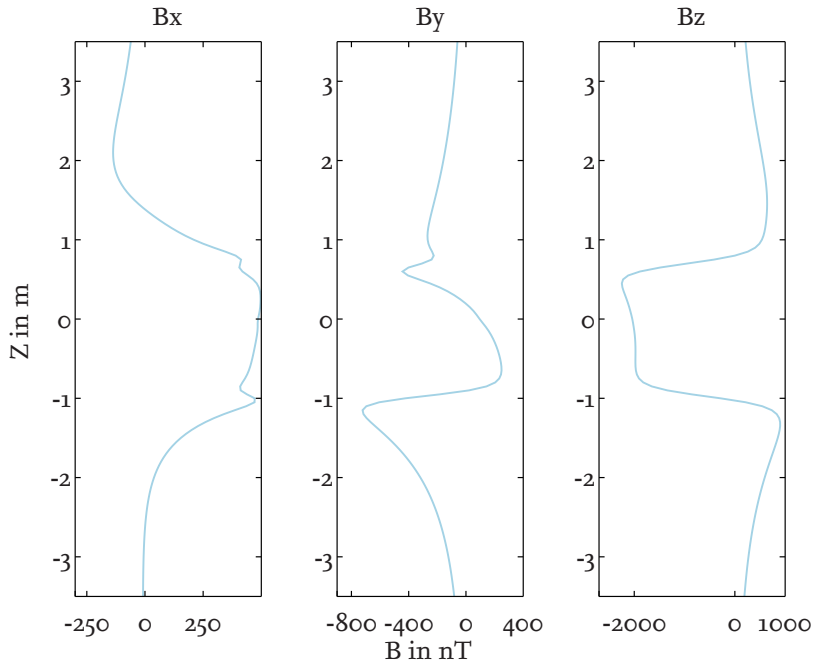

Figure A.7.: Magnetic field inside the borehole of the irregularly shaped body shown in Fig. A.6, assuming a homogeneous magnetization of 1 A/m in x-, 2 A/m in y- and 3 A/m in z-direction.

Listing A.1: Fast Implementation of the algorithm given by Sing and Guptasarma (2001)

```
function B = MagPolyhedron(Face, Vertices, Un, M, X, Y, Z)
    %Input: Faces, Vertices according to their Matlab definition
    %All faces have to be triangles
    %Un = outward pointing normals
    %M = [Mx My Mz], Magnetization
    %X, Y, Z : Row vectors, coordinates for the calculation of the field
    % Output: Magnetic field in nT
    %To reduce the memory footprint, coordinates are divided into chunks, if necessary
    %maxmem sets the maximum average array size in MB
    maxmem=20;

    Nf = size(Face,1);
    rg = [X(:) Y(:) Z(:)];
    Ndata = size(rg,1);

    Pd = (Un * M'); %Pole densities

    avgmem = Nf*3*Ndata*8/(1024^2);

    if avgmem>maxmem
        c = Nf*3*8/(1024^2);
        step = floor(maxmem/c);
    else
        step = length(X);
    end

    B = zeros(Ndata,3);

    for jj = 1:step:Ndata
        ia = jj;
        if ia+step>Ndata
            ie = Ndata;
        else
            ie = ia+step-1;
        end
        r = rg(ia:ie,:);
        chunksize = ie-ia+1;

        %Calculate matrices that contain the edges of all triangles
        %corrected to the origin
        %1) Edges of all Triangles
        P1 = Vertices(Face(:,1), :);
        P2 = Vertices(Face(:,2), :);
        P3 = Vertices(Face(:,3), :);
        %2)Reshape and subtract point of observation.
        % All Nf rows, the triangles repeat, but their coordinates are
        % shifted according to the respective point of observation
        % size(P1r)=[Nf*Nd,3]
        rr = reshape(repmat(r',Nf,1),3,Nf*chunksize)' ;
        P1r = repmat(P1,chunksize,1) - rr ;
        P2r = repmat(P2,chunksize,1) - rr ;
        P3r = repmat(P3,chunksize,1) - rr  ;
        clear r rr P1 P2 P3

        %Calculate solid angle for all faces and points of observation
        angle = SolidAngle(P1r, P2r, P3r, Nf, chunksize); %size(angle)=[Nf,Nd]
        %Length of all edges
        LX = [P2r(:,1)-P1r(:,1) P3r(:,1)-P2r(:,1) P1r(:,1)-P3r(:,1)];
        LY = [P2r(:,2)-P1r(:,2) P3r(:,2)-P2r(:,2) P1r(:,2)-P3r(:,2)];
        LZ = [P2r(:,3)-P1r(:,3) P3r(:,3)-P2r(:,3) P1r(:,3)-P3r(:,3)];
```

```
        L = sqrt(LX.^2+LY.^2+LZ.^2);

        Px = [P1r(:,1) P2r(:,1) P3r(:,1)];
        Py = [P1r(:,2) P2r(:,2) P3r(:,2)];
        Pz = [P1r(:,3) P2r(:,3) P3r(:,3)];

        b = 2*(Px.*LX + Py.*LY + Pz.*LZ);

        clear Px Py Pz
        %distances from the origin to the beginning of each edge
        r1 = [sqrt(sum(P1r.^2,2)) sqrt(sum(P2r.^2,2)) sqrt(sum(P3r.^2,2))];
        clear P1r P2r P3r
        b2 = b./(2*L);

        I1 = (1./L).*log((sqrt(L.*L+b+r1.*r1)+L+b2)./(r1+b2));
        I2 = (1./L).*log(abs(L-r1)./r1);
        temp = r1+b2;
        clear r1 b b2 L
        I=I1.*(temp~=0)+I2.*(temp==0);
        clear temp I1 I2
        P = sum(I.*LX,2);
        Q = sum(I.*LY,2);
        R = sum(I.*LZ,2);

        P = reshape(P,Nf,chunksize);
        Q = reshape(Q,Nf,chunksize);
        R = reshape(R,Nf,chunksize);
        %calculate products. S corresponds to Omega in the original publication
        lS = bsxfun(@times, Un(:,1), angle);
        nQ = bsxfun(@times, Un(:,3), Q);
        mR = bsxfun(@times, Un(:,2), R);

        mS = bsxfun(@times, Un(:,2), angle);
        lR = bsxfun(@times, Un(:,1), R);
        nP = bsxfun(@times, Un(:,3), P);

        nS = bsxfun(@times, Un(:,3), angle);
        mP = bsxfun(@times, Un(:,2), P);
        lQ = bsxfun(@times, Un(:,1), Q);

        Hx = sum(bsxfun(@times, (lS+nQ-mR), Pd));
        Hy = sum(bsxfun(@times, (mS+lR-nP), Pd));
        Hz = sum(bsxfun(@times, (nS+mP-lQ), Pd));

        B(ia:ie,:)=[Hx' Hy' Hz']*1e2;
    end
end

function angle=SolidAngle(P1r,P2r,P3r,Nf,Ndata)
    %Calculate the solid angle subtended by a triangle
    %Based on Oosteroom&Strackee
    nP1r = sqrt(sum(P1r.^2,2));
    nP2r = sqrt(sum(P2r.^2,2));
    nP3r = sqrt(sum(P3r.^2,2));
    angle = 2*atan2(dot(P1r,cross(P2r,P3r),2),...
        nP1r.*nP2r.*nP3r+nP1r.*dot(P2r,P3r,2) + nP2r.*dot(P1r,P3r,2) + nP3r.*dot(P1r,
            P2r,2));
    angle = -reshape(angle,Nf,Ndata);
end
```

A.6. Additional Listings

Listing A.2: Horizontal layer inversion using Matlab (Section 6.5.2)

```
function [MxInv,MyInv,MzInv,BInv,Cv,Ch]=bosum_multiple_layer_inversion_v3(BCorr,Z,Ri,
    iterations,number_of_neighbours,fit_limit)
%Calculates Magnetizations for a horizontal layer model.
%Input: BCorr:  corrected magnetic field anomaly in nT
%       Z:      Vertical Position in m (Vector)
%       Ri:     Borehole radius in m (Vector)

BCorr=BCorr*1e-9;
mu0=4*pi*1e-7;

%Initialize empty variables
Bz = zeros(length(BCorr),number_of_iterations);
Bx = Bz; By = Bz;

rx = Bx; ry = Bx; rz = Bx;

Mz = Bx; Mx = Mz; My = Mz;

dMz = Mz; dMx = Mz; dMy = Mz;

%Calculate layer heights
h = zeros(length(Z),1);
for ii=1:length(Z)
        if ii~=length(BCorr)
            h(ii)=abs((Z(ii)-Z(ii+1))/2);
        else
            h(ii)=h(ii-1);
        end
end

%Initial estimate for the magnetization
c1 = 2;
Mz(:,1) = -BCorr(:,3)/(mu0*c1/2);
Mx(:,1) =  BCorr(:,1)/(mu0*c1/4);
My(:,1) =  BCorr(:,2)/(mu0*c1/4);

%% Iterative improvement of magnetization
%Calculate geometric factors of influence and fill into matrix. Use
%number_of_neigbours in each direction

C = zeros(length(BCorr));
datalength = length(BCorr);

for ii = 1:datalength
    first_neighbour = ii-number_of_neighbours;
    last_neighbour = ii+ number_of_neighbours;
    if first_neighbour < 1
        first_neighbour = 1;
    end
    if last_neighbour > datalength
        last_neighbour = datalength;
    end

    for jj = first_neighbour: last_neighbour

        z = (Z(ii)-Z(jj));
```

```
        c = (z+h(ii))/sqrt((z+h(ii))^2+(Ri(ii))^2) -...
         (z-h(ii))/sqrt((z-h(ii))^2+(Ri(ii))^2);

        C(ii,jj)=mu0*c;
    end
end
Cv = -C/2;
Ch = C/4;

iteration = 2;
%Calculate Magnetic Field
Bz(:,1) = Cv*Mz(:,1);
Bx(:,1) = Ch*Mx(:,1);
By(:,1) = Ch*My(:,1);

while iteration < number_of_iterations
    Mz(:,iteration) = Mz(:,iteration-1) + dMz(:,iteration-1);
    Mx(:,iteration) = Mx(:,iteration-1) + dMx(:,iteration-1);
    My(:,iteration) = My(:,iteration-1) + dMy(:,iteration-1);

    Bz(:,iteration) = Cv*Mz(:,iteration);
    Bx(:,iteration) = Ch*Mx(:,iteration);
    By(:,iteration) = Ch*My(:,iteration);

    %Calculate residuals
    rx(:,iteration) = BCorr(:,1) - Bx(:,iteration);
    ry(:,iteration) = BCorr(:,2) - By(:,iteration);
    rz(:,iteration) = BCorr(:,3) - Bz(:,iteration);

    %Test threshold
    for kk = 1:datalength
        if abs(rx(kk,iteration)) <= fit_limit*1e-9;
            rx(kk,iteration) = 0;
        end
        if abs(ry(kk,iteration)) <= fit_limit*1e-9;
            ry(kk,iteration) = 0;
        end
        if abs(rz(kk,iteration)) <= fit_limit*1e-9;
            rz(kk,iteration) = 0;
        end
    end

    % Update Magnetization
    dMz(:,iteration) = -rz(:,iteration)./(mu0*c1/2);
    dMx(:,iteration) =  rx(:,iteration)./(mu0*c1/4);
    dMy(:,iteration) =  ry(:,iteration)./(mu0*c1/4);

    iteration = iteration + 1;
end

BInv  = [Bx(:,iteration-1) By(:,iteration-1) Bz(:,iteration-1)]*1e9;
MxInv = Mx(:,iteration-1);
MyInv = My(:,iteration-1);
MzInv = Mz(:,iteration-1);
```

Listing A.3: Calculation of the apparent inclination using Matlab (Section 6.7.4)

```
clear all

Azimuth = 0:0.5:359;

Dip = 0:0.5:88;

Mt = 1;
inclination = -68;
declination = 0;

MCz = sind(inclination)*Mt;
MCh = cosd(inclination)*Mt;

[DEC,PHI,DELTA] = meshgrid(declination, Azimuth, Dip);
MX = cosd(PHI).*cosd(DEC-PHI).*MCh.*cosd(2*DELTA)+cosd(PHI).*MCz.*sind(2*DELTA)-sind(
    PHI).*sind(DEC-PHI)*MCh;
MY = sind(PHI).*cosd(DEC-PHI).*MCh.*cosd(2*DELTA)+sind(PHI).*MCz.*sind(2*DELTA)+cosd(
    PHI).*sind(DEC-PHI)*MCh;
MZ = MCz*cosd(DELTA).^2-cosd(DEC-PHI).*MCh.*sind(DELTA).*cosd(DELTA);

INC = atan2(MZ, sqrt(MX.^2+MY.^2)) * 180/pi;
INC = squeeze(INC(:,1,:));

figure(1)
imagesc(Dip, Azimuth, INC)
set(gca,'YDir','normal')
xlabel('Layer Dip')
ylabel('Azimuth')
colorbar
title('Apparent Inclination')
```

Acknowledments

I would like to thank a number of people who greatly supported me during my thesis. First of all, Andreas Hördt, who supervised my thesis and gave me the possibility to participate in Expedition 330, and who managed to give an ideal combination of scientific freedom, guidance and support. I thank him for his serenity and trust, and his ability to point out gaps in my lines of argument. I am indebted to Christopher Virgil, who's previous and ongoing work built the foundations for this thesis. Martin Leven helped me to understand the inner workings of the GBM and assisted with all technical problems that occurred during the Expedition. I thank Martin Neuhaus for fruitful discussions and new impulses for our work with the GBM.

I thank Prof. Dr. Glaßmeier for agreeing to co-referee my thesis and for his non-bureaucratic support during my transition to Universität Braunschweig.

I thank all members of the Institut für Geophysik und Extraterrestrische Physik at Universität Braunschweig, who created a wonderful work environment. I enjoyed every minute of the numerous excursions, field trips, barbecue parties and coffee breaks. In particular I would like to thank Anita Przyklenk, who's one of the best office mates one could wish for.

I thank Nicole Mund and Sabine Filbrandt for their invaluable help in administrative matters and Kathrin Gebauer, Ernst Jelting and Bernd Stoll for their support in both official and private technical matters.

I thank Anthony Koppers and Jeff Gee for making the GBM measurements during Expedition 330 possible and for greatly supporting me before, during and after the Expedition. I thank Anthony Koppers, Toshitsugu Yamazaki and Jörg Geldmacher for organizing a successful and instructive Expedition.

I greatly thank the captain and crew of the Joides Resolution and all scientific participants of Expedition 330 for two busy, challenging and rewarding months at sea. In particular, I thank Louise Anderson, who kept my spirits high at all times and who welcomed me to Leicester for the analysis of the FMS datasets. I thank Kerry Swain, Jan-Jurie Kotze and Etienne Claasen for their invaluable technical support. I thank and acknowledge the paleomagnetic team, Jeff Gee, Nicola Pressling, and Hiroyuki Hoshi for providing the NRM data and for their helpful comments.

I also would like to thank my family for their continuous support, not only during this thesis: Mama, Papa, Florian, Benedikt, Maximilian, Anna-Maria, ich danke euch für alles! Marina, vielen Dank für deine Unterstützung bei allem, was ich mir so ausdenke.

The results presented in this thesis rely on the data collected at the magnetic observatories Eyrewell, Macquarie Island and Apia. I thank GNS Science, Geoscience Australia and Ministry of the Natural Resources & Environment - Meteorology Division (Western Samoa)

for supporting their operation and INTERMAGNET for promoting high standards of magnetic observatory practice (www.intermagnet.org). This research used samples and/or data provided by the Integrated Ocean Drilling Program (IODP). All logging data can be accessed via the IODP Log Database and all core data are available via the IODP LIMS Core Database. Equipment tests prior to Expedition 330 were funded by Ocean Leadership. Funding for this research was provided by DFG, project Ho1506/21-1 and Le1293/2-1.